Doctoral Dissertation
Doctoral Program in Materials Science and Technology (37th Cycle)

Electrochemical surface treatments for resorbable and permanent biomedical implants

By
Davide Pupillo
* * * * * *

Supervisor(s):
Prof. Sabrina GRASSINI, Supervisor
Prof. Francesco DI FRANCO, Co-Supervisor

Doctoral Examination Committee:
Prof. Andrea BRENNA, Referee, Polytechnic of Milan, Italy
Prof. Michele FEDEL, Referee, University of Trento, Italy
Prof. Giulio MALUCELLI, Polytechnic of Turin, Italy
Prof. Luigi CALABRESE, University of Messina, Italy
Prof. Maria Vittoria DIAMANTI, Polytechnic of Milan, Italy

Politecnico di Torino
2025

I hereby declare that, the contents and organisation of this dissertation constitute my own original work and does not compromise in any way the rights of third parties, including those relating to the security of personal data.

…….....

Davide Pupillo

Turin, 2025

Summary

Biomaterials are usually defined as materials used in contact with living body to treat or replace any tissue, organ or function in the body. The most important requirement of a biomaterials is the biocompatibility, i.e. they must perform with a specific application without disruption of normal body function. Nowadays, biomaterials are made of metal alloys, ceramics, polymers and their composites. Metallic implants were used as orthopaedic devices for temporary applications (e.g. plate, screw and pins) and permanent ones (e.g. joints). More recently, innovative metallic biomaterials have been used for the reconstruction of both hard and soft tissues using for example NiTi alloys, as shape-memory materials used for cardiovascular stent, and biodegradable metals for bone tissue regeneration. The selection of the metal is related to the specific medical application and can be divided in metals for permanent prosthesis and metals for biodegradable prosthesis. Metals used to realize permanent prostheses are required to stay in the host for a long time, so must be durable and reliable (e.g. stainless steels, Co–Cr alloys, Ti alloys). Metals used to realize biodegradable prosthesis are proposed to replace permanent biomaterials if implants are required to stay in the human body only for the time of tissue healing, avoiding secondary surgery (e.g. magnesium and its alloys, pure iron, and zinc and its alloy).

Key properties of metallic implants such as their corrosion resistance, their biocompatibility, their osteointegration ability, their antibacterial properties are strongly affected by their surface composition and features. The latter can be finely tailored by surface treatments, that can change not only the structure and morphology of the implants surface but can also allow to grow a functional coating. The challenge is to design surface treatments able to uniformly modify the metal or alloy surface, being cost-effective and easily scalable. In the light of the above, surface treatments carried out by electrochemical processes, such as anodizing and/or electroplating, are certainly particularly promising, since a correct selection of the process parameters (namely current density or potential, bath composition and temperature, etc.) allows to control the coating features.

The necessary surface modification depends on the kind of material. In the case of permanent implants, it is important to grant not only a good corrosion resistance over time, but also to promote osteointegration even in the presence of inflammatory conditions, and to have antibacterial properties. On the other hand, for biodegradable implants it is important to reach a very good control of the bio-

degradation rate, since the latter must match the healing process time. Notably, it is very important to hinder localized corrosion that can bring to local failure with detrimental effects for the implants. If we also consider the possibility to customize the implant for a specific patient using additive manufacturing techniques (e.g. laser powder bed fusion), it is also very important to control the surface finishing soon after the fabrication of the implants and to study the efficacy of the surface treatment proposed for cast materials also for 3D printed components in spite their different microstructure.

This research project is focused on the design and test of surface treatments for both titanium- and zinc-based metals. For both materials, a careful study of their corrosion resistance in different simulated body environments was carried out to highlight their strengths and weaknesses.

In the case of Ti alloys, several chemical and electrochemical surface treatments were carried out aimed at improving osteointegration without affecting corrosion resistance and to provide antibacterial properties, paying attention on the effect of inflammatory conditions on the implants. Surface functionalization was also carried out on 3D-printed biomedical plates with a special attention of polishing the surface left by the printing process.

In the case of pure zinc, we studied its corrosion resistance in different physiological solutions to understand limits and perspective of using this metal for biodegradable implants. The investigation started with a careful study of the corrosion resistance of zinc in different physiological environments in the attempt to better understand its behaviour not always clear due to some contradictory results reported in the literature. Then chemical conversion processes were carried out to tune the corrosion resistance of zinc with the goal to tune its biodegradation rate and reduce the initial ions release that can induce cytotoxicity. These investigations were carried out on both cast zinc and 3D-printed components to highlight (if any) the effect of this fabrication process.

Contents

List of Tables

List of Figures

1 Introduction

Biomaterials are usually defined as materials used in contact with living body to treat or replace any tissue, organ or function in the body. [1–3] The most important requirement of a biomaterials is the biocompatibility, [4] i.e. they must perform with a specific application without disruption of normal body function. Nowadays, biomaterials are made of metal alloys, ceramics, polymers and their composites.

After the Industrial Revolution in the 19th century, metallic materials were used to realize medical implants. The first implants were used for long bones fracture fixations. However, before Lister's aseptic surgical technique in the 1860s, the implantation of metal devices failed. [1] After that, predominated in the orthopaedic surgery, metallic implants were used as orthopaedic devices for temporary applications (e.g. plate, screw and pins) and permanent ones (e.g. joints), see Figure 1. 1.

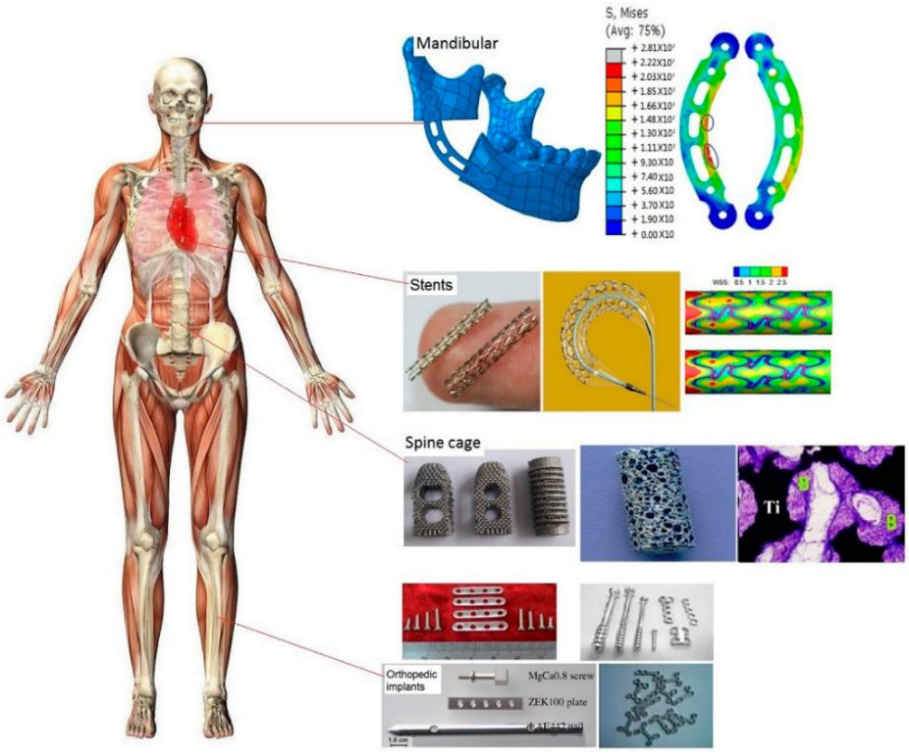

Figure 1. 1 *Different clinic applications for metal implants. Metal implants are mainly used in stents and hard tissue repair, which includes maxillofacial, spine and orthopaedic fixation implants. Image taken from [5]*

More recently, innovative metallic biomaterials have been used for the reconstruction of both hard and soft tissues using for example NiTi alloys, as shape-memory materials used for cardiovascular stent, and biodegradable metals, as magnesium-based, pure iron and zinc-based alloys for bone tissue regeneration, see Figure 1. 1. [6–8]

Despite the large number of commercial metallic alloys produced by industries, only few of them can be used to realize biomedical implants. Of these metallic materials, most are used in the orthopaedic field. These metallic alloys are classified considering the most predominant metallic component and can be divided in four groups: cobaltous-chromium alloys, stainless steels, titanium-based alloys and miscellaneous metals (e.g. NiTi alloys, magnesium alloys, zinc alloys and pure iron). [2,9] The first three groups have been approved by the United States Food and Drug Administration (FDA) and are commonly used. The last group were more recently developed thanks to their specific properties (e.g. NiTinol for shape memory properties and magnesium-based materials for biodegradability).

The most important characteristic for a biomaterial is the biocompatibility, i.e. the implanted material does not cause a harmful effect. [3] The implant needs of a good interaction with cells and tissues of the host. The requirements are different considering the medical application. For example, permanent orthopaedic implants need good mechanical properties and high corrosion resistance, in order to reduce ions release that can be associated to toxic elements, inducing inflammatory and allergic reactions in the human body. A metal that can be used for orthopaedic surgery can be inappropriate for a cardiovascular stent because of its thrombogenic properties.

The human body is a highly corrosive environment mainly made up of water, H2O, with cells containing 65–90 wt% of water. The composition of the human body is reported in Table 1. 1 [1,10]

Element	Wt %	At %
O	65.0	25.5
C	18.5	9.5
H	9.5	63.0
N	3.3	1.4
Ca	1.5	0.31
P	1.0	0.22
K	0.4	0.06
S	0.3	0.05
Na	0.2	0.3
Cl	0.2	0.03
Mg	0.1	0.1
Trace element	<0.01	<0.01

Table 1. 1 *Elements in the human body. Table taken from [1]*

About 95% wt of the human body is composed by oxygen, carbon, hydrogen and nitrogen. The rest is composed by calcium, magnesium and phosphorus as main components of bone and sodium, potassium and chloride ions as electrolyte of extracellular fluids and blood. In addition to these, there are other trace elements that are essential for physiological function as micronutrients but are toxic at high concentration. Among them, the most important are iron (necessary for oxygen transportation in blood), zinc (necessary for reproductive function, for DNA binding of zinc finger proteins), copper, molybdenum and manganese (contained in enzymes).

In addition, the presence of physiological fluids in human body can induce the corrosion of medical devices. In normal conditions, the human body fluids contain inorganic ions (see Table 1. 2), amino acids and proteins. [11]

Ion	Human tissue fluids	Human blood plasma
Na^+	142.0	142.0
HCO_3^-	4.2	27.0
K^+	5.0	5.0
HPO_4^{2-}	1.0	1.0
Mg^{2+}	1.5	1.5
Cl^-	147.8	103.0
Ca^{2+}	2.5	2.5
SO_4^{2-}	0.5	0.5

Table 1. 2 *The ionic concentrations (mM) of human blood plasma.*

Table taken from [1]

The temperature is about 37°C and the partial pressure of oxygen in the human body is about a quarter of the pressure of atmospheric oxygen, thus reducing the formation of the passive layer on the metal surface, and accelerating the corrosion rate. The pH value is usually between 7.2 and 7.4. However, in particular conditions, i.e. during inflammation after surgery, cell secretion induces the release of reactive oxygen species (ROS), and the local pH value may fall to 3. The presence of very noble species during inflammatory conditions can shift the corrosion potential toward more positive value thus increasing metals dissolution.[12–15]

The selection of the metal is related to the specific medical application. To reduce the possibility of a foreign body reaction, i.e. rejection or allergenic reaction, it is important that the metal shows good biocompatibility, bioactivity, corrosion resistance, adequate mechanical properties, and wear resistance. Since the metals are not completely inert for very long time, using a natural element that is still present in the human body is good strategy.

Considering the specific application, metallic biomaterials can be divided into two categories:

- **Metals for permanent prosthesis**
- **Metals for biodegradable prosthesis**

Metals used to realize permanent prostheses are required to stay in the host for a long time, so must be durable and reliable. The human body is a highly corrosive environment, not only for its composition (aqueous solution with dissolved oxygen, chloride ions, amino acids, proteins, etc.) but also for the mechanical stresses that can arise on the implant. For these reasons, metals commonly used for permanent load-bearing applications need good mechanical properties, good biocompatibility, high corrosion resistance in human body to reduce medical failure.

Metals used to realize biodegradable prosthesis are proposed to replace permanent biomaterials if implants are required to stay in the human body only for the time of tissue healing, avoiding secondary surgery.

Nowadays, the most used metals and metallic alloy for permanent implants are stainless steels, Co–Cr alloys, Ti and Ti alloys.

Stainless steels (SS) are widely used as a biomaterial for internal fixation devices due to their mechanical properties, corrosion resistance, low cost. [16–18] Stainless steels are iron-based alloys that contain a high percentage (11–30 wt%) of chromium and varying amounts of nickel. It is well known that the corrosion resistance of stainless steels depends on the formation of a very thin chromium oxide-rich passive film, typically 1 nm to 3 nm thick, whose composition, thickness, and protective action depend on the aggressive environments. [19,20] The addition of nickel as an alloying element induces the stabilization of austenite in iron and increases corrosion resistance but it is reported that nickel is highly toxic to the human body. The addition of molybdenum can increase resistance to pitting corrosion.

Considering the microstructure, SSs can be classified in martensitic, ferritic, austenitic, or duplex (i.e. austenitic plus ferritic). [21] Martensitic stainless steels are usually used for dental and surgical instruments thanks to high hardness. Ferrite and duplex stainless steels are not used for medical devices. Austenitic stainless steels are used for non-implantable medical devices thanks to corrosion resistance and moderate strength. Only austenitic stainless steels are used for implantable device, essentially AISI 316L and its variants.[1]

However, SSs show low biocompatibility, low bioactivity, and high elastic modulus and when implanted in the human body can release metal ions (Ni^{2+}, Cr^{3+} and Cr^{6+}) causing allergic reactions or toxic effect. For these reasons, SSs are usually used for temporary devices, due to their poor corrosion resistance in body fluids as long-term implants, from which harmful ions can be released to adjacent tissues.

Iron is a vital component in all human cells and plays a crucial role in oxygen transport through haemoglobin. However, excessive iron released from metallic implants can lead to high blood levels of free ferrous iron, which reacts with

peroxides to produce free radicals. These free radicals can damage DNA, proteins, lipids, and other cellular components, potentially leading to severe health issues like liver failure, shock, and adult respiratory distress syndrome. Chromium, as a trace element in the body, helps regulate blood sugar levels. A deficiency in chromium can lead to hyperglycaemia and glucosuria. Hexavalent chromium (Cr^{6+}) is toxic and carcinogenic, and contact with chromates can cause allergic contact dermatitis and skin ulceration. Nickel is found in urease, an enzyme that assists in urea hydrolysis, and in blood, it is mainly bound to albumin. Nickel deficiency can affect calcium incorporation into bones and disrupt bone growth. Nickel toxicity, often revealed through contact allergies, can also cause respiratory diseases such as acute pneumonitis and chronic rhinitis. Nickel is the primary alloying element that stabilizes austenite formation in iron and enhances corrosion resistance. Other alloying elements may be added to further improve resistance to specific types of corrosion or to achieve desired mechanical and physical properties. Molybdenum, for example, improves resistance to pitting corrosion caused by chromium carbide formation. In chromium steels, chromium has a strong affinity for carbon, leading to the formation of carbides in carbon-rich areas, typically at grain boundaries. These chromium carbides (Cr_3C_2, Cr_7C_3, $Cr_{23}C_6$) reduce the corrosion resistance of the steel around them. The addition of molybdenum, which also forms carbides, helps to trap carbon by forming molybdenum carbides.[1]

Stainless steel alloys are widely used in temporary devices after bone trauma, such as fracture plates, screws, and hip nails, as well as in permanent implants like total hip replacements, see Figure 1. 2.

Figure 1. 2 *Example of Stainless-Steel Orthopaedic Implant. Image taken from [22]*

Stainless steels are not used for long-term implant devices due to the susceptibility to localized corrosion, e.g. crevice corrosion and pitting, see Figure 1. 3. Crevice corrosion occurs in confined spaces where access to surrounding fluids is limited. This is commonly seen between the underside of a bone screw head and the countersunk area of the bone plate. It begins when oxygen is depleted in the crevice, while smaller chloride ions are drawn in by the metal ions released during anodic reactions. This decreases the pH in the crevice, accelerating metal oxidation. Passivation of stainless-steel implants can be enhanced by surface treatment for example in nitric acid before sterilization and packaging for medical use.

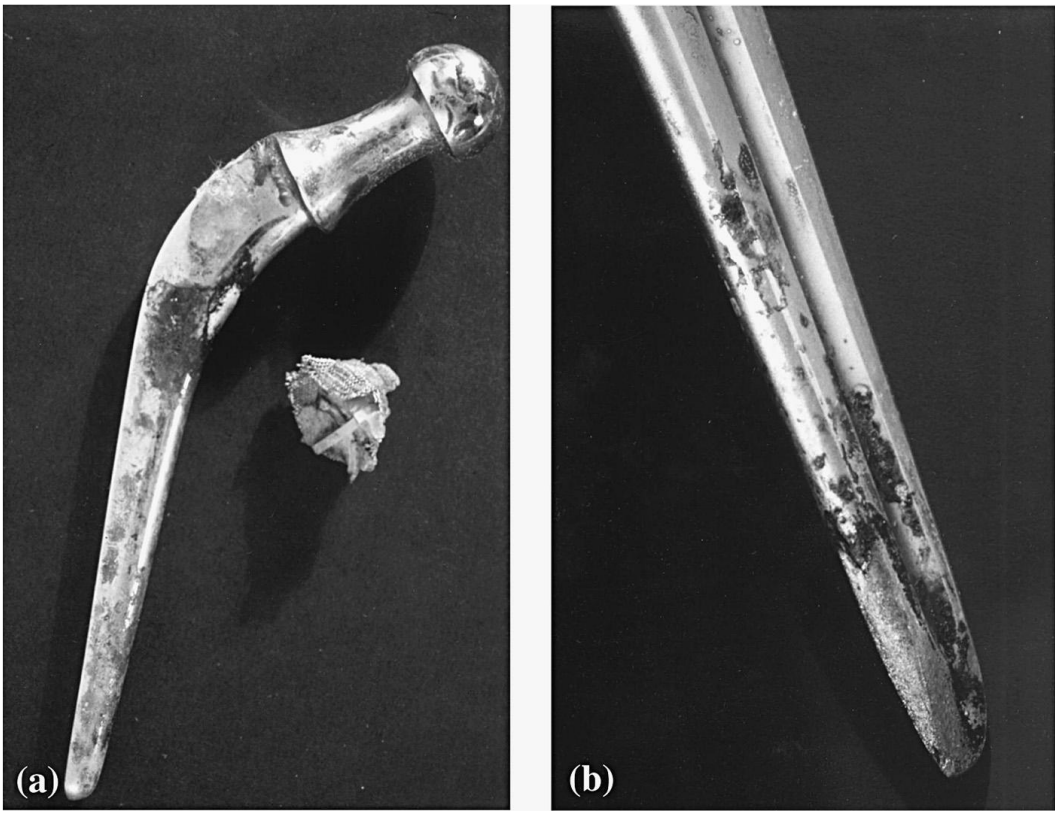

Figure 1. 3 *(a) Corrosion scale on a Charnley stainless steel stem, and (b) pitting and corrosion of a Muller stainless steel stem after implant removal. Image taken from [16]*

316L austenitic stainless steels are not sufficiently corrosion-resistant for long-term use in implants and are now mainly used in temporary devices such as internal fixation or traction devices, which are removed after healing.

As a result, 316L stainless steel has been largely replaced by more corrosion- and fatigue-resistant alloys such as Co-alloys and Ti alloys for permanent implants.

Cobalt-based alloys were first used in medical implants in the 1930s. The CoCrMo alloy vitallium was used as a cast dental alloy (see Figure 1. 4) and then adapted to orthopaedics applications in the 1940s. [23]

Figure 1. 4 *Vitallium alloy used for dental reconstruction.*

CoCr alloys show excellent mechanical properties for loadbearing applications and good corrosion resistance in physiological environment of about one order of magnitude higher if compared to SSs. The corrosion resistance is primarily attributed to chromium, molybdenum, and nickel. Cobalt is a vital trace element, mainly involved in the maturation of human red blood cells as part of vitamin B12. However, excessive cobalt exposure can cause significant health issues. Similar to chromium and nickel, cobalt enters the body through the lungs, ingestion, skin contact, or through products released by implants. In the case of hip replacements made from cobalt alloys, there is generally a local release of metallic particles, and in some cases, individuals experience a hypersensitivity reaction leading to more severe tissue damage near the prosthesis. Cobalt toxicity has been linked to systemic and neurological symptoms. Molybdenum is another essential trace element for several enzymes involved in cellular metabolism, and it is considerably less toxic than cobalt, chromium, and nickel. Acute toxicity from molybdenum has not been reported in humans. Tungsten shares a similar chemical structure with molybdenum. However, the biological role of tungsten has only been identified in prokaryotes, and not yet in eukaryotes. Tungsten toxicity is extremely low; however, implantable materials made from this metal degrade rapidly in the body and remain in the bloodstream, likely as tungsten particles.

Cobalt alloy was first used in hip implants in 1939, shortly after stainless steels. In vitro studies showed that CoCrMo alloys are much less toxic than pure cobalt or nickel, primarily due to their superior corrosion resistance. Tungsten, which is added to increase solid-solution strengthening and to control the distribution and size of carbides, can however impair the corrosion resistance and corrosion fatigue strength of Co-based alloys. Co-20Cr-15W-10Ni and Co-Ni-Cr-Mo-W-Fe alloys are restricted to short-term implants, such as bone plates and wire, due to both unsatisfactory corrosion resistance and a high amount of toxic nickel release when used for permanent implantation.[1]

The success of CoCrMo stems in total hip replacements during the 1960s confirmed that these alloys are well tolerated by the body. The excellent fatigue resistance of CoCrMo alloys makes them ideal for total joint replacements, see Figure 1. 5

Figure 1. 5 *Femoral bearing head and cups made from the F799 CoCrMo alloy. Image taken from [1]*

CoCrMo alloys are expensive, which limits their market share compared to stainless steels. However, cobalt-based alloys have not yet become common for fracture-fixation and research is ongoing into the potential use for coronary stents. Other challenges associated with cobalt-based alloys include stress shielding effects and metal toxicity. Cobalt alloys have a high Young's modulus (220–230 GPa), much higher than cortical bone (20–30 GPa), leading to uneven energy distribution from shock waves during walking and load-bearing. The interface between a stress-shielded bone and implant deteriorates as the bone weakens, potentially causing loosening and fractures.

Ti and Ti alloys are widely used for several biomedical applications because they have elastic moduli close to those of bones and lower density with respect to that of Co-Cr alloys and stainless steels.

Based on their microstructure after processing, titanium alloys are classified into four categories: α alloys, near-α alloys, α–β alloys, and β alloys. The elastic modulus of titanium and its alloys is approximately half that of stainless steels and cobalt-molybdenum alloys. Due to their lower modulus, superior biocompatibility, and enhanced corrosion resistance compared to stainless steels and cobalt-based alloys, titanium alloys are increasingly used in biomedical applications. These favourable properties led to the early adoption of commercial pure titanium (CP-Ti) and α+β Ti–6Al–4V alloys. The primary focus in titanium alloy design is on

mechanical properties, as titanium itself already exhibits excellent corrosion resistance. Among the long list of alloying elements of Ti alloys, V, Al, Nb, Zr, Mo, Fe and Ta are the most important for medical implants.

Titanium is unreactive in the human body and has no known biological role. It is non-toxic even in large amounts and is generally not rejected by the body, forming strong physical connections with the host bone. However, in vitro studies suggest that titanium can inhibit osteogenic differentiation of mesenchymal stem cells and may cause genetic alterations in connective tissue. Vanadium, a common alloying element in titanium alloys, has an ill-defined biological role and can elicit both positive and negative cellular responses, with toxicity typically associated with its compounds, such as oxides. Although there are few reports on the toxicity of vanadium in titanium alloy implants, recent studies have suggested a potential link between vanadium release and implant failure. Aluminium, a naturally abundant element, has little known biological function in humans. While its acute toxicity is only a concern in very high doses, chronic aluminium exposure has been associated with neurological issues, particularly Alzheimer's disease. Excessive aluminium exposure can also contribute to reduced skeletal mineralization (osteopenia) in infants, as it competes with calcium for absorption. There are concerns that prolonged aluminium exposure may increase the risk of conditions such as breast cancer and other neurological disorders. Niobium has minimal biological roles in humans, but some niobium compounds, such as niobates and niobium chloride, are toxic.

Despite these potential concerns, titanium alloys are considered more biocompatible than stainless steels and cobalt alloys due to their excellent corrosion resistance. The first-generation titanium alloy, Ti–6Al–4V (Ti64), has been linked to allergic reactions in the human body. In response, second-generation titanium alloys, such as β-titanium alloys, have been developed. Elements like Mo, Ta, and Zr, used as alloying elements in these alloys, are considered safer than vanadium and aluminium.

Titanium-based biomaterials are more inert and biocompatible for implant applications if compared to stainless steels and cobalt alloys, showing little to no reaction with surrounding tissues. When a bioinert material is implanted, the organism forms a capsule around it, recognizing it as foreign body. While this is a natural defence mechanism, the formation of this capsule tissue can contribute to implant loosening.

The successful integration of orthopedic implants with bone, known as osteointegration, is influenced by the implant's surface characteristics. However, titanium-based implants often face complications due to the toxic effects of titanium and the stress shielding phenomenon caused by mechanical incompatibility with surrounding tissues. Key challenges with these implants are: their inherent lack of biological reactivity, leading to poor bone attachment, wear, and pain [24]; the potential release of toxic elements such as vanadium and aluminum, which carry carcinogenic risks [25]; and insufficient antimicrobial properties, increasing the likelihood of bacterial colonization, resulting in tissue death and the need for additional surgery. The degree to which titanium implants promote bone matrix

growth and integrate with the surrounding bone is a primary determinant of their success in orthopedic surgery. Therefore, achieving reliable implant integration within the body is a long-standing problem in medicine and tissue engineering. While much research has centred on interface formation, a thorough in vitro and in vivo analysis of the relationship between surface structure and interface strength at the native implant site is essential. Factors such as surface topography (roughness, porosity), mechanical properties (hardness, corrosion resistance), biological interactions (binding to host bone, osteoinduction, osteoconduction, and osteogenesis), and antimicrobial properties (reducing bacterial fixation, bactericidal effects) are critical in the development of surface modification techniques for titanium and its alloys. [26]

Appropriate surface modifications improve the growth and biocompatibility of the bone matrix, enhance the long-term stability of the connection between new bone and the implant, and shorten the recovery period. Moreover, an antimicrobial surface coating during the bone healing process can inhibit bacterial growth to a significant extent, creating a more suitable physiological environment for bone tissue development, preventing postoperative infections, and reducing patient pain. A schematic representation of surface treatments usually used for Ti and Ti alloys for orthopaedic implants is reported in Figure 1. 6.

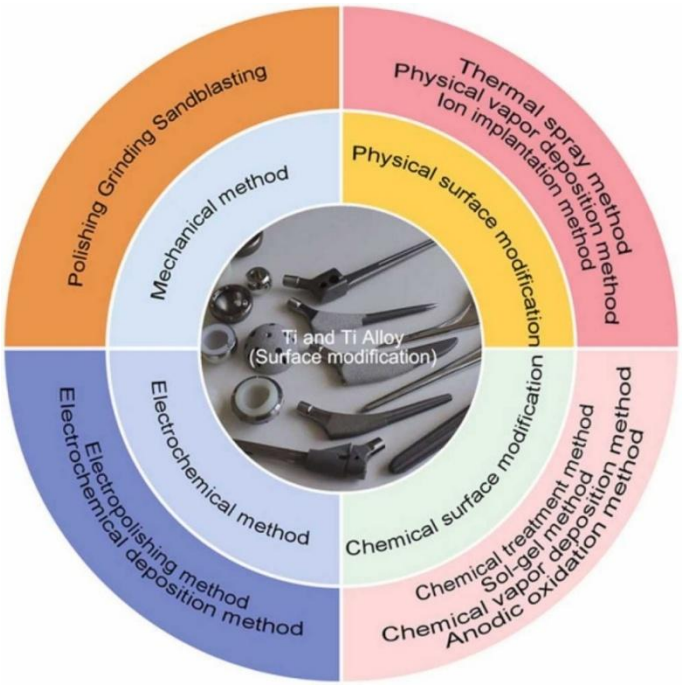

Figure 1. 6 *Schematic representation of surface treatments for Titanium-based materials. Image taken from ref [27]*

To enhance the bioactivity of Ti alloys by surface treatments, several strategies have been investigated [28–30]. For example, the presence of hydroxyapatite (HA, $Ca_{10}(PO_4)_6(OH)_2$) can enhance the osteointegration of foreign biomaterials due to its high biocompatibility with hard and soft tissues [31]. Therefore, inducing the incorporation or the growth of HA has been revealed as a good strategy to improve

the materials bioactivity. This can be reached, for instance, by an electrochemical conversion coating process as spark anodizing by precisely tailoring the operating conditions (formation voltage, electrolyte bath composition, etc.) [32–34]. Moreover, the growth of a thick anodic layer on the surface of Ti6Al4V alloy can enhance its corrosion resistance in body fluids and reduce the release of Al and V during the service life of the implant.

Surface treatments, such as electrophoretic deposition and electrodeposition, can be used to improve surface wettability, biocompatibility and antibacterial properties. The deposition of metals with antibacterials properties is a good strategy in order to reduce implant failure. Among them, Ag is one of the most studied metals as antibacterial agent due to its antibacterial capacity, relative cheapness and availability and its high activity against a wide range of microorganisms as microbes and parasites [35].

The traditional paradigm of metallic biomaterials requires metals with improved corrosion resistance in the body. Recently, a new class of biodegradable materials, known as "biodegradable metals" (BMs), has emerged as an alternative for biomedical implants, challenging this paradigm.[6,9,36]

Biodegradable metals can be defined as materials that are designed to gradually dissolve in the human body. The corrosion products released trigger a suitable host response, and the material eventually dissolves completely after fulfilling its role in supporting tissue healing, leaving no residual implant material. Consequently, the primary components of BMs should be essential metallic elements that can be metabolized by the human body and exhibit appropriate rates and mechanism of degradation.

The concept of biodegradation is already known in other classes of biomaterials. For example, biodegradable polymeric sutures made from poly(caprolactone) (PCL), poly(lactic acid) (PLA), poly(glycolic acid) (PGA), and their copolymers have been widely studied and used in the biomedical field to hold tissues together during the healing process following trauma or surgery. [37]

"Temporary" implants allow overcoming two major limitations of permanent biomedical devices: the high risk of chronic inflammation near the implant and the need for a second procedure to remove the device after tissue healing[6]. In the United States, over one million surgical procedures are performed each year to repair bone fractures, and approximately 30% of all orthopaedic surgeries consist of the removal of permanent metal implants once the bone tissue has fully healed[38]. As a result, the use of biodegradable materials is not only beneficial for patient health but also helps reduce healthcare costs.

Nowadays, biodegradable materials are attractive for orthopaedics and cardiovascular applications. In orthopaedics, BMs can be used to realise fixation implants such as screws, pins, or rods to support bone fractures. [38] In cardiovascular medicine, BMs can be used for the development of coronary stents, which are implanted in arteries during angioplasty, a procedure that restores the patency of obstructed coronary vessels. [37]

Metals used for “temporary” implants need different characteristics, such as biocompatibility, biodegradability and adequate mechanical properties.

Biocompatibility is the inherent ability of a biomedical implant to elicit an appropriate response in the body without causing any harmful effects on vital functions. The biodegradation of metallic materials is essentially a corrosion process in a biological environment. Electrode potential, Pilling-Bedworth ratio, and Pourbaix diagram, typically used to describe the corrosion of metals and their alloys, can also be used to describe the biodegradability of bioresorbable metallic implants and predict the resulting degradation products [13]. In addition to these criteria, a third basic requirement must be met: the metallic implant must have adequate mechanical properties, providing temporary mechanical support and then should dissolve completely over a prolonged period with an appropriate and tolerable degradation rate for the human body. Essentially, the degradation rate of the biomaterial within the body must be comparable to the healing kinetics of the injured tissue, so as to provide sufficient mechanical support for the desired time [17]. For bone repair, it has been reported that the degradation rates of bone implants should be lower than 0.5 and higher than 0.2 $mm \cdot y^{-1}$ to match the bone healing.[39]

Depending on the application, these times vary, so appropriate surface treatments are essential to adapt the properties of the biomedical device to the specific application.

In cardiovascular applications, vascular injuries are common and often significant following balloon angioplasty. The healing response of injured vessels progresses through three overlapping phases: inflammation, granulation, and remodelling, as illustrated in Figure 1. 7.

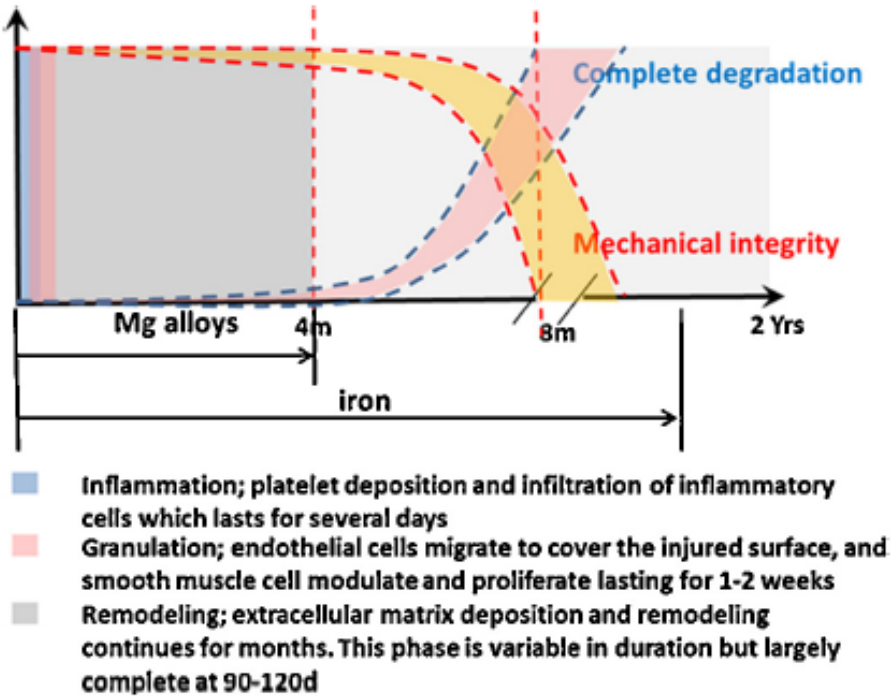

Figure 1. *7 The schematic diagram of degradation behaviour and the change of mechanical integrity of BM stents during the vascular healing process. Image taken from [40]*

Complete degradation of the device is anticipated after the vessel remodelling phase, which typically concludes within 90–120 days. Therefore, mechanical support should degrade very gradually over the first four months to ensure adequate stabilization of the injured vessels. [40,41]

Bone fracture healing follows three stages: inflammation, repair, and remodelling, as shown in Figure 1. 8. During the first two to three weeks post-fracture, a soft callus forms, marking the phase when bone fragments are no longer freely mobile. This initial soft callus provides some resistance to compression but exhibits tensile properties comparable to fibrous tissue, with an ultimate tensile strength of 4-19 $N \cdot m/mm^2$ and an elongation at rupture of 10–12.8%.

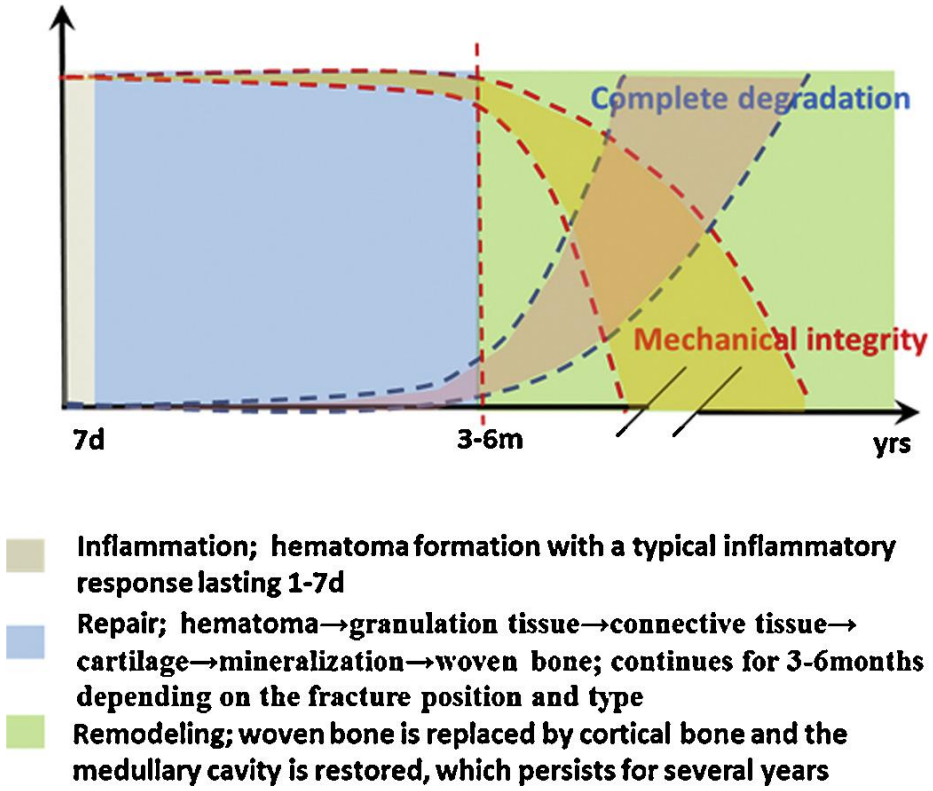

Figure 1. 8 *The schematic diagram of degradation behaviour and the change of mechanical integrity of BM implants during the bone healing process. Image taken from [40]*

As mineralization progresses, the callus transforms from the fragment ends toward the fracture centre, forming a hard callus with sufficient strength and rigidity to support low-impact movement by the end of the repair phase. The time required for full bone consolidation varies depending on factors such as fracture type, location, soft tissue involvement, and patient-specific characteristics (e.g., species, age, health condition, and concurrent injuries or diseases). For example, a spiral fracture in the upper limb typically unites within three weeks and consolidates in six weeks. For a transverse fracture, healing time doubles, and for fractures in the lower limb, it doubles again. Table 1. 3 provides a general estimate of healing times for different fracture types.

Fracture		Healing time (weeks)
Upper limb	Clavicle	5 - 7
	Fingers	4 - 8
	Scaphoid	> 10
	Humerus	5 – 8
	Radius and ulna	8 - 12
	Distal radius	3 - 4
Lower limb	Pelvis	6 – 10
	Femur	8 - 14
	Neck of femur	12 – 24
	Tibia	8 – 12
	Calcaneus	6
	Toes	6 – 8

Table 1. 3 *Bone healing time for different fractures. Table taken from.[40]*

Consequently, mechanical support should be maintained for approximately 12-24 weeks, depending on clinical conditions. [40,41]

Currently, bioresorbable metals in use can be divided into three major families: magnesium and its alloys, iron and its alloys, and zinc and its alloys. The degradation rates of metallic implants are summarized in Figure 1. 9. Mg-based alloys exhibit the highest degradation rates, approximately ranging from 0.8 to 2.7 $mm \cdot y^{-1}$, which is above the tolerable degradation rates of bone implants. The degradation rates of Zn-based alloys are mainly between 0.1 and 0.3 $mm \cdot y^{-1}$, appearing as prospective alternates. In contrast, the slowest degradation rates, less than 0.1 $mm \cdot y^{-1}$, are observed for Fe-based alloys.

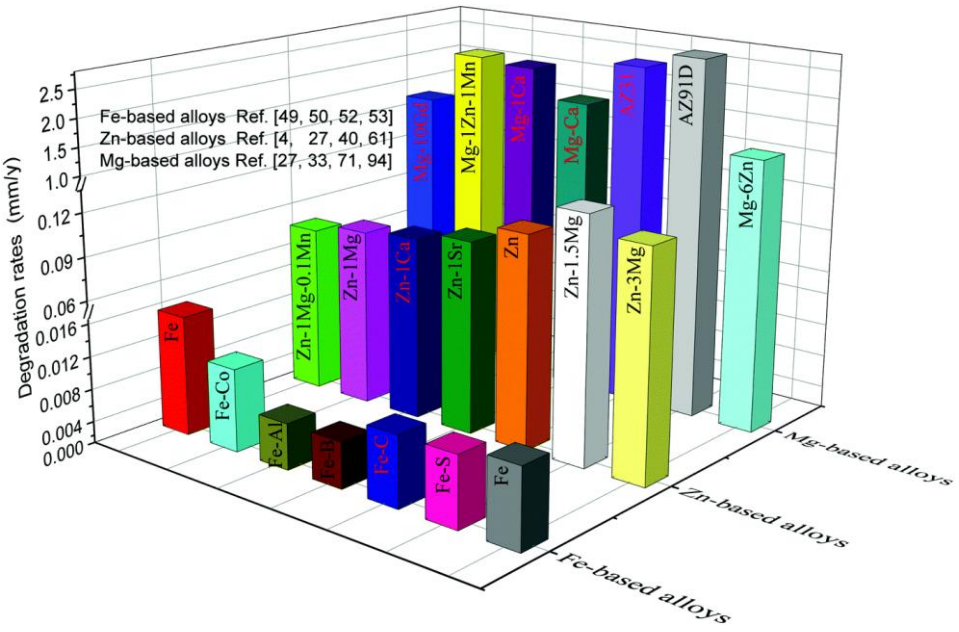

Figure 1. 9 *Degradation rates of Mg-, Fe-, and Zn-based alloys. Image taken from [39]*

The most studied bioresorbable metal is magnesium (Mg), followed by iron (Fe) and zinc (Zn). Zinc, with a standard reduction potential in aqueous solution at 25°C of -0.76 V vs. SHE, is between magnesium (-2.37 V vs. SHE) and iron (-0.44 V vs. SHE) [36], making it a promising material for bioresorbable applications. In fact, it exhibits a degradation rate which is intermediate between that of iron and magnesium, considered too slow and too fast, respectively.

Magnesium (Mg) shows a higher corrosion rate, and therefore to biodegradation, compared to iron and zinc. It is the most studied metal for bioabsorbable medical applications. Due to its low magnetic susceptibility, magnesium does not interfere with common imaging diagnostic methods such as Magnetic Resonance Imaging (MRI). [6]

The main advantages of magnesium include its biocompatibility and the ability of this metal to promote new bone formation. Several studies have demonstrated the functional properties of Mg-based implants, particularly their ability to support bone healing following a fracture. Furthermore, magnesium has a Young's modulus of about 40 GPa, a value similar to that of bone. The elastic modulus of trabecular bone ranges from 22.4 to 132.32 MPa, while that of cortical bone is much higher, ranging from 7.7 to 21.8 GPa. This is a parameter to consider carefully during the design process of an orthopaedic implant to avoid the phenomenon of stress shielding. This issue occurs when the elastic modulus of the implant exceeds that of natural bone, leading to a greater load on the implant and a corresponding reduction of load in the surrounding bone tissue, which causes a reduction in bone density and potentially bone fracture. Conversely, when the elastic modulus of the device is lower than that of natural bone, stress concentration in the bone can cause implant failure and bone atrophy. [42–44]

The main limitations of using magnesium as a material for temporary devices relate to its high corrosion rate in a physiological environment, which is associated with the release of gaseous hydrogen. Being a very low noble metal, the cathodic reaction associated with the oxidation of magnesium is H^+ reduction. The rapid corrosion of magnesium is due to the quick conversion of magnesium hydroxide [$Mg(OH)_2$] into magnesium chloride $MgCl_2$. This product is highly soluble and can therefore be transported or degraded. The dissolution of magnesium induces alkalinization (increase the pH) near the implant surface. This factor, combined with the development of hydrogen bubbles that may accumulate in gas pockets near the implant, can cause inflammation and necrosis of the surrounding tissues. Electrochemical tests, useful for evaluating the corrosion rate of magnesium, are conducted by partially immersing the metal samples in solutions that simulate the real physiological environment. The corrosion rate of magnesium is higher when tested in solutions containing only inorganic ions, compared to when solutions containing both inorganic ions and organic compounds are used. [44–46]

Some Mg-based degradable biomaterials are currently undergoing clinical trials or are already available on the market.

Figure 1. 10 *MAGNEZIX® screw (Syntellix AG, Hannover, Germany)*

The MAGNEZIX® compression screw (Syntellix AG, Hannover, Germany), see Figure 1. 10, is made from a fully bioabsorbable magnesium alloy (MgYREZr). This alloy, which received CE certification in 2013, contains rare earth elements and is compositionally similar to WE43. Clinical tests conducted in Germany on 26 patients have shown that these magnesium-based biodegradable screws are equivalent to common titanium screws for the surgical treatment of hallux valgus.[47]

Figure 1. 11 *Magmaris® stent (Biotronik AG, Bulach, Switzerland)*

In the cardiovascular field, Biotronik (Biotronik AG, Bulach, Switzerland), see Figure 1. 11, has designed Magmaris®, a biodegradable magnesium alloy stent containing rare earth elements, loaded with an antiproliferative drug that prevents unwanted cell growth that could reduce blood flow within the vessel. It is the only bioabsorbable coronary stent currently available on the market. Approximately 95% of the magnesium in this biomedical device is absorbed by the human body within 12 months. [48]

Iron shows a lower corrosion rate, and therefore to biodegradation, compared to magnesium and zinc. It is an essential nutrient for the human body and has unlimited bioavailability. A high amount of iron can be hazardous for cells and tissues as it can potentially disturb the redox balance of cells, leading to the

formation of radicals that disrupt the complex signalling network governing cell communication, with the risk of malignant tumour formation. For example, the metabolism of endothelial cells is not altered by Fe^{2+} ion concentrations below 10 μg/ml; however, the growth of endothelial tissue is inhibited at concentrations greater than 50 μg/ml. One of the limitations of pure iron is its high ferromagnetism, which prevents the use of magnetic resonance imaging (MRI) as an imaging technique to monitor the implant after the surgical operation. [7,49]

Research on degradable iron-based biomaterials, considered important for their mechanical performance, is already undergoing animal trials. The elastic modulus of iron (211.4 GPa) is much higher than that of magnesium (40 GPa). Iron has excellent mechanical strength, but its mechanical properties differ significantly from those of human cortical bone. Due to its ductility, pure iron is a good candidate for the production of biodegradable stents. It is well known that pure iron stents are safe, but they showed limited signs of degradation without causing thrombosis or excessive tissue inflammation, thus overcoming one of the limitations of Mg alloy stents. However, some studies have revealed that, due to the limited oxygen availability in certain tissues, the degradation rate of Fe is quite low. [50] To overcome these limitations, Fe-Mn alloys have been proposed, which have a higher corrosion rate compared to pure iron. [41] Consequently, these alloys, in addition to being non-ferromagnetic, degrade more quickly.

The suture anchors shown in Figure 1. 12 are an example of bioabsorbable iron implants to be used in the future in trauma and orthopaedic surgery. These devices, developed by researchers at the Fraunhofer Institute for Manufacturing Technology and Advanced Materials (IFAM; Bremen, Germany), are composites made up of 60% iron and 40% of a ceramic component, beta-tricalcium phosphate (TCP). [8]

Figure 1. 12 *Iron-based suture anchoring systems (Fraunhofer IFAM).*

Zinc, being one of the essential trace metals in human bodies, seems a promising candidate due to its adequate corrosion rate (between 0.1 and 0.3 $mm \cdot y^{-1}$ that match the bone healing) and oxygen reduction reaction (ORR) as the main cathodic process. [36,51,52] The most important limitation for the use of zinc for biomedical applications is related to mechanical properties compared to iron and magnesium. The strength and ductility of as cast zinc are generally below the mechanical benchmark for biodegradable implants, such as bone fixtures and stents, but can be enhanced by adding alloying elements. [53–56]

In the last decades, several papers have been published trying to study the corrosion mechanisms of zinc in human body [36,57–60], but some aspects remain unclear. Indeed, zinc oxidation and dissolution can be strongly influenced by the composition, temperature, and hydrodynamic conditions of the environment, thus the role of the employed electrolytic solution selected to mimic a physiological environment is very important. It is widely known that a key factor affecting the corrosion behaviour of zinc is chloride ion concentration, since Cl^- induces localized corrosion. However, a role is also played by the other compounds present in the electrolyte considering the complex nature of the (simulated) biological environments. Indeed, insoluble salt formation as well as protein adsorption or the presence of amino acids can affect the corrosion mechanism and thus the corrosion rate. In ref. [61] the effect of ammino acids (i.e. l-cysteine) in dissolution process was investigated. In ref. [58] a detailed investigation was carried out aimed to highlight the role of biomolecules and inorganic corrosion products in affecting the corrosion behaviour of zinc with immersion tests lasting for 168 h, that allowed to estimate the corrosion rate of this metal in four different simulated physiological solutions.

Another important property to consider during the design of a metallic biomaterial is its radiopacity, meaning the ability to be monitored by X-rays. This is particularly relevant for applications such as vascular stents, where it is necessary to monitor the catheter insertion into blood vessels during surgery and the correct placement of the stent at the end of the surgical procedure. Due to its low magnetic susceptibility, zinc does not interfere with Magnetic Resonance Imaging (MRI), just like magnesium.

Although essential element for human body, zinc implants can induce cytotoxic effects when implanted in human body. Surface modification is a leading method to improve the properties and add functions to implanted materials. For example, appropriate coatings can create a surface that promotes protein adsorption in biological fluids, enhancing cell-matrix interactions and growth factor production. Different modification methods could be used to achieve specific properties for various clinical applications, especially in orthopaedics'. However, the study of biodegradable zinc-based metals and their surface modification is still in the early stages. Traditional surface modification technologies are classified into chemical, mechanical, and physical types, depending on the coating materials and their formation (see Figure 1. 13). Chemical modification creates new compounds by chemically coating the surface. Physical modification uses physical processes to transfer atoms or molecules to the surface. Mechanical surface treatments modify

surface roughness or introduce superficial plastic deformation. These techniques aim to alter the surface properties of degradable metals while maintaining the original bulk properties.[27]

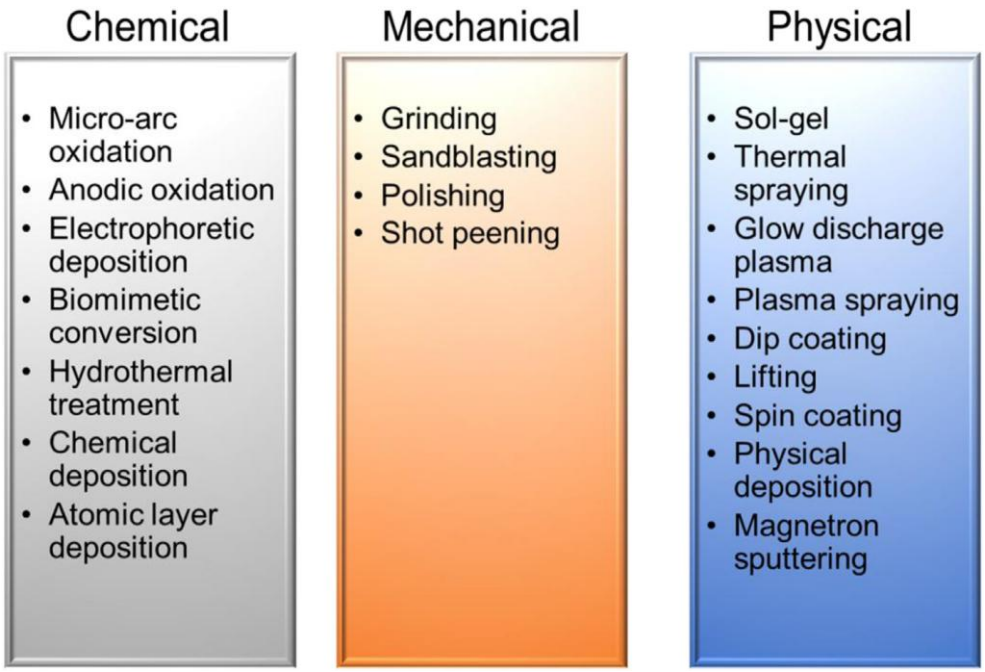

Figure 1. 13 *Typical surface modification methods. Image taken from ref [27]*

Anodic oxidation is an electrolytic process that involves using metal or alloy parts as the anode to form an oxide film on their surface. In contrast with PEO, anodizing does not require high voltage discharge. For example, Dong et al. [62] formed flower-like ZnO nanotube layers on pure Zn using anodic oxidation. The results showing that the resulting composite layer improved electrochemical activity and was better for bone fixation compared to the original zinc.

Electrophoretic deposition (EPD) is a technique where colloidal particles in a liquid move under an electric field and deposit onto an electrode. Sun et al. [63] used EPD to create a thick, even zinc-hydroxyapatite (HA) coating, which formed a new apatite layer after a week in simulated body fluids.

Chemical deposition is a practical, efficient, and affordable way to create bioactive coatings on metallic biomaterials. Phosphate-based coatings made this way are widely studied to improve how well zinc and its alloys work with the body and living cells. For example, Su et al. [64] created zinc-phosphate (ZnP) coatings on pure zinc, which improve bone-forming cells. Zhu et al. [65] explored a magnesium-based coating on pure zinc to improve the cell compatibility for bone stem cells.

Biodegradable organic and polymer coatings can shield the underlying material from the corrosive human environment. Examples of such polymers approved for medical use include PLA, PCL, and PGA, used in bone implants and cardiovascular devices. These are usually applied to biodegradable metals using physical

techniques like dip coating. For instance, Su et al. [66]suggested using a collagen coating on pure zinc, which enhanced its resistance to breakdown and improved its compatibility with bone-forming cells and blood vessel cells.

In general, it's crucial to think about how well degradable biomaterial parts interact with the body, as all parts of the implants will eventually be processed by the human system. Coatings should make the material more compatible with the body, help it integrate with bone (osseointegration), make it biologically active, give it antibiotic properties, or allow it to deliver drugs locally, especially in orthopaedic applications. Other examples of surface treatments are summarized in ref [27]

Surface modification method	Coating composition	Cytotoxicity	Osteogenic activity
PEO	ZnO	Observed in 100% extract	Few Ca,P enrichment
PEO	Zn_2SiO_4 ZnO	–	Regulate the growth of osteogenic
PEO-HT	ZnO $CaZn_2(PO_4)_2$	Observed in high-% extract	New CaP replaced after 10 days
Anodic oxidation	ZnO Dexamethasone graphene	Decrease	Promotes cell osteogenic differentiation and activity
Anodic oxidation	ZnO	–	Good for Ca–P information
Anodic oxidation	ZnO	Observed in 100% extract	–
HT	$CaCl_2$ NaH_2PO_4 $Sr_3(NO_3)_2$	No cell activity in the pure Zn	High ALP activity expression
Biomimetic conversion	Zn,Mg,Ca,P	No cytotoxicity under 50% extract	–
Biomimetic conversion	ZnO $Zn(OH)_2$	No cytotoxicity	Apatite attracts by $Zn(OH)_2$
EDP	Hybrid of polycarbonate tannic and copper	Observed in 100% extract	–
ALD	Zr, O	Observed in ZrO_2-100,300	Newborn bone found in ZrO_2-500 (8 week)
Magnetron Sputtering	DLC	Observed in 100% extract	–
Organic	Collagen	Observed in high-% osteoblasts extract	–
Chemical depositon	$Zn(OH)_2$ $Zn_3(PO_4)_2$ $CaZn_2(PO_4)_2$	Observed in high-% osteoblasts extract	New CaZnP apatite formed
Polymer	PLA	No cytotoxicity	–
Polymer	PLLA	Toxicity in the neointimal tissue as observed after 2 weeks	PLLA surface calcification
Polymer	Collagen based gelatin	hDF and AoSMC reduction in cell size	–
Polymer	PCCs	Observed in 100% extract	–
EDP	ZnO Mg_3P_2 Mg_7Zn_3	–	Had the ability to form the CaP

Figure 1. 14 *Effect of different surface modifications on the biocompatibility of Zn. Image taken from ref [27]*

2 Materials and Methods

Titanium foils (Aldrich, purity > 99.7%) with a thickness of 0.125 mm and Ti6Al4V (Goodfellow) titanium alloy with a thickness of 2 mm were used. Zn foils of 0.15 mm thickness and a purity >99.95% were obtained from Goodfellow. 3D printed samples were produced by laser powder bed fusion (LPBF) using different process parameters (see chapter below) to study the effect of microstructure on corrosion resistance.

For the experimental activities, different physiological solution was used, to better understand the effect of inorganic ions (i.e. calcium ions, chloride, carbonate, phosphates, and sulphate), organic species (i.e. amino acids and proteins) and inflammatory conditions (i.e. peroxide species). The different physiological solution used with the relative composition is reported in Table 2. 1.

Hanks′ Balanced Salt solution (HBSS) and Kokubo solutions are aqueous solutions that contain essentially inorganic species at pH =7.2. Dulbecco′s Modified Eagle′s Medium (DMEM) is a cell culture medium that contains both inorganic and organic species. A commercial DMEM solutions with low glucose concentration (Aldrich) with and without Fetal Bovine Serum (10% wt. as proteins source) were used, see compositions in Table 2. 1. In additions, at early stage of implantation of a medical device, the body produces an inflammatory response by producing superoxide species and a very acidic environment. The presence of very noble species can accelerate the corrosion rate inducing the release of metallic species with consequent cytotoxic effects. It is possible to simulate an inflammatory environment by adding to the normal physiological solutions peroxide species (H_2O_2) and changing the pH (by adding lactic acid). For the experimental activities inflammatory conditions with pH=5.2 (HBSS_IC) and severe inflammatory conditions with pH=2.2 (HBSS_SIC) simulating environment were used, see composition in Table 2. 1.

	HBSS	DMEM	DMEM + FBS	Kokubo	HBSS _IC_	HBSS _SIC_
NaCl	8	6.4	6.4	8	8	8
KCl	0.4	0.4	0.4	0.23	0.4	0.4
$CaCl_2$	0.2	0.2	0.2	0.36	0.2	0.2
$MgCl_2$	0.2	-	-	0.3	0.2	0.2
$MgSO_4 \cdot 7H_2O$	0.06	0.2	0.2	-	0.06	0.06
$K_2HPO_4 \cdot 3H_2O$	-	-	-	0.23	-	-
Na_2SO_4	-	-	-	0.07	-	-
NaH_2PO_4	0.25	-	-	-	0.25	0.25
Na_2HPO_4	0.06	0.124	0.124	-	0.06	0.06
D-Glucose	1	1	1	-	1	1
$Fe(NO_3)_3 \cdot 3H_2O$	-	0.0001	0.0001	-	-	-
Na-Pyruvate	-	0.11	0.11	-	-	-
Phenol red	-	0.015	0.015	-	-	-
HCl 1M	-	-	-	40ml	-	-
TRIS	-	-	-	6.045	-	-
NaHCO3	0.35	3.7	3.7	0.35	0.35	0.35
L-Arginine HCl	-	0.084	0.084	-	-	-
L-Cysteine	-	0.048	0.048	-	-	-
L-Glutamine	-	0.58	0.58	-	-	-
L-Histidine HCl	-	0.042	0.042	-	-	-
L-Isoleucine	-	0.106	0.106	-	-	-
L-Leucine	-	0.106	0.106	-	-	-
L-Lysine HCl	-	0.146	0.146	-	-	-
L-Methionine	-	0.03	0.03	-	-	-
L-Phenylanine	-	0.066	0.066	-	-	-
L-Threonine	-	0.095	0.095	-	-	-
L-Tryptophan	-	0.016	0.016	-	-	-
L-Tyrosine	-	0.072	0.072	-	-	-
L-Valine	-	0.094	0.094	-	-	-
Glycine	-	0.03	0.03	-	-	-
L-Serine	-	0.042	0.042	-	-	-
Cholinchloride	-	0.004	0.004	-	-	-
Folic acid	-	0.004	0.004	-	-	-
Myo-Inositol	-	0.0072	0.0072	-	-	-
Nicotinamide	-	0.004	0.004	-	-	-
Da-Ca-Pantothenate	-	0.004	0.004	-	-	-
Pyridoxal HCl	-	0.004	0.004	-	-	-
Riboflavin	-	0.0004	0.0004	-	-	-
Thiamine-HCl	-	0.004	0.004	-	-	-
H_2O_2	-	-	-	-	150 mM	150 mM
Lactic acid	-	-	-	-	-	150 mM
Fetal Bovine Serum	-	-	10% wt	-	-	10% wt

Table 2. 1 *Composition of different physiological solutions used expressed in g/L.*

The morphology was studied by Scanning Electron Microscopy (SEM) using a FEI Quanta 200 FEG SEM instrument at several magnifications in high vacuum mode and 30 KeV as accelerating voltage, combined with a X-ray energy dispersive system (EDX).

The crystalline structure and the corrosion product identification were investigated using a Pan Analytical Empyrean diffractometer with a Cu anode (Cu Kα radiation, λ = 0.15405 nm) equipped with PIXCel1D detector and 10°–90° as angle range. In order to achieve the highest signal-to-noise ratio, the operating conditions were 40 V and 40 mA.

Raman analysis was performed through a Renishaw inVia Raman Microscope spectrometer equipped with a microprobe (50×) and a CCD detector with a Nd:YAG laser with a wavelength of 532 nm.

Contact angle was measured using FTA 1000 instrument, with 5 μL droplets of deionized water. Measurements were repeated at least three times in several spots of the samples.

The identifications of organic species were evaluated by employing Fourier Transform Infrared Spectrometer (FTIR). A Spectrum One, Perkin Elmer equipment was used to record IR spectra and 8 scans between 4000 and 400 cm^{-1} at a resolution of 4 cm^{-1} were performed.

The estimation of the metal ions released in different physiological solutions was carried out by PerkinElmer Optima 2100 DV ICP-OES. Before analysis, a calibration line was recorded for each metal by using properly standard solutions.

To have information about the electronic properties of passive films, photocurrent spectroscopy was used. Physiochemical characterization of passive films and corrosion layers is a preliminary task for a deeper understanding of the corrosion behaviour of metals and alloys. In particular, corrosion mechanism is based on electron and ion transfer reactions at the metal/oxide and oxide/electrolyte interfaces depending on the nature of the redox couple in the solution (i.e. redox potential, $E_{red/ox}$), on the corrosion potential (E_{corr}), on the flat band potential (U_{fb}) of the semiconductive passive film and on its conductivity type (*p* or *n*-type)[67]. For this reason, the knowledge of solid-state properties of passive films is a fundamental tool for the location of the characteristic energetic levels of the *metals/passive film/electrolyte* interfaces, allowing the study of corrosion processes at a molecular level.

Photocurrent Spectroscopy (PCS) is a non-destructive technique based on the analysis of the electrochemical response, in terms of photocurrent and photopotential intensity, of the metal/passive film/electrolyte interfaces under irradiation with photons of suitable energy and intensity. The choice of analyzing under potentiostatic control is recommended due to the relevant role of the electrode potential in the establishment of electrochemical equilibria involving different metal oxidation states and reactivity of the passive films[68–70].

Besides the possibility related to the use of a very simple experimental set-up, PCS provides useful information on:

- energetics at the metal/passive film/electrolyte interfaces in terms of determination of passive film flat band potential (U_{fb}), internal photoemission thresholds and location of conduction and valence band edges;
- the oxide electronic structure and indirect determination *in situ* of the chemical composition of passive films through the knowledge of the optical band gap (E_g)[71].

Moreover, photocurrent response of passive film/electrolyte interface is strictly related to the number of absorbed photons. Therefore, PCS does not need special requirements in terms of surface finishing, allowing monitoring also long-term corrosion processes, where large changes in surface reflectivity are expected due to the formation of rough surface as a consequence of corrosion products covering. Finally, the risk of electrode modifications under illumination can be minimized by improving the sensitivity of the signal detection by using a lock-in amplifier, coupled to a mechanical light chopper, which allows to study very thin films (1 to 2nm thick) also under relatively low-intensity photon irradiation[69].

Conversely, the main limitations in the use of PCS are related to the following issues:

- only passive films having semiconducting or insulating properties can be investigated;
- surface layers with a band gap lower than 1 eV or higher than 5.5 eV require a more complex experimental set-up or are not accessible in aqueous solutions;
- complementary investigation based on the use of other techniques is necessary for the determination of structure and chemical composition of passive films.

The first two limitations are more apparent than real. In fact, according to the optical band gap values reported in the literature for amorphous or crystalline oxide films grown on a wide range of sp- and d- metals, most common metal oxides have bandgap values ranging within the optical limits of the PCS experimental set-up. Moreover, except for noble metals (i.e. Ir, Ru, etc.) where passive film growth occurs only at very high polarizing voltages, most metals are unstable in aqueous solutions and therefore photoactive films with insulating or semiconducting properties will spontaneously grow after immersion in the electrolytes. The third limitation is the principal one. Nevertheless, PCS can provide useful information regarding structure and composition of passive films if more realistic interpretative models are considered based on the valuation of the more complex electronic structure of amorphous passive layer[68–70].

PCS experimental set-up employed for the measurements performed in this Ph.D. work is reported in Figure 2. 1. It consists of a 450 W UV-Vis xenon lamp coupled with a Kratos monochromator. According to the lamp-monochromator system, working electrode is radiated with a photon flux at variable wavelength in a wide range of photon energies (5.5 to 1.5 eV) through a quartz window in the cell.

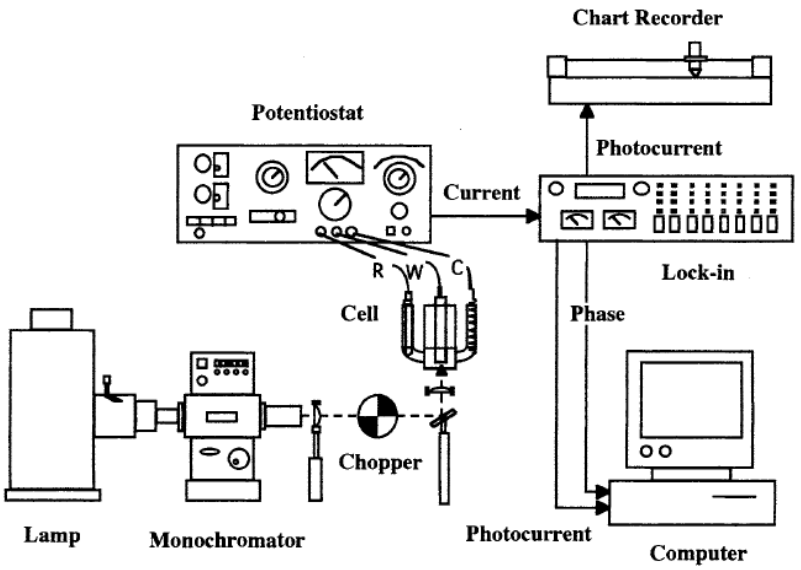

Figure 2. 1 *Experimental set-up employed for the Photocurrent Spectroscopy measurements. Image taken from [68].*

In order to detect weak photocurrent signals in the presence of large dark current, a chopper together with a lock-in amplifier is used. When the photocurrent is measured by means of the lock-in technique the illumination of the junction is interrupted several times per second (periodically chopped photon flux). In this case, the lock-in measures a signal whose intensity depends on the ratio between the chopping angular frequency, ω_c, and the time constant of the electrical equivalent circuit of the junction, τ, including also the electrolyte resistance ($\tau = R_tC_t$, with R_t and C_t representing the total resistance and capacitance of the junction respectively)[69].

To better understand the photoelectrochemical behaviour of a semiconductor/electrolyte junction under illumination, a briefly discussion regarding the main features and differences between a crystalline and an amorphous material is reported.

The structure of a semiconductor/electrolyte interface (SC/El) differs from that of the metal/electrolyte (M/El) interface due to the different mobile carriers' concentration. In addition, the potential drop, in the case of the metal/electrolyte interface, occurs mainly across the electrolytic double layer thus a change in the electrode potential U_E with respect to the reference electrode moves the Fermi level of the metal with respect to the electronic levels in the solution changing the photoemission threshold E_{th} as follow:

$$E_{th} = E_{th,0} + eU_E \qquad (2.1)$$

where $E_{th,0}$ represents the photoemission threshold at an arbitrary zero electrode potential value. Conversely, the potential drop at the SC/electrode interface occurs mainly across the space charge region inside the semiconductor. For the latter, the onset photocurrent energy threshold coincides with the band gap of the SC (E_g) that

is independent on the electrode potential. The total potential drop across the SC/El interface can be written as:

$$\Delta\Phi_{SC/El} = \{\phi_{SC}(\infty) - \phi_{SC}(0)\} + \{\phi_{SC}(0) - \phi_{El}(-\infty)\} \qquad (2.2)$$

where the first term in the right-hand side represents the Galvani potential drop from the bulk (zero electric field) to the surface of SC/El junction, whilst the second term represents the Galvani potential drop occurring into the compact and diffuse double layer (if any) of the electrolytic solution. According to the Galvani potential profile across the SC/El interface reported in Figure 2. 2, the region of the semiconductor, where the potential drop occurs, is defined as the space-charge region (i.e. X_{SC}).

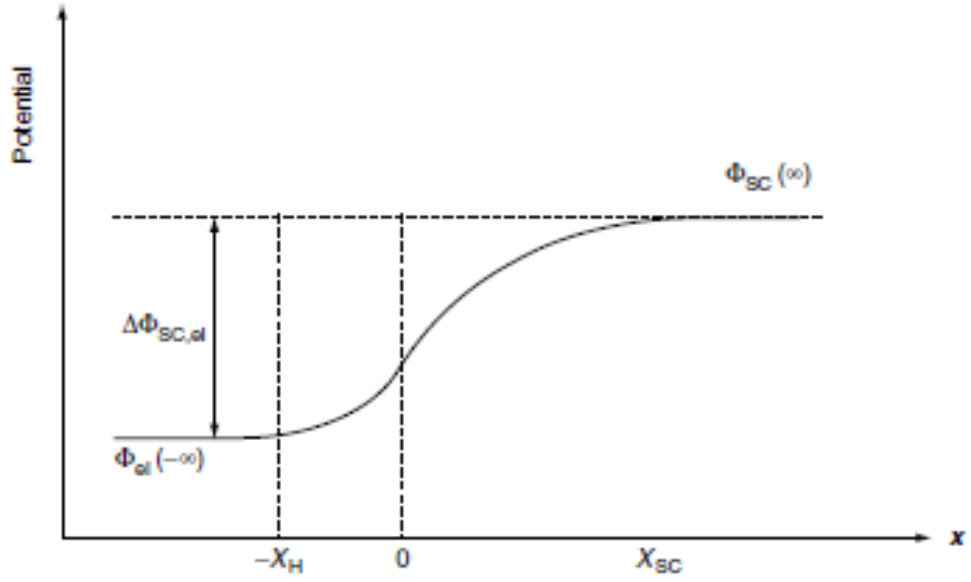

Figure 2. 2 *Galvani potential profile across the semiconductor/electrolyte (SC/El) interface. Image taken from [69].*

X_{SC} thickness change by changing the electrode potential according to the following equation:

$$X_{SC} = X_{SC}^{0}\left(\left|\Delta\Phi_{SC}\right| - kT/e\right)^{1/2} \qquad (2.3)$$

where X_{SC}^{0} is the space charge width in the semiconductor at 1 V of band bending and its value depends on the concentration of mobile carriers in the SC that is function of the doping level.

In Figure 2. 3, a schematic diagram of an n-type SC/electrolyte interface, in the energy-distance coordinates under slightly depleted (i.e. anodic polarization, $\Delta\Phi_{SC} > 0$) and flat band conditions (i.e. $X_{SC} = 0$), is also reported.

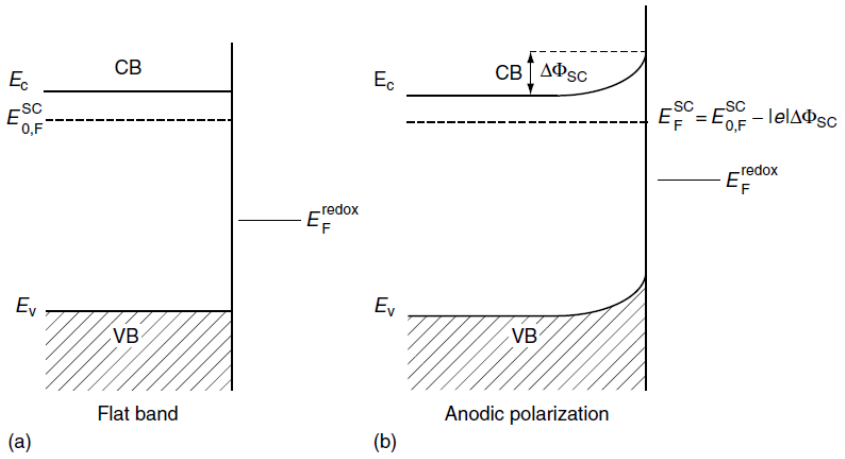

Figure 2. 3 *Electron energy levels in the SC/El junction a) at the flat band potential and b) under anodic polarization for an n-type semiconductor. Image taken from [69].*

When the potential drop within the semiconductor is zero (i.e. $\Delta\Phi_{SC} = 0$) the electrode potential U_E will be equal to U_{fb}, thus:

$$\Delta\Phi_{SC} = U_E - U_{fb} \qquad (2.4)$$

According to the Gärtner-Butler model, the absorption process of incident light in the bulk of the SC can be schematically represented as reported below in Figure 2. 4.

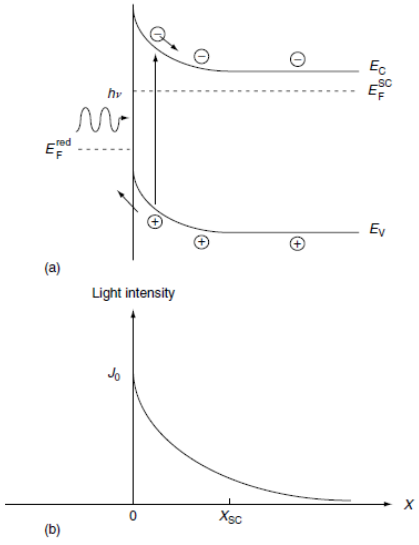

Figure 2. 4 *Schematic representation of a crystalline n-type SC/El interface under illumination where the generation of the electron-hole pair is also reported. Image taken from [69].*

where J_0 (cm^{-2} sec^{-1}) is the photon flux entering the SC corrected for the reflection losses at the SC/El interface which absorbed according to the *Lambert-*

Beer law. By assuming that each absorbed photon with energy $hv > E_g$ forms a free electron-hole couple, the number of electron-hole pairs generated per second and unit volume at any distance from the surface, *g(x)*, is given by:

$$g(x) = J_0 \alpha e^{-\alpha x} \qquad (2.5)$$

where the light absorption coefficient α (cm^{-1}) is a function of the incident light. According to the Gärtner-Butler model, the total photocurrent collected in the external circuit consists of two terms consisting of a migration, I_{drift}, and a diffusion term, I_{diff}. The first one considers the contribution of the minority carriers generated into the space-charge region, while the second accounts for the minority carriers entering the edge of the space charge region from the bulk field region ($x > X_{SC}$) of the SC. No light reflection at the rear interface is assumed, so that the light entering is absorbed within the SC. In addition, it is assumed that no recombination of the minority carriers occurs within the space-charge region due to the presence of an electric field which separates efficiently the photo-generated carriers, as well as for the carriers at the surface of the SC (i.e. the minority carriers coming at the depletion edge from the bulk region of the SC). According to the aforementioned assumption, the following equation, for a n-type SC, can be written as follow:

$$I_{ph} = I_{drift} + I_{diff} = eJ_0 \left[\frac{1 - \exp(-\alpha X_{SC})}{1 + \alpha L_h} \right] + ep_0 \frac{D_h}{L_h} \qquad (2.6)$$

where D_h and L_h are respectively the hole diffusion coefficient and the diffusion length and p_0 represent the hole equilibrium concentration. The same equation can also be written for a p-type semiconductor with D_n and L_n instead of D_h and L_h and n_0 (i.e. electron equilibrium concentration) instead of p_0[69]. For wide band gap SCs, where the concentration of minority carriers is very small into the bulk, the equation reported above can be simplified by neglecting the last term. Moreover, according to the definition of X_{SC}, and by assuming $\alpha X_{SC} << 1$ (slightly absorbed light) and $\alpha L_h << 1$ (small diffusion length for minority carriers), Butler derived the equation reported below for the photocurrent at a crystalline SC/El junction:

$$I_{ph} = eJ_0 \alpha X_{SC}^0 \left(U_e - U_{fb} - \frac{kT}{e} \right)^{1/2} \qquad (2.7)$$

Eq. 2.7 displays a quadratic dependence of the photocurrent on the electrode potential, that allows to find the flat band potential, U_{fb}, of the junction [69]. In fact, by neglecting the term *kT/e*, a plot $(I_{ph})^2$ vs. U_E may intercept the voltage axis at the flat band potential regardless of the employed λ as long as the assumption $\alpha X_{SC} << 1$ is respected. It is important to stress that all the equations discussed above pertain to the steady-state values of the *dc* photocurrent. The equations obtained for steady-state remain valid also for chopped conditions provided that the lock-in measured signal remains proportional to the steady-state chopped value[70].

In addition, a second important aspect embodied in Eq. 2.7 is the direct proportionality between the measured photocurrent and the light absorption coefficient. In fact, in the vicinity of the optical absorption threshold of the SC the relationship between the absorption coefficient and the optical band gap of the material, E_g, can be written as:

$$\alpha = A\frac{\left(h\nu - E_g^{opt}\right)^{n/2}}{h\nu} \qquad (2.8)$$

Thus, it is possible to derive the following equation:

$$Qh\nu = \left(h\nu - E_g^{opt}\right)^{n/2}\left(X_{SC}^{0}\sqrt{\left|U_e - U_{fb}\right|}\right) \qquad (2.9)$$

$Q = (I_{ph})/eJ_0$ represents the photocurrent collection efficiency and E_g^{opt} the optical threshold for the onset of photocurrent at the illuminated electrode. In fact, at constant electrode potential, it is possible to get the optical band gap of the material from the dependence of the photocurrent on the wavelength (i.e. the photocurrent spectrum of the junction) of the incident light at constant photon flux. In fact, by plotting $(Q\,h\nu)^{2/n}$ vs. $h\nu$ at constant electrode potential ($U_E - U_{fb} = \text{const.}$), it is possible to get a characteristic photon energy $h\nu_0 = E_g^{opt}$ where, for an ideal SC/El junction, E_g^{opt} is equal to the minimum distance in energy between the filled states of VB and empty states of CB, i.e. the band gap E_g. n can assume different values depending on the nature of the optical transitions between states of both the VB and the CB. In fact, optical transitions at the energies near E_g of a crystalline material can be direct or indirect. In the first case other particles do not participate apart from the incident photon and the electron of the VB while for the latter, the optical transition is assisted by the participation of lattice vibration. By assuming a parabolic electronic density of states distribution, i.e. DOS ($N(E) \propto E^{1/2}$) near the band edges, in the case of direct transition n is equal to 1 or 3, depending on whether the optical transitions are allowed or forbidden in the quantum mechanical sense[72]. Conversely, in the case of indirect optical transitions, the value of n is equal to 4. It is important to underlie that in the presence of strong surface recombination effects, the onset of photocurrent will occur at much higher band bending than that predicted by Gärtner-Butler equation[69].

Going from crystalline thick SC electrodes to very thin insulating or semiconducting corrosion films on metals, new interpretative models should be employed. In particular, the two models of DOS (i.e. density of states) usually considered for the interpretation of optical and electronic behaviour of insulating or semiconducting amorphous materials are showed in Figure 2. 5.

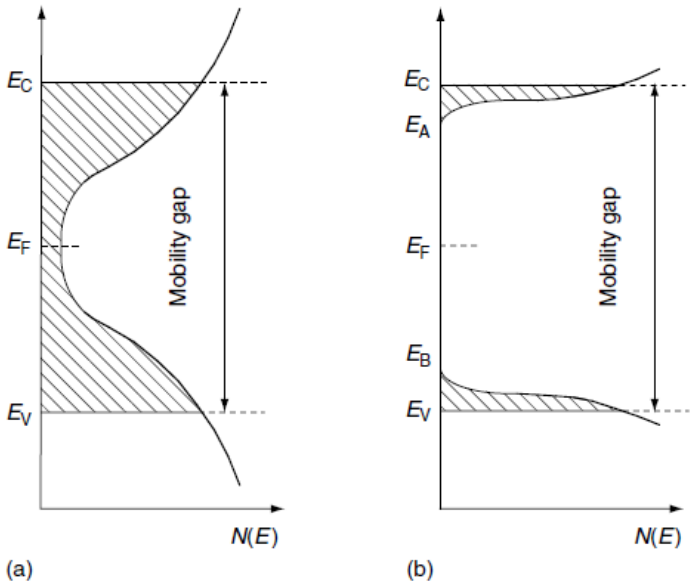

Figure 2. 5 *Representation of the density of electronic states as a function of energy according to different amorphous semiconductor models: a) Cohen-Fritzsesche-Ovinsky model and b) Mott and Davis model. The dotted areas represent the localized state while E_C and E_V are respectively the conduction and valence band mobility edges. Image taken from [69].*

The main feature of amorphous materials is the absence of long-range order in spite usually they retain the same short-range order with respect to the crystalline counterparts. Nevertheless, the band structure model can also be applied in the absence of long-range lattice periodicity. This means that the long-range disorder perturbs but does not annihilate the band structure allowing the presence of a finite density of states within the so called "mobility gap" ($E_C - E_V$) of the amorphous semiconductor (a-SC) or insulator. The DOS distribution reported in Figure 2. 5a (CFO model) accounts for the presence of defect states within the semiconductor that induce a continuous distribution of electronic states within the mobility gap. Conversely, the DOS distribution proposed by Mott and Davis can be attributed to an ideal amorphous material where only a long-range lattice disorder in considered (see Figure 2. 5b). The different electronic structure described for an amorphous semiconductor affects the generation and transport processes of photocarriers in amorphous materials and therefore the photoelectrochemical response of the a-SC/El junction.

In the case of amorphous material, by assuming a parabolic DOS distribution in the vicinity of the mobility edges of both conduction and valence bands, the following relationship holds:

$$\alpha h\nu = const\left(h\nu - E_g^m\right)^2 \qquad (2.10)$$

where $E_g^m = E_C - E_V$ is the mobility gap of the a-SC. The exponent 2 is reminiscent of the indirect optical transitions in crystalline material but now photons interact with the solid as a whole. This type of transition in amorphous materials is termed non direct. Because some tailing of states is theoretically foreseen for an a-SC by any proposed model of DOS, E_g^m represents an extrapolated rather than a real zero in the density of states. Notably, in the absence of appreciable differences in short-range order of amorphous and crystalline counterpart, the mobility gap of amorphous anodic films should be equal or larger than the band gap of the crystalline counterpart. Such a difference in optical band gap value can be assumed as a measure of the influence of lattice disorder. The difference $\Delta E_{am} = (E_g^m - E_g^{cryst})$ in the range of 0.1 to 0.35 eV, is in agreement with the expected extension of the localized states regions near the band edges due to the lattice disorder. Conversely, a mobility gap of passive film lower than the band gap of the crystalline counterpart must be interpreted as an indication that differences are present in the short-range order of the two phases due to the formation of a defective structure with a high density of localized states within the mobility gap as well as changes in the density of the passive film, which is known to affect also the value of the optical gap in amorphous materials[69].

To have information about corrosion resistance in physiological environment, electrochemical tests (open circuit potential, electrochemical tests and polarization curves) were carried out.

Electrochemical Impedance spectra are recorded at constant electrode potential by spanning the a.c. signal frequency. A purely sinusoidal voltage can be expressed as:

$$E = E_0 \sin(\omega t) \qquad (2.11)$$

where ω is the angular frequency, which is 2π times the frequency in Hz. The voltage signal can also be thought of as a rotating vector (or *phasor*) quantity whose length is the amplitude *E* and whose rotating frequency is ω[73]. The output signal will be a current response that usually is not in phase with the potential, thus the current is given by:

$$I = I_0 \sin(\omega t + \varphi) \qquad (2.12)$$

where φ is the phase angle. ϕThe impedance is defined as a kind of generalized resistance as follows:

$$Z = \frac{E}{I} \qquad (2.13)$$

The impedance response can be also described as having real and imaginary components, as follows:

$$Z = Z_{re} + jZ_j \qquad (2.14)$$

When the input and output are in phase, the imaginary part of the impedance has a value of zero and the impedance will have only a real contribution, Z_{re}. If the input and the output are out of phase, the real part of the impedance has a value zero and the impedance has only imaginary contribution Z_j. The relationship between the complex impedance and the phase angle is shown more clearly in the use of phase diagrams, as reported below:

$$Z = |Z|\exp(j\varphi) \quad (2.15)$$

Where |Z| represents the magnitude of the impedance vector and φ is the phase angle[74]. The variation of the impedance with frequency can be displayed in different ways. In *Bode plo*t log |Z| and φ are plotted as a function of log ω, while when the imaginary component Z_j is displayed as a function of the real one Z_{re}, an alternative representation of impedance is provided namely *Nyquist plot*[74].

However, critical issues in the interpretation of the EIS data consist of the determination of the most suitable equivalent circuit able to model the impedance results and on the physical meaning of the passive elements used for the equivalent circuit [67,75,76]. Basically, resistor, inductor and capacitor are the main passive components of an electrical circuit. The impedance of a resistor consists only of the real part, which is equal to the resistance of the resistor itself. When a voltage is applied across it, the current flowing through will be in phase with the applied potential. Capacitors are components that introduce capacitance into a circuit and thus are used for electrical energy storage in the form of electric field. The impedance of a capacitor consists only of the imaginary part and it increases by decreasing both the capacitance and the frequency of the applied signal. The current will be shifted of -90 degrees with respect to the applied voltage. An inductor is a component that introduces an inductance into a circuit and it is used for electrical energy storage in the form of a magnetic field. The impedance of an inductor increases by increasing the frequency of the applied voltage and the current through it will be shifted of 90 degrees with respect to the applied voltage.

When the assumption of a uniformly active electrode is not valid, a time-constant dispersion can be observed due to the variation along the electrode surface of reactivity or of current and potential, resulting in a 2-dimensional distribution. Time-constant dispersion can also be caused by a distribution of time constants reflecting a local property of the electrode, resulting in a 3-dimensional distribution. This variation can be modelled by a constant-phase-element (CPE), whose impedance can be expressed as follows:

$$Z_{CPE} = \frac{1}{(j\omega)^{\alpha} Q} \quad (2.16)$$

where ω is the frequency of the applied signal. Notably, the parameters α and Q are independent of frequency. When α is equal one, Q has units of capacitance and represents the capacity of the interface. Conversely, when α differs from one (i.e. $\alpha < 1$), Q has units of $s^{\alpha} / \Omega\ cm^2$ and the system shows behaviour that has been attributed to surface heterogeneity or to continuously distributed time constants for charge-transfer reactions[74], as displayed in Figure 2. 6.

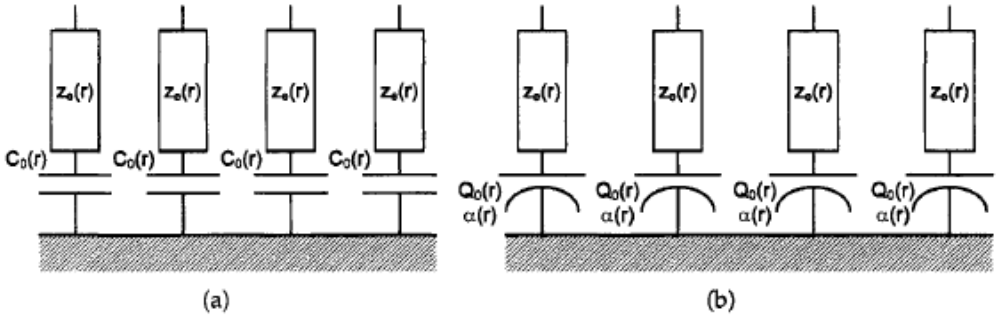

Figure 2. 6 *Schematic representation of time constant distribution for a blocking electrode in a) 2-dimensional and b) combined 2-dimensional and 3-dimensional distribution.*

In particular, according to the literature[74,77–79], $\alpha < 1$ can be associated to a passive film resistivity not constant on going from the metal to the electrolyte, allowing the use of the power-law theory. Indeed, according to previous works [79–81], the power law model provides physical meaning to the CPE behavior observed for passive films where a normal distribution of resistivity is assumed (i.e. 3D distribution), thus allowing to extract the corresponding effective capacitance associated to the CPE expressed as:

$$C_{eff} = \frac{\varepsilon\varepsilon_0}{\delta} \qquad (2.17)$$

where ε is the dielectric constant and ε_0 is the permittivity of vacuum equals to 8.8542×10^{-14} F/cm.

By assuming a dielectric constant independent of position into the passive film, it was found that the distribution of resistivity along the film thickness follows a power-low profile as reported below:

$$\frac{\rho}{\rho_\delta} = \xi^{-\gamma} \quad (2.18)$$

The parameter ξ is the dimensional position $\xi = y/\delta$, where δ represents the film thickness and y is the position through it. ρ_δ is the resistivity corresponding to $\xi = 1$ and γ is a constant that describes the variation of the resistivity. A distribution of resistivity that provides a bounded value for resistivity was proposed to be[82]:

$$\frac{\rho}{\rho_\delta} = \left(\frac{\rho_\delta}{\rho_0} + \left(1 - \frac{\rho_\delta}{\rho_0} \right) \xi^\gamma \right)^{-1} \qquad (2.19)$$

where ρ_0 and ρ_δ are the boundaries values of resistivity at the interfaces, while the relationship between the CPE parameters Q and α, the dielectric constant ε and the resistivity ρ_δ was found to be:

$$Q = \frac{(\varepsilon\varepsilon_0)^\alpha}{g\delta\rho_\delta^{1-\alpha}} \qquad (2.20)$$

where g is the interpolation formula defined as:

$$g = 1 + 2.88(1-\alpha)^{2.375} \qquad (2.21)$$

The effective oxide capacitance, C_{eff}, is derived by inserting eq. (2.21) in eq. (2.20), and thus the corresponding oxide thickness according to the following relationship:

$$C_{eff} = (\varepsilon\varepsilon_0)^{1-\alpha} gQ\rho_\delta^{1-\alpha} = \frac{\varepsilon\varepsilon_0}{\delta} \qquad (2.22)$$

When α and g are equal to 1, the CPE parameter Q represents the capacitance of passive films, where Q and α can be obtained due to the fitting of the EIS spectra, while ε can be obtained through independent measurements[78].

Notably, the power law model can be a useful tool for the estimation of oxide thicknesses. Nevertheless, it does not provide straightforward information regarding their corresponding corrosion resistance, that in turn is affected by many other parameters such as composition, morphology and electronic properties of passive films in terms of band gap (E_g), flat band potential (U_{fb}) and the presence of localized states in the gap.

Polarization curves represent, in the field of electrochemistry and corrosion processes, a fundamental tool providing crucial information about the kinetic of electrode reactions occurring on the surface of a metal immersed in an electrolyte[83].

In practical terms, polarization curves are obtained experimentally by applying a controlled variation of potential (ΔV) or current to the electrode under investigation and measuring the corresponding response. By plotting the potential against logarithm of current density, it is possible to obtain the characteristics of both the anodic and the cathodic reactions deriving the system's operating conditions. The E/log(i) graphs are called Evans diagram and describes the relationship between the electrode potential of a metal and the current density flowing through the metal-electrolyte interface[83].

An example of a metal exhibiting active corroding behaviour is iron immersed in an acidic solution, where the surface reactions are the anodic dissolution of iron and the reduction of water, leading to hydrogen evolution.(see Figure 2. 7)

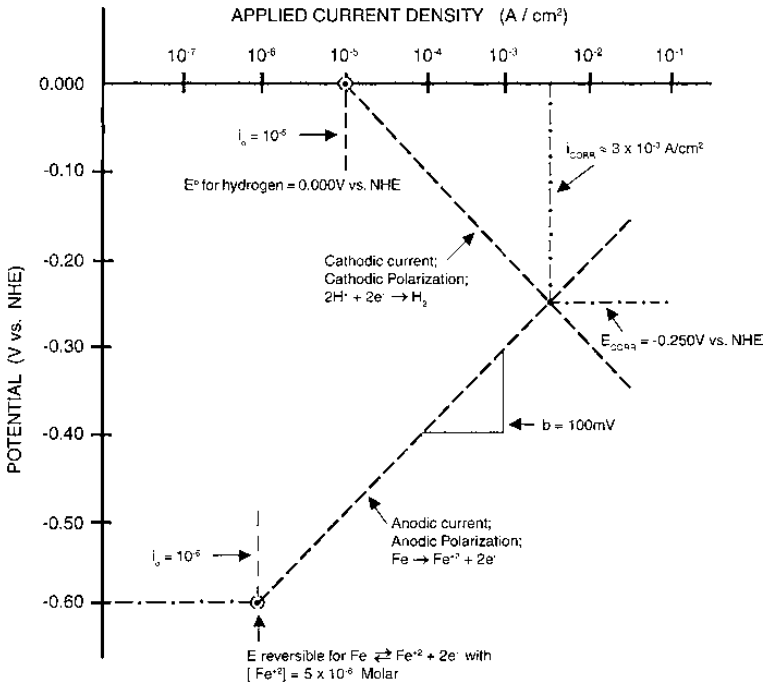

Figure 2. 7 *Evans diagram for Fe in acidic solution. Image taken from ref [84]*

The difference between the Evans diagram and the polarization curve is that the polarization curve data display applied current densities, whereas the Evans diagram displays the reaction rates in terms of current densities. The applied current density is the difference between the total anodic and the total cathodic current densities (reaction rates) at a given potential:

$$i_{app} = i_a - |i_c| \qquad (2.24)$$

using the convention in which the cathodic current density is defined as negative. At the corrosion potential (E_{corr}), the anodic and cathodic rates are exactly equal; thus the applied current density is zero.

Imposing an anodic current density on the iron with an external device results in the generation of the anodic branch of the polarization curve. Increasing the applied anodic current decreases the reduction reaction rate as the surface is polarized in the positive direction. At sufficiently large anodic current densities, the cathodic reaction is insignificant relative to the anodic current density, so the applied current density is virtually equal to the anodic current density. Measurements under these conditions allow the Tafel slope to be determined.

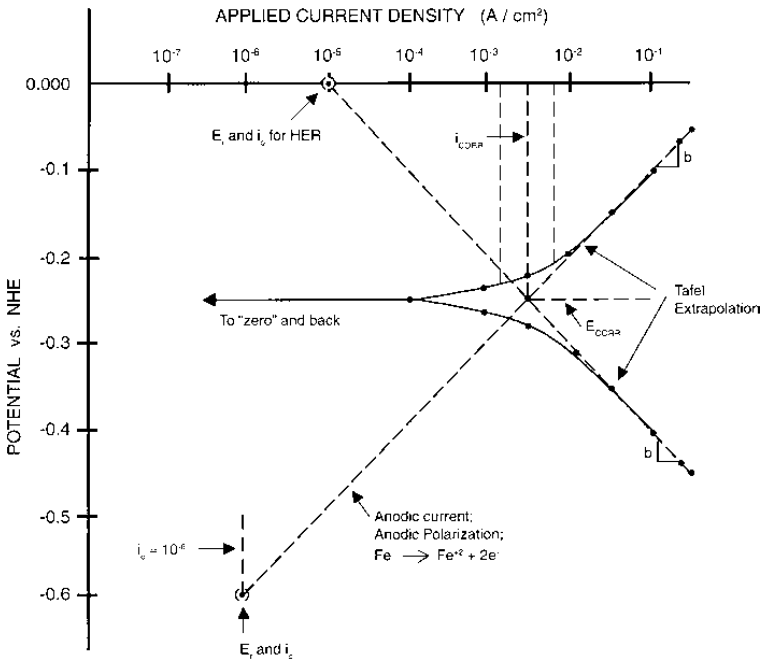

Figure 2. 8 *Polarization curve that would result for Evans diagram, see* ***Figure 2.*** *7. Image taken fron ref [84]*

The development of the cathodic branch of the polarization curve can be described in a qualitatively similar manner.

At potentials well away from the corrosion potential, the applied current density reflects the kinetics of only one of the reactions. Extrapolating the linear portions of the polarization curve (see Figure 2. 8) found at potentials well away from E_{corr} leads to an intersection at E_{corr}. This intersection corresponds to i_{corr}, the corrosion rate.[84]

3 Ti6Al4V alloys for permanent implants

3.1 Electronic properties of passive films in physiological environment

Ti and titanium alloy are covered by a thin oxide layer grown by air exposure. Indeed, due to the low reduction potential of titanium, this metal is not stable under oxygen atmosphere and therefore it is covered by a few nm thick TiO_2 layer (usually amorphous), that results to be very protective toward the aggressive environment. The latter can be thickened by anodizing and hard anodizing processes, leading to the formation of TiO_2 barrier and porous layers, respectively. The latter can make the surface of Ti and Ti alloys bioinert, thus affecting the behaviour of Ti implants in the human body.

In this work, to understand in which extent this statement is true, an electrochemical investigation was carried out to study the electronic properties of native titanium oxide and anodic TiO_2 trying to correlate these properties to their corrosion resistance in simulated body fluids.

Porous layers were grown in an aqueous solution containing calcium acetate (CA, $(CH_3COO)_2Ca \cdot H_2O$) and β-glycerol phosphate disodium pentahydrate (β-GPDS) up to a formation voltage of 200 V, while barrier layers were grown at 40 V in phosphoric acid solution. Photoelectrochemical measurements were carried out to examine the effects of anodizing conditions and alloying elements (specifically Al and V) on the optical band gap and flat band potential of the oxide layers. Additionally, electrochemical tests were performed in HBSS at 37°C to assess the reactivity of the samples as a function of metal composition and anodizing parameters. [85]

Titanium foils were etched for 30 seconds in a solution of hydrofluoric acid (39.5%), nitric acid (69.0%), and deionized water (1:4:5 vol.). The etched samples were then ultrasonically cleaned in deionized water for 10 minutes and dried in air for 24 hours before use.

Ti6Al4V alloy was prepared by mechanical polishing using SiC abrasive papers with P800, P1200, and P2400 grit. The polished samples were then degreased in an ultrasonic bath with acetone, followed by rinsing with deionized water.

The growth of both barrier and porous oxide layers was performed using a two-electrode configuration, with the metal (Ti6Al4V alloy or Ti) as the anode (working electrode) and a platinum net with a high specific surface area as the cathode (counter electrode).

The barrier-type anodic film was grown in 100 mM H_3PO_4 aqueous solution. [86,87] Anodizing process was performed galvanostatically at 5 mA cm^{-2}, up to 40 V. The final voltage was stabilized for 30 min.

To grow porous oxide layers, Ti6Al4V alloys and Ti were anodized up to 200V galvanostatically at 20 mA cm^{-2} in an aqueous solution 200 mM in calcium acetate (CA, $(CH_3COO)_2Ca \cdot H_2O$) and 40 mM in β-glycerol phosphate disodium pentahydrate (β-GPDS, $C_3H_7Na_2O_6P \cdot 5H_2O$). [85]

Photocurrent spectra relating to the air formed passive films grown on Ti and Ti6Al4V recorded at corresponding open circuit potential (~ 0 V vs. Ag/AgCl and ~ - 0.2V vs. Ag/AgCl for Ti and Ti6Al4V) are reported in Figure 3.1.1.

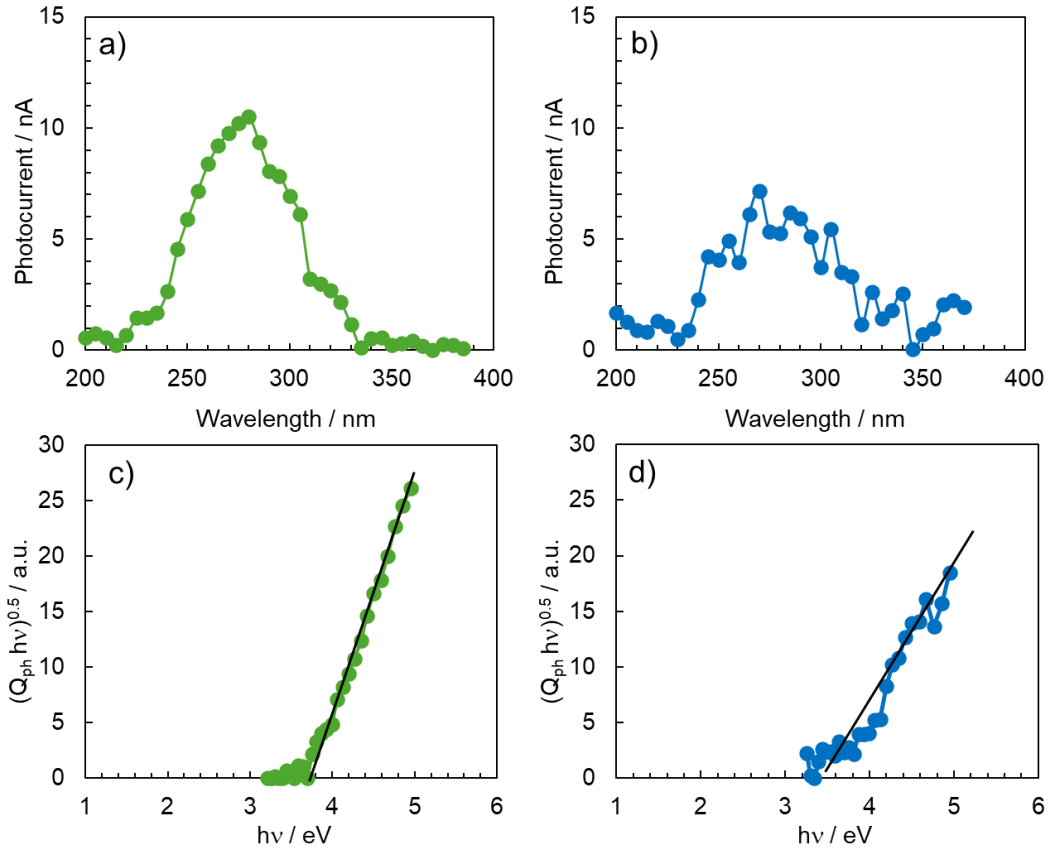

Figure 3.1.1 *Photocurrent spectra at corresponding OCP and $(Q_{ph}\ h\nu)^{0.5}$ vs. $h\nu$ recorded 0.1 M ABE for air formed film grown on a, c) Ti and b, d) Ti6Al4V alloy.*

The band gap values can be estimated assuming indirect optical transitions according to equation 3.1.1:

$$(Q_{ph}\ h\nu)^{0.5} \sim (h\nu - E_g) \qquad (3.1.1)$$

Where Q_{ph} is the photocurrent yield, that results proportional to the light absorption coefficient provided that photon energy ($h\nu$) is close to the band gap, E_g [88,89]. The estimated band gap for the air-formed film on Ti is 3.76 eV, while for

the air-formed film on Ti6Al4V is 3.62 eV. These values are higher than the optical band gaps reported for anatase (3.20 eV) and rutile (3.05 eV) TiO_2 polymorphs. This increase is typically attributed to the formation of a non-crystalline and/or defective titanium oxide. Indeed, deviations from perfect stoichiometry and/or the absence of long-range order can lead to the formation of localized states near the band edges. [90]. In these conditions optical band gap can be properly called mobility gap [91].

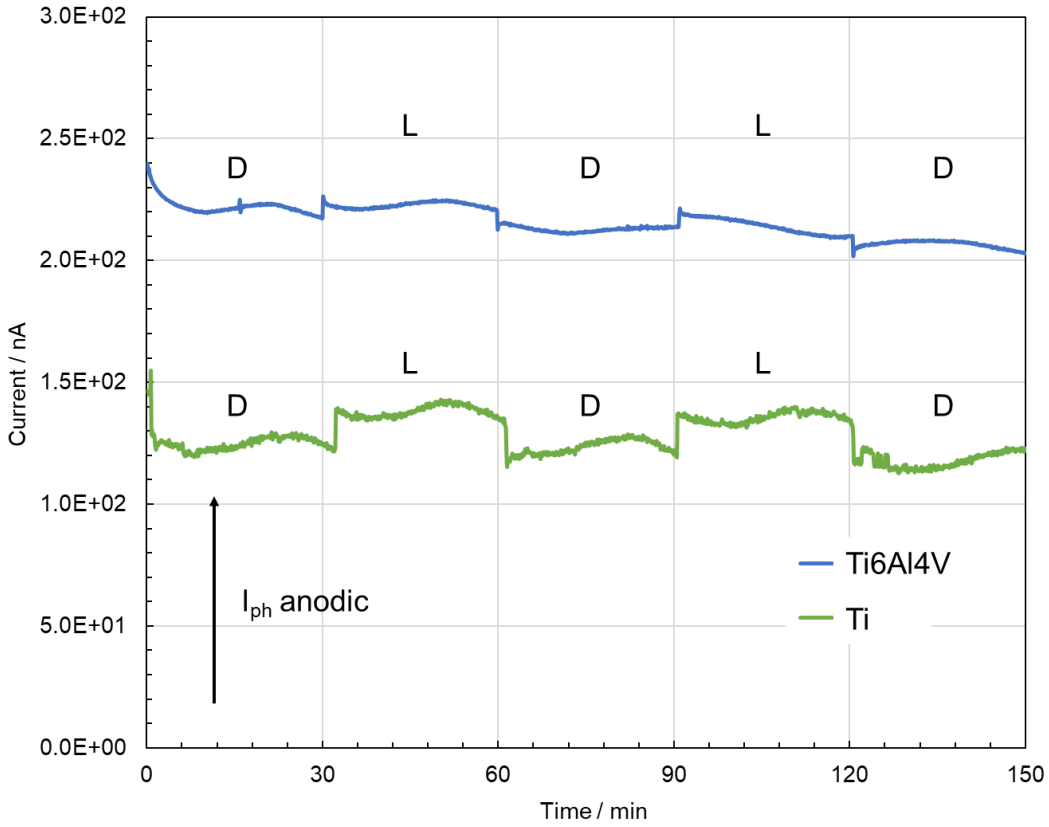

Figure 3.1.2 *Current vs time curves recorded in 100mM ABE at OCP for air formed film grown on Ti and TAV alloy by manually chopping the irradiation.*

Figure 3.1.2 discloses the current transients recorded at the open circuit potential for both air-formed films on Ti and Ti6Al4V under monochromatic light irradiation. The latter was periodically interrupted to measure the extra current due to the light absorption. The photocurrent is anodic, in agreement with the expected for n-type semiconducting behaviour of titanium oxide. However, it is noteworthy that a lower photocurrent (I_{ph}) was observed for the oxide grown on the alloy.

Figure 3.1.3 show the cell voltage vs. time transients recorded during the anodizing process in a phosphoric acid solution for Ti and Ti6Al4V alloys.

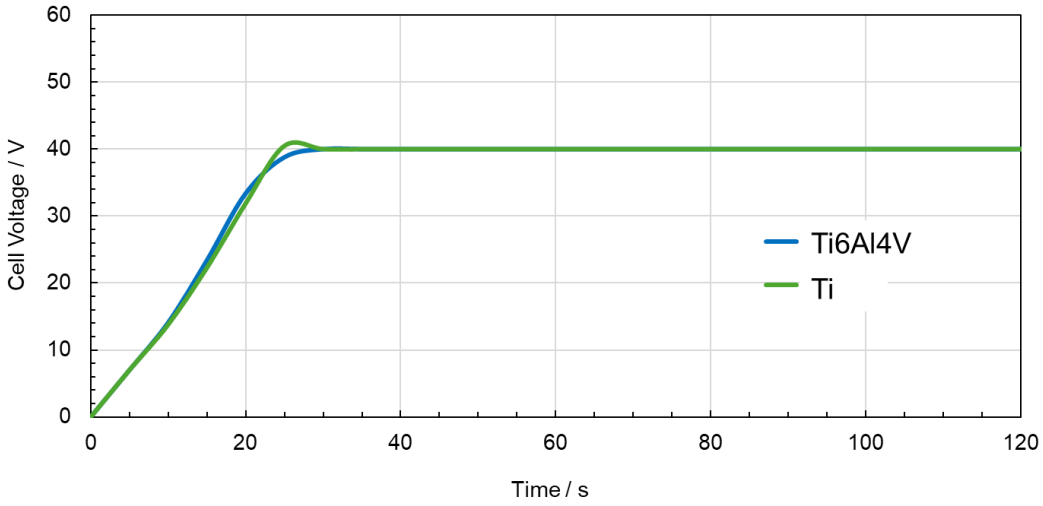

Figure 3.1.3 *Cell voltage vs. time recorded during the anodizing process of Ti and Ti6Al4V alloy 0.1 M H_3PO_4 galvanostatically at 5 mA cm^{-2}.*

In both cases, the voltage increases linearly until reaching the compliance limit of 40 V, which is then maintained for 30 minutes to promote the formation of a less defective film. This behaviour is consistent with the formation of a barrier-type anodic oxide.

According to the high field mechanism [92,93], the slope of the V vs time curve, dV/dt, is given by the following equation:

$$\frac{dV}{dt} = \eta \frac{iXM}{zF\rho} \qquad (3.1.2)$$

where i represents the current density (which is kept constant during the anodizing process), M is the molecular weight of the growing oxide, z is the number of electrons transferred per mole of formed oxide, F is the Faraday constant, ρ is the film density, X is the electric field strength across the growing layer, and η is the growth efficiency. For both Ti and Ti6Al4V alloys a dV/dt of ~ 1.6 V s^{-1} is estimated.

Assuming the formation of TiO_2 as anodic film on both samples, from eq. 3.1.2, with ρ_{TiO2} = 3.7 g cm^{-3} [94], X = 5.7 MV cm^{-1} can be estimated, corresponding to an anodizing ratio (i.e. the reciprocal of the electric field strength) of ~ 17 Å V^{-1}. Thus, assuming an equilibrium potential for Ti oxidation to TiO_2 of ~ -1.2 V vs SHE [95], formation voltages of 40 V (vs. cathode) correspond to anodic layer thickness of ~ 70 nm.

To estimate the optical band gap of the oxide layers, photocurrent spectra (photocurrent vs. irradiating wavelength curves) were recorded at 2 V vs. Ag/AgCl in 100 mM ABE (see Figure 3.1.4a-b).

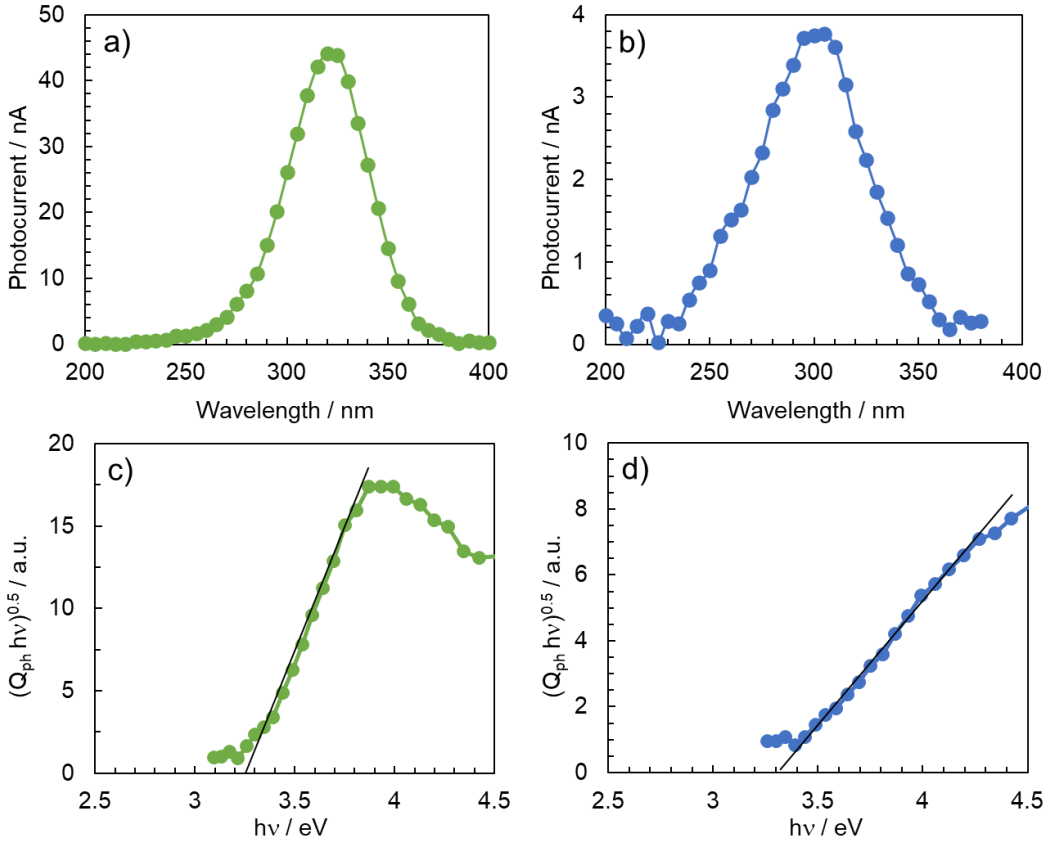

Figure 3.1.4 *Photocurrent spectra at 2 V vs Ag/AgCl and* $(Q_{ph}\, h\nu)^{0.5}$ *vs.* $h\nu$ *recorded 100 mM ABE for anodic oxides grown to 40 V on a, c) Ti and b, d) Ti6Al4V alloy.*

By assuming indirect optical transitions, an optical band gap (*Eg*) of 3.30 eV is estimated for the anodic film on Ti (see Figure 3.1.4c). This value aligns with previous reports in the literature for non-crystalline or defective titanium oxide. [87] For the anodic film grown on Ti6Al4V, a band gap of approximately 3.40 eV is estimated (see Figure 3.1.4d), which is slightly higher than that of the anodic film on Ti. This suggests an even lower crystalline character. The primary factor contributing to the differences in the photocurrent response between less crystalline/amorphous and crystalline thin films is the presence of various types of defects, which can alter the density of states (DOS) distribution. As a result, the optical band gap of an amorphous material may or may not coincide with that of its crystalline counterpart. This is further supported by the lower photocurrent measured for the anodic film on the alloy. In fact, in less crystalline/amorphous anodic oxides, geminate recombination effects involving generated photocarriers can reduce the recorded photocurrent signal. [96]

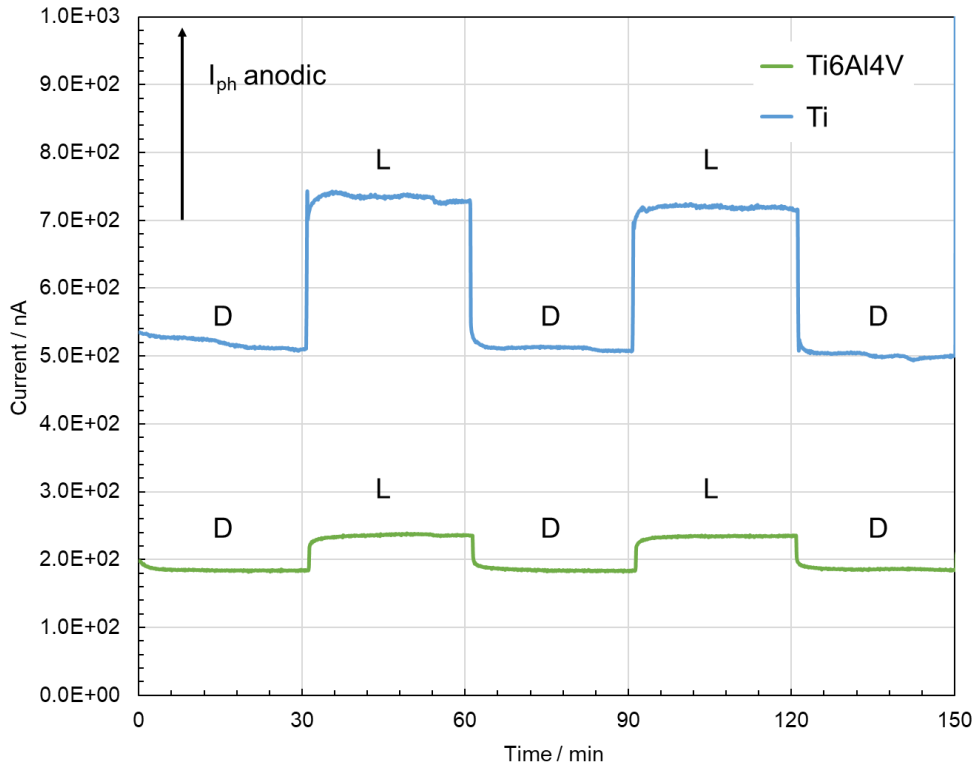

Figure 3.1.5 *Current vs time curves recorded, by manually chopping the irradiation, in 0.1 M ABE at 2 V vs Ag/AgCl for anodic oxides grown to 40 V on Ti and TAV alloy.*

Figure 3.1.5 shows the current vs. time curves recorded at 2 V vs. Ag/AgCl, where monochromatic irradiation was manually chopped for 40 V anodic films grown on Ti and Ti6Al4V. In both cases, the measured photocurrent is anodic, as expected for n-type semiconductors. However, a notably lower photocurrent (I_{ph}) was observed for the oxide grown on the alloy.

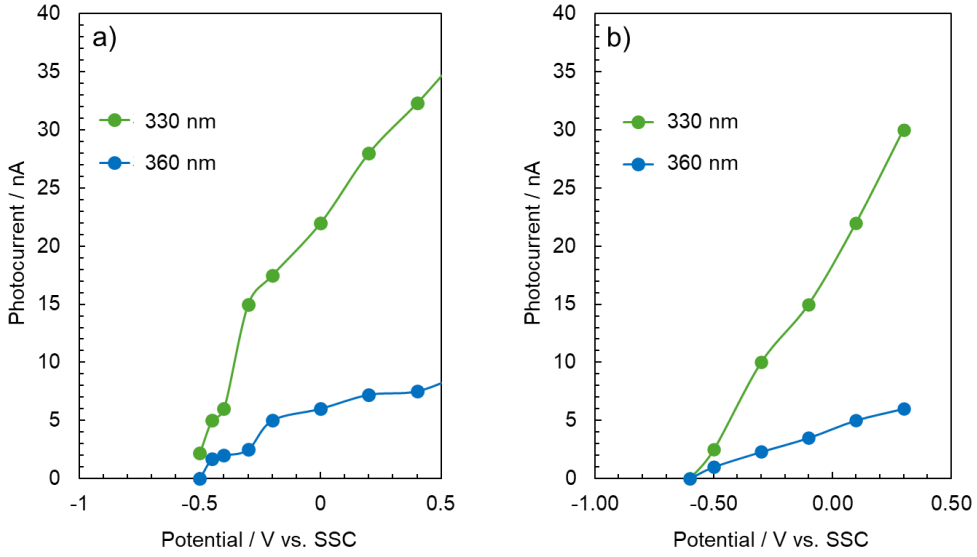

Figure 3.1.6 *Photocharacteristics recorded for anodic oxides grown to 40 V on (a) Ti and (b) Ti6Al4V alloy in 0.1 M ABE at different wavelengths.*

Figure 3.1.6 presents the I_{ph} vs. potential curves recorded at different wavelengths. As expected for *n*-type semiconducting materials, I_{ph} decreases as the potential shifts in the negative (i.e. cathodic) direction.

The zero-photocurrent potential can be used to estimate the flat band potential (E_{FB}) of the oxides, which is directly related to the oxide Fermi level (E_{ox}^{F}) according to the following equation [89]:

$$E_{ox}^{F} = -|e|E_{FB} + |e|E_{ref} \quad (3.1.3)$$

where e is the electron charge and E_{ref} is the potential of the reference electrode (Ag/AgCl) with respect to the vacuum scale. For anodic films on Ti and Ti6Al4V, the flat band potentials (E_{FB}) are approximately -0.5 V vs. Ag/AgCl and -0.6 V vs. Ag/AgCl, respectively. The slightly more negative E_{FB} for the anodic film on the alloy suggests that the Fermi level of the anodic film on Ti6Al4V is closer to the conduction band edge than that of the anodic film on Ti.

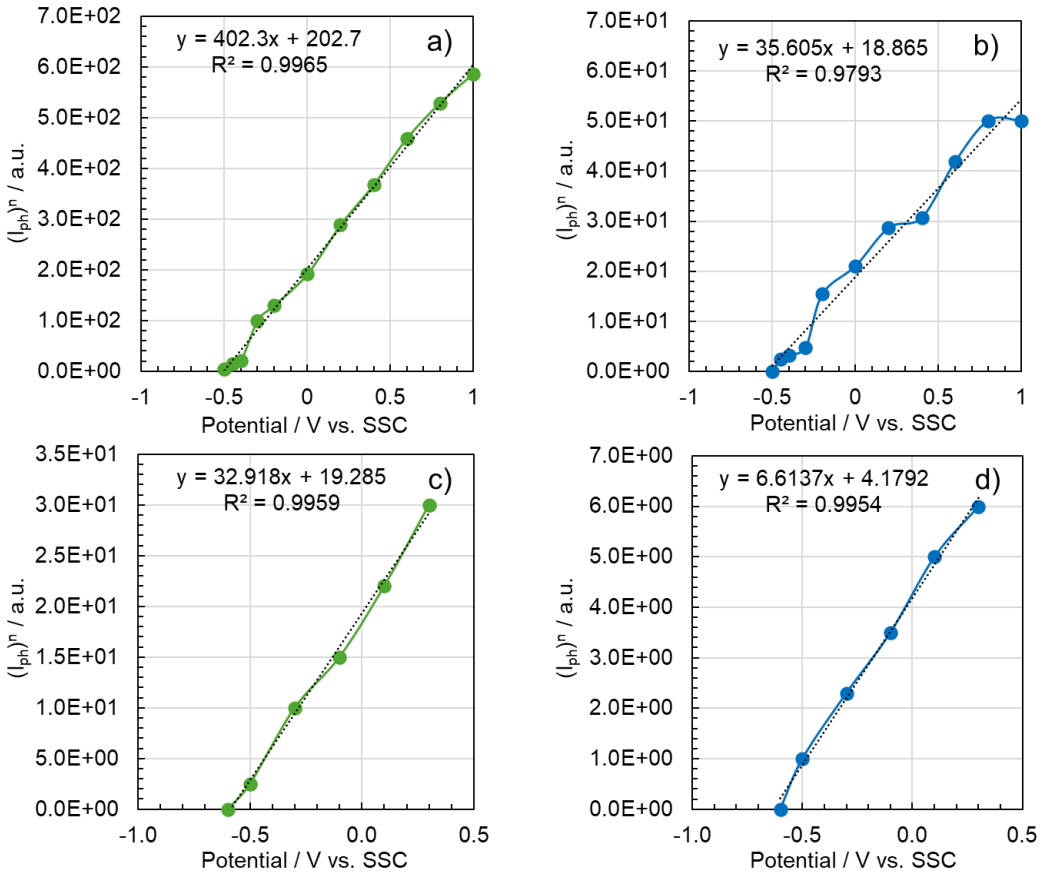

Figure 3.1.7 *Fitting of photocharacteristics related to anodic oxides grown on Ti and Ti6Al4V to 40 V. Ti: a) l = 330 nm and b) l = 360 nm. Ti6Al4V: c) l = 330 nm and d) l = 360 nm.*

The photocharacteristics were fitted (see Figure 3.1.7) according to the following power law:

$$I_{ph}^{n} \propto E \qquad (3.1.4)$$

The best-fitting exponent *n* was found to be 1.7 for the anodic film on Ti for both irradiating wavelengths (see Table 3.1.1).

Sample	λ / nm	n
Ti 40 V	330	1.7
	360	1.7
Ti6Al4V 40 V	330	1
	360	1
Ti 200 V	300	2
	330	2
	360	2
Ti6Al4V 200 V	320	0.85
	360	0.5
	400	0.5

Table 3.1.1 *Comparison between the exponent n estimated from the best fitting according to Eq. (3.1.4) of the photocharacteristics relating to anodic films on Ti and Ti6Al4V alloy.*

According to the Gärtner-Butler model, which is valid for crystalline semiconductor/electrolyte junctions, the dependence of photocurrent on electrode potential should be quadratic (i.e. $n = 2$). For amorphous materials, *n* is expected to decrease. In general, *n* values depend by the characteristic of the passive film, such as the crystallinity, the number of photocarriers and the mobility. [97]The observed *n* value slightly lower than 2 can be explained by the lack of long-range order in the thin amorphous TiO_2, leading to a consequent reduction in the mobility of the photogenerated charge carriers. [98] In the case of the photocharacteristics recorded for the anodic layer grown on the Ti6Al4V alloy (see Figure 3.6b), the best-fitting exponent *n* is 1, indicating that the photocurrent has a linear dependence on electrode potential. This suggests an even lower mobility of the photogenerated carriers, likely due to their presence in localized states.

During anodizing, Ti, Al, and V have very similar transport numbers, meaning they are incorporated from the base alloy into the anodic layer roughly in proportion to their respective percentages in the alloy. According to the experimental photoelectrochemical findings, this incorporation does not significantly affect the electronic properties of the barrier layers.

Figure 3.1.8 shows the growth curve (cell voltage vs. time) for Ti and Ti6Al4V anodized in CA and β-GPDS-containing solution at 20 mA cm^{-2}.

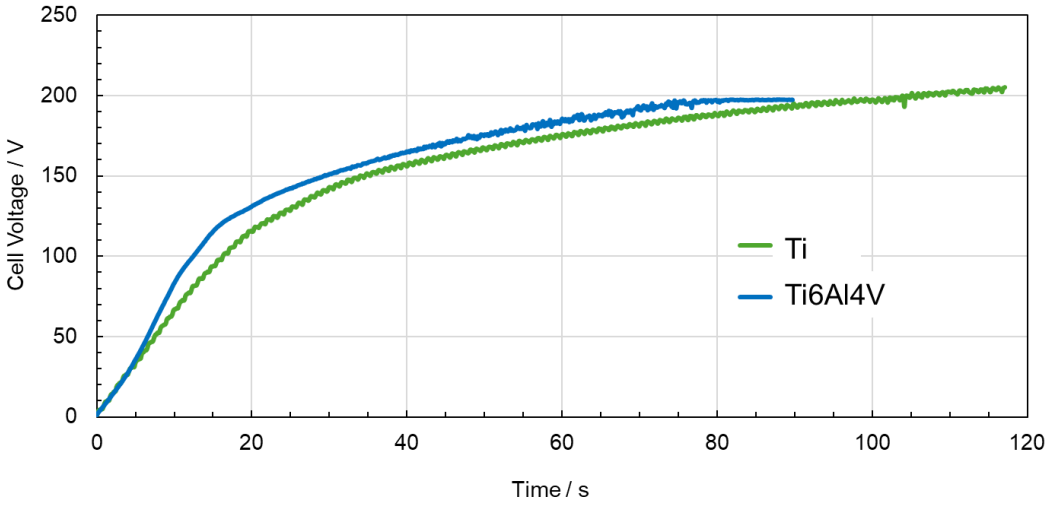

Figure 3.1.8 *Growth curve of Ti and Ti6Al4V alloy in 0.2 M CA and 0.04 M β-GPDS, anodized galvanostatically at 20 mA* cm^{-2}.

During the initial stages of the anodizing process, a linear relationship between cell potential and time is observed, which is typical of the growth of a barrier anodic oxide, resulting in a compact and uniform oxide film. [94] For cell potentials greater than approximately 50 V, the oxygen evolution reaction occurs, resulting in a change in the slope of the growth curve and a decrease in the efficiency of the anodizing process. Higher cell potentials lead to dielectric breakdown of the oxide film, causing the formation of an outer porous structure in a hard anodizing regime. This is further evidenced by the oscillations in the growth curve for cell potentials exceeding around 165 V. Under hard anodizing conditions, the electric field is so high that the film continuously breaks and repairs, resulting in a porous oxide whose composition is influenced not only by the electrolyte used but also by the metallic substrate composition. [99] Under these anodizing conditions, porous layer thickness is estimated to be ~2.5 μm, according to what reported by Ishizawa and Ogino. [100]

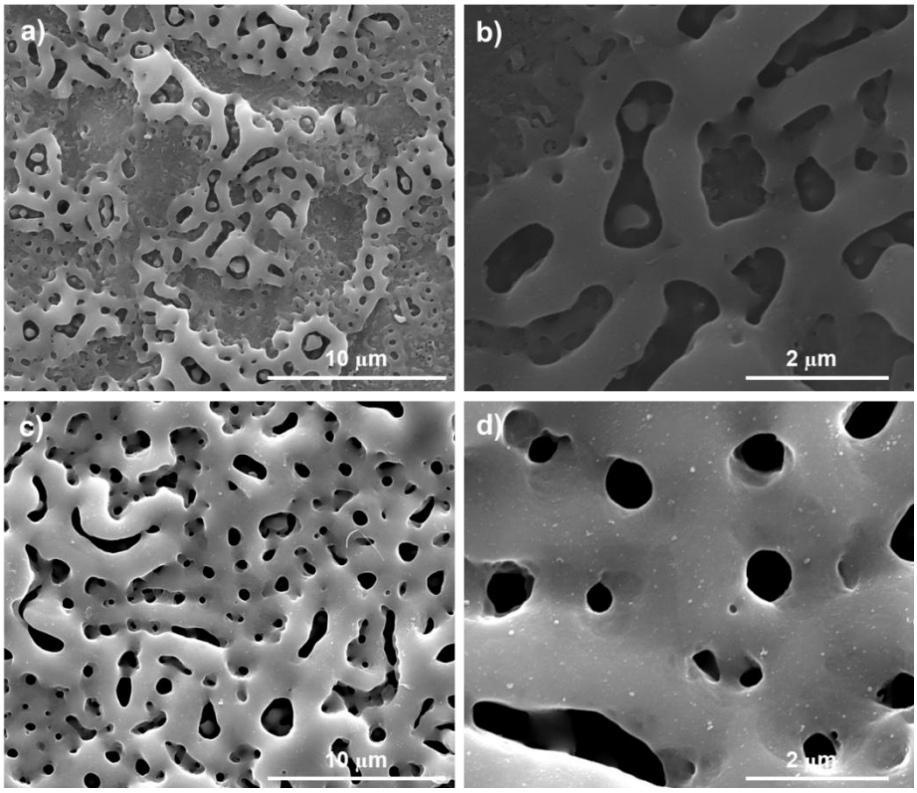

Figure 3.1.9 *SEM micrographs of surface of anodic layers grown in 0.2 M CA and 0.04 M β-GPDS at 20 mA cm^{-2} to 200 V on (a), (b) Ti and (c), (d) Ti6Al4V alloy.*

Figure 3.1.9 shows SEM micrographs of Ti and Ti6Al4V after anodizing to 200 V, revealing a multiscale porous structure with a wide distribution of pore diameters. The oxide is cracks free if compared to previous results reported in the literature for anodic layers grown in more concentrated CA and β-GPDS-containing solutions. [101]

	Ti		Ti6Al4V	
Element	**Wt %**	**At %**	**Wt %**	**At %**
O	29.5	55.1	32.6	57.1
Ti	67.4	42.1	54.1	31.7
Al	/	/	3.5	3.7
V	/	/	1.8	1
Ca	1.1	0.9	3.5	2.5
P	2	1.9	4.5	4

Table 3.1.2 *EDX analysis related to the compositions of anodic oxides grown on Ti and Ti6Al4V to 200 V.*

EDX analysis (see Table 3.1.2) indicates that the anodic layers contain Ti and O, as well as Ca and P. For films grown on Ti6Al4V, the analysis also reveals the

presence of Al and V, which were incorporated into the oxide during the anodizing process. [102]

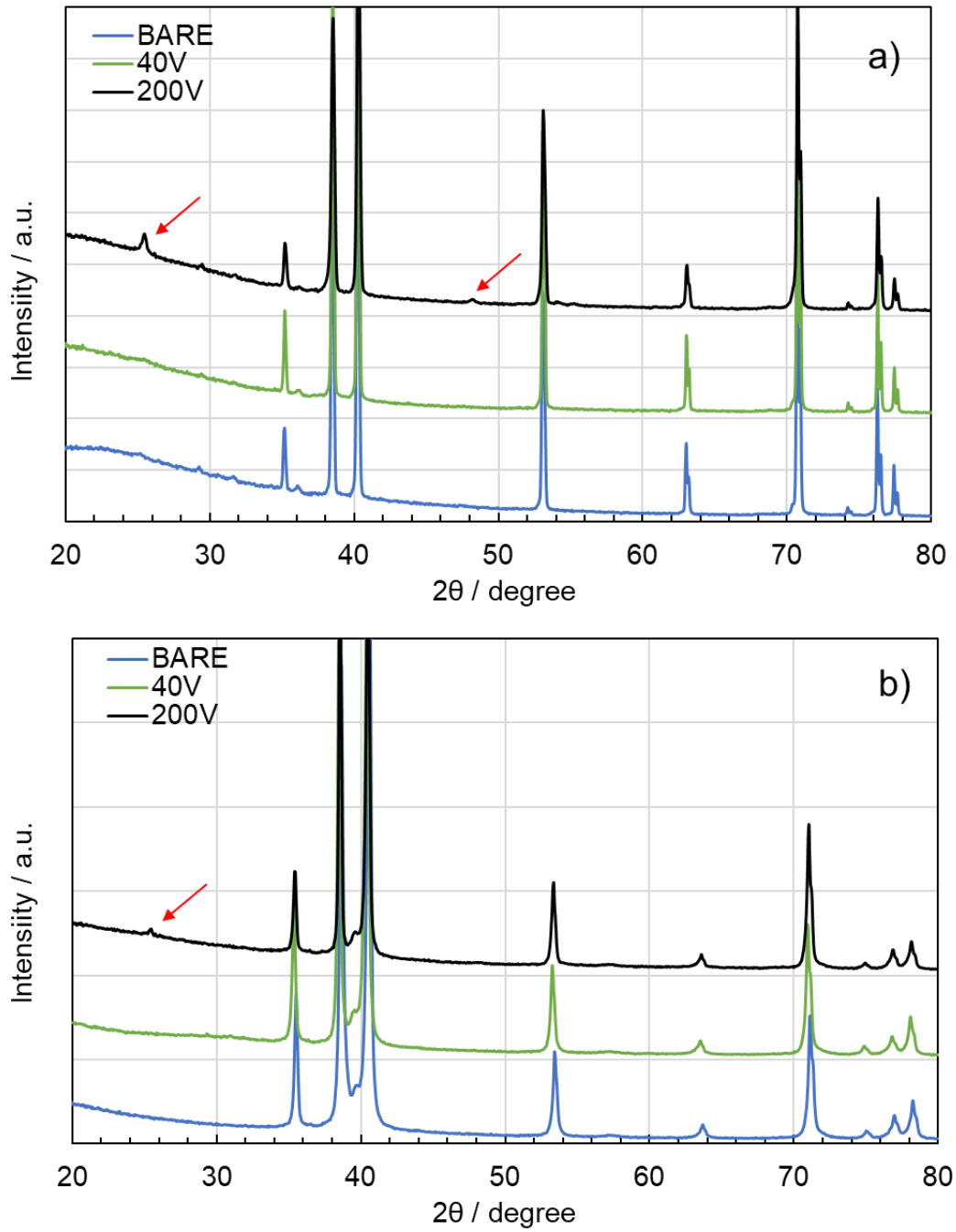

Figure 3.1.10 *XRD patterns of anodic layers grown on a) Ti and b) Ti6Al4V alloy.*

Figure 3.1.10 presents the X-ray diffraction patterns recorded for Ti and Ti6Al4V after anodizing to 40V and 200V, in comparison to the bare samples. In addition to the reflections from the substrates (bare Ti and Ti6Al4V), the (101) and (200) reflections of anatase, corresponding to $2\theta = 25.3°$ and $48.05°$ respectively, are detected for the anodic oxides grown on Ti, indicating the formation of this TiO_2 polymorph. [103] For the anodic oxide grown on Ti6Al4V, only the (101) reflection is present, and it is less intense, suggesting a lower crystallinity.

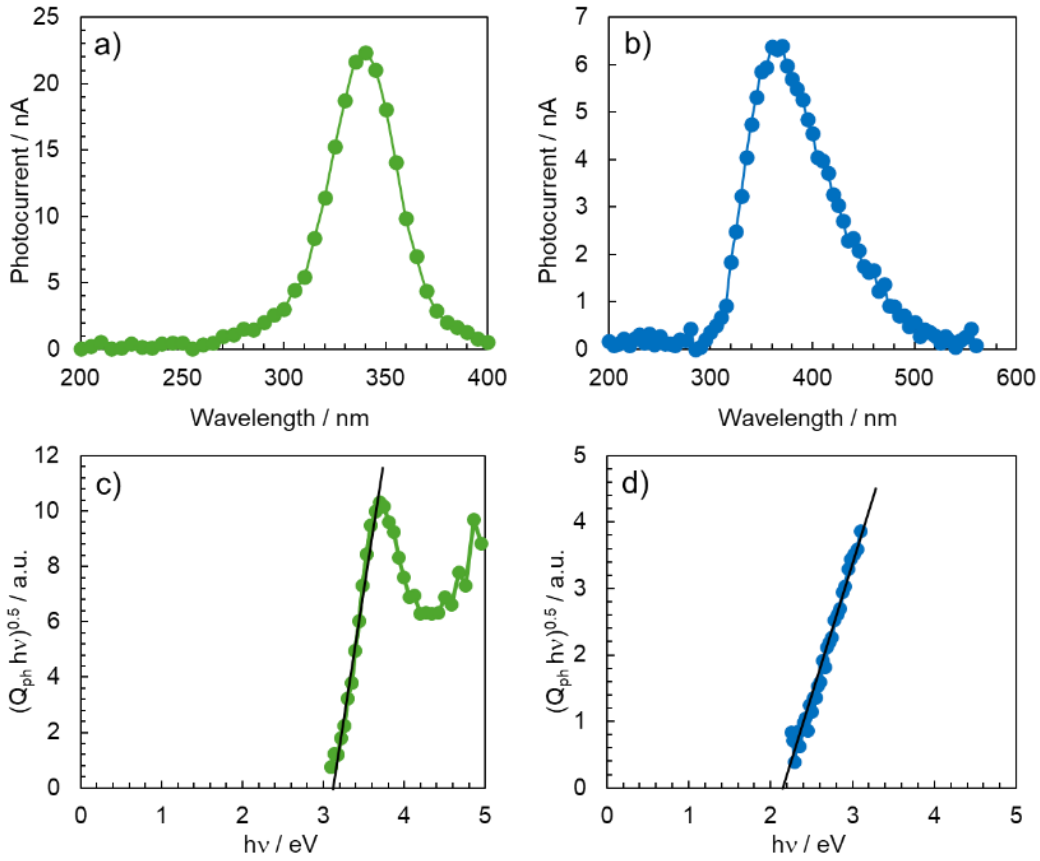

Figure 3.1.11 *Photocurrent spectra at 2 V vs Ag/AgCl and $(Q_{ph}\ h\nu)^{0.5}$ vs. $h\nu$ recorded 0.1 M ABE for anodic oxides grown to 200 V on a, c) Ti and b, d) Ti6Al4V alloy.*

The photocurrent spectra for Ti and Ti6Al4V after anodizing to 200 V recorded in 0.1 M ABE are shown in Figure 3.1.11. Two main differences are observed: the photocurrent is lower for the anodic oxide grown on Ti6Al4V compared to that grown on Ti, and the light absorption threshold of the anodic film on Ti6Al4V is shifted toward lower photon energy compared to the oxide on Ti. The optical band gap, estimated using equation (3.2), is 3.20 eV for the 200 V anodic film on Ti, which matches the value reported in the literature for anatase, [103] in agreement with the XRD pattern. In contrast, see Figure 3.1.11d, a significantly lower value of 2.15 eV is estimated for the 200 V anodic film on Ti6Al4V.

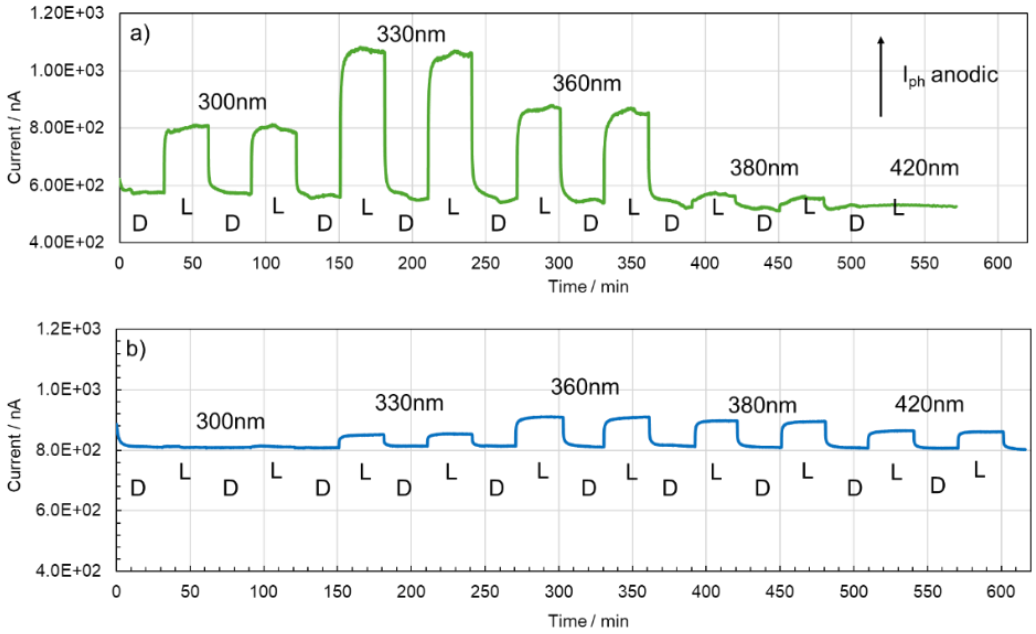

Figure 3.1.12 *Current vs time curves recorded, by manually chopping the irradiation, in 0.1 M ABE at 2 V vs Ag/AgCl for anodic oxides grown to 200 V on a) Ti and b) Ti6Al4V alloy.*

The photocurrent recorded for both films is anodic, as confirmed by the current vs, times shown in Figure 3.1.12. Interestingly, for the oxide grown on Ti6Al4V, a stationary anodic photocurrent was observed under 420 nm irradiation (see Figure 3.1.12b).

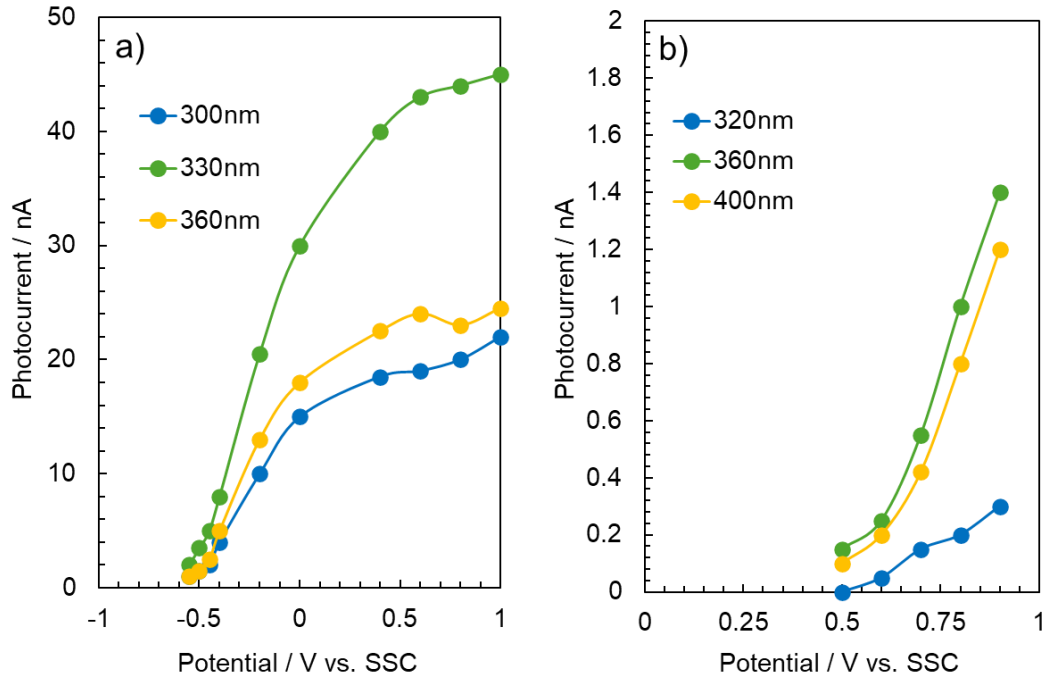

Figure 3.1.13 *Photocharacteristics recorded in 0.1 M ABE at different wavelengths for anodic oxides grown to 200 V on (a) Ti and (b) Ti6Al4V alloy.*

Other important experimental observations come from the photocharacteristics in Figure 3.1.13, where the shape of the photocharacteristics varies significantly depending on the metallic substrate. Specifically, the photocurrent vs. electrode potential curves for the anodic oxide grown on Ti to 200 V (see Figure 3.1.13a) can be fitted using equation (3.1.4), with an exponent *n* close to 2 (see fitting in Figure 3.1.14), which is attributed to the higher degree of crystallinity compared to the oxide grown at 40 V.

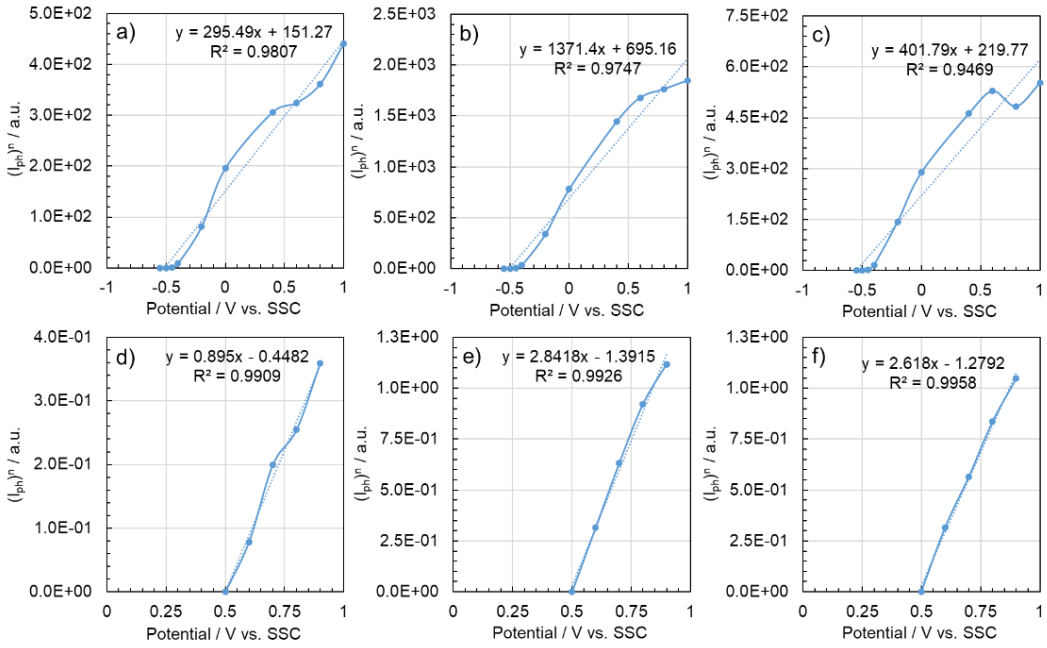

Figure 3.1.14 *Fitting of photocharacteristics related to anodic oxides grown on Ti and Ti6Al4V to 200 V. Ti: a) λ = 300 nm, b) λ = 330 nm and c) λ = 360 nm. Ti6Al4V: d) λ = 320 nm, e) λ = 360 nm and f) λ = 400 nm.*

The photocharacteristics in Figure 3.1.13b of the anodic layer grown on the Ti6Al4V alloy can be fitted using equation 3.1.4 (see fitting in Figure 3.1.14), with an exponent *n* significantly lower than 1 (supralinear curves), suggesting strong recombination processes (see Table 3.1.1). Furthermore, the zero-photocurrent potential for the 200 V anodic film on Ti6Al4V (0.5 V vs. Ag/AgCl) is noticeably more positive than that of the 40 V barrier film, which shifts E_{ox}^{F} toward the mid-gap, according to equation 3.1.4. This shift is not observed in the 200 V anodic oxide on Ti, where the zero-photocurrent potential (-0.5 V vs. Ag/AgCl) closely matches that of the 40 V barrier film.

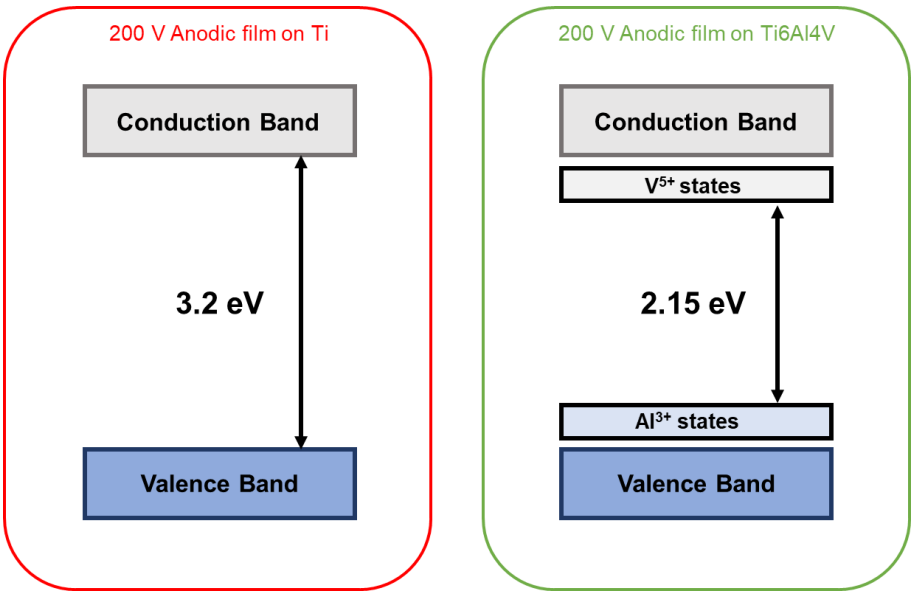

Figure 3.1.15 *Scheme of band structure of 200 V anodic film grown on Ti and Ti6Al4V.*

The photoelectrochemical findings can be explained by the changes in the electronic properties of the oxide induced by incorporation of Al^{3+} and V^{5+} ions during the anodizing process of Ti6Al4V causing a doping of titanium oxide. Anodic TiO_2 is a n-type semiconductor due to its self-doping, since it is usually substoichiometric (TiO_{2-x}) and thus donor levels are usually present close to the conduction band due to oxygen vacancies (i.e. Ti^{3+}). Al^{3+} ions incorporated into TiO_2 matrix behave like Ti^{3+} leading to the formation of oxygen vacancies (donor states close to the conduction band). Conversely, the presence of V^{5+} ions into TiO_2 crystalline matrix can cause the formation of acceptor states (close to the valence band) inside the mobility gap (see scheme of Figure 3.1.15), responsible for the shift of E_{FB} toward more positive values. These doping mechanisms, due to the incorporation of Al^{3+} and V^{5+} ions into TiO_2 matrix, can be also expressed according to the Kröger–Vink notation[104,105]:

$$Al_2O_3 \xrightarrow{TiO_2} 2\ Al'_{Ti} + 3\ O_O^x + V_O^{\cdot\cdot} \qquad (3.1.5)$$

$$V_2O_5 \xrightarrow{TiO_2} 2\ V_{Ti}^{\cdot} + 5\ O_O^x + \frac{1}{2} V_{Ti}^{''''} \qquad (3.1.6)$$

Moreover, these states can be responsible for optical transitions under photon energies lower than TiO_2 band gap explaining the lower absorption threshold. And since these states are localized, the mobility of photogenerated charges is very low explaining the low best fitting exponent n found for the photocharacteristics. This does not imply a change in conduction band edge energy level, that is reported to happen when a mixed oxide is prepared with two or more cations present in comparable concentration. [106]

Figure 3.1.16 shows polarization curves recorded at 2 mV s^{-1} in Hank's Balanced Salt Solution at 37°C. Polarization curves were recorded at the same scan rate to compare the results.

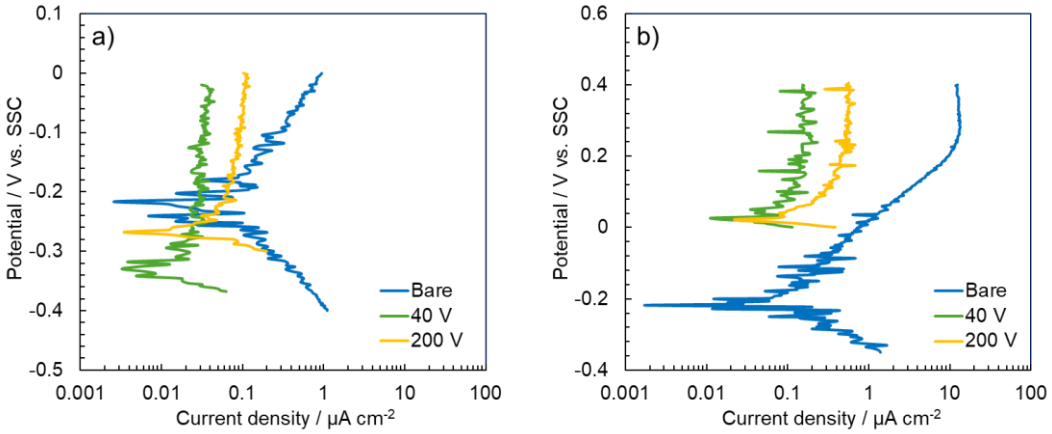

Figure 3.1.16 *Polarization curves recorded in HBSS for air formed and anodized samples on (a) Ti and (b) Ti6Al4V alloy.*

For all samples the cathodic branch of the polarization curves is related to the oxygen reduction reaction. In the case of the bare samples the current in the anodic branch is due to passivation of the metals while for the anodized samples, it is due the re-passivation reactions occurring in the oxide.

Metal	**Sample**	**E_{corr} [V] vs. Ag/AgCl**	**i_{corr} [µA/cm^2]**
Ti	Bare	-0.22	5×10^{-2}
	40 V	-0.34	8×10^{-3}
	200 V	-0.27	1×10^{-2}
Ti6Al4V	Bare	-0.20	6×10^{-2}
	40 V	0.02	3×10^{-2}
	200 V	0.01	6×10^{-2}

Table 3.1.3 *E_{corr} and i_{corr} estimated from polarization curves of Figure 3.1.16.*

In Table 3.1.3 E_{corr} and i_{corr} estimated by Tafel method from polarization curves are reported. As reported in ref [84], the logarithmic nature of the current density axis can amplify errors in extrapolation. To increase the accuracy of the extrapolation, for Bare samples, the anodic and cathodic lines were drawn by considering ±200mV vs. E_{corr}. For the anodized samples, the anodic lines were drawn by considering +100mV vs. E_{corr} while for the cathodic lines we consider the entire cathodic branchs. For both Ti and Ti6Al4V, barrier type anodic oxide shows the lowest corrosion current density and passivity current density. The higher passive current density measured for the anodized samples at 200V compared to 40V can be related to the different electronic properties (e.g. the number of defects).

In the case of porous type anodic oxides, i_{corr} value (~10^{-2} μA/cm^2) estimated for the oxide grown on Ti is lower with respect to i_{corr} estimated for bare sample (~5 × 10^{-2} μA/cm^2). For the oxides grown on Ti alloy, i_{corr} estimated for the porous type anodic oxide and for bare sample are almost equal (~6 × 10^{-2} μA/cm^2) and higher with respect to that estimated for porous type anodic layer grown on Ti. This result can be related to the electronic properties of the anodic oxides. In fact, in the case of 200 V oxide grown on Ti, E_{corr} (~ -0.27 V vs. Ag/AgCl, see Table 3.1.3) is more anodic than flat band potential estimated from the photocharacteristic curve (~ -0.5 V vs. Ag/AgCl). The anodic layer is polarized in reverse bias regime and, therefore, the oxide behaves as insulating material, hindering oxidation and/or reduction reactions.

In the case of 200 V oxide grown on Ti6Al4V, E_{corr} (~ 0.01 V vs. Ag/AgCl, see Table 3.1.3) is more cathodic than flat band potential estimated from the photocharacteristic curve (~ 0.5 V vs. Ag/AgCl), therefore the anodic layer is polarized in forward bias regime leading to a less blocking behaviour toward oxidation/reduction reactions. Moreover, according to the photoelectrochemical characterization, 200 V anodic oxide grown on Ti6Al4V alloy has localized electronic states inside the mobility gap that can increase the electronic conduction through the anodic layer.

$$O_2 + 4e^- + 2H_2O \rightarrow 4OH^- \qquad (3.1.7)$$

$$10Ca^{2+} + 8OH^- + 6HPO_4^{2-} \rightarrow Ca_{10}(PO_4)_6(OH)_2 + 6H_2O \qquad (3.1.8)$$

$$10Ca^{2+} + 6PO_4^{3-} + 2OH^- \rightarrow Ca_{10}(PO_4)_6(OH)_2 \qquad (3.1.9)$$

The less blocking character of the porous anodic oxide grown on Ti6Al4V alloy leads to oxygen reduction reaction (eq. 3.1.7), that occurs in a confined environment (the pore of the anodic layer) inducing a local alkalinization, see Figure 3.1.17.

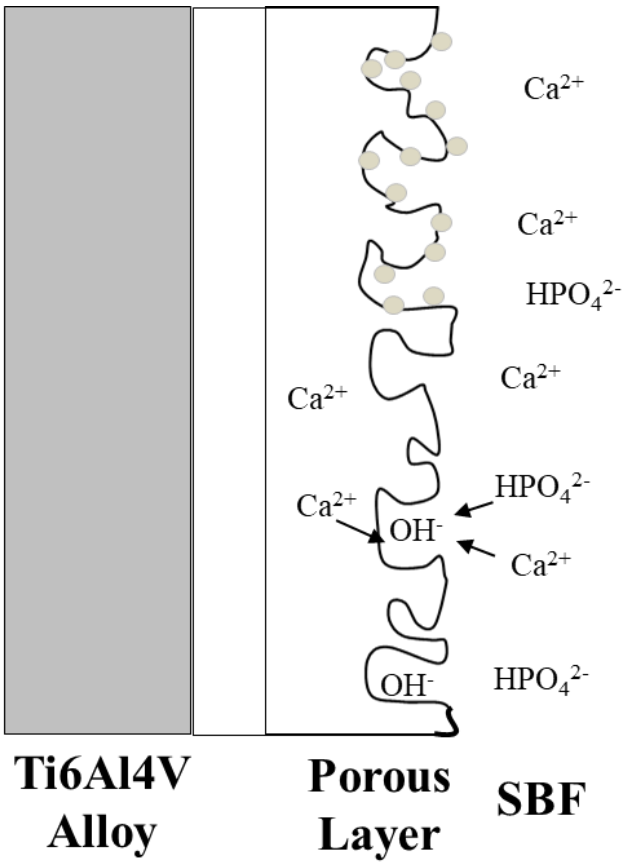

Figure 3.1.17 *Schematic representation of HA growth.*

This, together with the release of Ca^{2+} ions incorporated into the oxide during the anodizing process, leads to the growth of HA (see eq. 3.1.8 and 3.1.9), improving the bioactivity of the TAV alloy. It is noteworthy to mention that the growth of a thick anodic layer hinders the release of V ions into the human body environment. [102]

In summary, we investigated the electronic properties of TiO2 layers grown by anodizing and hard anodizing on Ti and Ti6Al4V alloys to understand how these properties affect the corrosion resistance and reactivity of these materials in a simulated body fluid environment. Ti and Ti6Al4V alloys were anodized at 5 mA cm^2 to 40 V in 0.1 M H_3PO_4 to form barrier-type oxides, enabling a comparison of their electronic properties. Photoelectrochemical characterization showed that both barrier layers are n-type semiconductors, with band gaps of 3.3 eV for Ti and 3.4 eV for Ti6Al4V, slightly higher than that of crystalline TiO_2, indicating the formation of amorphous oxides. The flat band potential of the barrier anodic films on Ti and Ti6Al4V are close to each other, with a slightly more negative value measured for the oxide grown on the alloy.

Ti and Ti6Al4V alloys were also anodized to 200 V at 20 mA cm^{-2} in a calcium acetate and β-glycerol phosphate disodium pentahydrate aqueous solution to form porous oxides, as confirmed by SEM micrographs. EDX analysis showed that calcium and phosphorus were incorporated during the anodizing process. Interestingly, the porous layers on Ti6Al4V also contained Al and V, incorporated

from the underlying alloy. Photoelectrochemical characterization estimated a band gap of 3.2 eV for the porous film on Ti, which corresponds to the band gap reported for anatase (consistent with the XRD reflections), with a flat band potential very similar to that of the barrier layer. In contrast, the porous film on Ti6Al4V exhibited optical transitions at much lower energy (2.15 eV), which can be attributed to the incorporation of Al^{3+} and V^{5+} ions into the TiO_2 matrix during hard anodizing. The inclusion of these aliovalent ions, relative to Ti^{4+}, leads to the formation of localized allowed states within the TiO_2 gap, causing a significant shift of the oxide flat band potential to more positive values.

This marked alteration in the electronic properties of the porous oxide on Ti6Al4V may explain the comparable (or even higher) corrosion current density observed in Hank's Balanced Salt Solution after hard anodizing to 200 V, relative to bare and 40 V anodized Ti6Al4V. Consequently, the hard anodizing process does not significantly affect the reactivity of the alloy in a biological environment.

3.2 Surface functionalization to enhancing osteointegration and antibacterial properties

The work reported in this chapter is focused on the optimizations of a multi-step process aimed to improve the biocompatibility and induce antibacterial activity of Ti6Al4V alloys for biomedical applications. This multilayer coating and the three-step electrochemical process can be advantageous from many points of view. Every single step is important to give to the final coating the desired properties, i.e. antibacterial and biocompatibility properties. The anodizing process allows to cover the alloy surface with a thick porous and well adherent TiO_2 layer to hinder Al and V release, to improve surface wettability and to provide a high specific surface for accelerating HA growth rate. Such porous film provides a good pattern for hosting Ag to provide antibacterial properties, whose release rate in turn is slowed down due to the sealing of pores with a HA-containing alginic acid gel deposited during the electrophoresis deposition (EPD). This step is very important because the gel can uptake electrolyte during immersion, thus Ag can still fulfil its antibacterial action but, at the same time, its release is slowed down so that cannot be cytotoxic (as Ag could be if the release rate is particularly high). And, finally, the presence of HA provides the seed for further HA growth and, thus, can lead to a better osteointegration.

Therefore, the three-step electrochemical process, see Figure 3.2.1, provides a route for a smart functionalization of Ti6Al4V alloys. Moreover, this process can be fully scaled at the industrial level and can help in decarbonizing the fabrication industrial processes.

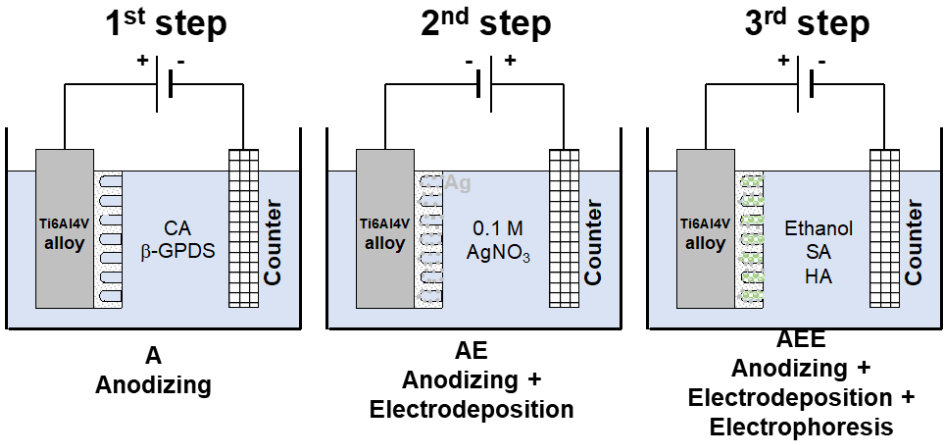

Figure 3.2.1 *Schematic representation of multistep process*

The success of this multifunctional coating is studied by evaluating the morphological/compositional changes after the surface treatment by using Scanning Electron Microscopy (SEM), Energy-Dispersive X-ray Spectroscopy (EDX), and Raman spectroscopy. Electrochemical tests (Electrochemical Impedance Spectroscopy measurements and polarization curves) are carried out in Hanks′ Balanced Salt solution (HBSS) at 37°C to evaluate coating corrosion

resistance. Finally, *in vitro* tests are necessary to study cytocompatibility, antibacterial activity and hemocompatibility of the surface-modified Ti6Al4V alloy. [2]

For the experimental campaign Ti6Al4V alloy was used. The samples were mechanically polished using SiC abrasive papers, degreased using acetone and rinsed with deionized water.

Briefly, thew first step is a hard anodizing process carried out on Ti6Al4V alloys in 0.2 M calcium acetate and 0.04 M β-glycerol phosphate disodium pentahydrate aqueous solution. Anodic oxide growth was carried out galvanostatically at 20 mA cm^{-2} and the voltage compliance was set to 200 V, see experimental part in chapter 3.1.

The second step is an electrodeposition process carried out to have antibacterial properties. A three-electrode configuration, where anodized Ti6Al4V alloy was the working electrode, a Pt mesh was the counter electrode, and a silver/silver chloride (SSC) was the reference electrode. The electrodeposition process was carried out in 100 mM silver nitrate aqueous solution galvanostatically at 1 mA cm^{-2} for 2 s.

The last step is electrophoretic deposition (EPD) process of Hydroxyapatite/sodium alginate layer. The EPD suspension was prepared by dissolving 4 g l^{-1} sodium alginate in deionized water for 10 min. Then the solution was additionally treated in an ultrasonic bath for 10 min and was also stirred at 600 rpm for 5 min [107] . Ethanol was added to the solution in a ratio of 4/6 with respect to deionized water. Afterwards, HA (1 g l^{-1}) particles were slowly added to the solution and the pH was adjusted to 7.9 by the addition of NaOH. The EPD process was carried out in a two-electrode configuration with continuous stirring at 100 rpm. A stainless-steel sheet (AISI 316L) was used as counter electrode. EPD process was carried out potentiostatically at 7 V for 7 minutes.

Figure 3.2.2 shows representation of the 1st step and the growth curve (cell voltage vs. time) for the Ti6Al4V sample. During the early stages of anodizing process, the cell potential linearly depends on time indicating the growth of a barrier-type anodic oxide film [108].

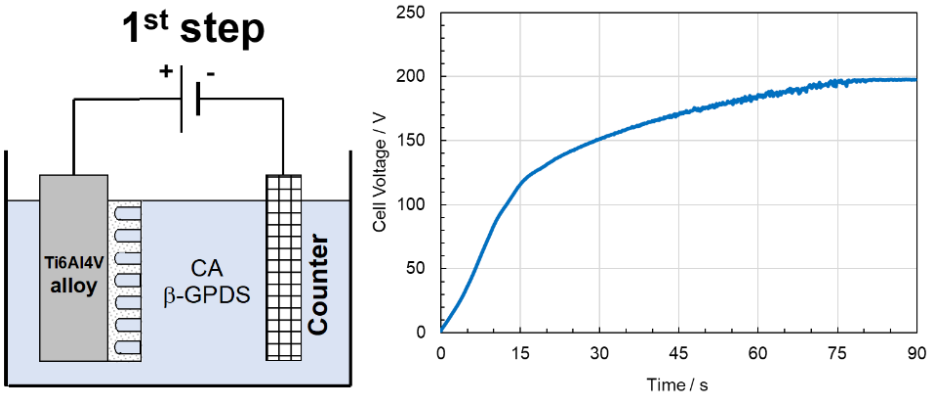

Figure 3.2.2 *Schematic representation of the 1st step and Cell voltage vs time curve related to the growth of the anodic oxide on Ti6Al4V alloy in CA and β-GPDS-containing solution.*

For cell potential higher than ~ 50 V, the oxygen evolution reaction reduces the efficiency of the anodizing process. Much higher cell potential leads to the formation of an outer porous structure in a hard anodizing regime due to the dielectric breakdown of the oxide layer [109].

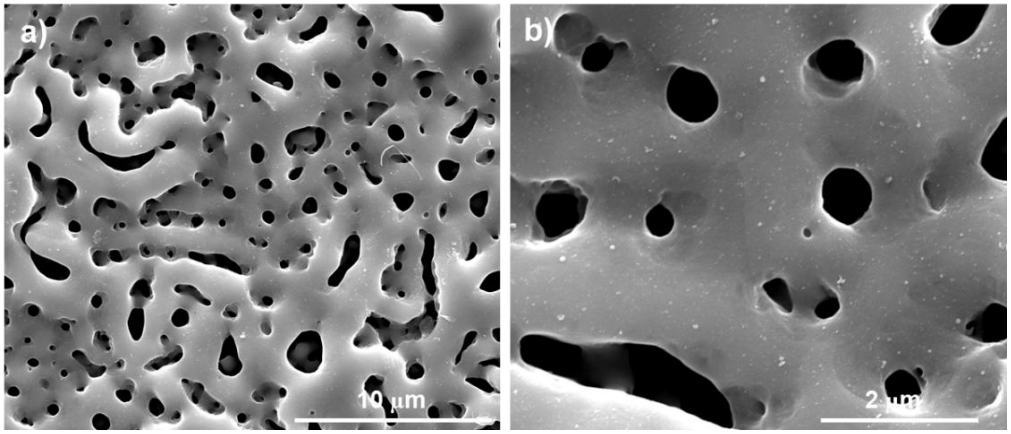

Figure 3.2.3 *SEM micrographs related to anodized sample at different magnification.*

Figure 3.2.3 shows SEM micrographs of the anodized Ti6Al4V material, revealing a multiscale porous structure with a wide range of pore diameters. In comparison to previous results in literature for anodic layers grown in more concentrated CA and β-GPDS-containing solutions [34], this oxide is crack-free.

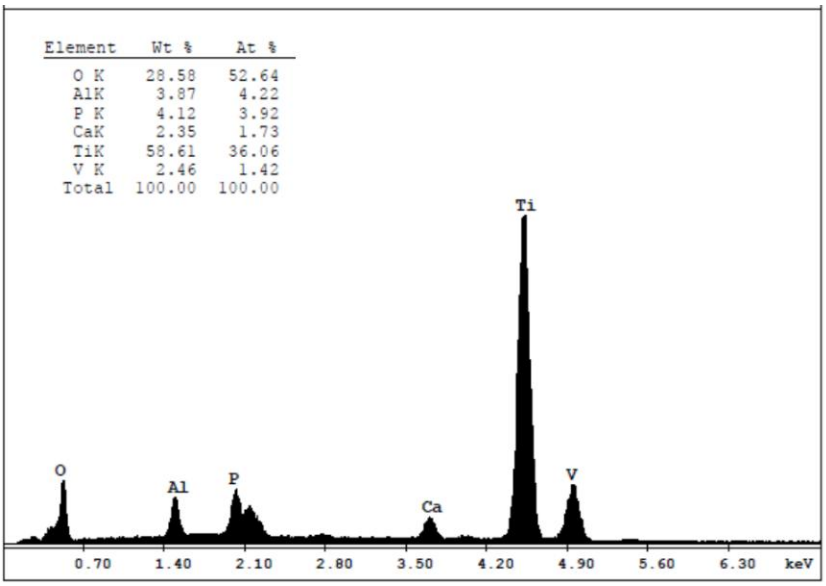

Figure 3.2.4 *EDX analysis with relative quantification of Ti6Al4V after the anodizing process.*

EDX analysis (see Figure 3.2.4) indicates that the anodic layers contain Ti and O, but also Ca and P with a ratio of about 0.44. Incorporation of phosphorus occurs early in the anodizing process due to the high electric field driving negatively charged phosphate ions toward the metal/oxide interface during this stage.

Conversely, calcium ions are incorporated under sparking conditions as local melting phenomena of TiO_2 occur, followed by solidification upon contact with fresh electrolyte. As reported in ref. [102], the incorporation of calcium and phosphorus species can be also due to formation of colloidal solutions of polyphosphate complexes with di-, tri- or multivalent metal cations, such as $Ca_3P_6O_{18} \cdot xH_2O$ or $Na_2Ca_2P_6O_{18} \cdot xH_2O$, which are transformed to $CaO{\cdot}P_2O_5$ under the high temperatures and pressures at breakdown sites. Further, $(Ca_2P_6O_{18})^{2-}$ species may exist in the solution whose incorporation is assisted by the electric field during the anodizing process. Therefore, a Ca/P ranging between 0.33 and 0.5 is expected in in the anodic layer, which is close to that estimated by EDX.

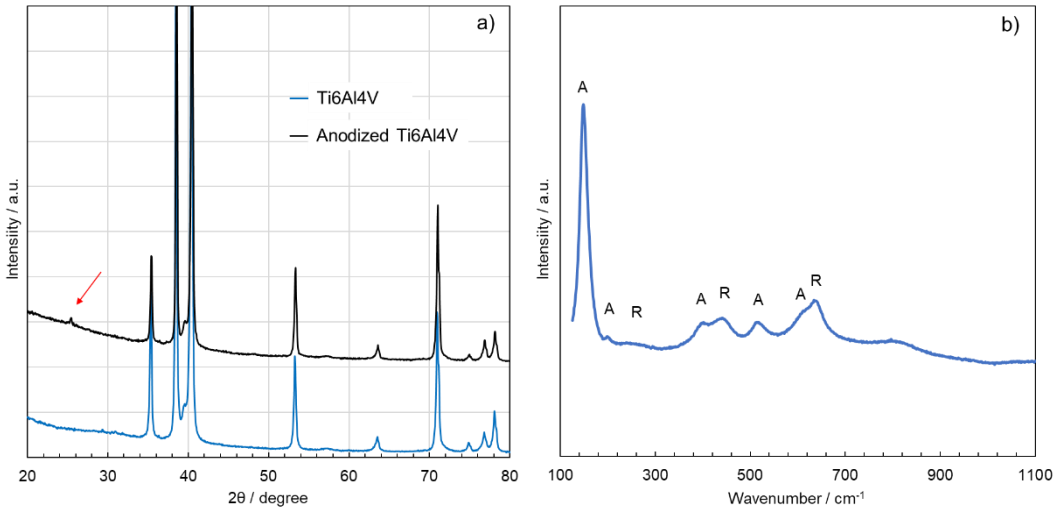

Figure 3.2.5 *a) XRD diffractograms related to bare Ti6Al4V alloy and anodized sample. b) Raman spectrum related to anodized sample A: anatase, R: rutile polymorphs.*

X-ray diffraction of the as anodized samples, see Figure 3.2.5a, reveals (101) reflection of TiO_2 anatase polymorph [110].

Its presence was also confirmed by Raman Spectroscopy, see Figure 3.2.5b, together with the presence of rutile polymorph. The tetragonal structure of anatase belongs to the space group D_{4h} and has two formula units per primitive cell, leading to six Raman active phonons: $3E_g$ (144, 196 and 638 cm^{-1}), $2B1_g$ (398 and 519 cm^{-1}) and $1A1_g$ (513 cm^{-1}) [111]. Rutile has four Raman active modes: $1B1_g$ (143 cm^{-1}), E_g (235 and 447 cm^{-1}) and $A1_g$ (609 cm^{-1}). The Raman bands are shifted by few cm^{-1} with respect to pure crystalline anatase phase, suggesting the formation of a defective TiO_2 layer. The presence of both TiO_2 polymorphs could be related to a higher bioactivity and cytocompatibility of the coating [112].

After anodizing, silver (Ag) was electrodeposited using a galvanostatic process with a cathodic current density of 1 mA/cm^2. The deposition time was carefully regulated to ensure precise control over the circulating charge and subsequently the amount of Ag deposited.

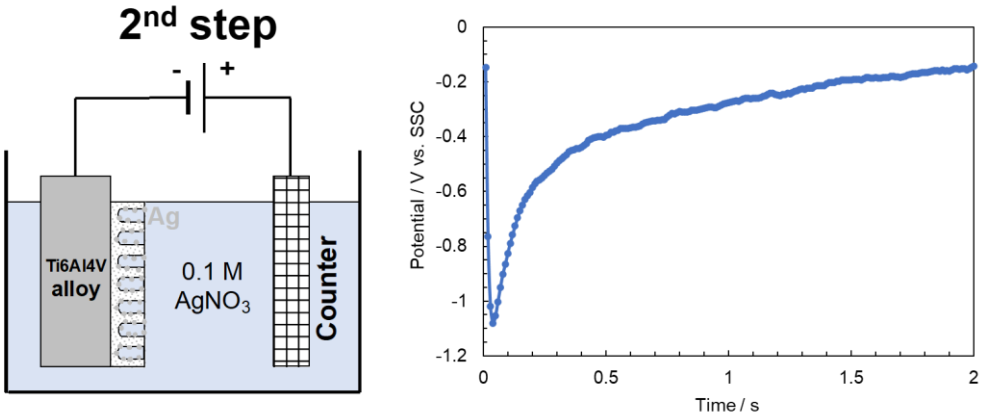

Figure 3.2.6 *Schematic representation of the 2nd step and Potential vs time curve recorded during Ag electrodeposition carried out galvanostatically at 1 mA cm^{-2} for 2 s.*

Figure 3.2.6 shows the potential transient recorded during electrodeposition process. Initial potential peak is usually related to the nucleation of electrodeposited metal whilst the second part of the potential vs time curve is usually related to the growth of deposited nuclei that can proceed at lower overpotential values [113].

The presence of Ag was confirmed by SEM micrographs and EDX analysis (see Figure 3.2.7), as well as by XRD diffraction (see Figure 3.2.8)

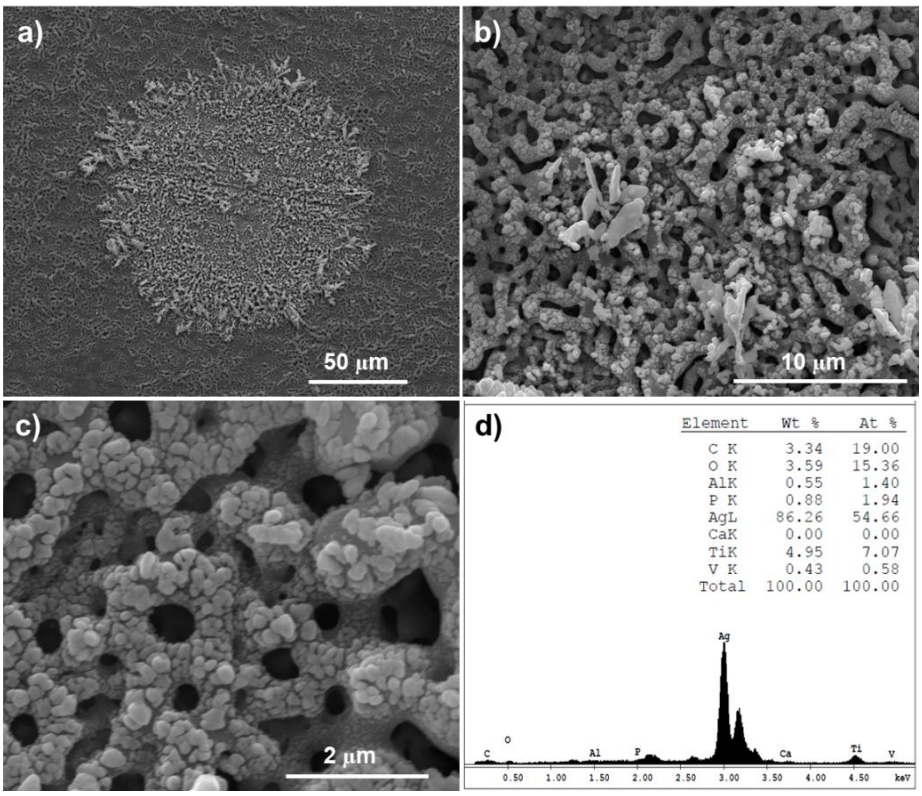

Figure 3.2.7 *SEM micrograph and EDX analysis related to the anodized Ti6Al4V sample after electrodeposition process.*

SEM micrographs reveal that Ag is present on the surface as aggregates at μm scale, composed by Ag nanoparticles [114]. These aggregates are not uniformly distributed along the whole surface of the sample, but Ag is still present since it is detected by EDX also in those areas where μm-sized aggregates miss, suggesting that the silver is also inside the porous structure.

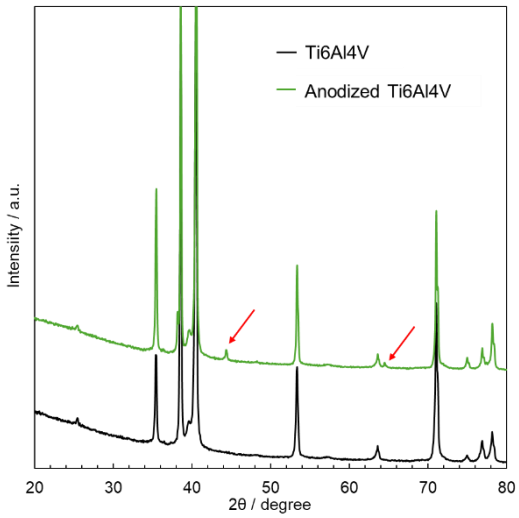

Figure 3.2.8 *XRD diffractograms related to anodized Ti6Al4V alloy before and after silver electrodeposition.*

Indeed, reflections of crystalline Ag are present in the diffraction pattern (see Figure 3.2.8) at 44° and 64.5° corresponding to (200) and (220) planes, respectively. [115,116] The amount of incorporated Ag into the coating was crucial to obtain long-term and efficient antibacterial properties and hemocompatibility without cytotoxicity. It is noteworthy to mention that these electrodeposition parameters (i.e. 1 mA cm^{-2} for 2 s) are the result of an optimization process of operating conditions that guaranteed antibacterial properties. However, the presence inside the pores of the anodic layer of alginic acid gel (see below) allows to slow down the release of Ag that, in high amount, can also become cytotoxic [117].

Finally, an electrophoretic deposition (AEE samples) step was carried out on Ag containing anodized samples by polarizing the electrodes at 7 V vs the counter electrode in an ethanol/water suspension containing HA microparticles (1 g L^{-1}) and sodium alginate (4 g L^{-1}). In spite the presence of a thick anodic layer under the imposed anodic potential, a significant current circulates across the electrode/electrolyte interface. The oxidation process sustaining this current is oxygen evolution, i.e.:

$$2H_2O \rightarrow O_2 + 4H^+ + 4e^- \quad (3.2.1)$$

with consequent hydrogen ions production inside the pores, since this reaction mainly occurs at the bottom of the pores where the electric field is higher. The

electric field also drives negatively charge alginate ions toward the bottom of the pores, where they find an acidic environment and, since it is known that alginate solutions form gels at pH < 3 [118], the electrophoresis and neutralization of alginate ions in acidic region results in the formation of alginic acid (H–Alg) deposits starting from the bottom of the pores, according to the reaction:

$$Alg^- + H^+ \rightarrow H\text{-}Alg \qquad (3.2.2)$$

At the same time, the electric field also drives HA particles inside the pores of the coatings since the latter carry a negative charge due to the adsorbed alginate ions. Such particles are embedded inside the alginic acid gel.

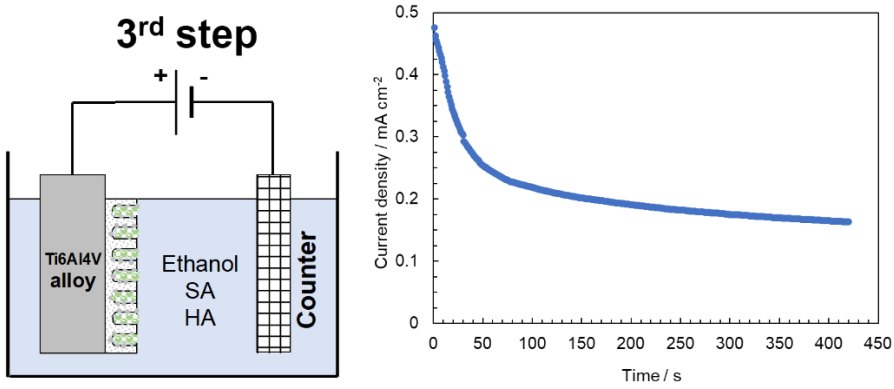

Figure 3.2.9 *Schematic representation of the 3rd step and current density vs time curve recorded during electrophoretic deposition.*

The current density vs time transient recorded during potentiostatic deposition is reported in Figure 3.2.9, clearly showing that *i* decreases soon after the polarization in agreement with the ongoing pores' filling.

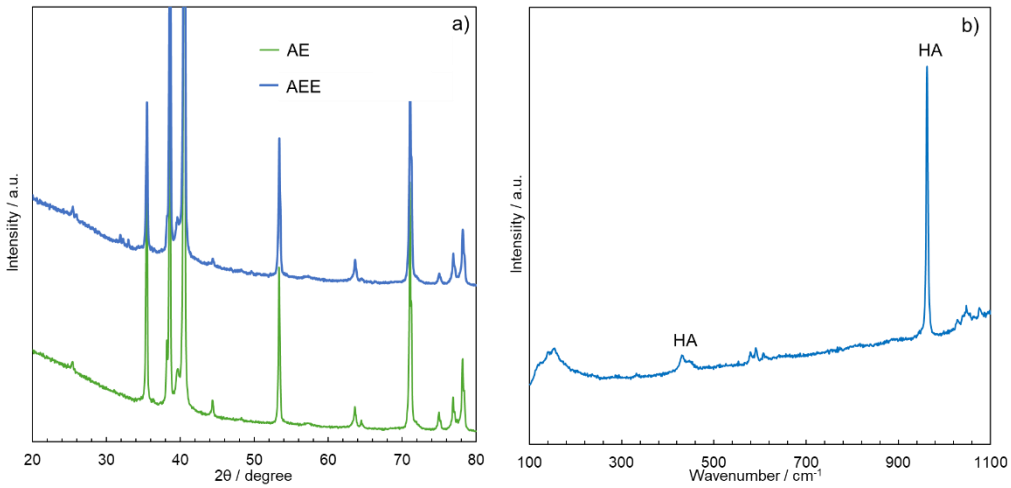

Figure 3.2.10 *a) XRD diffractograms related to Ti6Al4V alloy before and after electrophoretic deposition. b) Raman spectrum related to sample after electrophoretic deposition.*

The successful incorporation of HA particles is confirmed by the XRD patterns (see Figure 3.2.10a) showing the reflections of hydroxyapatite [8], and by Raman Spectroscopy (see Figure 3.2.10b). In particular, PO_4^{3-} features in HA are visible by ν_1 symmetric stretching (P-O) mode at 960 cm^{-1} and ν_2 bending vibrations at 438 cm^{-1} [119,120].

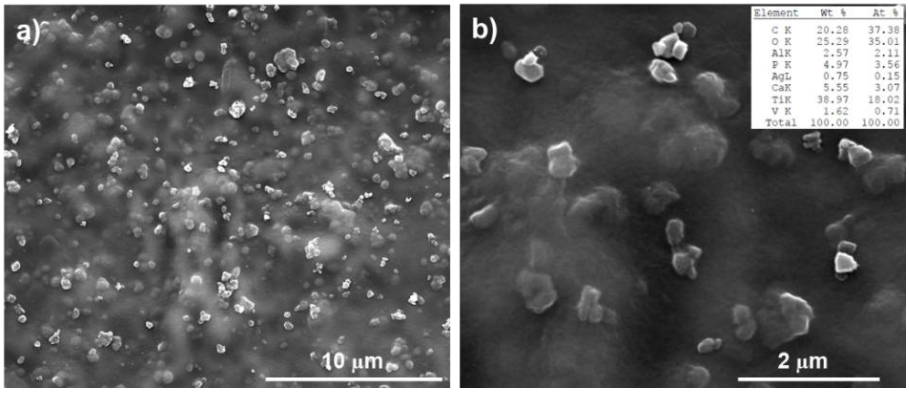

Figure 3.2.11 *SEM micrograph and EDX analysis related to the anodized Ti6Al4V sample after electrophoretic process.*

A significant change in the surface morphology is evident in the SEM micrographs reported in Figure 3.2.11, demonstrating that the entire pores have been effectively sealed off. EDX analysis indicated a Ca/P ratio of approximately 0.85 in the anodic layer, lower than that found in hydroxyapatite (HA) due to the signal originating from this layer but higher compared to what was measured before the electrophoretic deposition process. Notably, silver signals were still observable using X-ray diffraction (XRD) and EDX analysis, confirming that no significant loss of silver occurred during the electrophoretic step (see Figure 3.2.10a and Figure 3.2.11b respectively). In addition, during the electrophoretic deposition, the anodic potential can induce the oxidation of Ag particles, which nevertheless has antibacterial action. The release rate in turn is slowed down due to the sealing of pores with a HA containing alginic acid gel deposited during the electrophoresis.

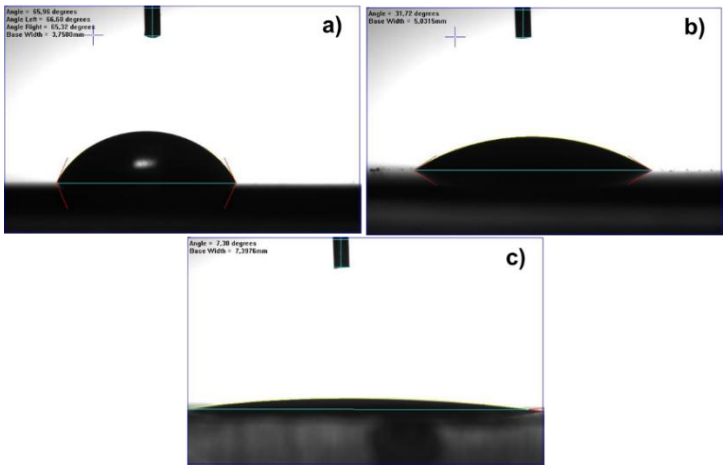

Figure 3.2.12 *Water contact angle values of bare a) Ti alloy, b) anodized and c) AEE samples.*

The wettability of the samples was assessed using water contact angle measurements. As demonstrated by Figure 3.2.12, a water contact angle of 64 degrees was measured for bare Ti6Al4V. After anodizing treatment, this value decreased to 29° and further reduced to 8° following electrophoresis processing. This significant increase in hydrophilicity is crucial for enhancing cell adhesion and proliferation by improving the surface properties necessary for biocompatibility. [121,122]

The decrease in water contact angles after anodizing and further reduction upon electrophoretic deposition can be explained by the presence of alginate gel material. Alginate has a high degree of hydrophilicity, [123] which results in lowered wetting angles when present on the surface.

The Ti6Al4V before and after electrochemical treatments were immersed in Hanks' balanced salt solution (HBSS) 37°C and left at the open circuit potential (OCP) for 1 h before recording EIS spectra (see Figure 3.2.13).

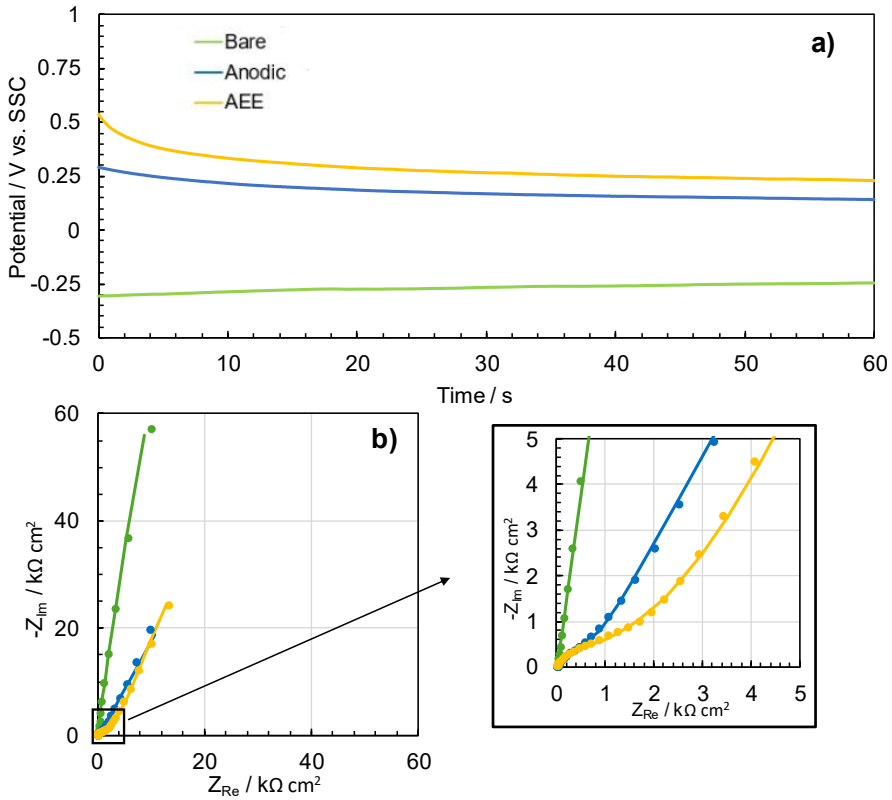

Figure 3.2.13 *a) Open circuit potential measurements and b) EIS spectra recorded at corresponding E_{corr} in HBSS at 37 °C related to bare Ti6Al4V alloy, anodized sample and AEE sample*

The spectra were fitted using different equivalent circuits, see Figure 3.2.14.

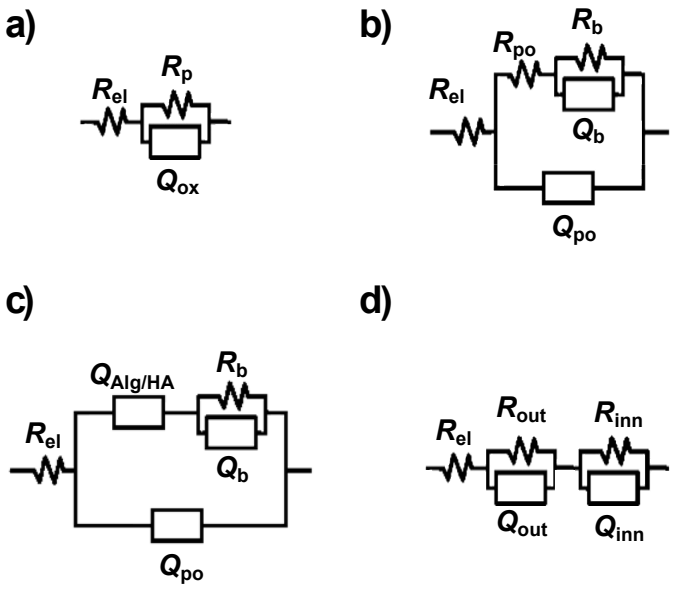

Figure 3.2.14 *Equivalent electrical circuits (EECs) used to model the electrochemical behaviour of a) Bare Ti6Al4V alloy, b) anodized sample, c) AEE sample and d) samples after 1 month immersion in HBSS.*

The best fitting parameters are reported in Table 3.2.1.

	R_{el} [Ω cm²]	R_p [Ω cm²]	Q_{ox} [μS sⁿ cm⁻²]	n	χ^2
Bare Ti6Al4V	17	1.77×10^6	27	0.92	9×10^{-4}

	R_{el} [Ω cm²]	R_{po} [Ω cm²]	Q_{po} [μS sⁿ cm⁻²]	n	Q_b [μS sⁿ cm⁻²]	n	R_b [Ω cm²]	χ^2
Anodized	33	1500	21	0.69	42	0.72	5×10^5	3.2×10^{-3}

	R_{el} [Ω cm²]	Q_{po} [μS sⁿ cm⁻²]	n	$Q_{Alg/HA}$ [μS sⁿ cm⁻²]	n	Q_b [μS sⁿ cm⁻²]	n	R_b [Ω cm²]	χ^2
AEE	25	0.37	0.91	162	0.25	64	0.85	4.5×10^5	6.7×10^{-4}

Table 3.2.1 *Fitting parameters related to the impedance spectra shown in Fig.* Figure 3.2.13 *recorded for the bare Ti6Al4V, anodized and AEE samples according to the EEC shown in* Figure 3.2.14*a-c.*

For air-formed passive film on Ti6Al4V alloy, a simple one-time constant equivalent electrical circuit (EEC) can be used to model the impedance spectrum as shown in Figure 3.2.14. This circuit includes R_P for polarization resistance and is in parallel with Q_{ox}, which represents the non-ideal capacitance of the thin oxide layer. The electrolyte resistance R_{el} is also included in this model.

The air-formed passive film on bare Ti6Al4V alloy exhibits a high polarization resistance (~ 10^6), which explains its bio-inert nature. A completely different behaviour is shown by the anodized alloy and by the AEE sample. In fact, in accordance with the morphology of the samples (see before for the discussion on

SEM micrographs), the electrochemical behaviour can be modelled with different EECs. As for anodized alloy, the EEC is shown in Figure 3.2.14b and comprises Q_{po}, a CPE modelling the pore wall non ideal capacitance, in parallel with a series between R_{po}, the electrolyte resistance inside the pore, and the (R_b Q_b) parallel, related to the barrier oxide layer presence at the bottom of the pore. Corresponding fitting parameters are reported in Table 3.2.1.

A different EEC (see Figure 3.2.14c) must be employed to model the electrochemical behaviour of AEE sample soon after the fabrication process. In this case, despite the pore structure is analogue to that of the anodized sample, the pore is filled with HA embedded in alginic acid gel. In this case, the deposition products inside the pore were modelled with a $Q_{Alg/HA}$ CPE element, accounting for a series of parallels (RC), i.e. a distribution of time constants along the pore modelling the complex structure of HA/alginic acid gel [124]. Fitting parameters are reported in Table 3.2.1.

The overall impedance values measured for both anodized and AEE samples are significantly lower compared to those of bare Ti6Al4V alloy. This result is not related to the inhomogeneity of the deposited silver particles and alginate/HA layer but depends on the electronic properties of the anodic oxide film, see Chapter 3.1. This observation suggests that the anodic oxide film grown on Ti6Al4V is not as insulating as the air-formed passive layer, in accordance with previous findings from literature [125]. From a synergistic electrochemical and photoelectrochemical characterization, it was noted that for a thick anodic oxide grown on Ti6Al4V corrosion potential is more cathodic than oxide flat band potential. Therefore, in free corrosion conditions as when the sample is immersed in Hanks' balanced salt solution, the anodic layer is polarized in forward bias regime leading to a less blocking behaviour toward oxidation/reduction reactions [125].

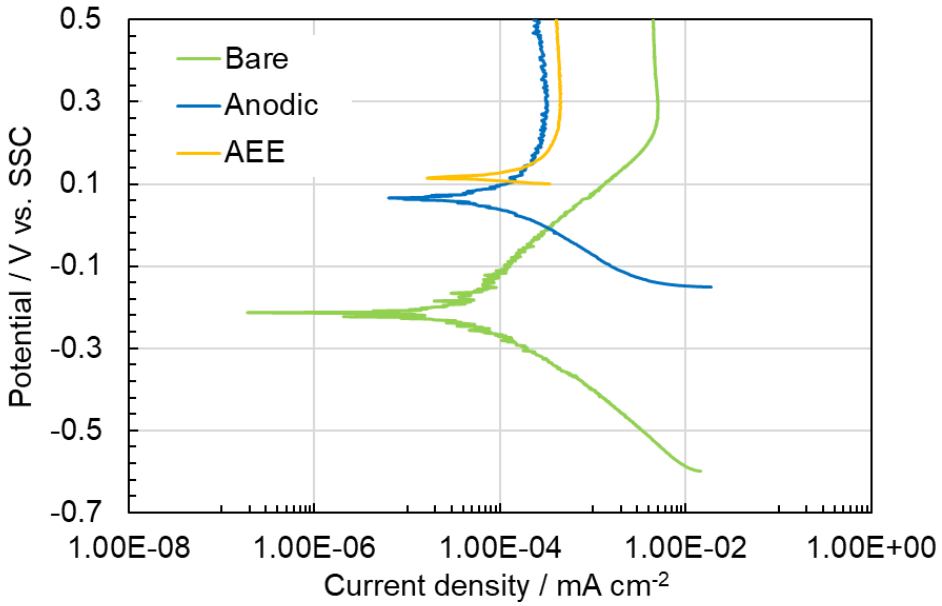

Figure 3.2.15 *Polarization curves related to bare Ti6Al4V alloy, anodized and AEE samples recorded in HBSS at 37 °C.*

This behaviour is also confirmed by the polarization curves recorded in Hanks' balanced salt solution at 37°C for bare Ti6Al4V alloy, anodized and for AEE samples (see Figure 3.2.15). The multifunctional coating shifts the corrosion potential toward more positive value, but the corrosion current density is comparable or even higher than that estimated for bare alloy. This indicates that during immersion in Hanks' balanced salt solution the coating does not hinders the reactivity of the material. In addition, the anodized and AEE samples show a more regular passive region due to the presence of the anodic layer.

To evaluate the impact of surface treatments on hydroxyapatite growth, Ti6Al4V alloys were immersed in Hanks' balanced salt solution at 37°C up to 2 months. The resulting surface morphologies as a function of immersion time in HBSS are shown in Figure 3.2.16.

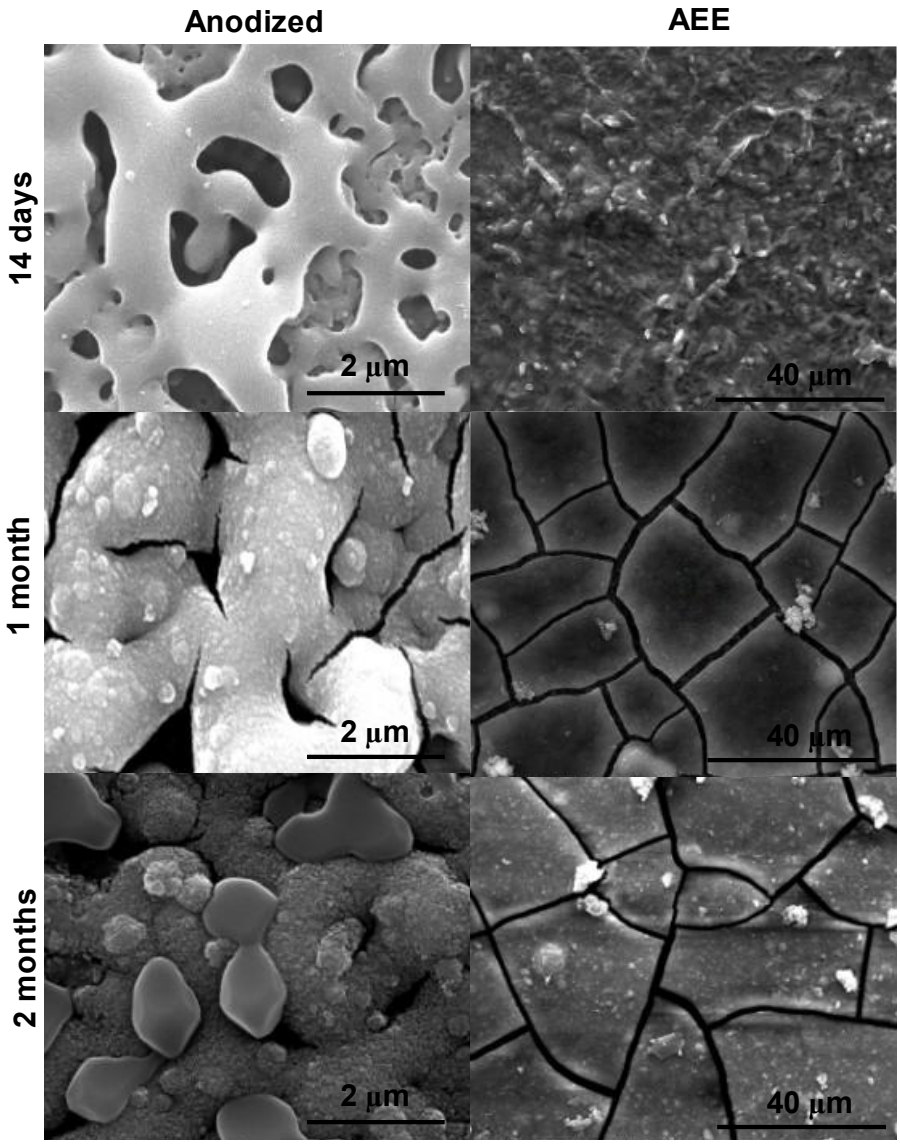

Figure 3.2.16 *SEM micrograph related to anodized and AEE sample after immersion up to 2 months in Hanks' balanced salt solution.*

For anodized Ti6Al4V alloys, the porous structure of the anodic layer was almost completely filled with clear HA deposits on its surface (see Figure 3.2.16a-b) after 1 month of immersion. For the sample treated using a three-step electrochemical process, HA formation occurred shortly after the fabrication step as previously reported (see Figure 3.2.11).

After one month in HBSS at 37°C, a typical "mud" structure indicative of a thick HA layer can be observed on the surface. Additionally, Raman spectra confirm the presence of HA, see Figure 3.2.17.

These observations based on SEM micrographs were also used to properly modelling the electrochemical behaviour of the systems to fit the impedance spectra reported in Figure 3.2.14.

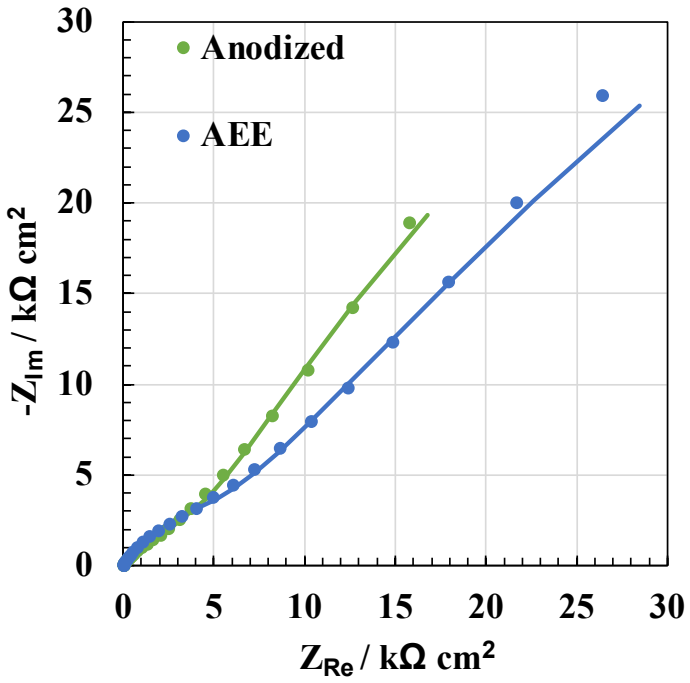

Figure 3.2.17 *Nyquist representation of EIS spectra related to anodized sample and AEE sample after 1 month in HBSS recorded at corresponding E_{corr}. Fitting according to EEC shown in Figure 3.2.14d.*

In this case, both impedance spectra related to anodized and AEE samples were fitted according to the EEC reported in Figure 3.2.14d, i.e. R_{el} in series with two parallels (RQ), (R_{inn} Q_{inn}) and (R_{out} Q_{out}) accounting for the morphology of the system that, after 1 month of immersion in Hanks' solution, can be assumed as the series of two compact layers. This is the consequence of the fact that there is an internal filled porous structure covered by a HA layer, thicker in the case of AEE sample immersed for 1 month. Fitting parameters are reported in Table 3.2.2. The overall decrease in impedance with immersion time indicates enhanced bioactivity, which is crucial for achieving proper osteointegration of biomedical devices.

	R_{el} [Ω cm²]	Q_{out} [μS sⁿ cm⁻²]	n	R_{out} [Ω cm²]	Q_{inn} [μS sⁿ cm⁻²]	n	R_{inn} [Ω cm²]	χ^2
Anodized	18	29	0.56	5000	57	0.73	1.4×10^5	1.4×10^{-3}
AEE	21	9.3	0.68	4500	34	0.57	3.0×10^5	1.4×10^{-3}

Table 3.2.2 *Fitting parameters (out: outer layer, inn: inner layer) related to the impedance spectra shown Figure 3.2.17 recorded for the bare Ti6Al4V, anodized and AEE samples according to the EEC shown in Figure 3.2.14.*

Based on the reported results, it's possible to note that three-step electrochemical processing offers a smart functionalization route for Ti6Al4V alloys. Reported bioactivity is peculiar of the AEE sample and is the consequence of a tailored electrochemical process. In fact, the anodizing process allows to cover the alloy surface with a thick porous and well adherent TiO_2 layer. Such porous film provides a good pattern for hosting Ag, whose release rate in turn is slowed down due to the sealing of pores with a HA containing alginic acid gel deposited during the electrophoresis. The latter can uptake Hanks' balanced solution during immersion, thus the bottom of the porous anodic film is in contact with the electrolyte even if sealed by the biopolymer. The bioactivity of AEE sample can be explained by an increased reactivity that leads to the growth of HA with immersion in Hanks' balanced salt solution. In fact, at the corrosion potential, the half-cell cathodic process is O_2 reduction, i.e.:

$$O_2 + 4e^- + 2H_2O \rightarrow 4OH^- \qquad (3.2.3)$$

The reaction produces OH^- and therefore alkalinization occurs at the bottom of the pores, also by taking into account a lower diffusion coefficient for OH^- species insides the pores with respect to the bulk. The half-cell anodic process is Ti oxidation from the alloy beneath or the oxidation of Ti^{x+} ($x < 4$) to Ti^{4+} contained in the oxide compensating the Ti lost from the layer due to dissolution phenomena. According to ref. [102], for the anodic layers prepared in calcium and phosphate containing solutions, Ca^{2+} ions and Ti^{4+} ions are released during immersion in Hanks' balanced salt solution with a higher rate for the former ions. Therefore, the simultaneous production of OH^- due to reaction (3.2.3) and the release of Ca^{2+} ions favour the precipitation of HA according to the following equations [31]:

$$10Ca^{2+} + 8OH^- + 6HPO_4^{2-} \rightarrow Ca_{10}(PO_4)_6(OH)_2 + 6H_2O \qquad (3.2.4)$$

$$10Ca^{2+} + 6PO_4^{3-} + 2OH^- \rightarrow Ca_{10}(PO_4)_6(OH)_2 \qquad (3.2.5)$$

After the three-step process, Ti6Al4V samples must first be tested *in vitro* to ensure that cell viability is not compromised. To test for a possible toxic effect due to components that can be released from the device made in Ti6Al4V during prolonged application such as for the bone implant, a viability test was carried out

using the cell medium in which the different samples were incubated separately (extract test). The medium was collected at different times, within a two-week period, and administered to the 3T3 fibroblast cells. Fibroblast were used as a model to measure the in vitro cell viability of biomaterials used for implants for the human body [126,127]. Results were analysed according to the ISO10993-5 standard guidelines [128,129]. By morphological inspection, cells showed normal morphology (no toxic response including detachment, lysis, extensive vacuolization, reduction of cell growth) and no change in their number and can be classified of grade 0 [130,131] (see Figure 3.2.18). Moreover, after the treatments the cells were submitted to one of the most common tests used, the MTS test [130,131]. MTS assay is based on the measure of the mitochondrial metabolic activity and is routinely used as index of cellular viability and proliferation. According to the ISO10993-5 guidelines, a biomaterial is considered cytotoxic when its viability is below 70% (see Figure 3.2.18). After exposure of 3T3 fibroblast cells to conditioned cell medium for 48 h, we found 100% cell viability, for all the samples at all exposure times, indicating that there is no release of any substances that induce cell toxicity or abnormal cell growth.

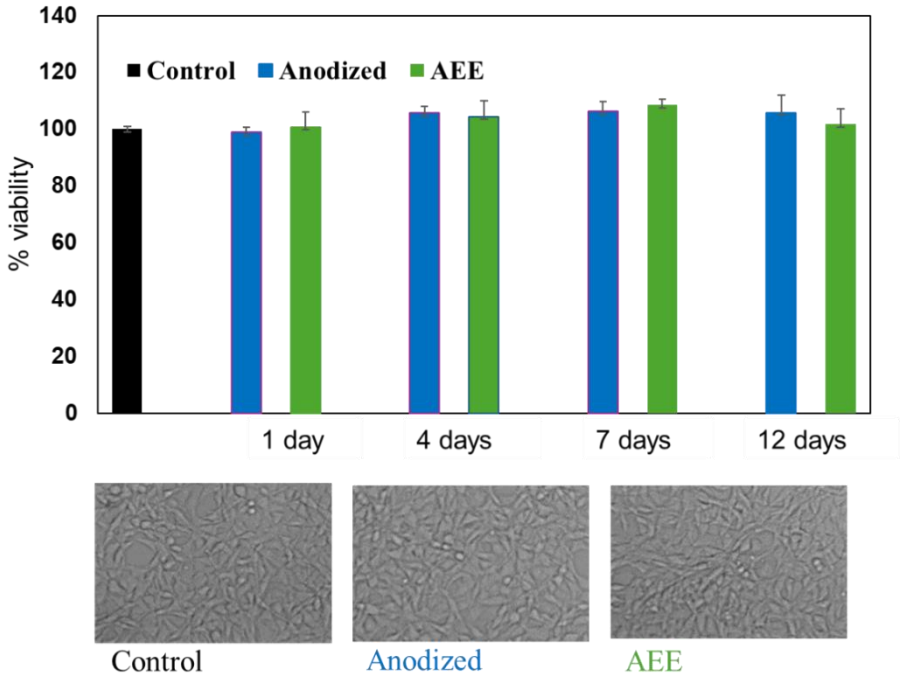

Figure 3.2.18 *Cytocompatibility analysis. Morphological images of 3T3 cells: untreated (Control) or treated with cellular medium in which Ag and No Ag samples were immersed for 12 days. MTS viability assay of 3T3 cells treated with the cellular medium in which Ag and No Ag samples were immersed for different times (1, 4, 7, 12 days).*

The insertion of bone implants causes a vascular trauma to the bone, with the break of the blood vessels and following contact of the implant with the blood [132]. *In vitro* hemocompatibility is one of the biological evaluations recommended by ISO 10993-4 guidelines for the medical devices [133]. In particular, erythrocytes

wellness or destruction is a hemocompatibility index. To evaluate this effect, the samples were incubated with erythrocytes for 4 h. Hemocompatibility tests were carried out for bare Ti6Al4V samples, after the anodizing process and after the complete three-step process. As shown in Figure 3.2.19, haemolysis ratio was analysed by using a spectrophotometric test, which measures the amount of free plasma Haemoglobin (Hb). In Figure 3.2.19 is evidenced that the haemolysis percentage induced by the presence of the biomaterials in the blood sample was comparable to the untreated control, whereas whole hemolysis was observable in the sample treated with Triton-X, used as positive control. To confirm the results, photographs of the tubes of untreated human erythrocytes, incubated with the positive control (tritonx100) and with the different samples after centrifugation, were also shown in Figure 3.2.19. The result was supported by erythrocyte microscopic analysis, where the morphology of the treated erythrocytes is similar to the control (untreated), see Figure 3.2.19. Test results confirmed the hemocompatibility of the samples treated with the three-step process.

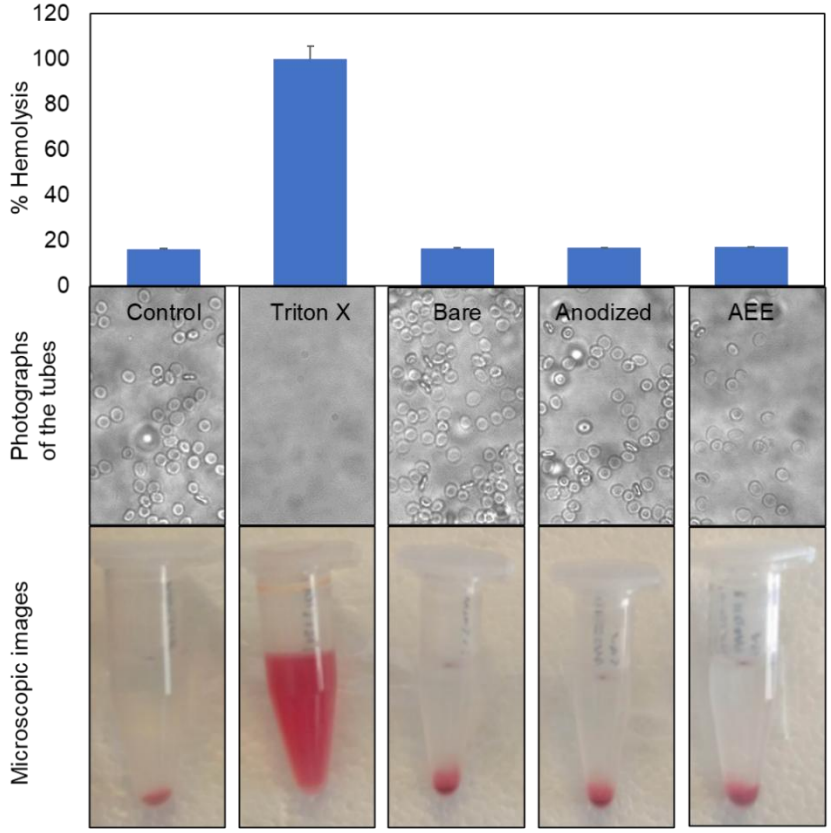

Figure 3.2.19 *Hemocompatibility analysis. Histogram relative to the absorbance of released Hb after treatment with the different samples. The values are expressed as the percentage respect to the positive control (TritonX), $p < 0.05$ vs control. Photographs of the tubes of human erythrocytes untreated, incubated with the positive control (tritonx100) and with the different samples after centrifugation. Microscopic images of hemolysis assay of erythrocytes (Control) or incubated with Triton-X (positive control) and with the different samples.*

Implant-associated infections are a major problem in surgery. Bacteria have the potential to adhere to the implant, grow and develop to form biofilms [134]. There is great interest in new methods of coating bone implants that reduce bacterial colonization (adhesion) or release antimicrobial agents from the implant surface resulting in improved survival of bone implants [135]. There are multifunctional technologies that combine both of the aforementioned approaches, anti-adhesive and antimicrobial agents. *Pseudomonas arginouse* bacteria were used to study the antibacterial effects of the samples before and after anodizing process and after the whole three-step process. Aliquots of the o.n. bacteria growth were incubated in a tube containing LB for 120 min. Successively the bacteria were gently dropped in the centre of the surface of the samples. After 1h, the sample with bacteria were incubated in LB medium and the bacterial growth was monitored spectrophotometrically every 1 h (see Figure 3.2.20) [136]. The difference in the growth curves for the tube containing the samples with Ag were detected with respect to the bare Ti6Al4V alloy and anodized Ti6Al4V samples. The results indicating that the Ag deposited through the electrodeposition process provides high antibacterial properties (see Figure 3.2.20). This effect is also clearly evident from the photographs of the tubes, where in the tube with the samples containing Ag the bacterial culture medium is clear, indicating an absence of bacterial growth (see Figure 3.2.20). Antibacterial effect it might be based on the release of silver cations from Ti6Al4V surface.

These cations disrupt bacterial wall, cause DNA alteration, lead to reacting oxygen species production and inactivate essential proteins [137].

Bacterial adhesion was also investigated by SEM analysis. Experimental results (Figure 3.2.20) indicated that bacteria were present only on bare Ti6Al4V alloy, indicating that the coating has anti-adhesive bacterial properties. Hydrophilic, highly hydrated, and non-charged surfaces have been shown *in vitro* to prevent many bacterial adhesions by limiting the contact between bacterium and potential surface placement sites [138]. In an effort to better understand these events, biomaterials that exhibit multiple properties, namely antimicrobial agents that can be released and reduced bacterial adhesiveness, have become an important area of research.[2]

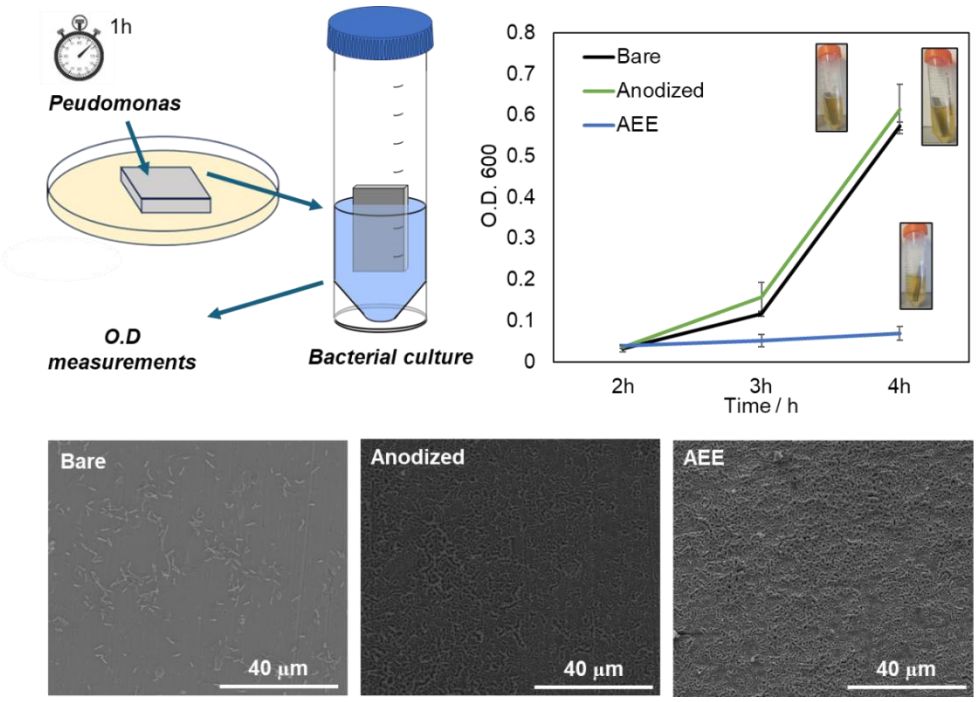

Figure 3.2.20 *Antimicrobial and antiadhesion properties. Schematic representation of bacteria experiment. The bacteria were gently dropped in the center of the surface of the biomaterials slide. After 1 h, the biomaterial with bacteria were incubated in LB medium and the bacterial growth was monitored spectrophotometrically. Histogram of optical density (O.D.600) measured every 1 h with relative photographs tubes containing the bacterial after 4 h and SEM image of bacteria adhesion of the devices after 4 h.*

In summary, a three-step electrochemical process was proposed to fabricate coatings on Ti6Al4V alloys, tailoring their morphology, composition, and thus enhancing their bioactivity for biomedical applications. The process consists of:

- **Anodizing step**: Growth of a thick porous oxide layer.
- **Electrodeposition step**: Depositing Ag nanoparticles for antibacterial properties.
- **Final electrophoretic step**: Deposition of alginate and hydroxyapatite into the pores

The final coating was characterized in HBSS to verify compatibility with human body environments while promoting proper HA (hydroxyapatite) growth essential for osteointegration. Characterization after 1 month immersion time using EIS spectra and SEM confirmed reduced barrier layer resistance and thickening of the outer hydroxyapatite layer, leading to a typical "mud" structure.

The coatings also demonstrated cytocompatibility, hemocompatibility, and antibacterial properties, distinguishing them from bare alloy and anodized samples. This tailored coating process enhances material suitability for applications requiring optimal integration with biological tissues while maintaining desirable biocompatible characteristics.

3.3 3D printed biomedical plates: corrosion behaviour as a function of surface treatments

The optimization in the last years of additive manufacturing offers numerous advantages for the production of biomedical prostheses, improving both the functionality and customisation of medical devices. In particular, it possible to realise customised prostheses based on the patient's anatomical scans, ensuring a perfect fit and improved comfort. The possibility of realizing prostheses in titanium, cobalt chrome and stainless steel, offering high biocompatibility, corrosion resistance and lightness, making them ideal for bone and dental implants. Technologies such as selective laser melting (SLM) or direct metal laser sintering (DMLS) allow the production of complex geometries, including lattice designs that reduce the weight of the prosthesis without compromising strength. Porous structure realized by 3D printing promote bone growth around the prosthesis, improving implant stability and reducing the risk of rejection. Compared to traditional manufacturing methods (such as milling or casting), 3D printing reduces manufacturing time and material waste costs. Additive printing uses only the necessary material, reducing waste compared to subtractive methods, making production more sustainable. Thanks to these advantages, metal 3D printing is revolutionising the biomedical sector, offering more advanced, efficient and affordable solutions for patients.

Despite the advancement of 3D printing technology for biomedical applications, one significant challenge remains related to the quality of surface finishing that occurs shortly after the fabrication process. The resulting surface is typically covered by un-melted powder material, which can easily be released and spread into host tissues. Additionally, these spherical-shaped powder particles may lead to the formation of crevices on the implant surface, further increasing localized corrosion susceptibility.

To address this issue effectively, it is crucial to design suitable surface treatments that remove any inhomogeneity from the 3D printed metals and alloys without compromising their overall corrosion resistance. This would involve careful consideration of the treatment methods and parameters to ensure optimal cleaning while preserving essential mechanical properties necessary for good biocompatibility and performance in biological environments.

For the experimental activities, 3D samples were produced by laser powder bed fusion process using an SLM 280HL machine using Ti6Al4V ELI-grade powder from SLM Solutions Group AG (Lübeck, Germany) with a mass density of 4.43 g/cm^3 and a 20–63 μm size distribution. All the samples were made by preheating a CP-Ti solid substrate at 200°C. Argon was used to decrease the oxygen level to 0.1% by filling the build chamber. Firstly, the effect of printing parameters on microstructure, mechanical properties and corrosion resistance was investigated. Sample were printed with Hatch distance of 120 μm, Layer thickness of 30 μm and building orientation of 90°. An overview of the nine process parameter combinations that are used in the process is provided in Table 3.3.1.

ID sample	P / W	V / mm s^{-1}	P/V / J mm^{-1}	Scanning Strategy / °
0.11 / 15°	150	1400	0.11	15
0.11 / 45°	150	1400	0.11	45
0.11 / 90°	150	1400	0.11	90
0.25 / 15°	350	1400	0.25	15
0.25 / 45°	350	1400	0.25	45
0.25 / 90°	350	1400	0.25	90
0.41 / 15°	350	850	0.41	15
0.41 / 45°	350	850	0.41	45
0.41 / 90°	350	850	0.41	90

Table 3.3.1 *ID samples and relative process parameters used*

For the experimental campaign, samples reproducing biomedical plates usually used for humerus fracture fixation were used, see Figure 3.3.1.

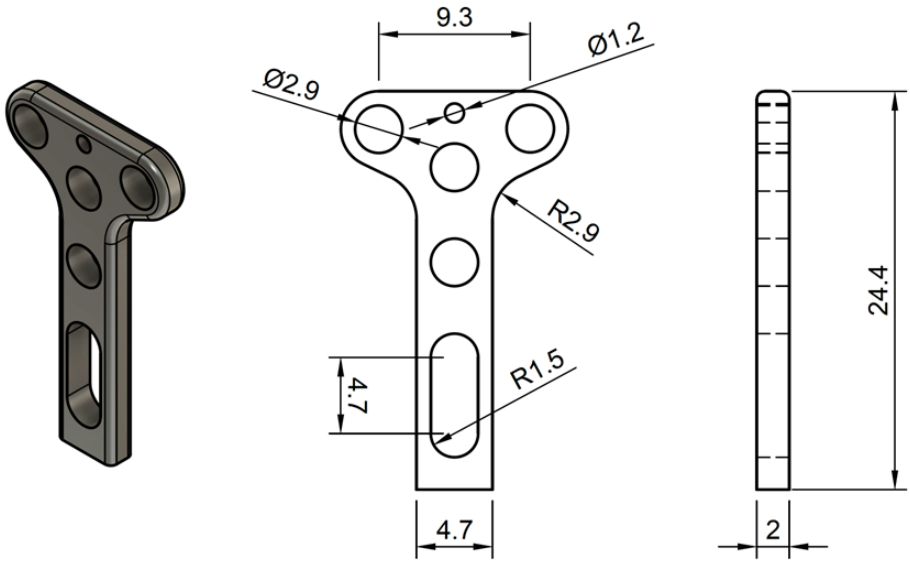

Figure 3.3.1 *3D CAD model and quoted sketch of the printed biomedical plates.*

The printing process was conducted at a 90-degree angle and with the longitudinal axes of the plates perpendicular to the printing surface. This configuration allowed for minimizing the area on the plate that came into contact with support structures, thereby reducing potential issues related to adhesion and stability during the printing process. Three Line Energy Density (LED) values (i.e. 0.11 J/mm, 0.25 J/mm, and 0.41 J/mm) as well as three distinct scan algorithms were examined. The scanning strategies that were employed are as follows: a 0°

starting angle, a 180° limiting scanning window, and increasing scanning angles of 15°, 45°, and 90° between successive layers. The sample are identified by using the LED values and scanning strategies (i.e. 0.11 / 15°, 0.11 / 45°,0.11 / 90°, 0.25 / 15°, 0.25 / 45°, 0.25 / 90°, 0.41 / 15°, 0.41 / 45°, 0.41 / 90°). In Table 3.3.1, process parameters used are reported. Vacuum stress relief treatment was not performed on the samples as reduced cross-section geometries and a 90° printing orientation significantly mitigate residual stress. Three samples were produced for each set of process parameters. Microstructural examination of samples longitudinal sections, density measurements, and corrosion resistance testing were conducted using three distinct repetitions of 3D specimens. Additional specimens shaped like dog bones were fabricated to perform tensile testing. Density measurements on 3D samples were performed using the Archimedes method at room temperature following ASTM B96208. Each specimen mass in both air and fluid were measured using a Mettler Toledo balance with a precision of 0.1 mg. The relative density of the printed samples was estimated using the Ti6Al4V density, which is 4,43 g/cm^3. The dog bone-shaped samples with a rectangular cross-section (15 × 2 mm) and a suitable gauge length of 30 mm were made as a reduction of Standard ASTM/E8 to assess the mechanical performance in terms of ultimate tensile strength and ductility (elongation to failure). The Galdabini universal testing machine was employed for the tensile tests. To evaluate microstructural modifications resulting from varied process parameters, specimens were etched with Kroll's reagent and examined using an Olympus optical microscope following grinding and polishing procedures. Metallographic observations were conducted on longitudinal sections of the samples. The as-printed samples (AP) were characterized without further treatment to determine if there is a correlation between different process parameters and corrosion resistance. Subsequently, 3D samples were chemical etched (CE) in a solution of 1:4:5 vol ratio of HF (40%): HNO_3 (68%): H_2O in an ultrasonic bath for 5 minutes. The chemical etching treatment was optimized to remove unfused powder from the surface. Finally, the samples were anodized in aqueous solution to growth a thick porous layer to improve corrosion resistance and osteointegration. The anodizing process was carried out galvanostatically at 20 mA cm^{-2} and a voltage compliance of 200V in an aqueous solution containing 0.2M calcium acetate ($(CH_3COO)_2Ca \cdot H_2O$) and 0.04M β-glycerol phosphate disodium pentahydrate (β-GPDS, $C_3H_7Na_2O_6P \cdot 5H_2O$). A two-electrode configuration was used: the alloy as the anode (working electrode) and Al foil as the cathode (counter electrode).

Figure 3.3.2 displays the results of the mechanical characterization and density measurements as a function of the printing conditions for each set of process parameters.

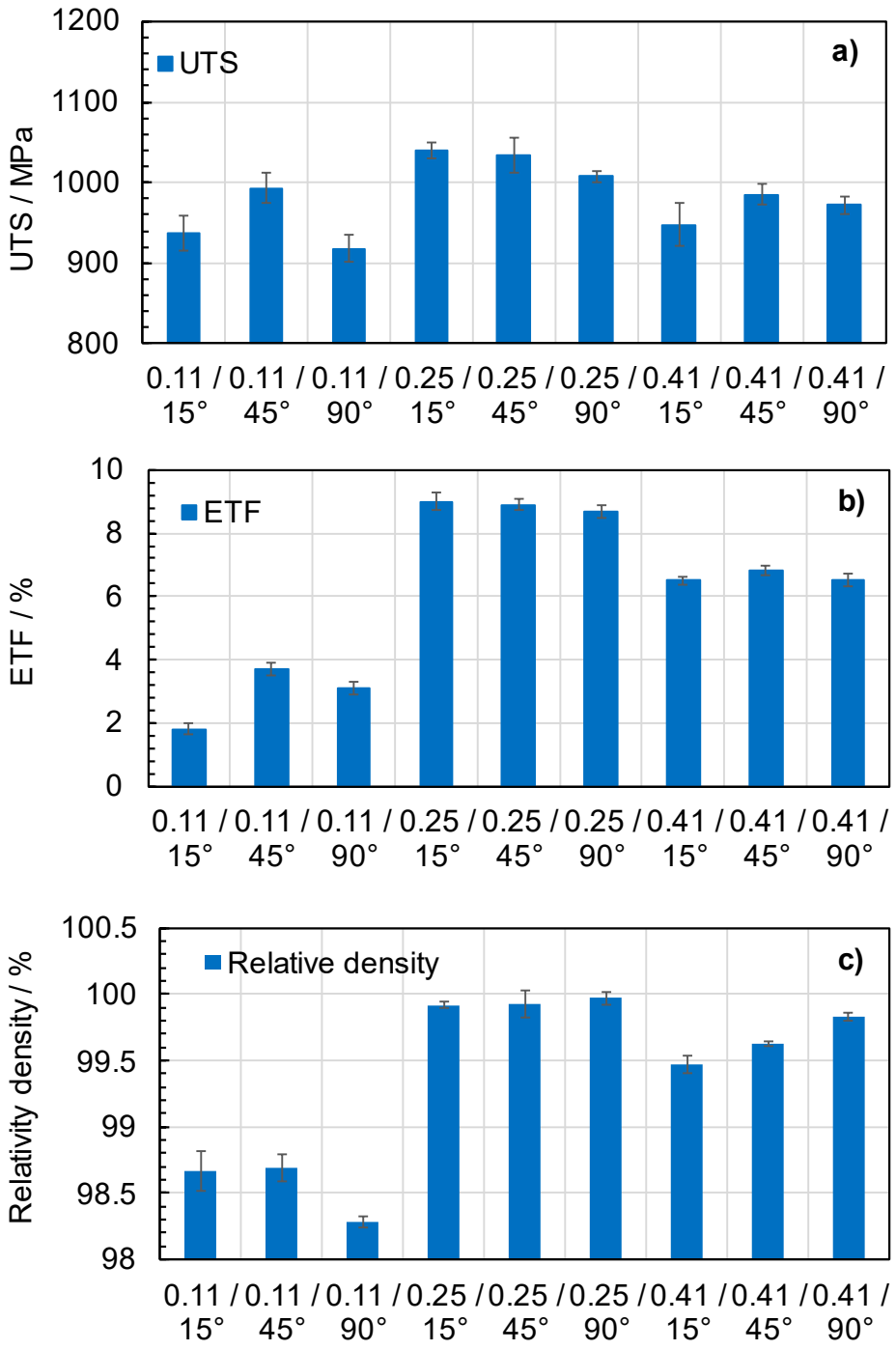

Figure 3.3.2 *Mechanical characteristics a) UTS, b) ETF and c) density for each process parameters.*

The mechanical characterization of the samples in terms of Ultimate Tensile Strength (UTS) and Elongation to Failure (ETF) is shown in Figure 3.3.2a, highlighted that low (0.11 J/mm) and high (0.41 J/mm) LED values determine a decrease in the mechanical resistance of the material and of its ductility compared to the values obtained for LED equal to 0.25 J/mm. According to Figure 3.3.2c, the highest density values are measured for LED 0.25 J/mm, while for lower or higher LED values the density of the material tends to decrease.

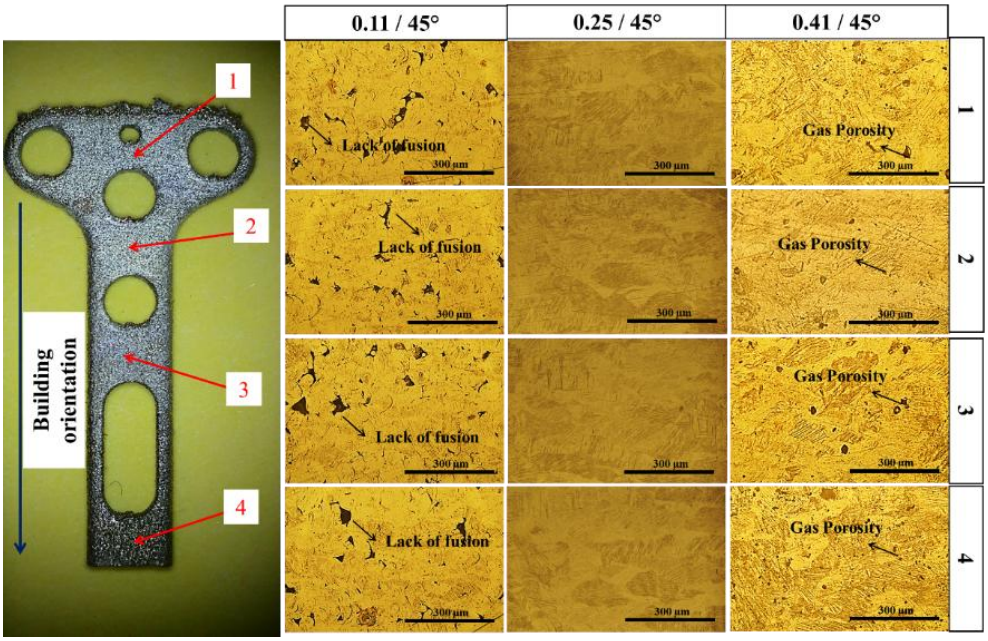

Figure 3.3.3 *Micrographs for as-built 3D Ti6Al4V sample longitudinal sections were taken using an optical microscope for 0.11 J/mm, 0.25 J/mm, and 0.41 J/mm LED and a 45° scan strategy.*

The microstructural analysis results in Figure 3.3.3 demonstrated the presence of porosity due to lack of fusion and gas porosity with 0.11 J/mm and 0.41 J/mm LEDs, respectively. These defects are explained by trends previously discussed regarding material resistance and density characteristics as process parameters vary. Defects of high porosity due to gas or lack of fusion produce a reduction in the strength and ductility characteristics of the material. The porosity detected is uniformly distributed near the external surface of the samples, as shown in Figure 3.3.3, the porosity detected is not connected with continuity. The microstructure observed for all samples is lamellar α', formed after rapid cooling associated with the printing process. The α' lamellar structure forms within the stable β grains at high temperatures. The average size of the original β grain, within which the structure α' develops, depends on the value of LED. As the value of LED increases, the average size of the original grain β increases. In the case shown in Figure 3.3.3, corresponding to the scan strategy value of 45°, the average original grain size β is 80 µm when LED is 0.11 J/mm, 110 µm at 0.25 J/mm, and 150 µm at 0.41 J/mm.

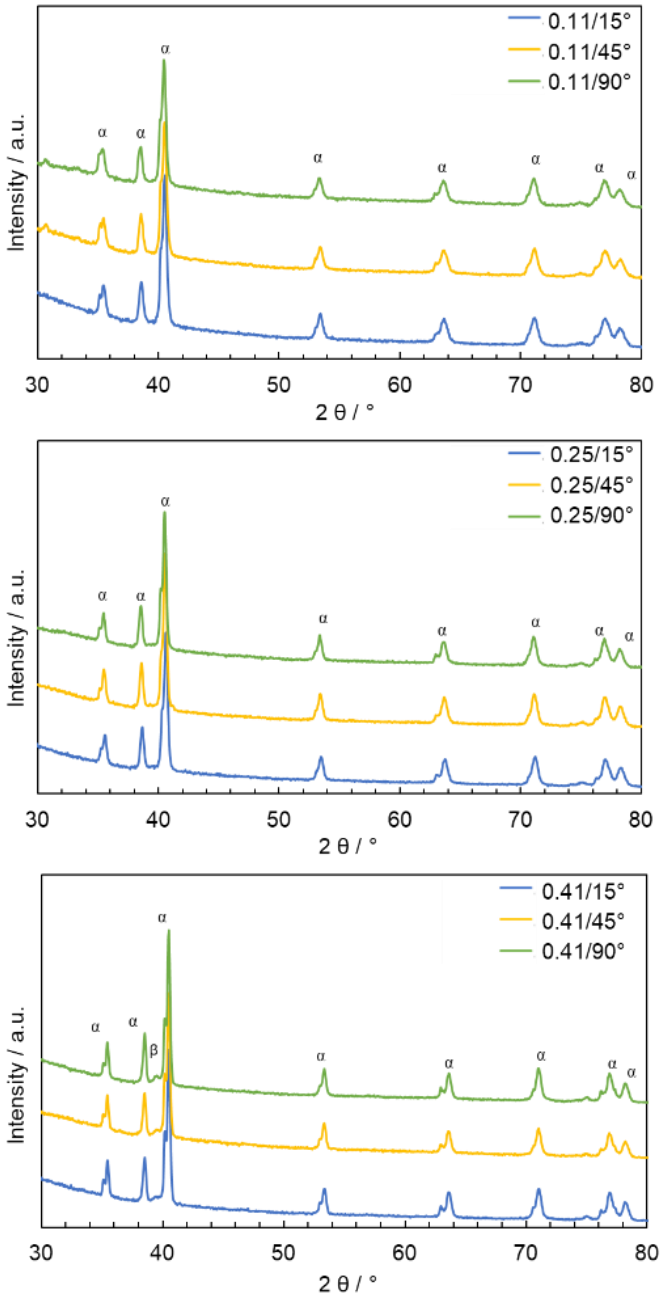

Figure 3.3.4 *XRD pattern for as printed 3D Ti6Al4V sample.*

In Figure 3.3.4, XRD patterns show a dominance by the α' /α-Ti phases for different LED values used. A weak reflection related to relating to β phase at $2\theta =$ 39.7° is present for 3D samples produced with 0.41 J/mm as LED value. This condition is due to an intensification of the material heat treatments for high LED associated with low layer thickness values. As reported in literature, the formation of phase α + β is enabled starting from phase α' which is formed in the first instance. Varying the scanning strategy for fixed LED value, homogeneous trends of the XRD pattern are observed [139,140].

Figure 3.3.5 shows SEM micrographs of as-printed 3D-printed Ti alloys.

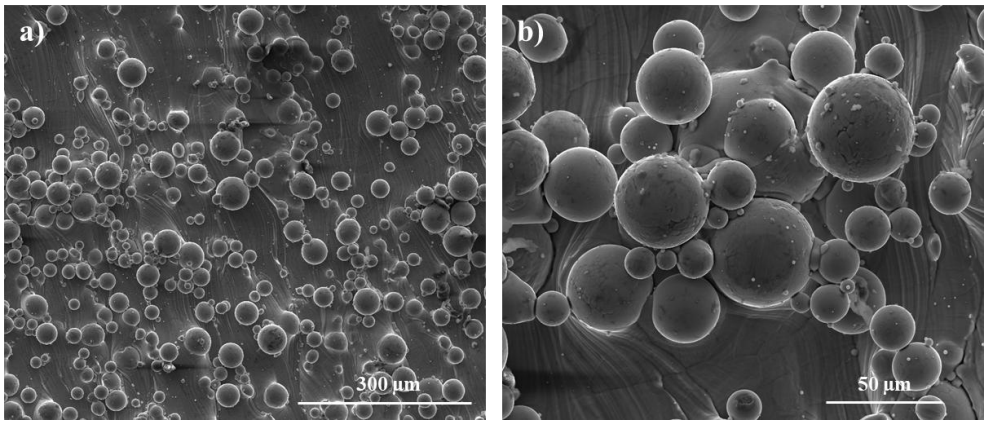

Figure 3.3.5 *SEM micrographs of as printed samples at different magnifications.*

It is evident that un-fused powder remains on the surface of the as-printed samples, typical of 3D printed materials produced using LPBF technology. This inhomogeneity leads to an uneven wettability of the surface, as evidenced by contact angle measurements showing significant variability across the surface (see Figure 3.3.6).

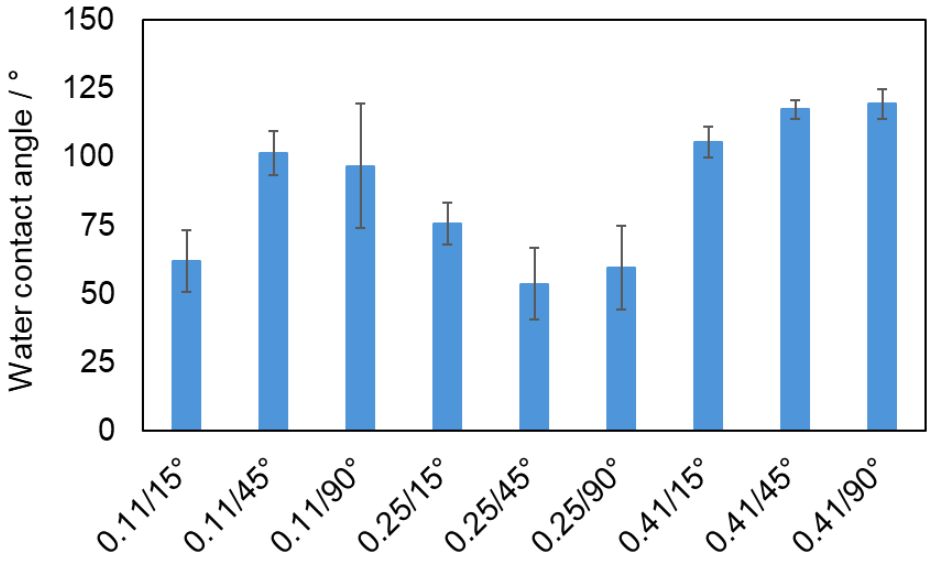

Figure 3.3.6 *Contant Angles relating to As Printed 3D Samples*

The unfused particles on the surface are likely to be detached by the alloys and could spread throughout the host tissue, especially when exposed to flowing solutions or wear. Therefore, a preliminary treatment by using hydrofluoric acid and nitric acid aqueous solution was carried out to remove them from the surface before implantation.

The chemical etching process effectively removes unfused powder particles, leading to an improvement in terms of homogeneity of surface as shown by the SEM micrograph in Figure 3.3.7.

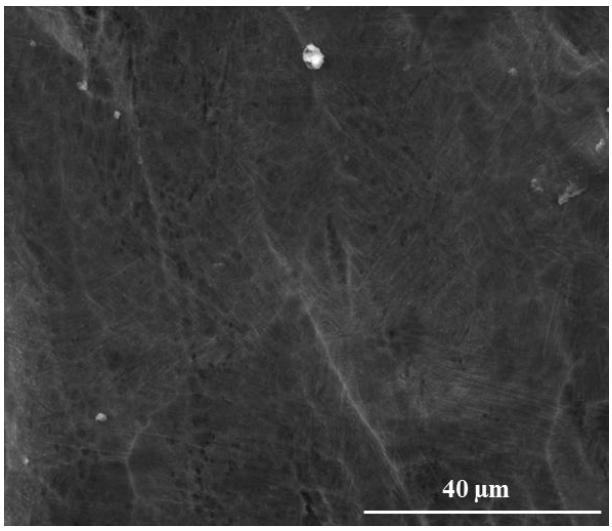

Figure 3.3.7 *SEM micrographs of chemically etched samples*

The measured water contact angles, shown in

Figure 3.3.8, indicate minimal variation in terms of wettability between samples post-chemical etching if compared to as-printed samples.

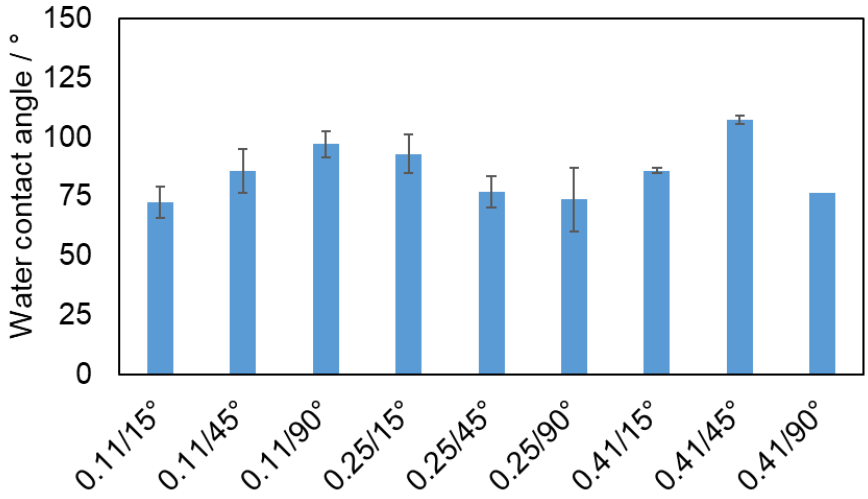

Figure 3.3.8 *Contant Angles relating to chemically etched 3D samples*

Chemically etched samples were then anodized at a current density of 20 mA cm^{-2} up to 200V as described before. Despite the variations revealed by optical microscopy of the printed samples compared to cast alloy microstructures, the voltage-time transient under galvanostatic conditions was similar to that recorded with cast alloys, see Figure 3.3.9.

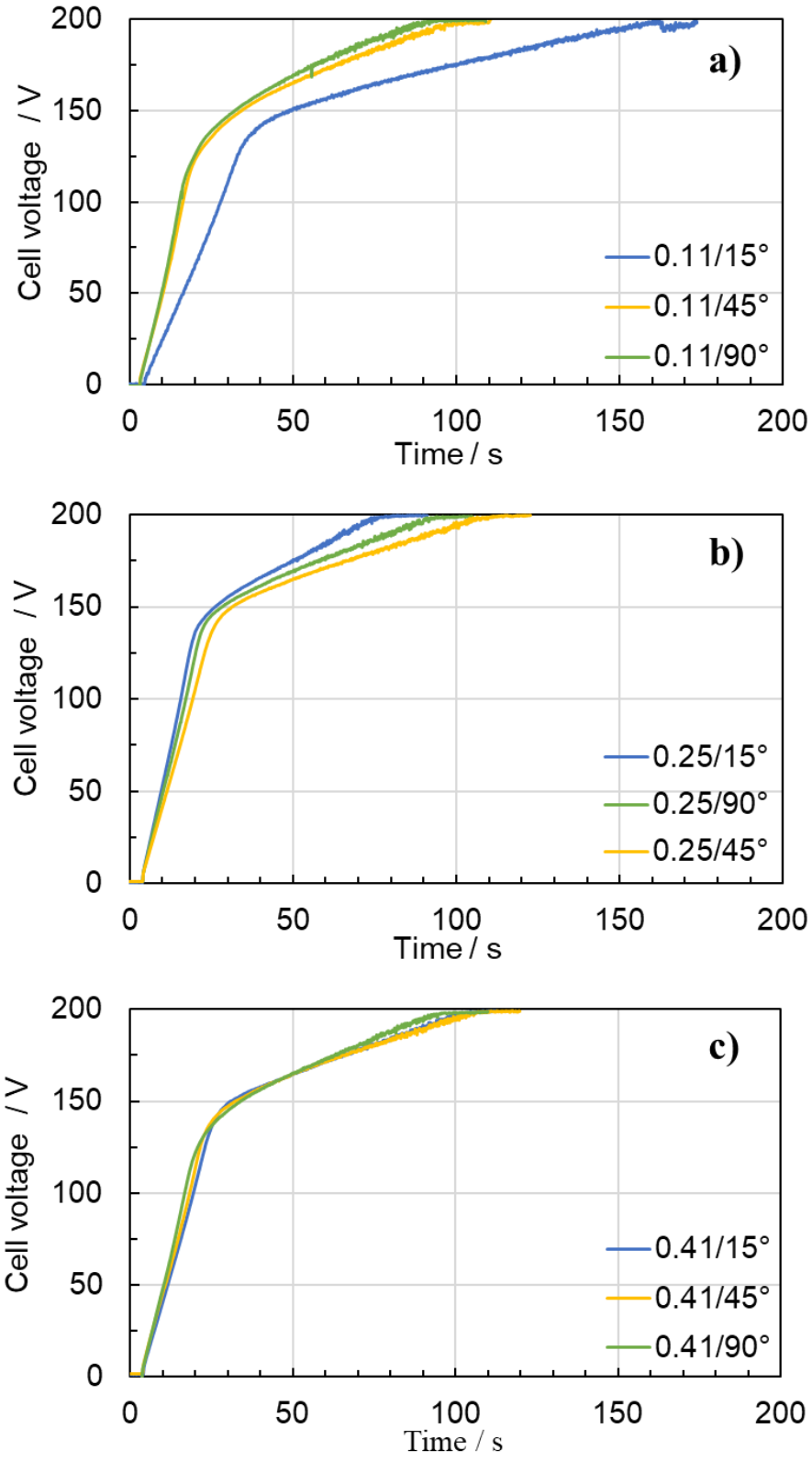

Figure 3.3.9 *Cell voltage versus time curve related to the growth of the anodic oxide on Ti6Al4V alloy for different printing parameters*

In Figure 3.3.10a-c, SEM micrographs show the porous oxide layer grown on 3D printed samples after the anodizing process. EDX analysis in Figure 3.3.10d confirm the incorporation of calcium and phosphorus in the anodic layer.

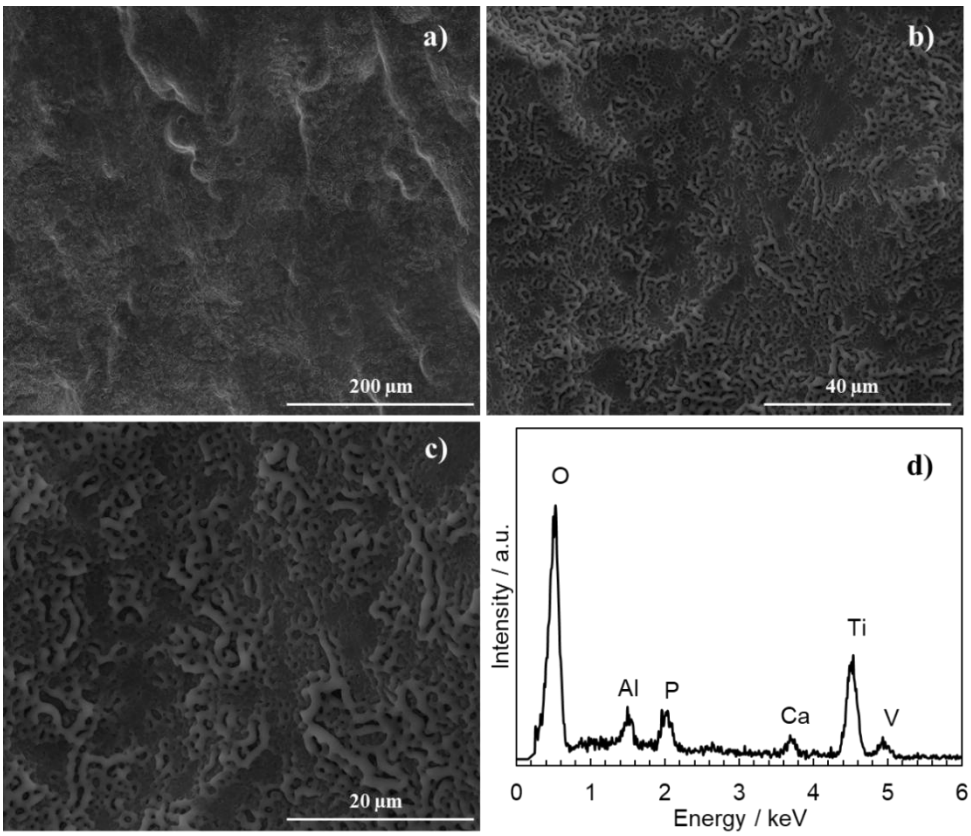

Figure 3.3.10 *SEM images at different magnifications and EDX analysis of anodized 3D Ti6Al4V samples.*

The treatment results in nearly uniform contact angles across the entire surface (57° ± 10°), suggesting the formation of a highly hydrophilic layer as shown in Figure 3.3.11.

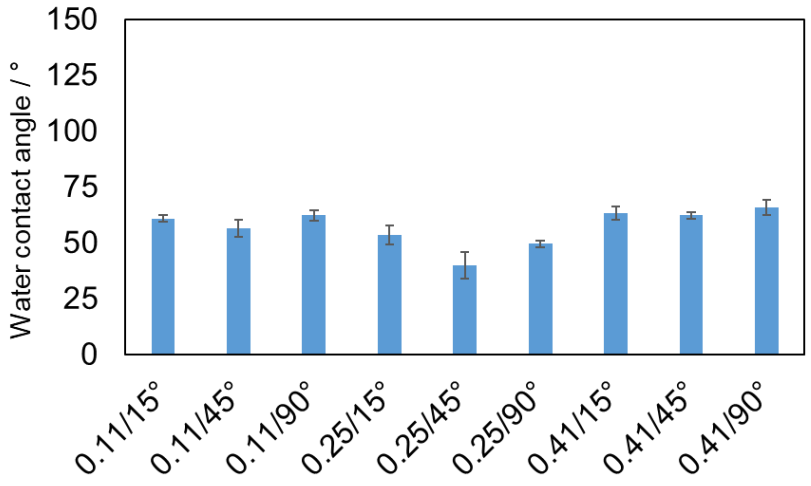

Figure 3.3.11 *Contant Angles relating to anodized 3D samples.*

According to Raman Spectroscopy, see Figure 3.3.12, the anodic film is mainly constituted by anatase as suggested by the Raman bands at E_g (144, 196, and 638 cm^{-1}), B_{1g} (398 and 519 cm^{-1}) and A_{1g} (513 cm^{-1}).

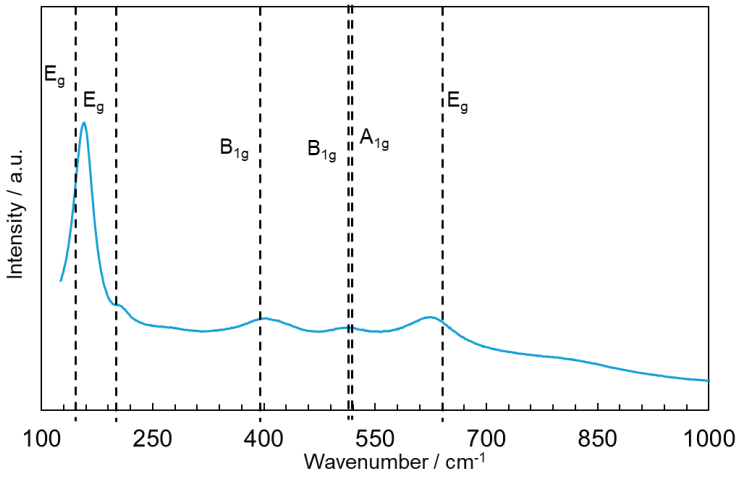

Figure 3.3.12 *Raman spectrum related to anodized 3D sample*

The Raman bands exhibit a slight shift compared to crystalline TiO_2 phase, indicative of the formation of a defective layer. It is noteworthy that, as reported for cast alloys, anodization leads to the incorporation of calcium and phosphate ions from the electrolyte, resulting in improved osteointegration properties. (see EDX in Figure 3.3.10). [141–143]

Photoelectrochemical characterizations were conducted to obtain information about the electronic properties of the anodic films on 3D-printed alloys, which significantly affect the corrosion resistance of the samples. Figure 3.3.13 shows the photocurrent spectrum (photocurrent vs wavelength curve) recorded at 1.5 V vs. SSC in HBSS.

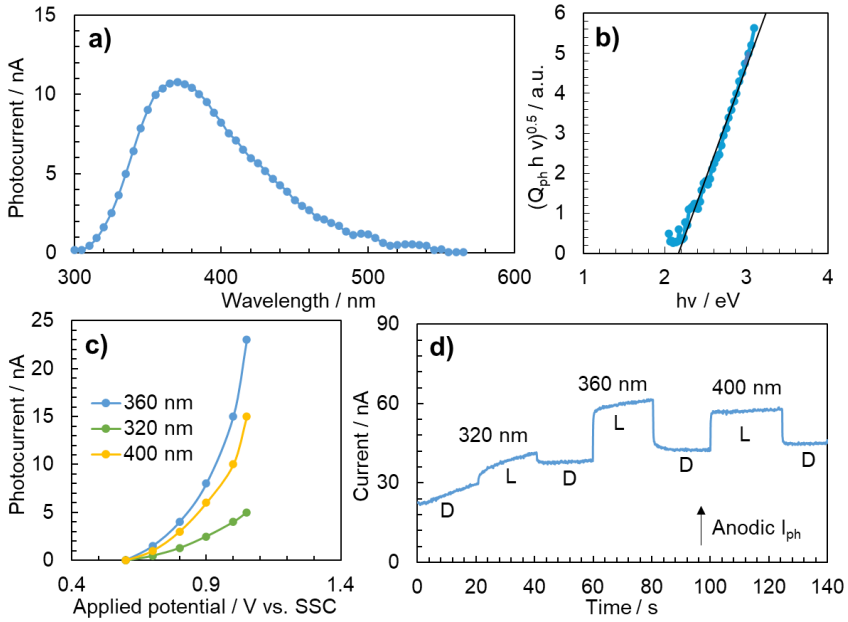

Figure 3.3.13 *Photoelectrochemical characterization in HBSS of anodized 3D Ti6Al4V samples a) Photocurrent spectrum recorded at 1.5 V vs. SSC b) $(Q_{ph}\ h\nu)^{0.5}$ vs. hv relating to Figure 3.3.13 a, c) photocharacteristics recorded at different wavelengths and d) current vs. time curves recorded by manually chopping the irradiation at different wavelengths. L: light, D: dark.*

Assuming indirect optical transitions, it is possible to estimate the band gap values according to the following equation:

$$(Q_{ph}\, h\nu)^{0.5} \sim (h\nu - E_g) \qquad (3.3.1)$$

where, for photon energy in the vicinity of band gap, Q_{ph}, the photocurrent yield, is proportional to the light absorption coefficient, hν is the photon energy and E_g is the optical band gap.

The estimated band gap for the anodic layer is approximately 2.15 eV, which is significantly lower than that reported in literature for TiO_2 anodic films (3.3 eV) in agreement with the experimental results in Chapter 3.2. on anodic films grown on cast Ti6Al4V. Briefly, the low optical band gap can be explained by considering the incorporation of Al^{3+} and V^{5+} ions into TiO_2 matrix during the hard anodizing process. The incorporation of such aliovalent ions with respect to Ti^{4+} induces the formation of allowed localized states inside the gap of TiO_2.The anodic film exhibits n-type semiconductor characteristics, as confirmed by recording photocurrent transients under constant irradiating wavelengths (see Figure 3.3.13d) and by the photocharacteristics, i.e. photocurrent vs potential curves (see Figure 3.1.13c). Notably, for the oxide grown on 3D samples, stationary anodic photocurrent was measured (Figure 3.1.13d) and the photocurrent decreases by shifting the potential toward the negative direction as expected for n-type SC, and the zero-photocurrent potential can be assumed as an estimate of the flat band potential of the oxide.

The corrosion resistance of 3D-printed samples before or after successive surface treatments was studied through electrochemical impedance spectra (EIS) and polarizations curves. In Figure 3.3.14 EIS spectra in Bode representation, recorded at the corresponding open circuit potential, and polarization curves related to as printed 3D samples recorded in HBSS at 37°C are reported.

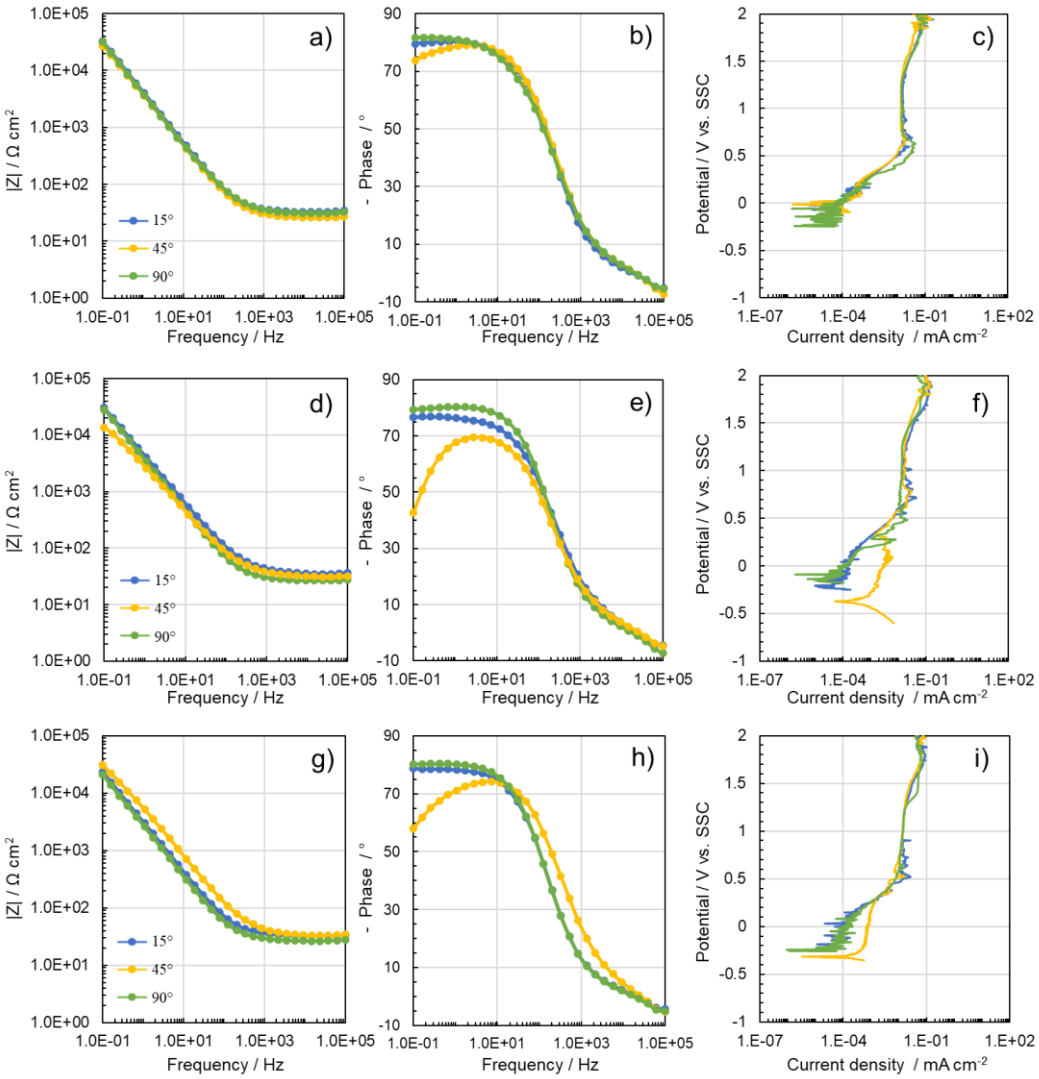

Figure 3.3.14 *EIS spectra and polarization curves related to as printed 3D samples with a, b, c) 0.11 J/mm, d, e, f) 0.25 J/mm and g, h, i) 0.41 J/mm as LED value.*

For as-printed 3D samples, the EIS spectra can be simulated using a simple one-time constant equivalent circuit (EC), see Figure Figure 3.3.15a. The circuit comprises an electrolyte resistance R_{el} in series with a parallel combination of polarization resistance (R_{pol}) and Q_{dl}, representing not ideal double layer capacitance.

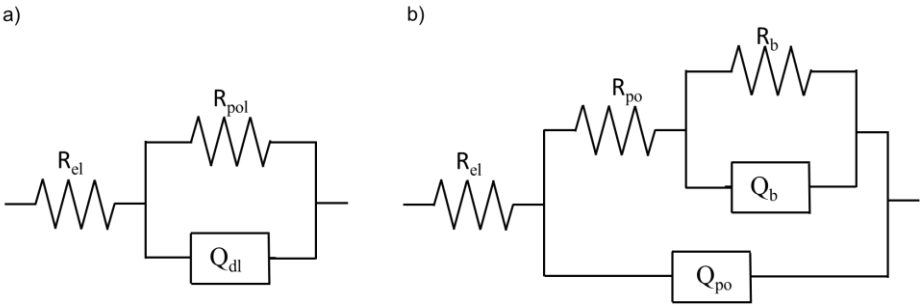

Figure 3.3.15 *Electric equivalent circuits (EEC) used for the fitting of EIS spectra.*

To estimate the effective double layer capacitance from the CPE value, we used the following relationship [144]:

$$C_{dl} = {Q_{dl}}^{1/n} {R_{el}}^{(1-n)/n} \qquad (3.3.2)$$

The contribution to the measured capacitance arising from the thin TiO_2 passive layer grown by air exposure on the surface of the alloys is negligible, since due to the negative open circuit potential, the layer is very close to or below its flat band potential, thus being under forward bias regime [145,146]. The corresponding fitting parameters are presented in Table 3.3.2.

Process parameters	R_{el}/Ω cm²	R_{pol}/Ω cm²	C_{dl} /F cm⁻²	χ^2
0.11/15°	33	3.00E+06	1.76E-05	1.30E-03
0.11/45°	27	2.85E+05	2.17E-05	2.22E-03
0.11/90°	32	5.00E+06	2.08E-05	4.26E-03
0.25/15°	36	4.00E+06	1.48E-05	2.00E-03
0.25/45°	32	2.80E+04	1.80E-05	1.47E-03
0.25/90°	27	2.24E+06	2.39E-05	2.00E-03
0.41/15°	33	3.00E+06	2.55E-05	1.10E-03
0.41/45°	33	9.30E+04	1.03E-05	2.10E-03
0.41/90°	27	2.00E+06	3.33E-05	1.56E-03

Table 3.3.2 *Fitting parameters related to the impedance spectra shown in Figure 3.3.14 recorded for as printed 3D samples.*

The polarization resistance is notably high but for plates printed with a scanning strategy of 45°, lower R_{pol} values at least an order of magnitude are measured. For these sample, a very negative open circuit potential is observed, indicating a not uniform passivation. These results agree with the polarization curves reported in Figure 3.3.14 showing a higher corrosion current density for alloys printed with 45° scanning strategy. All as-printed samples display a passivity range, between 0.5 and 1.5 V vs. SSC, and an anodic peak related to vanadium ions release. In addition, current oscillations are evident, suggesting metastable pits or debris detachment on the surface. Ti alloys are not susceptible to pitting, especially in low chloride ion concentration; this condition can be attributed to the roughness left after 3D printing process (typically ranging between 5 to 40 μm [147]).

Figure 3.3.16 displays the impedance spectra (Bode representation) for chemically etched samples recorded in HBSS solution at 37°C at corresponding open circuit potentials (U_{oc}).

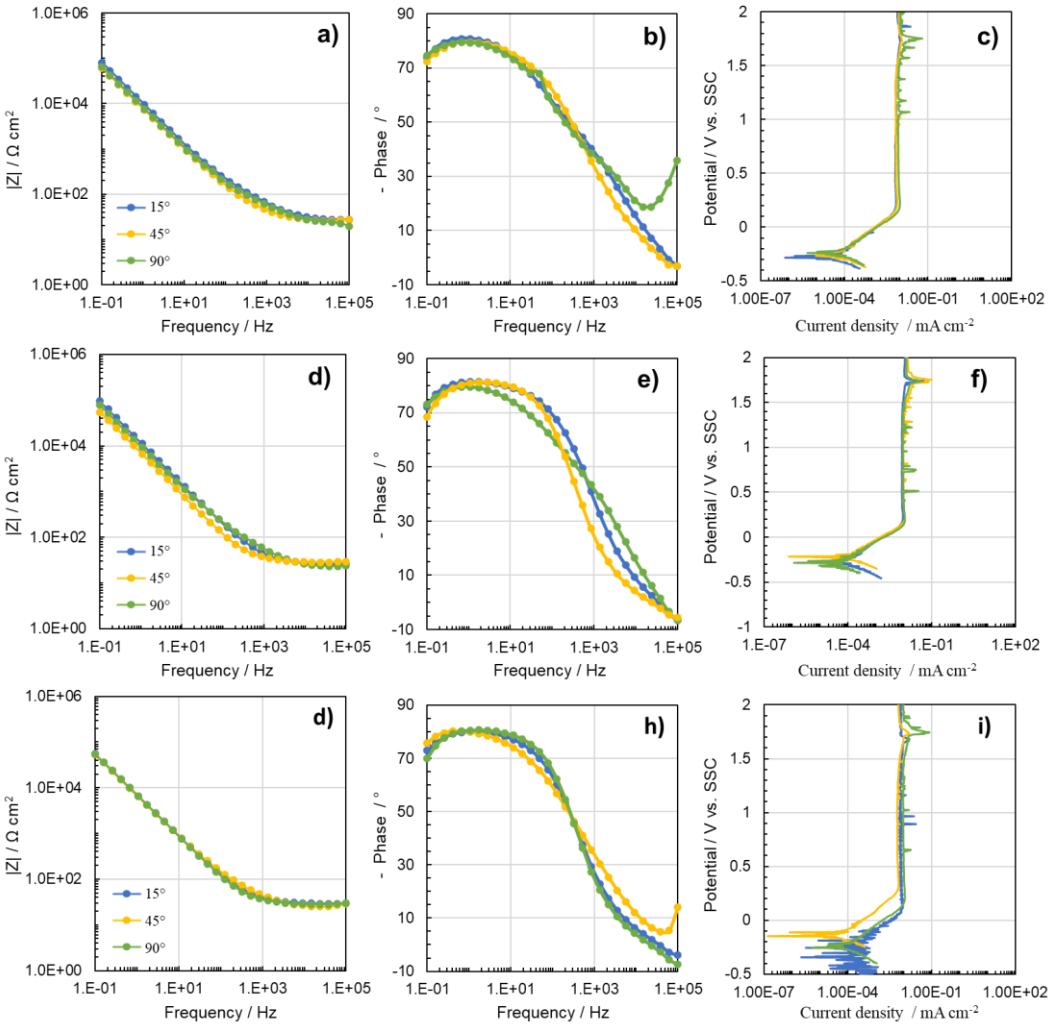

Figure 3.3.16 *EIS spectra and polarization curves related to chemically etched 3D samples with a, b, c) 0.11 J/mm, d, e, f) 0.25 J/mm and g, h, i) 0.41 J/mm as LED value.*

After the chemical etching a slight increase of the overall impedance is observed if compared to as printed samples. The fitting parameters according to the EEC of Figure 3.3.15a, are reported in Table 3.3.3.

Process parameter	R_{el} / $\Omega \cdot cm^2$	R_{pol} / $\Omega \cdot cm^2$	C_{dl} /F cm^{-2}	χ^2
0.11/15°	32	4.00E+06	4.18E-06	3.14E-03
0.11/45°	27	1.20E+06	6.33E-06	4.70E-03
0.11/90°	25	6.00E+06	4.24E-06	2.35E-03
0.25/15°	27.4	1.20E+06	6.33E-06	4.70E-03
0.25/45°	29.6	2.80E+05	1.21E-05	2.40E-03
0.25/90°	25	6.00E+06	4.24E-06	2.35E-03
0.41/15°	29	3.40E+05	1.22E-05	2.50E-03
0.41/45°	29	8.00E+05	7.18E-06	1.10E-03
0.41/90°	28	4.00E+06	4.29E-06	6.40E-03

Table 3.3.3 *Fitting parameters related to the impedance spectra shown in Figure 3.3.16 recorded for chemically etched 3D samples.*

The polarization curves recorded at 37°C in HBSS solution display a passivation range from approximately +0.2 V vs. SSC up to about +2 V, wider than those of as-printed samples. In addition, less pronounced anodic peaks due to vanadous ion dissolution are evident. The results obtained in terms of overall impedance and i_{corr} show that the corrosion resistance obtained for 3D samples are comparable to the results obtained for cast Ti alloy. [13,148,149] However, current oscillations are clearly visible in the polarization curves also for etched samples.

Figure 3.3.17 shows EIS spectra in Bode representation related to anodized 3D printed

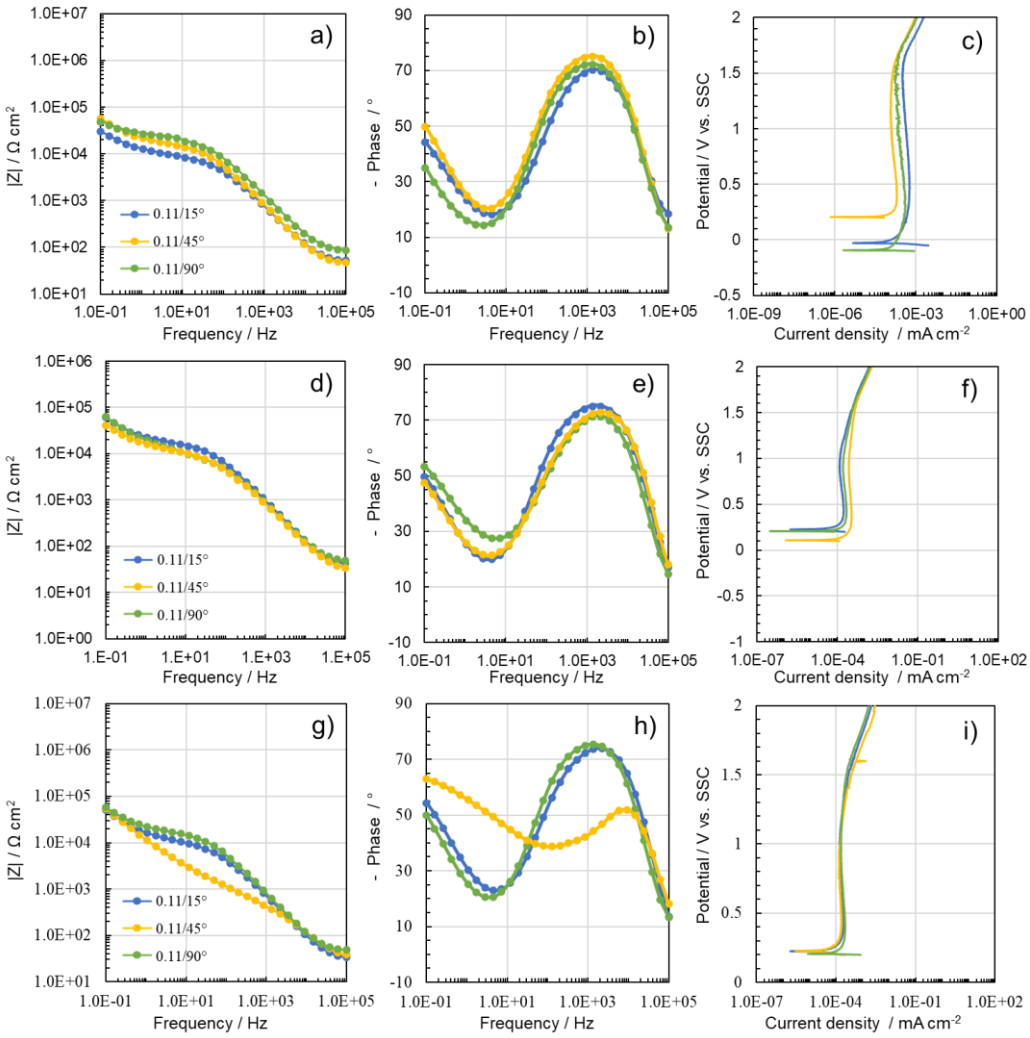

Figure 3.3.17 *EIS spectra and polarization curves related to anodized 3D samples with a, b, c) 0.11 J/mm, d, e, f) 0.25 J/mm and g, h, i) 0.41 J/mm as LED value.*

For anodized alloys, the EEC consists of a Q_{po}, a CPE modelling the pore wall non ideal capacitance, in parallel with a series between R_{po}, the electrolyte resistance inside the pore, and the (R_b Q_b) parallel, related to the barrier oxide layer presence at the bottom of the pore, see Figure 3.3.15b. The fitting parameters reported in Table 3.3.3 highlight an increased overall impedance due to the presence of porous anodic layers.

Process parameter	R_{el} / Ω·cm²	C_{po} / F cm^{-2}	R_{pol} / Ω·cm²	R_b / Ω·cm²	C_b /F cm^{-2}	χ^2
0.11/15°	27	7.69E-08	1.00E+04	4.10E+05	2.57E-06	2.50E-03
0.11/45°	27	8.33E-08	2.50E+04	2.80E+06	1.50E-06	2.95E-02
0.11/90°	27	2.55E-08	2.80E+04	1.10E+05	1.32E-05	8.00E-02
0.25/15°	37	1.10E-07	1.62E+04	5.00E+06	8.01E-07	1.40E-03
0.25/45°	28	1.21E-07	1.01E+04	3.00E+06	5.24E-07	3.10E-03
0.25/90°	43	1.19E-07	9.32E+03	3.00E+06	2.56E-07	2.90E-03
0.41/15°	30	1.61E-07	9.61E+03	4.00E+06	8.09E-07	2.80E-03
0.41/45°	30	5.33E-09	1.08E+03	6.00E+06	4.04E-07	4.40E-03
0.41/90°	27	1.03E-07	1.75E+04	3.74E+06	1.69E-06	2.80E-02

Table 3.3.4 *Fitting parameters related to the impedance spectra shown in Figure 3.3.17 recorded for 3D samples after the anodizing process.*

Notably, the contribution attributed to the barrier film is similar to that measured with as built and not anodized alloys. The open circuit potential in HBSS (~ 0.4 V vs Ag/AgCl) is lower than the flat band potential, thus the barrier film is under forward bias regime with an impedance comparable to that of not anodized alloys. However, the presence of a thick porous layer introduces a further contribution to the impedance, which raises significantly.

Figure 3.3.17 shows polarization curves related to a 3D sample after the anodizing process. The anodic oxide layer shifts the corrosion potential toward more positive values, decreases passivity current density, and reduces corrosion current density compared to as-printed and chemically etched samples. Furthermore, no current oscillations are evident in the polarization curves, suggesting that the anodic film inhibits the formation of metastable pits and/or debris detachment on the surface. Based on these reported results, the corrosion resistance for anodized 3D samples is superior to that of as-built and chemically etched samples for all printing parameters.

In order to have information about the corrosion behaviour of 3D Ti alloys in inflammatory conditions (HBSS_IC) and severe inflammatory situations (HBSS_SIC), impedance spectra were recorded at the open circuit potential and polarization curves at 37°C. The EIS spectra and polarization curves are presented in Figure 3.3.18, while the corresponding fitting parameters are reported in Table 3.3.5 and Table 3.3.6.

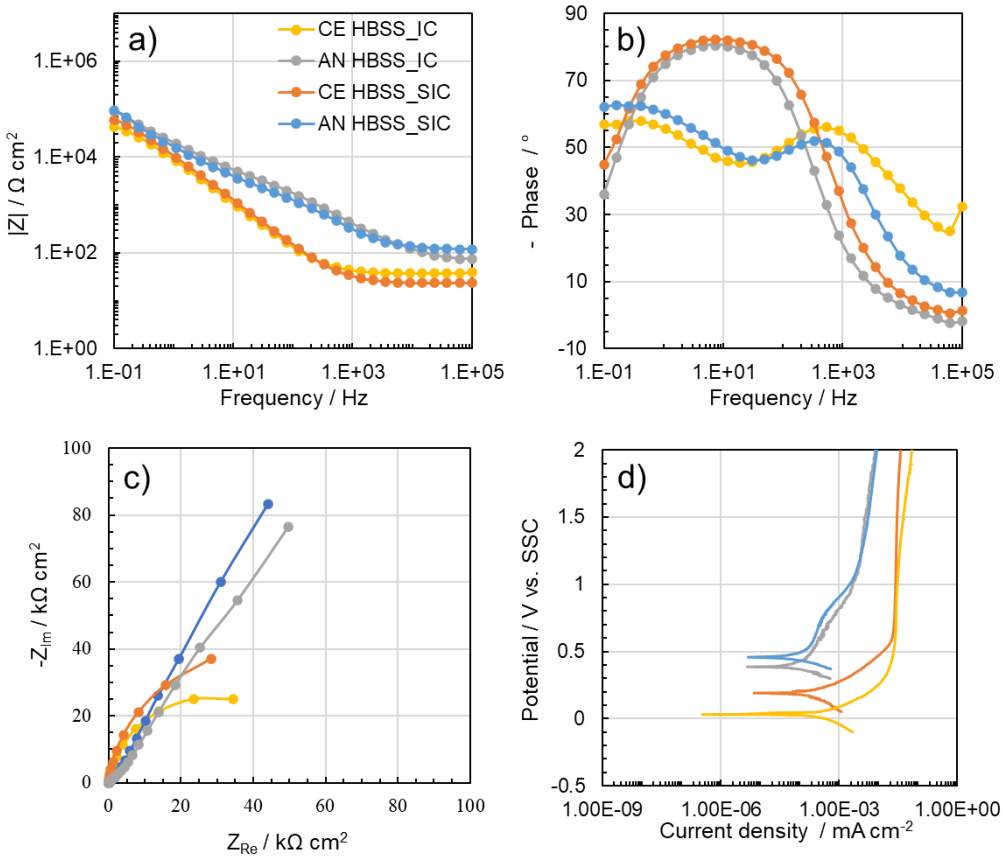

Figure 3.3.18 *EIS spectra and polarization curves related to chemically etched and anodized 3D samples with 0.25 J/mm as LED value in inflammatory and severe inflammatory conditions.*

Simulating solutions	**R_{el} / Ω·cm²**	**R_{pol} / Ω·cm²**	**C_{dl} / F cm⁻²**	**χ^2**
HBSS_IC	37	5.7E+04	1.10E-05	5.80E-04
HBSS_SIC	24	9.02E+04	1.52E-05	6.47E-04

Table 3.3.5 *Fitting parameters related to the impedance spectra shown in Figure 3.3.18 recorded for 3D samples after the chemical etching process in inflammatory and severe inflammatory conditions.*

Simulating solutions	R_{el} / Ω·cm²	C_{po} / F cm^{-2}	R_{pol} / Ω·cm²	R_b / Ω·cm²	C_b /F cm^{-2}	χ^2
HBSS_IC	55	1.52E-7	9225	0.70E+6	4.85E-8	4.85E-8
HBSS_SIC	75	4.52E-7	3182	1.20E+6	4.55E-8	4.55E-8

Table 3.3.6 *Fitting parameters related to the impedance spectra shown in Figure 3.3.18 recorded for 3D samples after the anodizing process in inflammatory and severe inflammatory conditions.*

EIS spectra and relative fitting parameters show that there is a reduction of about two orders of magnitude for the polarization resistance of chemically etched samples in inflammatory conditions compared to Hanks' balance salt solution. No significant change was observed in impedance for anodized 3D sample. In addition, a reduction of about one order of magnitude for C_b recorded in inflammatory conditions (see Table 3.3.6), was observed if compared to anodized 3D sample in HBSS (see Table 3.3.4). The presence of high-oxidizing species like H_2O_2 increases the measured OCP values, therefore the anodic film is under reverse bias regime, thus the occurrence of electrochemical reactions on the sample surface is hindered. [146] Polarization curves in Figure 3.3.18 shows that there is substantial shift for the E_{corr} to more positive values, a reduction in terms of i_{corr} and i_{pass} for 3D sample after anodizing process if compared to chemically etched samples.

Long-term immersion tests were conducted to evaluate the corrosion resistance under inflammatory conditions (HBSS_IC) for chemically etched and anodized samples. Figure 3.3.19 reports the EIS spectra recorded at corresponding open circuit potentials in HBSS_IC immediately following a one-week immersion period at 37°C.

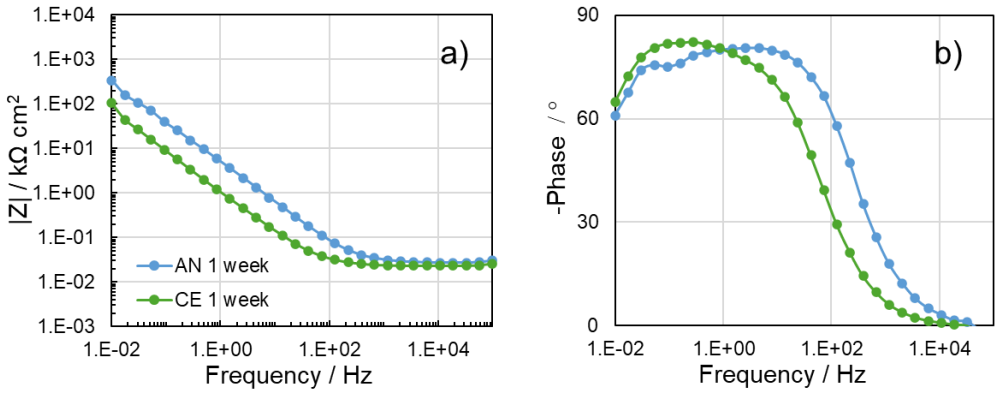

Figure 3.3.19 *EIS Spectra in Bode representation for chemically etched and anodized 3D Ti6Al4V samples after 1 week of immersion in simulated inflammatory conditions*

In both cases a one-time constant circuit (see Figure 3.3.15b) very well fits the spectra and the corresponding fitting parameters are reported in Table 3.3.7.

Sample	R_{el} / $\Omega \cdot cm^2$	R_{pol} / $\Omega \cdot cm^2$	C_{dl} / F cm^{-2}	χ^2
Chemically etched	24	3.6E+05	9.86E-05	1.2E-02
Anodized sample	28	2.9E+05	1.80E-05	1.5E-03

Table 3.3.7 *Fitting parameters related to the impedance spectra shown in Figure 3.3.19 recorded for 3D samples after 1 week of immersion in inflammatory conditions.*

The magnitude of C_{dl} raised by almost one order of magnitude after 1 week of immersion, which can be attributed to the reduction of TiO_2 passivity layer thickness. Despite high polarization resistance values remaining consistent with both surface treatments ($R_{pol} \sim 10^5$ Ω cm^2), the overall impedance decreased with respect to that measured before the immersion test. SEM micrographs reveal corrosion phenomena on alloy surfaces after 1 week of immersions. According to the micrographs in Figure 3.3.20, corrosion mainly takes place in some areas of the sample as selective attack of the edge of the melt pool probably assisted by the presence of chlorides ions. In contrast, anodized samples exhibit a uniform dissolution of the outer porous oxide layer during immersion in HBSS_IC, leaving their surfaces still protected (see Figure 3.3.20).

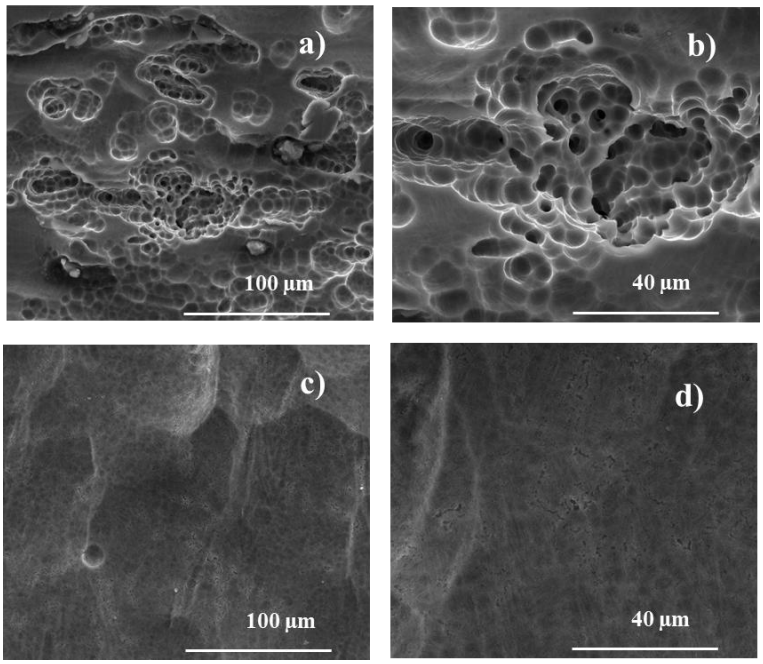

Figure 3.3.20 *SEM micrographs for a) and b) chemically etched and c) and d) anodized 3D Ti6Al4V samples after 1 week of immersion in simulated inflammatory conditions*

Ti ions release of about 35 µg cm^{-2} after 1 week of immersion in HBSS_IC, see Figure 3.3.21, is still under the threshold limit of 200 µg/cm^2/7 days granting biocompatibility of the plates [150–152] Al and V ions release is under the detection limits of the instruments. [153]

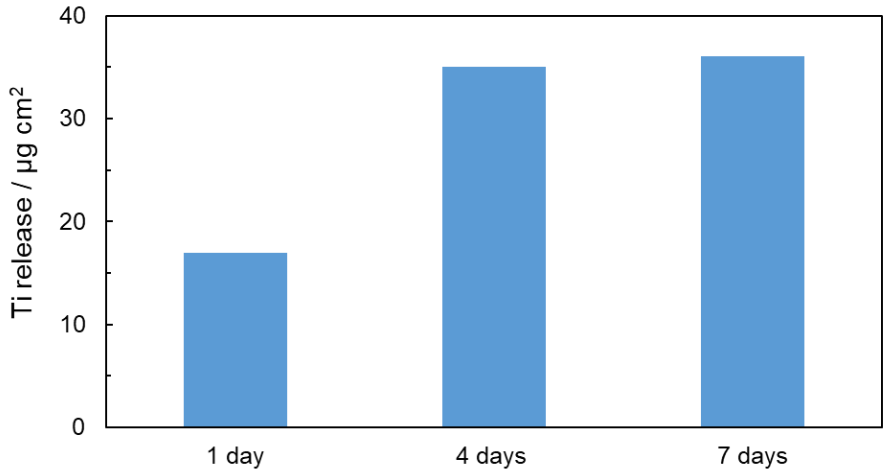

Figure 3.3.21 Titanium ion release from anodized sample after 1 week of immersion in HBSS_IC.

In summary, Ti6Al4V plates were fabricated by 3D printing using various scanning strategies. According to mechanical characterization and microstructure analysis, there was no significant impact on corrosion behaviour by changing the printing parameters. The mechanical characterization indicated reduced strength and ductility due to gas porosity (LED = 0.41 J/mm) and lack of fusion (LED = 0.11 J/mm). X-ray pattern confirmed that all printing parameters resulted in reflections of alpha phase, with beta phase present for those built at LED = 0.41 J/mm. SEM micrographs show unfused powder on the surface of as-built samples that could be effectively removed using chemical etching process in acidic aqueous solutions. Anodizing process in calcium acetate and beta-glycerolphosphate containing aqueous solution led to the formation of porous TiO_2 layers containing Ca and P. The latter is a n-type semiconductor with a very positive flat band potential according to its photoelectrochemical characterization. Corrosion resistance in both 3D printed surfaces was strongly influenced by chemical etching and anodizing treatments. Anodized samples were found to reduce the formation of metastable pits and debris detachment on the surface, resulting in enhanced corrosion resistance under aggressive conditions like those typical of inflammatory situations. Under inflammatory conditions, the anodic film effectively hinders localized corrosion phenomena, preventing the release of harmful products due to selective attack at edge melt pool areas. [153]

4 Zinc for biodegradable implants

4.1 Corrosion behaviour in physiological environment

Zinc, being one of the essential trace metals in human bodies, seems a promising candidate to realize biodegradable implants if compared to iron- and magnesium-based materials thanks to adequate corrosion rate in physiological environment. [36,51,52] In the last decades, several papers have been published trying to study the corrosion mechanisms of zinc in human body [36,57–60], but some aspects remain unclear. Indeed, zinc oxidation and dissolution can be strongly influenced by the composition, temperature, and hydrodynamic conditions of the environment, thus the role of the employed electrolytic solution selected to mimic a physiological environment is very important. It is widely known that a key factor affecting the corrosion behaviour of zinc is chloride ion concentration, since Cl^- induces localized corrosion. However, a role is also played by the other compounds present in the electrolyte, especially as concerns the complex nature of the (simulated) biological environments. The aim is to compare the corrosion behaviour of commercially pure Zn during immersion up to 4 weeks at 37 °C in different electrolytic solutions mimicking physiological environment, i.e. Hanks' Balance Salt Solution (HBSS), Dulbecco's modified Eagles' medium (DMEM) and DMEM with 10% of fetal bovine serum (DMEM + 10% FBS), see composition in Table 2. 1. Morphological characterizations, electrochemical tests, weight loss, and ion release measurements show that the corrosion mechanism is significantly affected by the physiological solution used.

For the experimental campaign, pure zinc (purity: >99.95 wt.%) were used. Prior to immersion test, the samples were chemically etched in 5% wt. nitric acid aqueous solutions for 30 seconds and then ultrasonically cleaned in acetone and distillate water for 10 min. Samples were used after 12 hours of exposure in air.

Plate samples (2 cm^2) were used for immersion tests. The ratio of the solution volume to the sample area was set as 20 mL cm^2 as reported in ASTM G3-72. Samples were put in 50 mL sterile centrifuge tubes with 40 mL of solution and incubated at 37 ◦C. The test periods were 1, 3, 7, 14, 21 and 28 days respectively. In order to remove corrosion product layer, the corroded samples were firstly cleaned in 100 g/L NH_4Cl for 5 min at 70°C according to ISO 8407:2009, and then washed by distilled water and dried to acquire the final weight.

To quantify hydrogen evolution evolved by cathodic reaction, zinc samples were immersed in different physiological solutions by using 250 ml glass bottles sealed with DURAN™ Bromobutyl Rubber Stopper. Hydrogen accumulated in the

bottle headspace were analyzed using a 500 µl Manual Gas Tight Syringes by an HP 6890 Series GC system equipped with a Supelco GC 60/80 CarboxenTM-1000 packed column and a thermal conductivity detector.

A schematic representation of the experimental setup is reported in Figure 4.1.1.

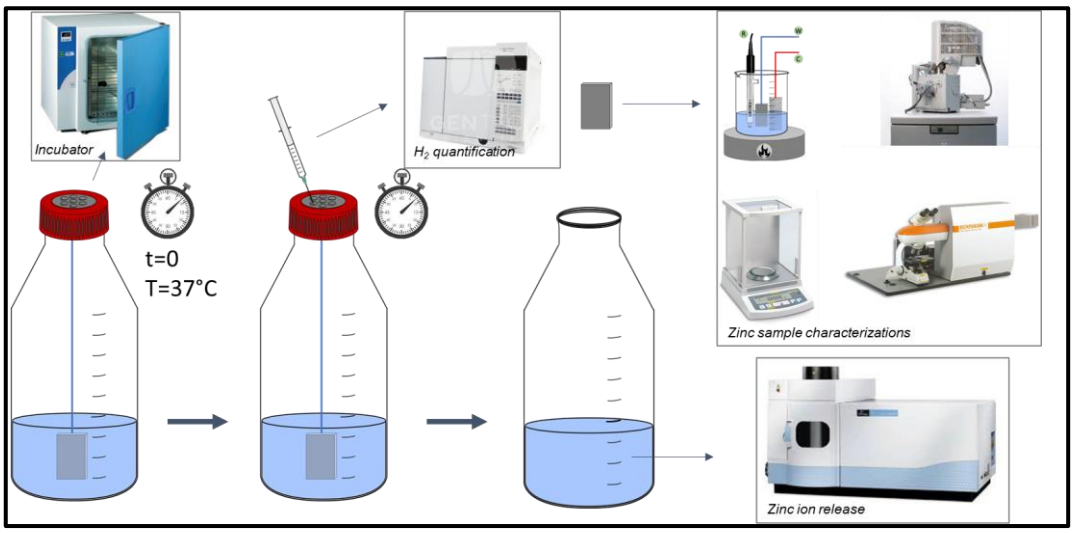

Figure 4.1.1 *Schematic representation of experimental campaign*

For indirect cytotoxicity tests (see Figure 4.1.2), sterile samples were incubated with Dulbecco's modified Eagle medium (DMEM, Sigma-Aldrich) at 37 °C for 24 h with a volume/surface ratio of 5 ml/cm^2. MC3T3-E1 preosteoblastic cells purchased from Sigma-Aldrich (ECACC) were cultured in DMEM added to 10% fetal bovine serum, 1% glutamine, and 1% antibiotic at 37 °C and in a 5% CO_2 atmosphere. Osteoblastic cells were seeded into Petri discs and incubated with normal DMEM at 37 °C and 5% CO2. After 24 h, the medium was replaced with treated media. The proliferation rate was evaluated using an optical microscope.

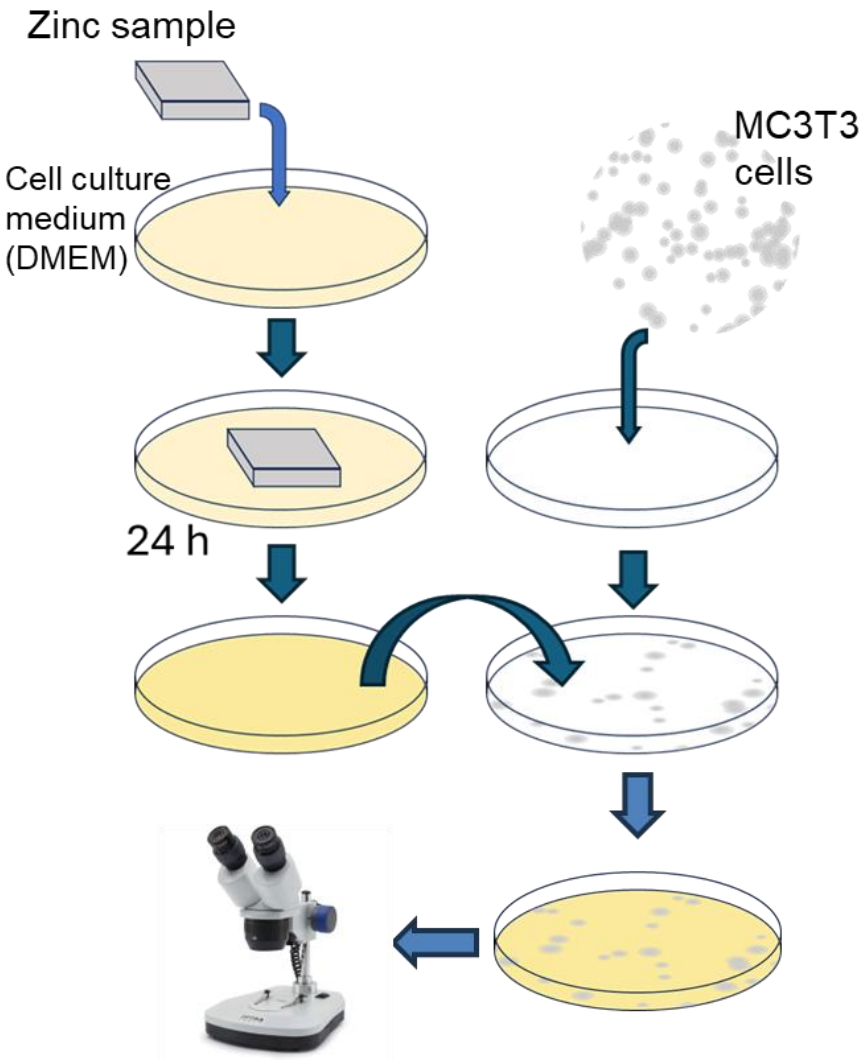

Figure 4.1.2 *Schematic representation of in vitro cytotoxic test.*

Zinc coupons were immersed at 37°C in physiological media. The surface morphology of zinc samples after immersion in different solutions are shown in Figure 4.1.3 and the corresponding EDX analysis in Figure 4.1.44. After 1 day of immersion, SEM micrographs and EDX analysis reveal the presence of corrosion products on samples immersed in HBSS, while they are not detected on samples immersed in DMEM and DMEM + 10% FBS (see Figure 4.1.3a-c).

EDX analysis reveals the presence of Ca and P on surface immersed to HBSS for 1 day (see Figure 4.1.4a). After 7 days of immersion, different morphologies are detected (see Figure 4.1.3g-i). In particular, intergranular corrosion was observed in DMEM and corrosion attacks affecting all the surface were detected for DMEM + 10% FBS. After 21 days of immersion, the sample exposed to HBSS is totally covered by corrosion products with lamellar shape (see Figure 4.1.3m), prevalently composed by Mg, P and Ca (see Figure 4.1.4c).

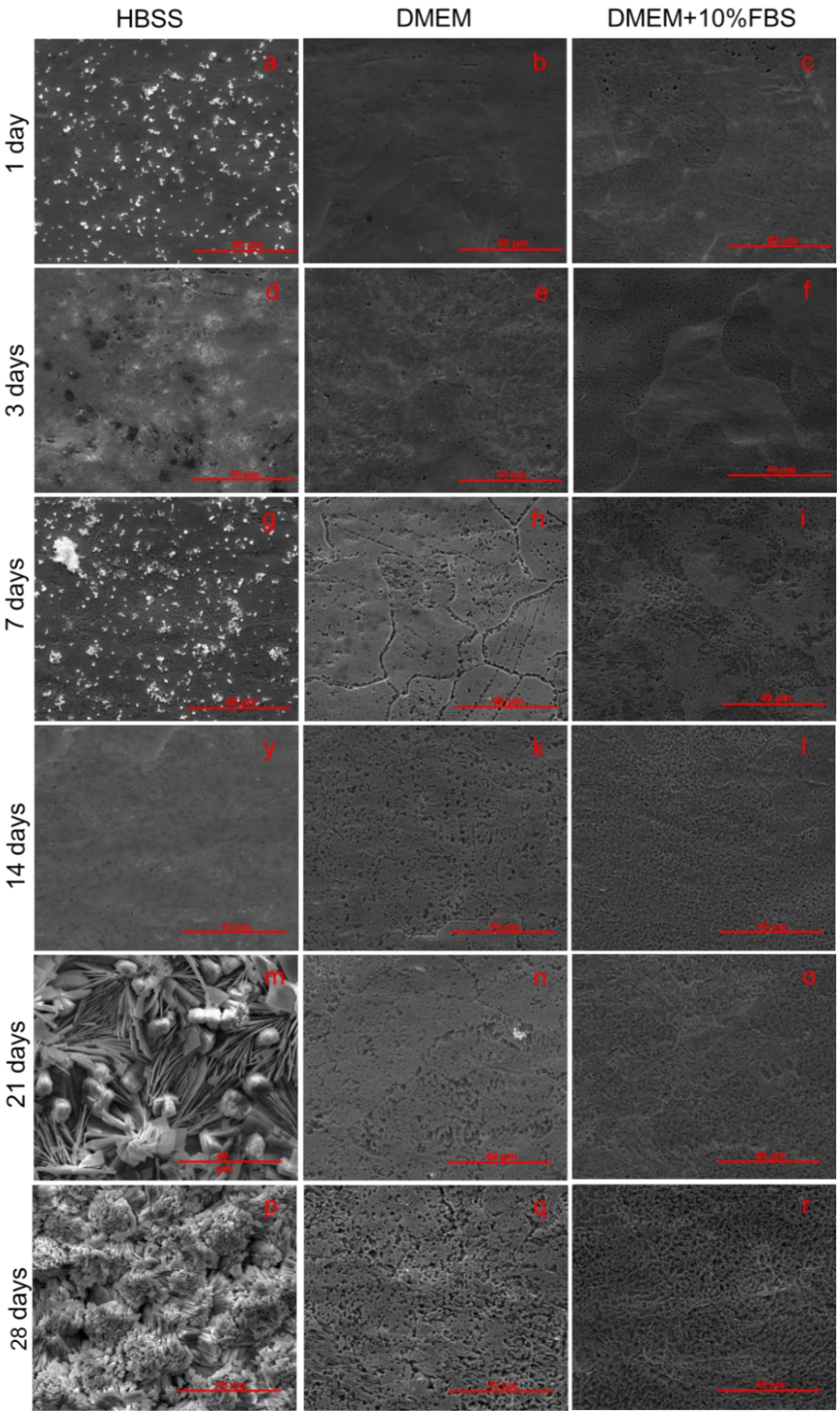

Figure 4.1.3 *SEM micrographs of Zinc samples after immersion in HBSS, DMEM and DMEM + 10% FBS*

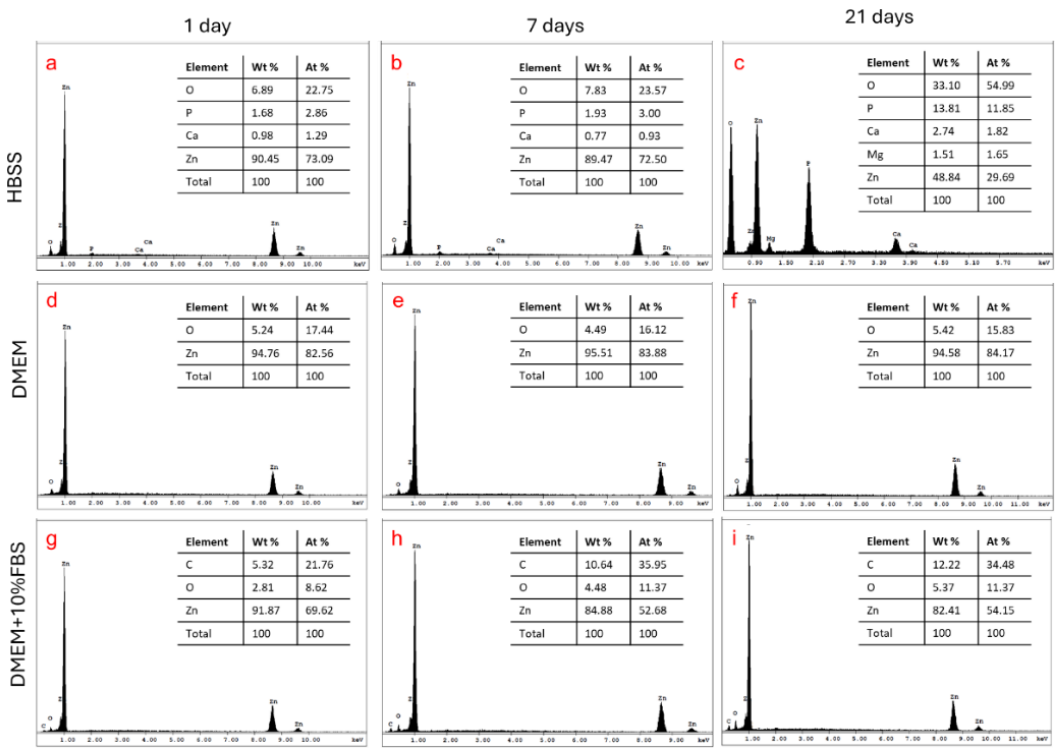

Figure 4.1.4 *EDX analysis of Zinc samples after 1 day, 7 days and 21 days of immersion tests in HBSS, DMEM and DMEM+FBS*

According to Raman spectra reported in Figure 4.1.5, these corrosion products mainly consist of zinc-calcium phosphates. According to the active Raman modes, hopeite ($Zn_3(PO_4)_2$), scholzite ($CaZn_2(PO_4)_2$) and tarbuttite (Zn_2PO_4OH) were identified. A band for hopeite in the Raman spectrum is observed at 940 cm^{-1} and is assigned to the v_1 PO_4 symmetric stretching mode. Other Raman bands are observed at 1150, 1059, 1000 and 995 cm^{-1} and are assigned to the v_3 PO_4 antisymmetric stretching modes. The Raman spectrum of tarbuttite shows an intense band centred at 965 cm^{-1} assigned to the v_1 symmetric stretching mode. The Raman spectrum of scholzite shows an intense band at 1000 cm^{-1} that is assigned to the v_3 antisymmetric stretching modes of the PO_4. A band is observed at 923 cm^{-1} with a second band at 935 cm^{-1}. These bands are assigned to the v_1 PO_4 symmetric stretching modes.[154–156]

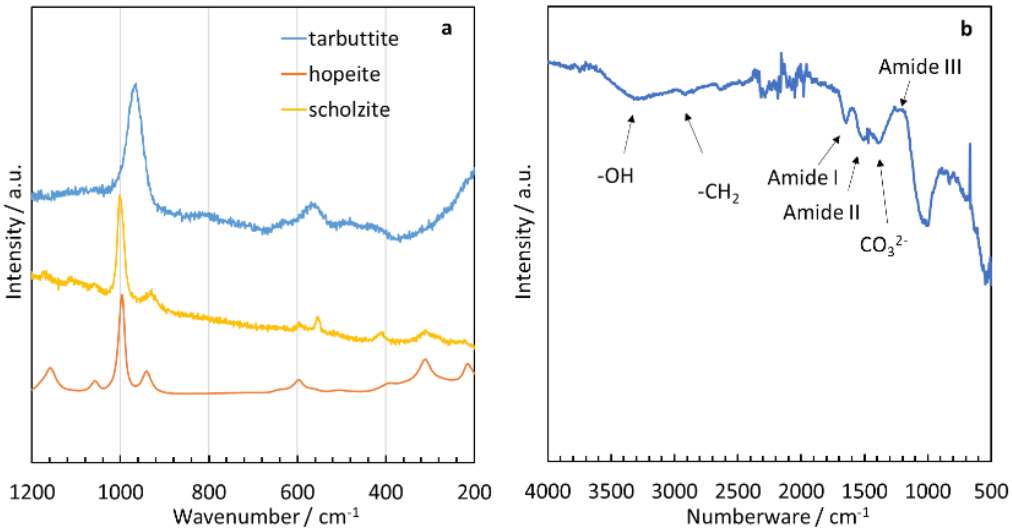

Figure 4.1.5 *a) Raman spectra related to zinc samples immersed in HBSS and b) FT-IR spectrum related to zinc sample immersed in DMEM + 10% FBS.*

EDX analysis shows a very high percentage of carbon for sample after immersion in DMEM + 10% FBS (see Figure 4.1.4g-i) if compared to HBSS and DMEM (see Figure 4.1.4a-f), due to adsorption of organic species. This hypothesis has been confirmed by recording FTIR spectrum for pure Zn immersed in DMEM + 10%FBS, reported in Figure 4.1.5b. Band located at 2900 cm^{-1} are related to stretching vibrations in C-H. Bands located at around 1650 cm^{-1}, 1550 cm^{-1}, and 1250 cm^{-1} correspond to Amide I (stretching vibrations of C═O and C—N groups), Amide II (N—H bending, C—N and the C—C stretching vibrations), and Amide III, respectively.[60] FTIR data therefore demonstrates adsorption of proteins on the surface of Zn after immersion in DMEM+FBS.

Figure 4.1.6 shows mass variation and corrosion rate for different immersion times and different physiological solution. Due to the presence of large amounts of corrosion products, positive mass variation was detected for zinc in HBSS, therefore a chemical surface treatment in ammonium chloride was carried out to selectively remove these compounds before checking the sample weight. After the removing of corrosion products, a mass loss is measured. The weight loss is significantly higher in HBSS as compared with DMEM w/o FBS. However, is interesting to note that the mass loss is almost independent on immersion time for HBSS. Indeed, the weight loss is not affected appreciably by immersion time, thus suggesting that the corrosion products (i.e. zinc-calcium phosphates) hinder the corrosion process. Indeed, the corrosion rate in HBSS is ~ 0.7 mg cm^{-2} day^{-1} but decreases to $1.8 \cdot 10^{-2}$ mg cm^{-2} day^{-1} after 4 weeks of immersion. Conversely, in the case of DMEM without and with 10% FBS there is an increase of the weight loss after 3 days of immersion, while it does not change appreciably for longer immersion time. The corrosion rate in DMEM w/o FBS is lower if compared to HBSS and decreases to $1.3 \cdot 10^{-2}$ mg cm^{-2} day^{-1} after 4 weeks of immersion. This does not mean that the corrosion process stops since the surface morphology of zinc

changes according to the SEM micrographs. It is likely that the corrosion becomes more localized thus not significantly contributing to total weight losses.

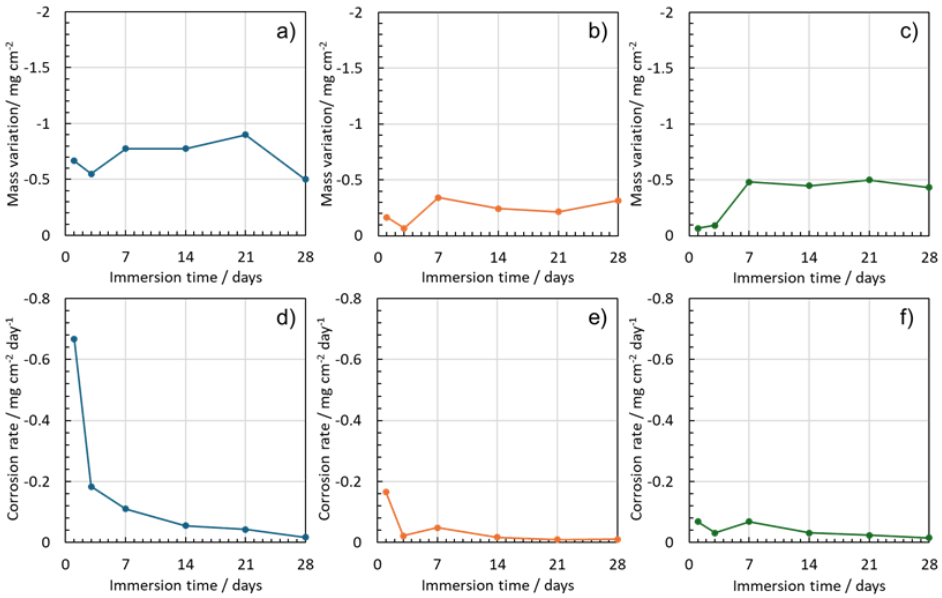

Figure 4.1.6 *Mass variation and corrosion rate of Zinc samples after different time of immersion tests in HBSS, DMEM and DMEM + FBS and after removing corrosion products.*

Figure 4.1.7 reports the concentration of zinc ions released during immersion in physiological media as a function of time, obtained by ICP-OES. The zinc ions released in HBSS are two orders of magnitude lower than that measured in DMEM and DMEM + 10% FBS, as expected due to the formation of thick corrosion products layers (conversion coating) on the surface of the metal with consequent zinc ions consumption. Moreover, the values measured in DMEM and DMEM + 10% FBS are almost independent on immersion time in agreement with the mass loss experiments.

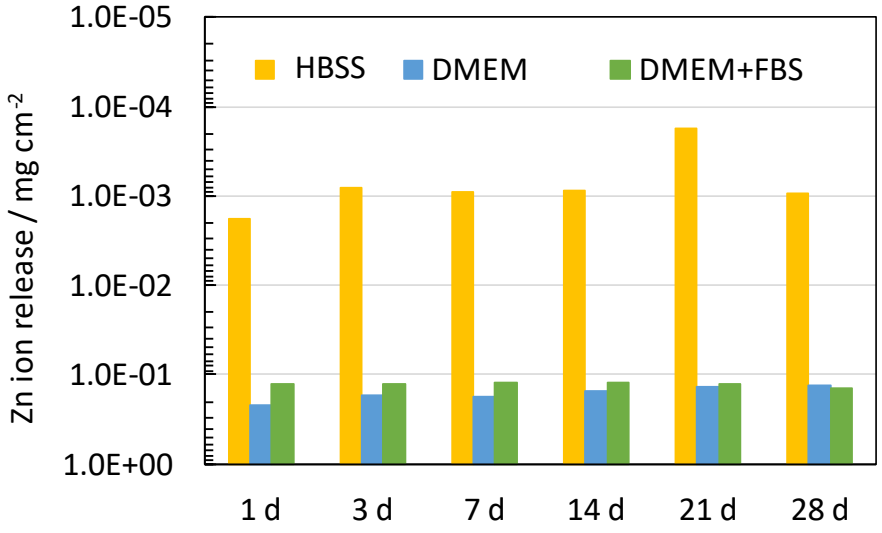

Figure 4.1.7 *Zinc ions release related to zinc samples after different time of immersion tests in HBSS, DMEM and DMEM + FBS*

In Figure 4.1.8, EIS spectra and polarization curves, recorded in different physiological solutions with and without oxygen, are shown. For EIS spectra recorded at OCP (open circuit potential) in presence of oxygen, the overall impedance measured in physiological solutions (blue lines) is about 400 Ω cm^2 in HBSS, 1100 Ω $cm^{2,}$ in DMEM and 4000 Ω cm^2 in DMEM+FBS (see Figure 4.1.8a-c). The highest overall impedance recorded in the case of DMEM + FBS can be explained considering the protein adsorption on the sample surface. In presence of oxygen, polarization curve recorded in DMEM + FBS (see Figure 4.1.8d-f), allows to estimate a corrosion current density, i_{corr}, lower than those recorded in HBSS and DMEM, in agreement with the results of EIS spectra. It is noteworthy to mention that a pitting potential of about - 0.8 V vs. SSC can be estimated for the immersion in all physiological solutions.

To better understand the corrosion mechanism with a specific focus on the cathodic reactions, EIS spectra and polarization curves were recorded in the same physiological solutions in a O_2-free atmosphere (see yellow lines in Figure 4.1.8).

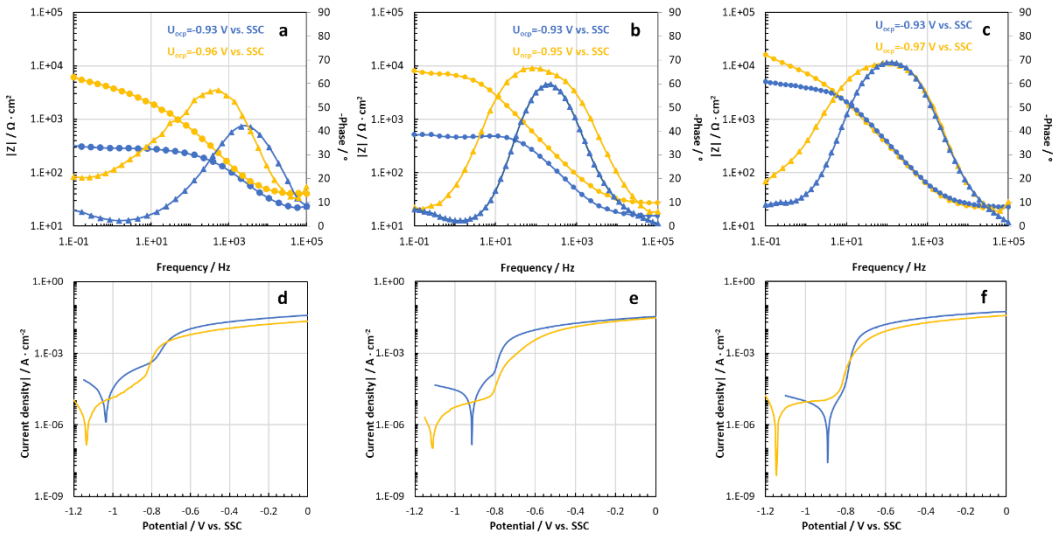

Figure 4.1.8 *EIS spectra, in Bode representation, recorded at corresponding Open Circuit Potential (U_{ocp}) and polarization curves in different solution at 37°C with oxygen (blue lines) and without oxygen (yellow lines) after immersion of 1h.*

In EIS spectra, the overall impedance measured in O_2-free atmosphere is higher than that measured in O_2-containing atmosphere in all physiological solutions. More specifically, in HBSS and DMEM the overall impedance is at least one order of magnitude higher in O_2-free atmosphere with respect to O_2-containing atmosphere, while in the case of DMEM+FBS solution it is about three times higher.

The polarization curves recorded in O_2-free atmosphere show a corrosion potential E_{corr} shifted in cathodic direction with respect to O_2-containing atmosphere, while the pitting potential is the same. The estimated corrosion current densities i_{corr} in O_2-free atmosphere are lower with respect to O_2-containing atmosphere and it is noteworthy to mention that i_{corr} does not change by changing

the physiological solutions. These results allow to highlight that oxygen reduction reaction (ORR) is the main cathodic process, as has been previously reported in literature [157–159]. To further support this conclusion, hydrogen quantification was carried out using GC as described before. After 28 days of immersion in all physiological solutions, the amount of evolved hydrogen is below GC detection limits, suggesting that HER as cathodic process is negligible.

To have information about the corrosion resistance of zinc sample as a function of immersion time, electrochemical measurements were carried out up to 4 weeks in different physiological solution at 37°C. Open circuit potential were measured for 30 minutes before checking the final corrosion potential, see Figure 4.1.9.

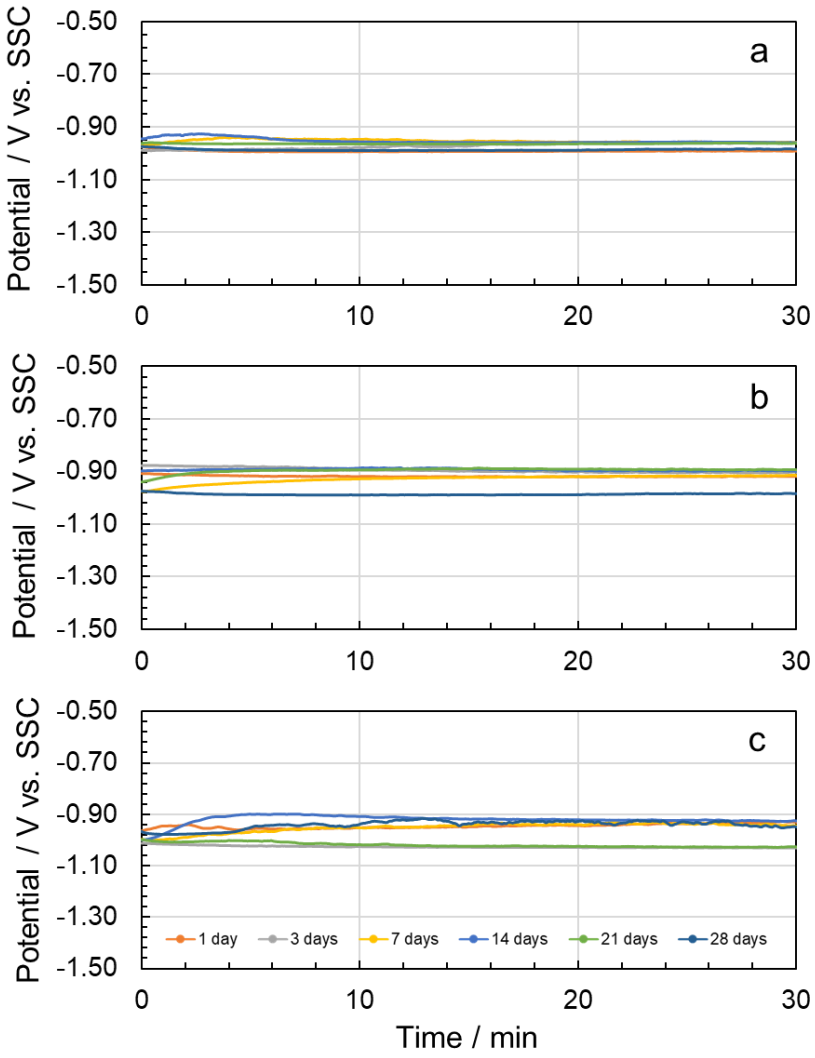

Figure 4.1.9. *Open circuit potential measurements related to zinc sample in a) HBSS, b) DMEM and c) DMEM+FBS as a function of immersion time*

In Figure 4.1.10a-f, EIS spectra in Bode representation, recorded in different solutions as a function of immersion time are reported.

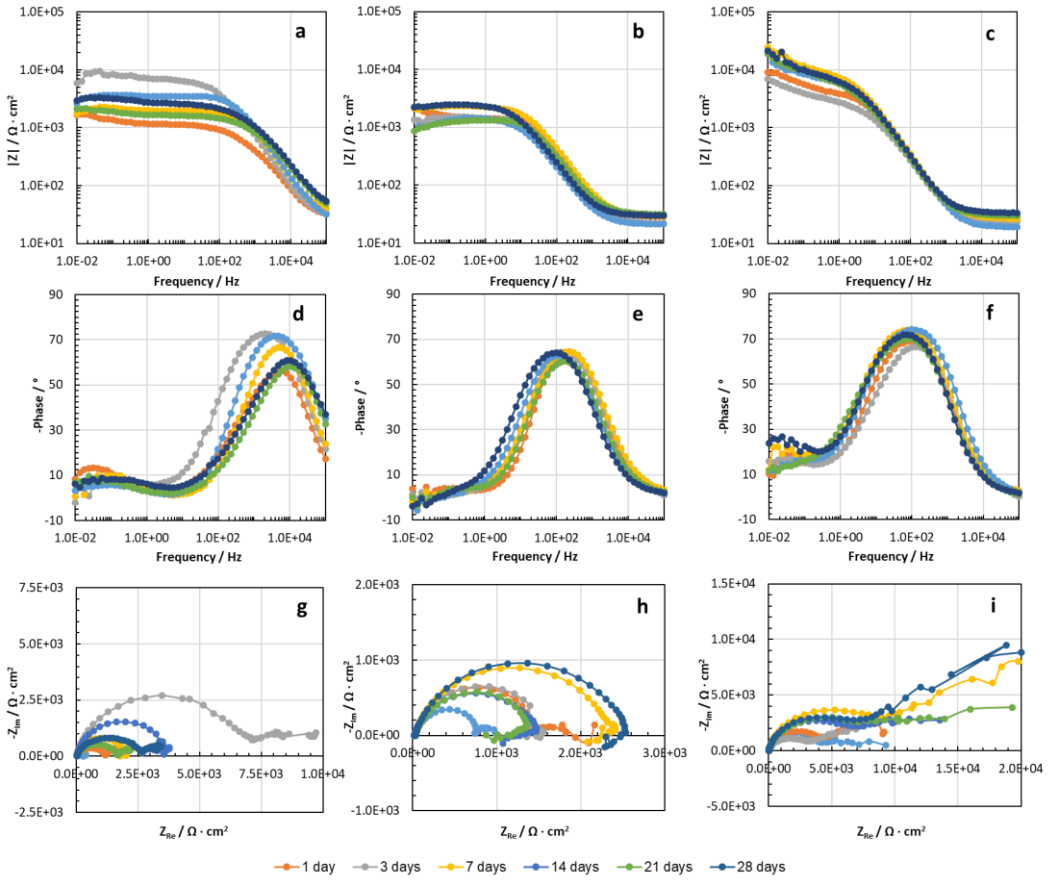

Figure 4.1.10 *EIS spectra, in Bode and Nyquist representation, recorded at corresponding Open Circuit Potential in a, d, g) HBSS, b, e, h) DMEM and c, f, i) DMEM+FBS at 37°C after different time of immersion tests.*

The overall impedance recorded for samples immersed in HBSS increases during the first week of immersion (from $4 \cdot 10^2$ to $8 \cdot 10^3$ Ω cm^2), while after 1 week of immersion, the overall impedance remains almost constant. This finding can be explained by the growth of the corrosion products layer, whose presence was highlighted by SEM micrographs). As evident in the Nyquist representation, since the early stage of immersion the spectra recorded in HBSS show a high frequency capacitive loop followed by a portion of a lower frequency loop. Notably, the size of the latter is not appreciably affected by the immersion time. Conversely, the high frequency capacitive loop has a diameter that increases up to 3 days of immersion, reaching a lower value for higher immersion time.

A slightly different behaviour is shown by Zn in DMEM solution. Indeed, the overall impedance is about 1100 Ω cm^2 at the beginning of the test and changes in a narrow range for 4 weeks (i.e. between $1.4 \cdot 10^3$ and $2.4 \cdot 10^3$ Ω· cm^2). However, immersion time has a significant influence on the shape of the EIS spectrum as better evident in their Nyquist representation. Indeed, soon after immersion in DMEM the spectrum shows a high frequency capacitive loop followed by a portion of a lower frequency loop, while after the first day of immersion a high-frequency capacitive loop coupled with a low-frequency inductive loop is evident.

When fetal bovine serum is added to this solution, the impedance is higher and ranges between $6 \cdot 10^3$ and $1.6 \cdot 10^4$ $\Omega \cdot cm^2$ during the immersion up to 4 weeks. In this solution, since the early state of immersion the spectra show a high frequency capacitive loop followed by a portion of a lower frequency loop.

The EIS spectra can be rationalized in the frame of kinetic models for reaction involving the formation of an adsorbate intermediate and its successive oxidation, as detailed explained in ref [160]. Kinetic models are superior to the use of electrical circuit analogues because the same model can account for different behaviour shown by the metal as a function of the electrolyte composition. Zinc oxidation is a two-step reaction occurring with the formation of an adsorbate intermediate (Zn^+_{ads}) and its successive oxidation to Zn^{2+} according to the following scheme (ref. [159]):

$$Zn \overset{K_1}{\rightarrow} Zn^+_{ads} + e^- \qquad \text{(eq. 4.1.1)}$$

$$Zn^+_{ads} \overset{K_2}{\rightarrow} Zn^{2+} + e^- \qquad \text{(eq. 4.1.2)}$$

Assuming that the adsorption of reaction intermediate Zn^+_{ads} obeys a Langmuir isotherm [159], the corresponding faradic impedance is a function of k_1 and k_2, of the Tafel slope for both electron transfer steps and of the surface coverage. The relation providing the equivalent impedance is:

$$Zn^{-1} = R_t^{-1} + \frac{A}{j\omega + B} \qquad \text{(eq. 4.1.3)}$$

where R_t, A and B depend on the above cited parameters. The equivalent circuit corresponding to this impedance can be different depending on kinetic parameters including the surface coverage, and can be represented as follows:

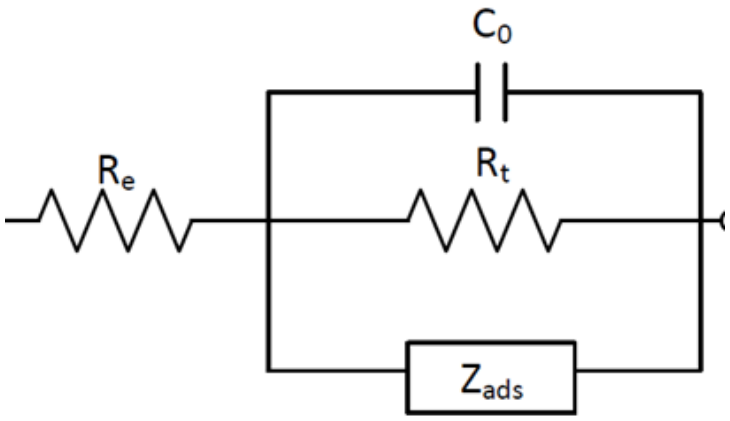

Figure 4.1.11 *Equivalent electrical circuits (EECs) used to model the electrochemical behaviour of zinc sample after immersion in different physiological solution.*

where adsorption impedance, Z_{ads}, is expressed as:

$$Z_{ads} = \frac{j\omega+B}{A} \qquad \text{(eq. 4.1.4)}$$

When A = 0, the faradaic impedance reduces to $Z_F = R_t$ and the interfacial impedance only exhibits one time constant. When A < 0, the interfacial impedance shows two capacitive semicircles and when A > 0, the interfacial impedance has a high-frequency capacitive loop and low-frequency inductive loop such that the low-frequency limit for the capacitive loop is $R_e + R_t$. For all values of A, the same expression provides the low-frequency limit for the impedance [160]. Equation (4.1.4) is a mathematical expression that cannot be expressed as an equivalent circuit with defined passive elements when A < 0, while when A > 0 it is possible to fit the spectra with the electrical circuit reported in Figure 4.1.11 where Z_{ads} corresponds to an inductance in series with a resistance (see Table 4.1.1).

	R_e [Ω cm^2]	Q_o [μS s^n cm^{-2}]	n	R_t [Ω cm^2]	L [H cm^2]	R [Ω cm^2]
3d	22	1.46E-05	0.84	8.34E+03	1.69E+02	1.79E+03
7d	30	9.2E-06	0.85	3.39E+04	3.02E+05	2.33E+03
14d	22	2.2E-05	0.84	5.1E+03	1.02E+04	1.50E+03
21d	33	8.6E-06	0.9	4.97E+03	1.11E+04	1.40E+03
28d	30	1.8E-05	0.84	1.87E+03	2.04E+05	2.49E+03

Table 4.1.1 *Fitting parameters related to the impedance spectra recorded in DMEM*

Polarization curves were also recorded after different immersion times in all physiological solutions around the open circuit potential (see Figure 4.1.12).

The i-V curves are independent of the immersion time for DMEM, while a shift of the corrosion potential is evident for HBSS and DMEM + FBS. Notably, in the latter case a low and constant passivity current is measured in the anodic branch up to the pitting potential (-0.8 V(Ag/AgCl)).

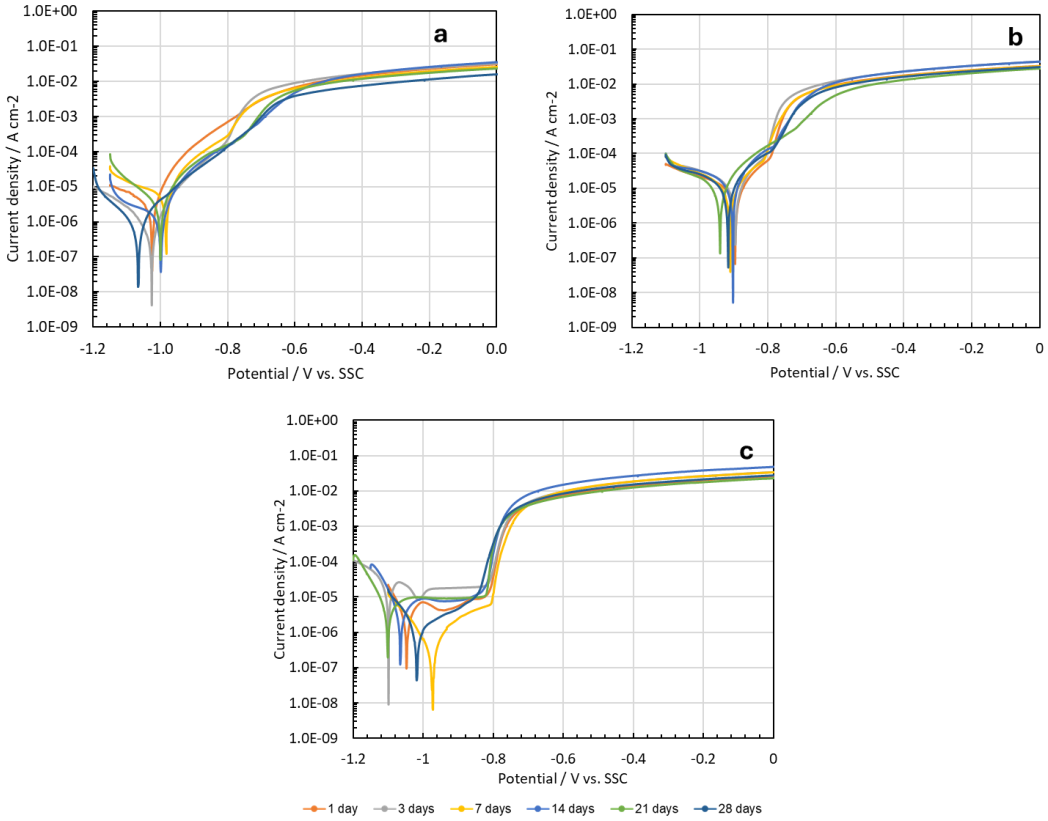

Figure 4.1.12 *Polarization curves recorded in a) HBSS, b) DMEM and c) DMEM+FBS after different time of immersion tests.*

The results obtained considering surface morphologies characterization, electrochemical tests, mass variation test and ions release show that the corrosion mechanism for zinc immersed in different physiological solutions changes significantly. In general, the results show generalized corrosion for samples immersed in HBSS with the formation of a corrosion product layer of the surface. The samples immersed in DMEM and DMEM + 10% FBS show different localized corrosion without the formation of a corrosion product layer and a higher zinc ion release, see Figure 4.1.3 and Figure 4.1.7.

The values estimated by ICP-OES are lower than that estimated by the mass losses, which is expected for HBSS due to generalized corrosion with formation of a chemical conversion coating. In the case of DMEM and DMEM+FBS this finding can be explained by precipitation phenomena that reduce the Zn^{2+} ion concentration in solution due to the formation of Zinc oxide and/or hydroxide. The cross check of mass losses and ICP ion release allows to get a reliable estimation of the zinc release rate and of the metal corrosion rate, crucial for the design of shape and thickness of biodegradable implants as a function of the composition of the electrolyte. According to the experimental findings, it seems that after 3 days of immersion, independently from the physiological solution where the tests are carried out, the mass loss and the ion release become almost constant, suggesting that the zinc corrosion rate is very low. However, the electrochemical tests and the information provided by morphological investigation as a function of time clearly show that the

corrosion process is different in the investigated physiological solutions. In HBSS solution a thick zinc-calcium phosphate layer grows on the surface of the metal hindering further degradation process. Indeed, during the initial immersion, the anodic reaction is zinc dissolution and the dominant cathodic reaction is oxygen reduction. Zn^{2+} ions can react with ions such as HCO_3^- and HPO_4^- to form a less soluble corrosion product that deposits on the surface, with an increase of corrosion resistance, essentially constituted by hopeite ($Zn_3(PO_4)_2$), scholzite ($CaZn_2(PO_4)_2$) and tarbuttite (Zn_2PO_4OH). According to the measured mass losses, after the first day of immersion there is an initial mass loss in the order of 1 mg cm^{-2} corresponding to a thickness reduction of 1.4 μm. But due to the presence of these compact corrosion products, further thinning of the metal is almost negligible. When Zn is immersed in DMEM, there is no evidence of formation of this layer, due to the lower concentration of phosphate ions as well as due to complexation of Zn ions by amino acids, e.g. L-Cysteine [61]. The SEM images show the occurrence of localized corrosion but, since open circuit potential is lower that the pitting potential, it is likely that localized intergranular corrosion occurs. Despite the different corrosion behaviour, also in this solution the degradation rate becomes almost constant after the first days of immersion, probably because the mass loss is lower due to the occurrence of localized corrosion making mass changes less appreciable. For pure zinc samples this type of mechanism is not related to the presence of metallic impurities but to a crystalline type attack. [161]The real surface is not atomically flat and homogenous, but it contains in general many defects such as dislocations, vacancies and grain boundaries. The grain boundaries are locations where the atoms are less solidly bound and are preferentially attacked. The addition of 10% of Fetal Bovine Serum (FBS) reduces intergranular attack probably due to the adsorption of proteins of the zinc surface that uniformly cover the metal. In any case, in DMEM without and with FBS the corrosion rate is even lower than that measured in HBSS and becomes negligible after the 1 – 3 days of immersion.

The results of this study demonstrate that significantly different corrosion behaviour of pure Zn is observed in the here used three different simulated physiological solutions; not only as concern the corrosion rate but moreover also the corrosion mechanisms. Therefore, the choice of the electrolyte for studying biodegradation of Zn is crucial and should be carefully considered in view of best simulating the true biological environment. Moreover, and noteworthy, in all physiological solutions here studied, corrosion is drastically slowed down after only few days immersion, becoming almost negligible after initial burst of dissolution. This raises questions on the suitability of zinc for biodegradable implants, even before assessing its biocompatibility.

Finally, we investigated the cytotoxicity of zinc samples as possible material for biomedical applications. Cytotoxicity tests were carried out in vitro using the preosteoblastic cell line, MC3T3-E1. Cell culture was carried out using media derived from incubation with zinc samples for 24 h at an established volume/surface ratio.

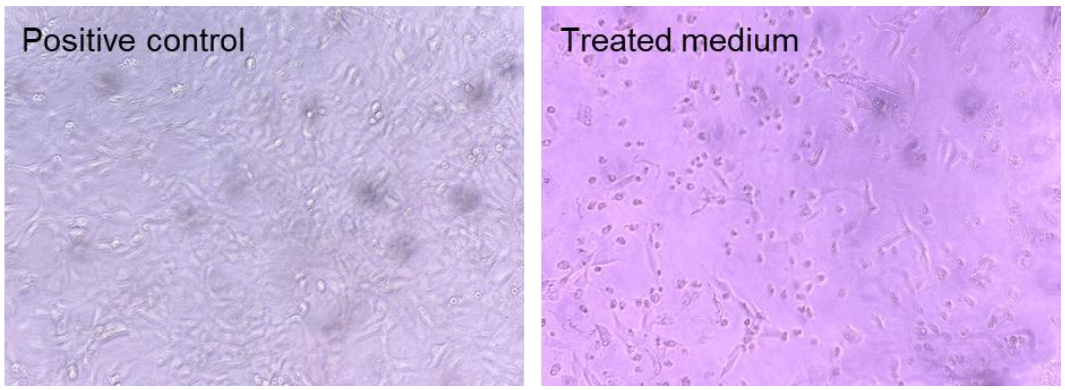

Figure 4.1.13 *Optical micrographs of osteoblast cells*

Optical micrographs (see

Figure 4.1.13) shows that the viability of the cells grown with the incubated media was abundantly down 70% with respect to the control viability, thus confirming the cytotoxicity of the tested materials, according to the followed ISO standard.[162]

In summary, corrosion behaviour of zinc samples was investigated in different physiological solutions, namely HBSS, DMEM and DMEM + 10 % FBS, as function of immersion time. The results obtained considering surface morphologies characterization, electrochemical tests, mass variation test and ions release, show that the corrosion mechanism for zinc samples changes significantly by changing the physiological solutions. Samples immersed in HBSS show generalized corrosion with the formation of a corrosion product layer on the surface while those immersed in DMEM and DMEM + 10%FBS show corrosion without the formation of a corrosion product layer and consequently a higher zinc ion release. The presence of a high concentration of phosphate ions in HBSS, the chelating action towards zinc ions of amino acids in DMEM and DMEM + 10% FBS, combined with a lower buffering action with respect to HBSS, can explain this different behaviour.

Electrochemical characterizations and hydrogen quantification test reveal that HER as cathodic process in Zn corrosion is negligible.

In vitro tests confirm the cytotoxicity effect of zinc sample for osteoblast cells.

4.2 Surface functionalization for tuning wettability and hindering biofouling

Having evaluated the potential cytotoxic effect of zinc used for biomedical applications in the physiological environment, the aim of this chapter is to optimise surface treatments to improve the corrosion resistance of zinc in the physiological environment. Among surface modification techniques, chemical conversion has advantages such as low cost, rapid coating production, adaptability for uneven surfaces and for very complex shape, and minimal impact on the mechanical properties of the metallic substrate.

In addition, chemical grafting of functional hydrophobic molecules, minimizing the direct contact of metals with corrosive media, has been proven effective in reducing initial corrosion rates by preventing corrosive ions from reaching the surface.

Polydimethylsiloxane is known for its strong hydrophobic properties, which prevent ion penetration, thereby protecting the metal substrate from corrosive media. This method not only enhances surface stability but also contributes to a prolonged resistance against degradation or chemical attacks in environments that expose metallic components.

The effect of surface treatment on corrosion resistance of Zn substrates was evaluated at each preparation step using potentiodynamic polarization measurements, electrochemical impedance spectroscopy, ions release after immersion on physiological media.

For the experimental campaign, pure zinc substrates were used to deposit the rough $ZnSn(OH)_6$ coating. The $ZnSn(OH)_6$ coatings were grown by chemical conversion process in a stannate-ion-containing aqueous medium at 82 °C for 30 min. The chemical composition of the bath is presented in Table 4.2.1.[163]

Bath composition	**Concentration (g L^{-1})**
NaOH	10
$K_2SnO_3 \cdot 3H_2O$	50
$NaC_2H_3O_2 \cdot 3H_2O$	10
$Na_4P_2O_7$	50

Table 4.2.1 *Composition of the electrolyte for the chemical conversion process.*

Zn specimens after deposition of $ZnSn(OH)_6$ were used as substrates for the grafting of PDMS (polydimethylsiloxane). The PDMS-coated surfaces were prepared by horizontally placing these substrates in a glass Petri dish and covering them with approximately 20 μL/cm² silicone oil (PDMS), which was then pipetted onto the entire surface. Subsequently, these samples were illuminated using a 1 kW

ultraviolet lamp at working distance of 30 cm for about 30 minutes. After this treatment, the remnant ungrafted PDMS oil on the surfaces was removed by dissolving it in toluene.

The corrosion resistance was evaluated by electrochemical measurements and by the respirometry approach. A schematic representation is shown in Figure 4.2.1.

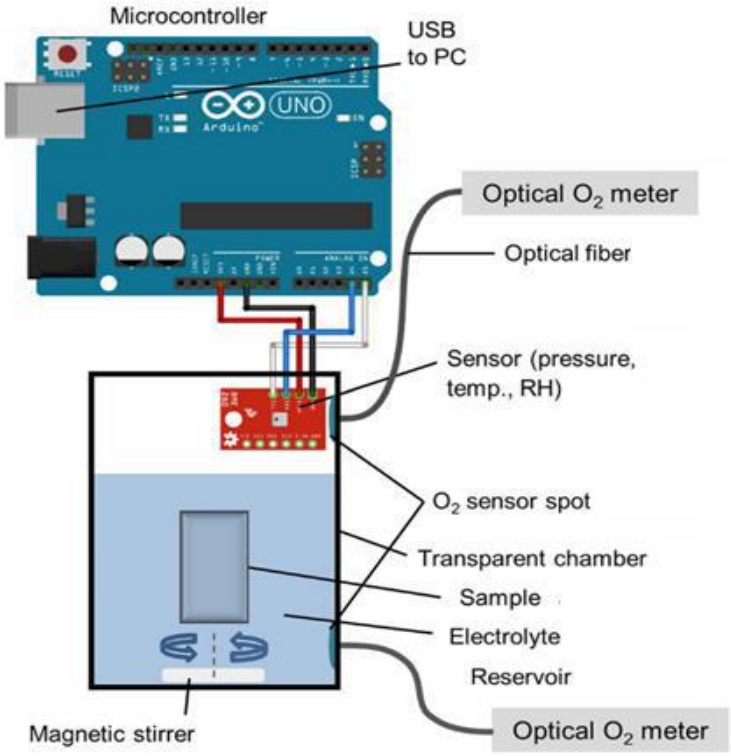

Figure 4.2.1 *Respirometric immersion setup with oxygen measurements in both liquid and gas phases.*

The total pressure was monitored with a digital pressure. The H_2 partial pressure was derived, and the O_2 partial pressure was measured with an optical O_2 meter. The solution was stirred at 200 rpm to enable gas exchange between the gas and liquid phases. The presence of H_2 was verified *via* an amperometric H_2 microsensor. A manometric closed setup was used with an electrolyte volume of around 90 mL at room temperature, and the samples have an area of ~8 cm^2. Hanks' solution at pH of 7.4 was used as an electrolyte. To perform the respirometric measurements, the hydrogen carbonate was omitted due to the CO_2 formation during its buffering effect, which affected the total pressure measurement.

Immersion tests were performed in different simulating solutions at 37 °C as Hanks' solution (HS), Dulbecco's modified eagles' medium (DMEM), and DMEM with 10 % of fetal bovine serum (DMEM+FBS) for 1 week. To reduce bacterial growth, 1 % of penicillin-streptomycin was added to the simulating solutions. To estimate the Zn and Sn release in solution, samplings were carried out for each type

of solution after 1, 4, and 7 days and diluted 1:10 with 2 wt.% nitric acid aqueous solution. A PerkinElmer Optima 2100 DV was used for ICP–OES analysis.

To have information about the biotoxicity assessment of coated Zn surfaces, *Escherichia coli* (*E. coli*, DH-5alpha) expressing cytoplasmic green fluorescent protein (GFP) were generated using the pGLO bacterial transformation kit (Bio-Rad, Feldkirchen, Germany). The stock culture was generated from an agar stock plate, from which one or two colonies were transferred to a growth medium. All cultures were incubated overnight at 37 °C in 5 mL of Tryptic Soy Broth growth medium (Becton Dickinson, Heidelberg, Germany) and kept shaking continuously in an orbital shaker at a speed of 150 turns min^{-1}. The concentration of bacteria was measured using UV-Vis spectroscopy at a wavelength of 600 nm wavelength (OD_{600nm}) compared to pure medium (control) and calculated according to the equation: 1.00 OD_{600nm} = 8 × 10^8 CFU mL^{-1}.[164] Bare and coated Zn specimens (15 × 15 mm) were immersed in a diluted GFP-expressing *E. coli* bacteria suspension in 0.5 vol.% L-arabinose at an optical density of ~ 0.30 for 24 h at 37 °C. Material samples for all surfaces were mounted in a 10 cm cell culture dish and immersed in 30 ml LB medium (Carl Roth, Karlsruhe, Germany). After 24 h, the bacteria suspension was removed and specimens were washed three times with PBS, followed by imaging at least four positions per specimen and 3 - 4 individual specimens per condition. Image stacks (368 × 368 × 22 μm with a voxel size of 0.7 × 0.7 × 2 μm) were acquired at each position using fluorescence microscopy and confocal reflection microscopy. All specimens were imaged using an upright laser scanning confocal microscope system (Leica, SP5) with a 20x/1.0NA dip-in objective lens. Image stacks were maximum projected using Python-based image processing. From these images, the bacteria-covered areas were segmented based on the local fluorescence image intensity relative to the overall fluorescence intensity. "[9]

Figure 4.2.2 presents schematically the formation process of UV-grafted PDMS on Zn surfaces after chemical conversion coating.

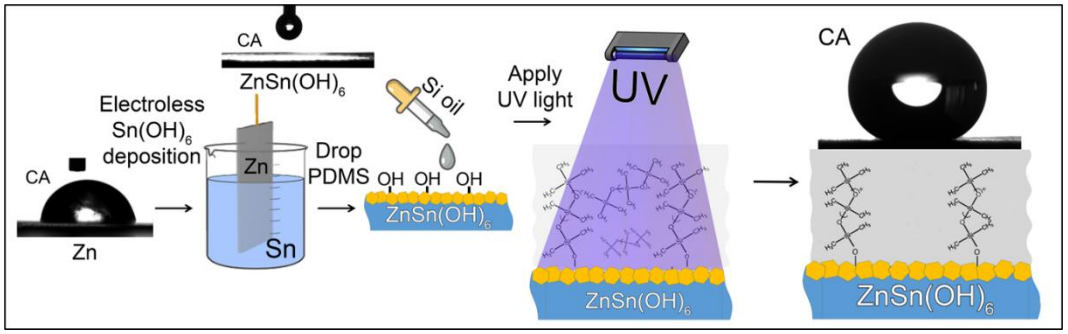

Figure 4.2.2 *Schematic representation of the PDMS-coated $ZnSn(OH)_6$ formation process.*

Zn substrates were etched in a 5 wt.% nitric acid aqueous solution to remove native oxide before surface treatments. The water contact angle (WCA) shown in Figure 4.2.2 is 85.3° ± 3.0° for pure zinc and is below the detection limit of the

goniometer, *i.e.*, superhydrophilic surface, after chemical conversion. Figure 4.2.3 SEM micrographs and EDS analysis of zinc sample after chemical conversion.

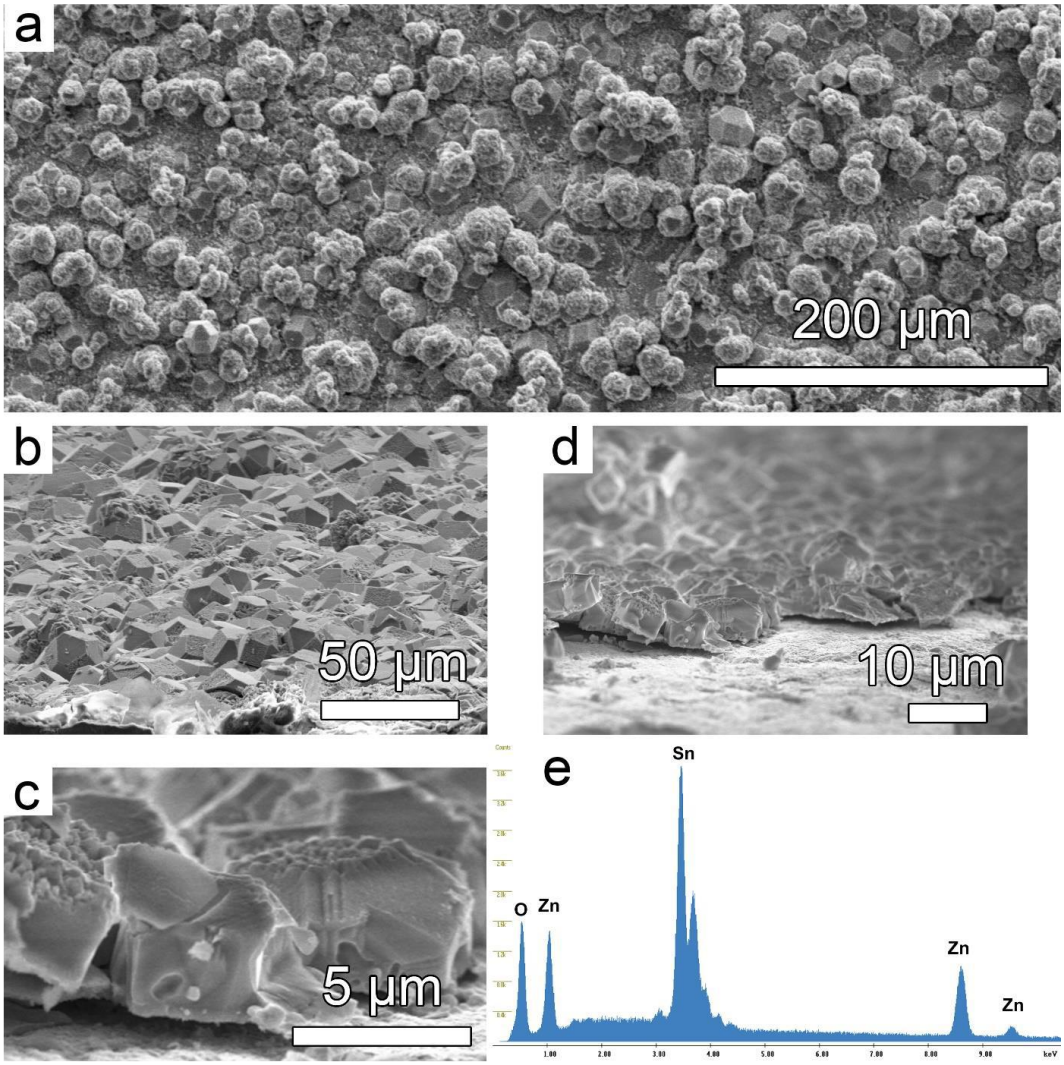

Figure 4.2.3 *Top-, tilted-view, cross-sectional SEM images and corresponding EDS spectrum of the $ZnSn(OH)_6$ samples.*

Figure 4.2.3 shows that the samples are covered by in a coating composed of truncated octahedrons thickness of 6 - 15 μm.

After chemical conversion process, polydimethylsiloxane (PDMS, silicone oil) was UV-grafted to reduce the surface wettability and thus improve corrosion resistance. [165–167] The UV-grafting process is simple, versatile, highly specific, and non-destructive, *i.e.* the morphology conversion coating is preserved (see Figure 4.2.4).

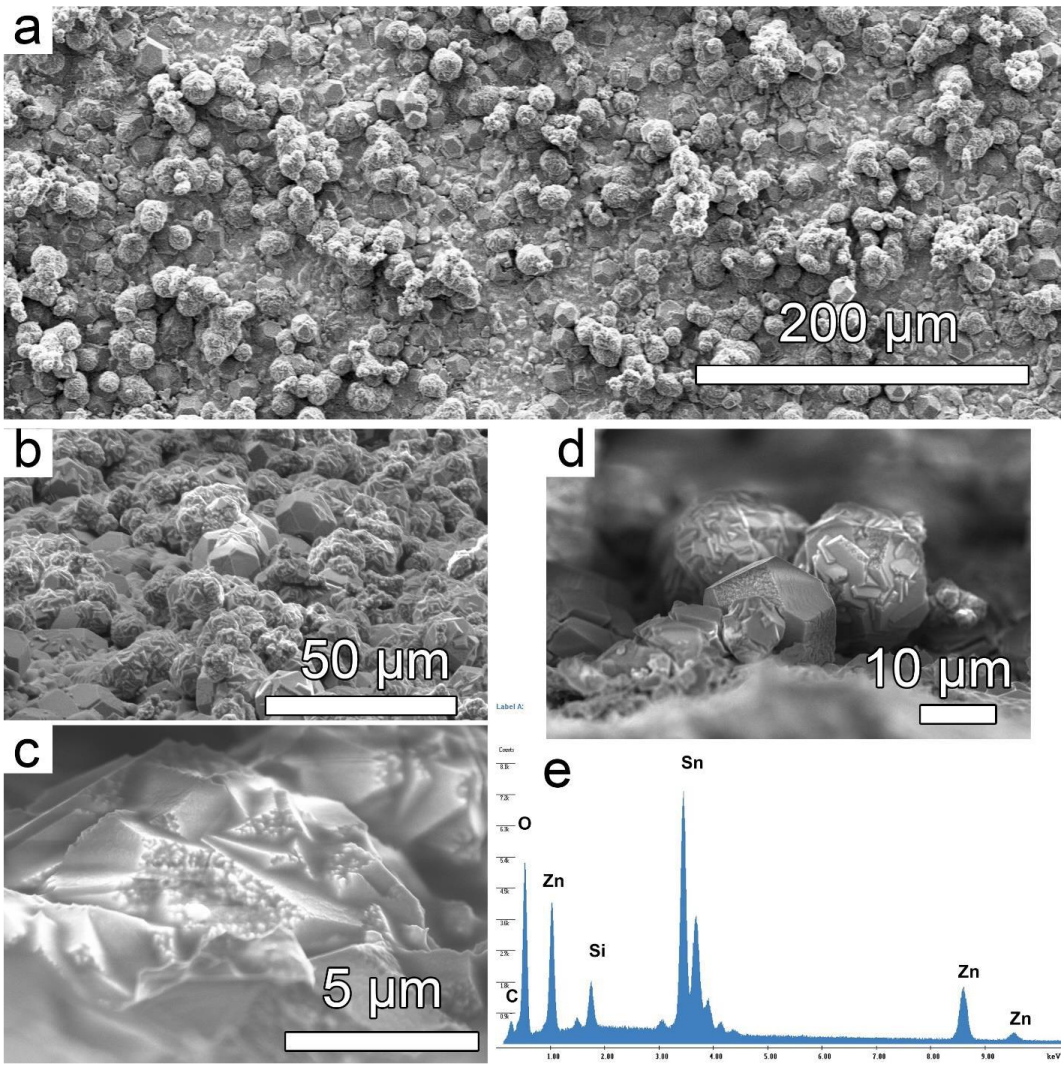

Figure 4.2.4 *Top-, tilted-, cross-sectional SEM images and corresponding EDS spectrum of the $ZnSn(OH)_6$/PDMS samples.*

Silicone oil was deposited onto the surface, followed by exposure for 30 minutes to UV light by using a Hg lamp with a peak wavelength of 320 nm. According to DFT (Density Functional Theory) calculations, the cleavage of the PDMS molecule is specific and occurs at the trimethylsiloxane terminal groups. This led to the application of an UV-grafting step involving silicone oil onto superhydrophilic $ZnSn(OH)_6$ surfaces. [168] The UV-grafting process of PDMS results in the formation of a layer with a thickness of ~9 nm. The grafting of PDMS onto $ZnSn(OH)_6$ surfaces was confirmed by scanning electron microscopy and EDS analysis, see in Figure 4.2.4.

The apparent water contact angle (WCA) for the $ZnSn(OH)_6$/PDMS samples shown in Figure 4.2.2 was measured to be 161.4° ± 5.4°, indicating superhydrophobic behaviour. This measurement suggests that the surface properties of the treated specimens are highly hydrophilic.

Attenuated total reflectance Fourier-transform infrared (ATR-FTIR) analysis was carried out on Zn, $ZnSn(OH)_6$, and $ZnSn(OH)_6$/PDMS substrates. The FTIR spectra in the wavenumber range of 250 - 3500 cm^{-1} are shown in Figure 4.2.5.

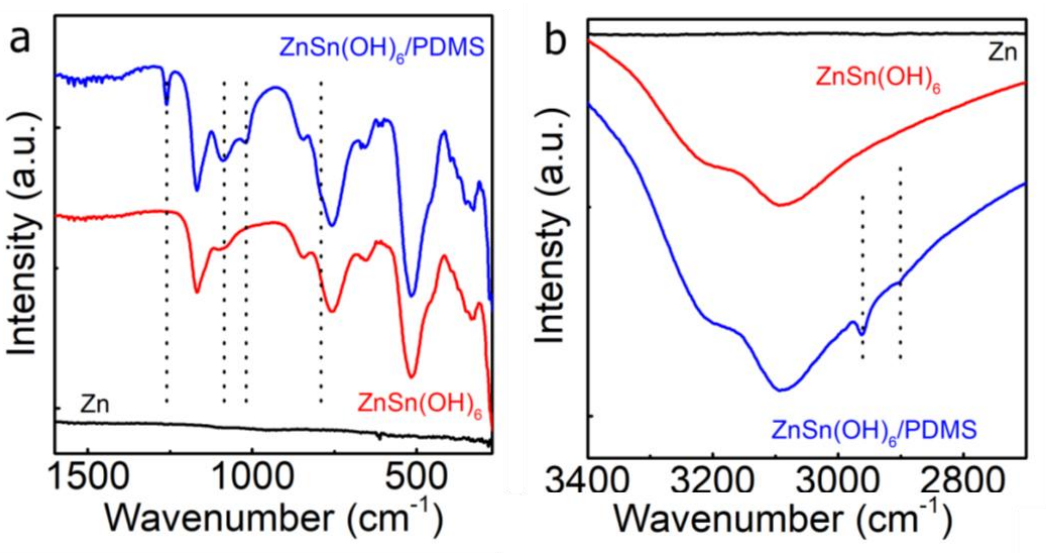

Figure 4.2.5 *ATR-FTIR measurements of plain and $ZnSn(OH)_6$-deposited Zn samples with and without PDMS coating.*

A wide band in the 3100 – 3300 cm^{-1} region is associated with OH stretching vibrations indicating the presence of hydroxyl groups. The absorption band at 1164 cm^{-1} was due to bending vibrations of the ZnSn-OH bonds. The peaks at 1258, 1083, 1014, and 788 cm^{-1} are the fingerprint for PDMS.[169] The PDMS peak at 1258 and a shoulder at 788 cm^{-1} are due to CH_3 deformation and CH_3 rocking in $Si{-}CH_3$, respectively, and the two adjacent peaks at 1083 and 1014 cm^{-1} are due to $Si{-}O{-}Si$ asymmetric deformation (Figure 4.2.5a). Figure 4.2.5b shows the symmetric and asymmetric CH_3 stretching peaks at 2961 and 2902 cm^{-1}, respectively.[170] This analysis confirms the successful UV-grafting of the plain silicone oil molecules to the $ZnSn(OH)_6$ surfaces.

To evaluate the corrosion resistance in physiological environment, polarization curves were acquired in in HBSS and DMEM with and without FBS (Figure 4.2.6).

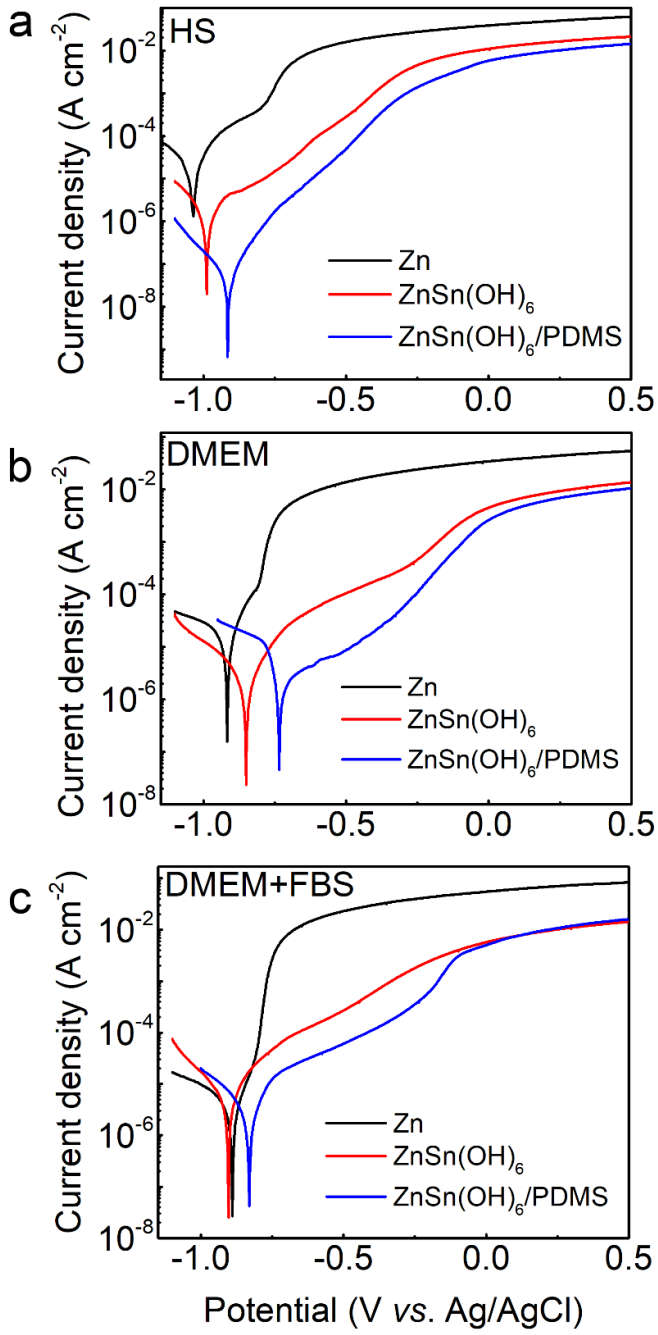

Figure 4.2.6 *Potentiodynamic polarization curves were measured on bare Zn, ZnSn(OH)6, and ZnSn(OH)$_6$/PDMS surfaces in (a) HBSS, (b) DMEM, and (c) DMEM + FBS buffer solutions.*

The results demonstrate the reduction in terms of current densities after surface treatments if compared to bare zinc. Notably, there is also a substantial shift of the corrosion potential (E_{corr}) to more positive values in all physiological solutions.

In addition, electrochemical impedance spectra (EIS) were recorded at the open circuit potential in different physiological solution and are shown in the Bode plot in Figure 4.2.7.

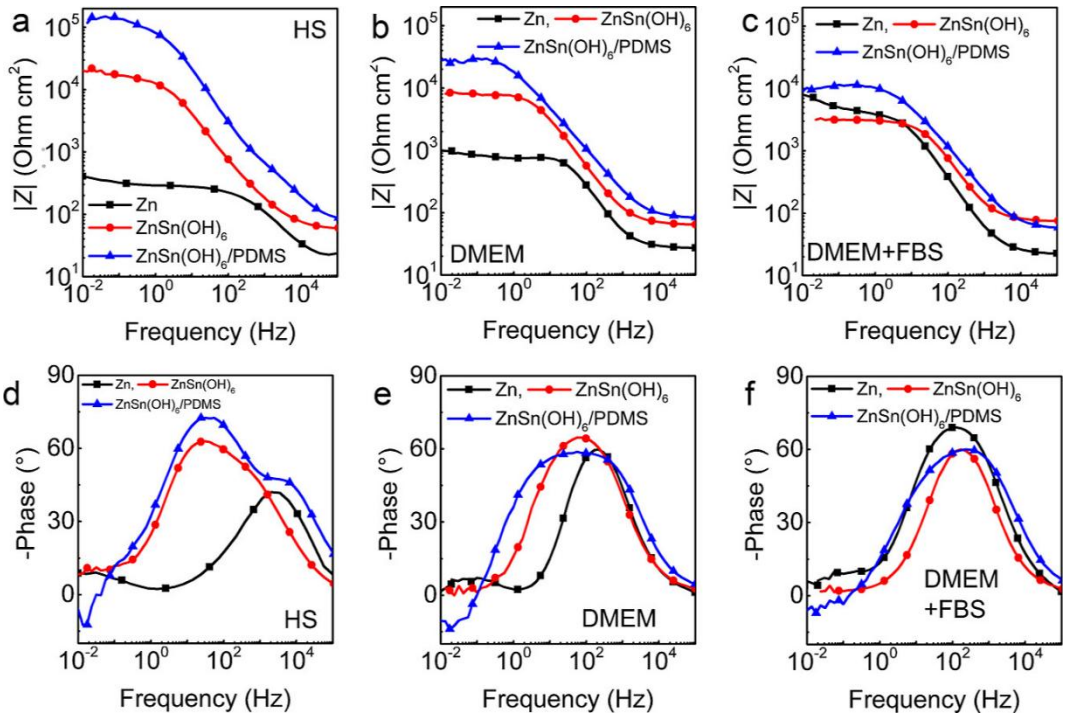

Figure 4.2.7 *EIS measurements of the bare Zn, ZnSn(OH)6, and ZnSn(OH)6/PDMS surfaces in (a,d) HBSS, (b,e) DMEM, and (c,f) DMEM + FBS buffer solutions.*

It is evident that the presence of chemical conversion coating increases the overall impedance. The increase is more pronounced when these samples are grafted with PDMS. The impedance spectra were modelled according to EEC reported in Figure 4.2.8 and the corresponding fitting parameters are summarized in Table 4.2.2 and Table 4.2.3.

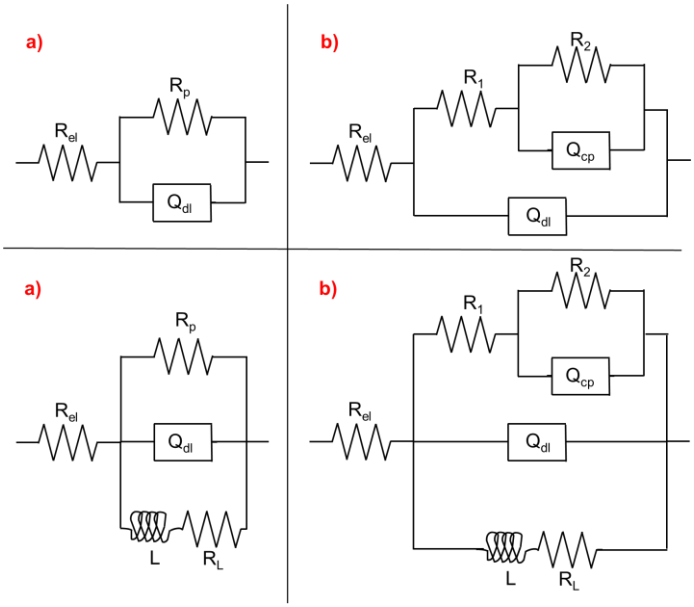

Figure 4.2.8 *Equivalent electrical circuits used to model the electrochemical performance of (a) bare Zn and ZnSn(OH)6 in DMEM with and without FBS, (b) ZnSn(OH)6 in HBSS, (c) ZnSn(OH)6/PDMS in DMEM with and without FBS, and (d) ZnSn(OH)6/PDMS in HBSS.*

The bare zinc samples can be modelled by using the EEC in Figure 4.2.8a. In particular it is composed by a parallel between a polarization resistance due to the ongoing corrosion process, R_P, and a constant phase element, Q_{dl}, accounting for the non-ideal double layer capacitance, in series with the electrolyte resistance, R_{el} The lower R_p is estimated in HBSS while higher values were measured in DMEM+FBS due to the adsorption of proteins. [45,171]

For the coated samples in DMEM with and without FBS, the spectra can be fitted by the same simple equivalent circuit as for the bare samples (Figure 4.2.8b). The higher electrolyte resistance can be explained by the morphology of the coating, which creates a more tortuous pattern for the current line with a consequent increase of R_{el}. The conversion $ZnSn(OH)_6$ coating increases the polarization resistance, whose values are further increased when PDMS is grafted on top. Notably, when polymer covers the conversion coatings a small inductive loop appears at low frequency, that can be due to adsorption phenomena involving intermediates for H_2 evolution [172] and/or oxidized zinc from the substrate. [173]

The overall impedance also increases when the Zn specimens are tested in HBSS (Figure 4.2.7a). However, a second time constant is required to model the electrical performance of the coated metal in HBSS (Figure 4.2.8b), and the corresponding fit parameters are reported in Table 4.2.2**.** The latter can be explained by the high concentration of phosphate ions present in the HBSS solution. As soon as Zn is dissolved in the active region that is still present beneath the conversion $ZnSn(OH)_6$ coating, Zn phosphate, which is almost insoluble, precipitates leading to a partial sealing of the $ZnSn(OH)_6$ surface.

Specimen/ Medium	R_{el} [Ω cm^2]	R_p [Ω cm^2]	Q_{dl} [μS s^n cm^{-2}]	n	L [kH cm^2]	R_L [Ω cm^2]
Zn in HBSS	19	275	17	0.71	-	-
Zn in DMEM	28	765	11	0.89	-	-
Zn in DMEM+FBS	23	4468	12	0.84	-	-
$ZnSn(OH)_6$ in DMEM	64	8162	8.9	0.82	-	-
$ZnSn(OH)_6$ in DMEM+FBS	76	3050	5.6	0.85	-	-
$ZnSn(OH)_6$/ PDMS in DMEM	79	3.4×10^4	9.7	0.72	51	3.5×10^5
$ZnSn(OH)_6$/ PDMS in DMEM+FBS	70	1.2×10^4	6.3	0.76	45	2.7×10^5

Table 4.2.2 *Electrochemical impedance spectroscopy data is modelled according to the equivalent circuit as shown in Figure 4.2.8a,c.*

Specimen /Medium	R_{el} [Ω cm²]	Q_{dl} [μS sⁿ cm⁻²]	n	R_1 [Ω cm²]	R_2 [Ω cm²]	Q_{cp} [μS sⁿ cm⁻²]	n	L [kH cm²]	R_L [Ω cm²]
$ZnSn(OH)_6$	59	8.6	0.75	1260	1.6×10^4	0.67	0.97	-	-
$ZnSn(OH)_6$/PDMS	85	1.4	0.77	1640	1.4×10^5	0.21	1	6.6×10^3	5.7×10^4

Table 4.2.3 *Electrochemical impedance spectroscopy data in HBSS is modelled according to the equivalent circuit as shown in* Figure 4.2.8b,d.

Based on these results, we can conclude that upon coating Zn with zinc hydroxystannate, the overall impedance increases in all the investigated electrolytes, the highest being measured when the chemical conversion is followed by the plain PDMS coating. The $ZnSn(OH)_6$/PDMS specimens provided the highest corrosion protection in all three physiological solutions.

In addition, the corrosion kinetics of the bare and coated Zn specimens were further investigated by respirometric measurements in modified Hank's solution. Briefly, monitoring the cathodic reactions in aqueous media, specifically the hydrogen evolution reaction (HER) and the oxygen reduction reaction (ORR), allows for the inference of the amount of anodic reaction. The H_2 partial pressure was derived by monitoring the total pressure, whereas the O_2 partial pressure was measured using an optical O_2 meter. The respective molar changes were calculated using the ideal gas law and then converted to charges using Faraday's law. The dissolved O_2 concentration in the liquid phase was measured using the O_2 meter, while the dissolved H_2 concentration was calculated using Henry's law. The solution was stirred to facilitate gas exchange between the gas and the liquid phases. The presence of H_2 was confirmed by using an amperometric H_2 microsensor. The O_2 partial pressure was monitored in the gas phase. The total O_2 consumption was almost entirely from the gas phase, as is evident from the equilibration of the two phases. Note that for Zn corrosion, in addition to the regular 4-electron ORR pathway, there is also a 2-electron pathway that results in the formation of H_2O_2.[173] Since the experimental setup could not detect H_2O_2, the conversion to anodic charge is imprecise but must be in the range of the two pathways. Therefore, the total cathodic charges were calculated using the 4-electron pathway, which will eventually dominate as H_2O_2 decomposes. In particular, as the concentration increases, the two molecules are likely to react to form O_2 and H_2O, which ultimately contributes to the 4-electron pathway. Assuming that the ORR pathway remains unchanged for the different coatings, the cathodic charges can be used to compare their corrosion rates. However, even in the extreme scenario where peroxide formation is the only process and the coated samples corrode exclusively *via* the 4-electron ORR mechanism, the bare Zn samples would still exhibit significantly higher corrosion rates.

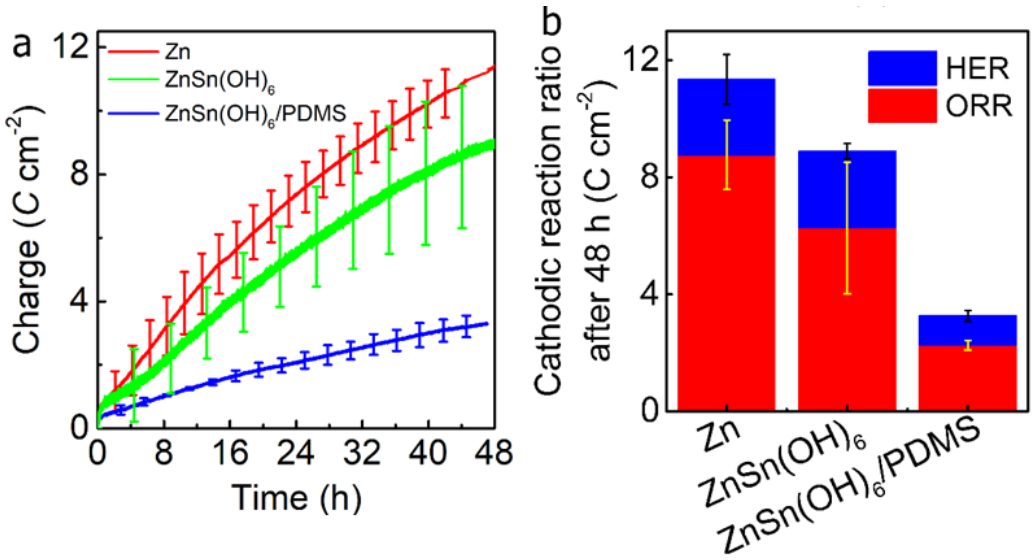

Figure 4.2.9 *(a) Total cathodic charge densities (ORR+HER) were obtained for 48 h in the modified Hank's electrolyte using the respirometric measurements. (b) Cathodic reaction ratio ORR and HER after 48 h of exposure to the modified Hank's electrolyte.*

Figure 4.2.9a summarizes the respirometric total charge measurements of the Zn, $ZnSn(OH)_6$, and $ZnSn(OH)_6$/PDMS specimens. The corrosion current density was calculated from the linear fit slope of the total charge density as a function of time and was found to be 52.8, 44.4, and 15.8 μA cm^{-2} for bare Zn, $ZnSn(OH)_6$, and $ZnSn(OH)_6$/PDMS specimens, respectively. The latter indicates that the PDMS coating results in a threefold reduction of the corrosion rates compared to both the Zn and $ZnSn(OH)_6$ counterparts, which is consistent with the potentiodynamic polarization and electrochemical impedance spectroscopy measurements. Figure 4.2.9b presents the ratio between hydrogen evolution reaction (HER) and oxygen reduction reaction (ORR) for the corresponding specimens. While the bare Zn exhibits the highest cathodic charge density, it also shows the highest ORR/HER ratio of ~77 %. The $ZnSn(OH)_6$ and $ZnSn(OH)_6$/PDMS specimens exhibit the ORR/HER ratio of ~70 %. It is known that Zn corrodes primarily by ORR in alkaline media, while in neutral electrolytes, it exhibits a mixed ORR and HER response.[174] As shown, the difference between Zn and $ZnSn(OH)_6$/PDMS is substantial. Here, the cathodic reaction difference is attributed to the protective performance of the developed coatings. Although it is known that pH increases due to the ORR during Zn corrosion, we did not observe a significant change in pH of the electrolyte during the experiment. The difference in cathodic reaction ratio could be attributed to a local increase in pH near the specimen surface, which could lead to a shift in the ORR ratio in the case of bare Zn.

Zn, $ZnSn(OH)_6$, and $ZnSn(OH)_6$/PDMS sample were immersed for 7 days to have information about the long-term protection of the coatings. The SEM micrographs in Figure 4.2.10 after 7 days of immersion shown corrosion attack for bare zinc samples, while there is no evidence of corrosion attack on the surface of the $ZnSn(OH)_6$/PDMS samples for all physiological media. The EDS analysis also

reveals that the C and Si peaks are still clearly observed for $ZnSn(OH)_6$/PDMS samples. Moreover, EDX analysis reveal the presence of Ca and P on $ZnSn(OH)_6$/PDMS sample indicating the precipitation of calcium phosphates. As reported in literature, the presence of silicones play an important role in bone formation and calcification. [175]

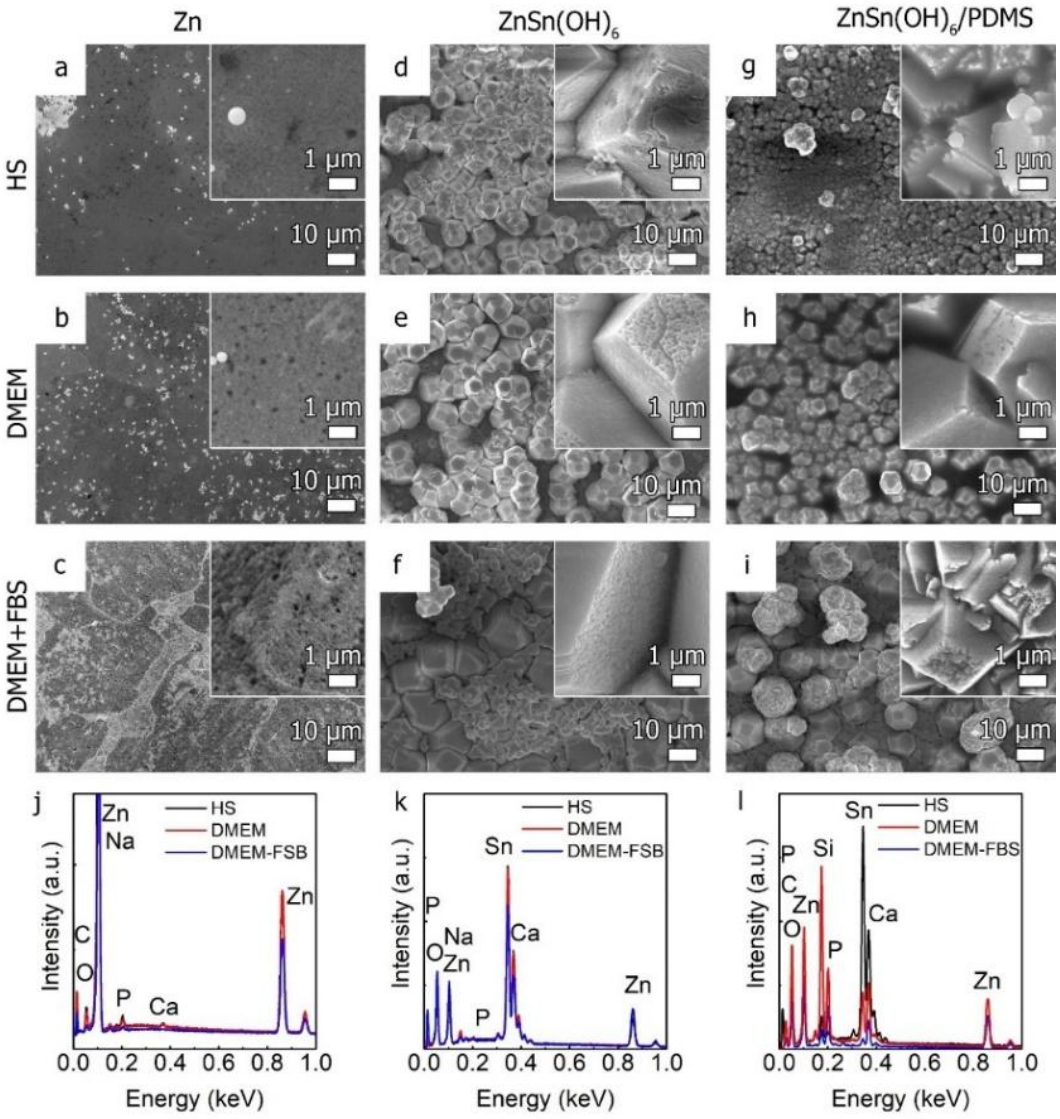

Figure 4.2.10 *SEM images of Zn, $ZnSn(OH)_6$, and $ZnSn(OH)_6$/PDMS specimens after 7 days of immersion in (a, d, g, j) HS, (b, e, h, k) DMEM, and (c, f, i, l) DMEM-FBS solutions. (j-l) EDS spectra of Zn (j), $ZnSn(OH)_6$ (k), and $ZnSn(OH)_6$/PDMS (l) specimens after 7 days of immersion in HS, DMEM, and DMEM-FBS solutions.*

ICP-OES reveals that Sn ions concentration was negligible after immersion in physiological media (see Figure 4.2.11).

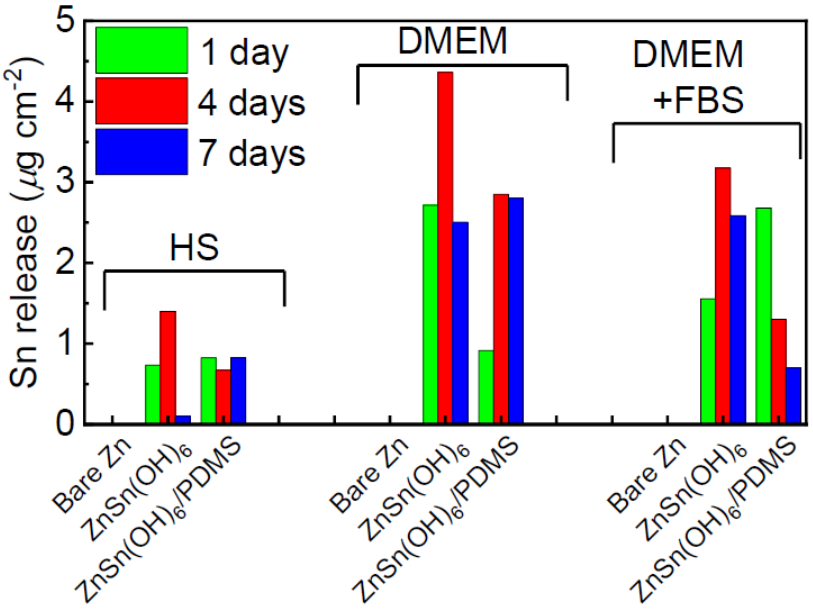

Figure 4.2.11 *The ICP-OES release test of the Sn4+ concentration in the physiological solutions after one week of immersion.*

Impedance spectra were recorded in the physiological solutions at the corresponding open circuit potential after 7 days of immersion, see Figure 4.2.12.

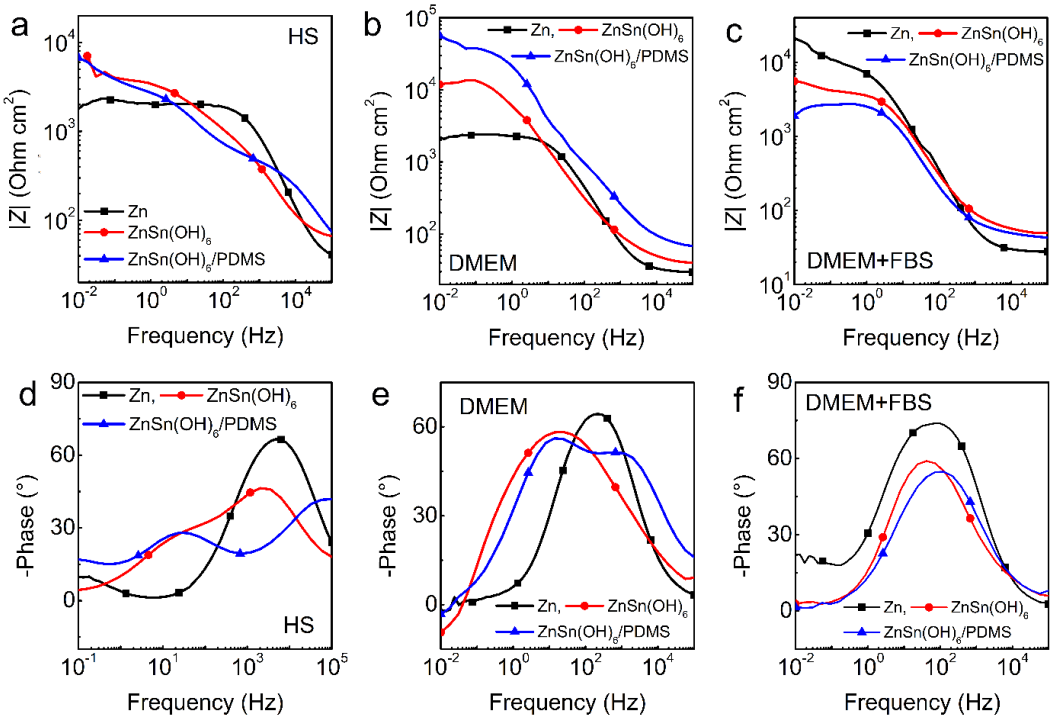

Figure 4.2.12 *Electrochemical impedance spectroscopy measurements of the bare Zn, ZnSn(OH)6, and ZnSn(OH)6/PDMS surfaces after 1 week of continuous immersion in (a, d) HBSS, (b, e) DMEM, and (c, f) DMEM+FBS buffer solutions.*

The overall impedance does not change appreciably for the coated alloys in spite the long immersion time.

The release of Zn ions, see Figure 4.2.13, was quantified by ICP-OES after 1, 4, and 7 of immersion.

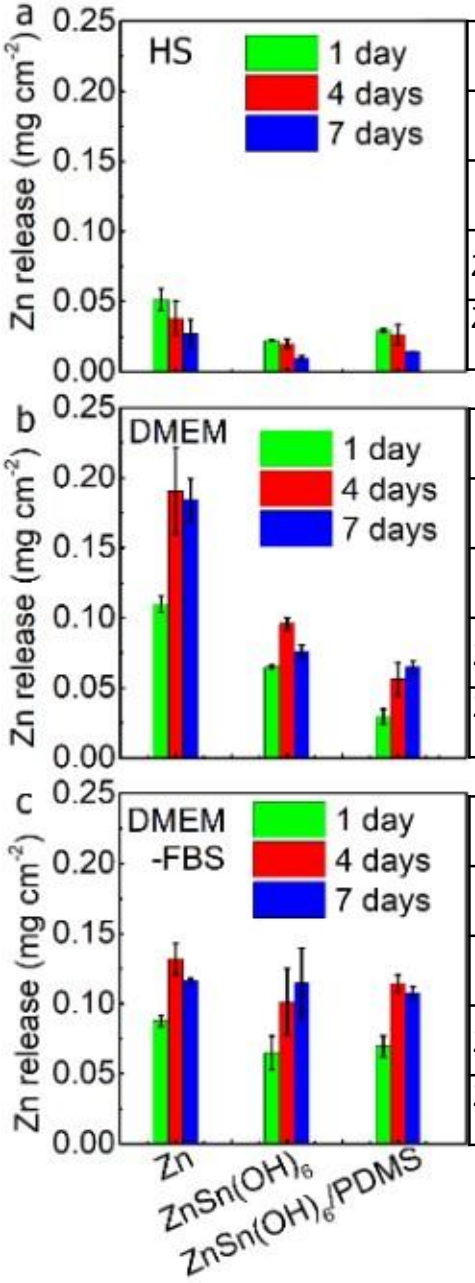

	Zn release in HS (mg cm^{-2})		
	1 day	4 days	7 days
Zn	0.051	0.038	0.027
$ZnSn(OH)_6$	0.022	0.020	0.010
$ZnSn(OH)_6$ / PDMS	0.088	0.139	0.116

	Zn release in DMEM (mg cm^{-2})		
	1 day	4 days	7 days
Zn	0.110	0.191	0.184
$ZnSn(OH)_6$	0.065	0.096	0.076
$ZnSn(OH)_6$ / PDMS	0.030	0.056	0.065

	Zn release in DMEM+FBS (mg cm^{-2})		
	1 day	4 days	7 days
Zn	0.088	0.140	0.116
$ZnSn(OH)_6$	0.065	0.101	0.115
$ZnSn(OH)_6$ / PDMS	0.070	0.114	0.108

Figure 4.2.13 *ICP measurements of Zn, $ZnSn(OH)_6$, and $ZnSn(OH)_6$/PDMS, surfaces after (a) 1, (b) 4, and (c) 7 days of immersion in (a) HBSS, (b) DMEM, and (c) DMEM-FBS.*

In Hanks' Balanced Salts Solution, the presence of $ZnSn(OH)_6$ significantly reduces the Zn^{2+} ions release, due to its protective effect. In DMEM a higher concentration of zinc ions was measured compared to HBSS and there is still evidence of a beneficial effect of the surface treatments. However, in DMEM+FBS the measured Zn ions release appears to be independent by the coatings. These results can be related by different corrosion mechanisms of Zn, which vary depending on the composition of the different simulated body fluid used. In HBSS, the high concentration of phosphate induces the precipitation of Zn phosphate,

almost insoluble, on the metal surface reducing the concentration of Zn^{2+} in the solution. DMEM contains several amino acids, that can chelate Zn ions, leading to the precipitation of Zn salts. In DMEM+FBS, proteins can be adsorbed onto the surface of bare Zn, inhibiting reducing the corrosion rate. [176]

To evaluate the potential toxicity, Zn samples were immersed in a solution of GFP-expressing *Escherichia coli,* used as transducer to evaluate cytotoxicity. Zn has been shown to have an antibacterial effect, but at high concentration can be toxic to cells.[177]

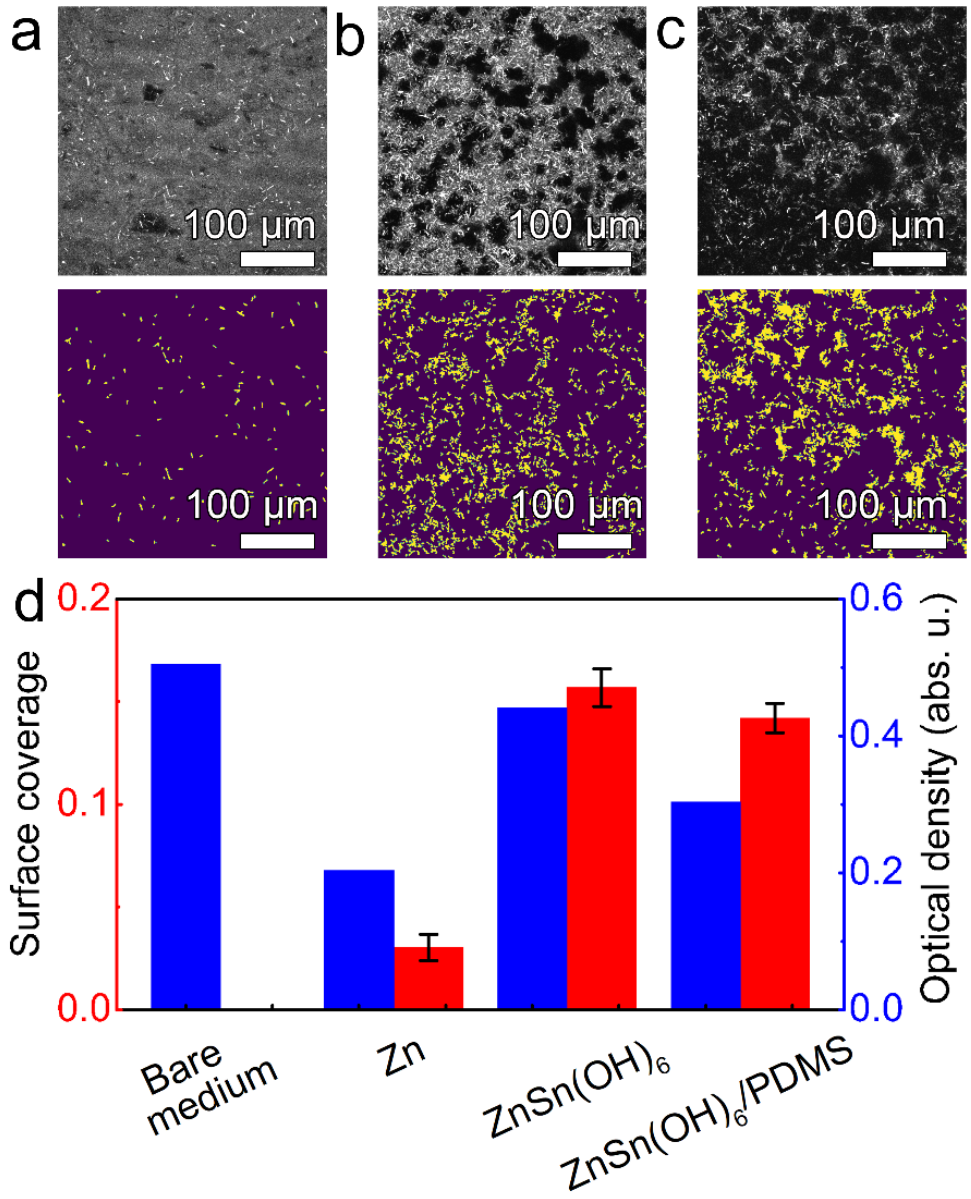

Figure 4.2.14 *(a-c) Typical raw and processed confocal microscopy images of non-motile live GFP-expressed E. coli on (a) bare Zn, (b) $ZnSn(OH)_6$, and (c) $ZnSn(OH)_6$/PDMS specimens. (d) Corresponding surface coverage of non-motile live GFP-expressed E. coli on the specimens shown in (a-c) and optical density measurements of bacteria growth after 24 h in the growth medium with and without bare and coated Zn specimens.*

The results of the bacterial growth and surface adhesion studies are summarized in Figure 4.2.14. As anticipated, both the number of non-motile bacteria attached to the exposed Zn specimens and motile bacteria in the growth medium showed the lowest optical density values due to the increased corrosion rates indicating that Zn alone has the greatest negative impact on bacterial cells (Figure 4.2.14a,d). Both $ZnSn(OH)_6$ and $ZnSn(OH)_6$/PDMS coated specimens showed higher bacterial adhesion and optical density values of bacterial growth in the medium. This indicates that there was a smaller effect on *E. coli* compared to bare Zn and medium control (Figure 4.2.14b-d). However, the bacterial surface coverage varied between the $ZnSn(OH)_6$ and $ZnSn(OH)_6$/PDMS surfaces. While a bacterial monolayer is observed on the former (Figure 4.2.14b), patchy bacterial assemblies are present on the latter (Figure 4.2.14c). This difference in bacterial assembly is attributed to the lower adhesion strength of bacteria to the PDMS-coated surfaces, where UV-grafted silicone oil serves as a lubricating layer. Such patches form during the subtraction and rinse processes, *i.e.*, the exposure of the specimens to the liquid-air interface during their harvesting is enough to partially remove bacteria from the specimen surface. The latter is consistent with previous studies.[178,179]

In summary, the results show that the proposed surface treatments enhance the corrosion resistance of zinc as biodegradable material in physiological environment. Potentiodynamic polarization, electrochemical impedance spectroscopy and long-term immersion were carried out in three physiological media. The results indicate that zinc-hydroxystannate layer only modestly improves the biocorrosion resistance of Zn; however, it introduces a rough high surface area layer of hydroxyl groups, which are used to graft PDMS molecules by their selective cleavage under UV irradiation. The grafting of hydrophobic PDMS molecules increase the corrosion resistance in biological environment of zinc by reducing the current density of both the cathodic and the anodic branches and indice a notable shift of the corrosion potential to more positive values in all physiological solutions. The results are also conformed by electrochemical impedance spectroscopy measurements, where PDMS-coated samples demonstrated the highest polarization resistance in all three simulated body fluids. The immersion for 7 days in physiological media demonstrate that the presence of PDMS enhance the precipitation of hydroxyapatite, since silicones play an important role in bone formation and calcification. Finally, the enhancement of corrosion resistance of the coated Zn specimens reduces the cytotoxicity of the released Zn ions, while the adhesion strength of bacteria weakens on PDMS-coated surfaces due to the lubricating effect of the UV-grafted silicone oil.

4.3 3D printed zinc components: corrosion behaviour as a function of surface treatment

In this chapter some preliminary results related to 3D zinc samples produced by additive manufacturing process after surface treatment for biomedical applications are presented. In particular, surface treatments such as chemical etching and chemical conversion were optimized in order to improve the corrosion resistance of 3D samples in simulated body environment. A chemical etching in acid aqueous solution was optimized to have a smoother surface without unfused powder left by the printing process. In addition, chemical conversion processes were carried out to improve the corrosion resistance and reduce zinc ions release. Chemical conversion in this case is a good strategy thanks to the adaptability for uneven surfaces and with very complex shape.

3D samples were produced by a Concept Laser MLab machine and zinc powder with a purity of 99.995% purchased by IMR (metal powder technologies). In Figure 4.3.1 SEM micrographs of zinc powder are presented.

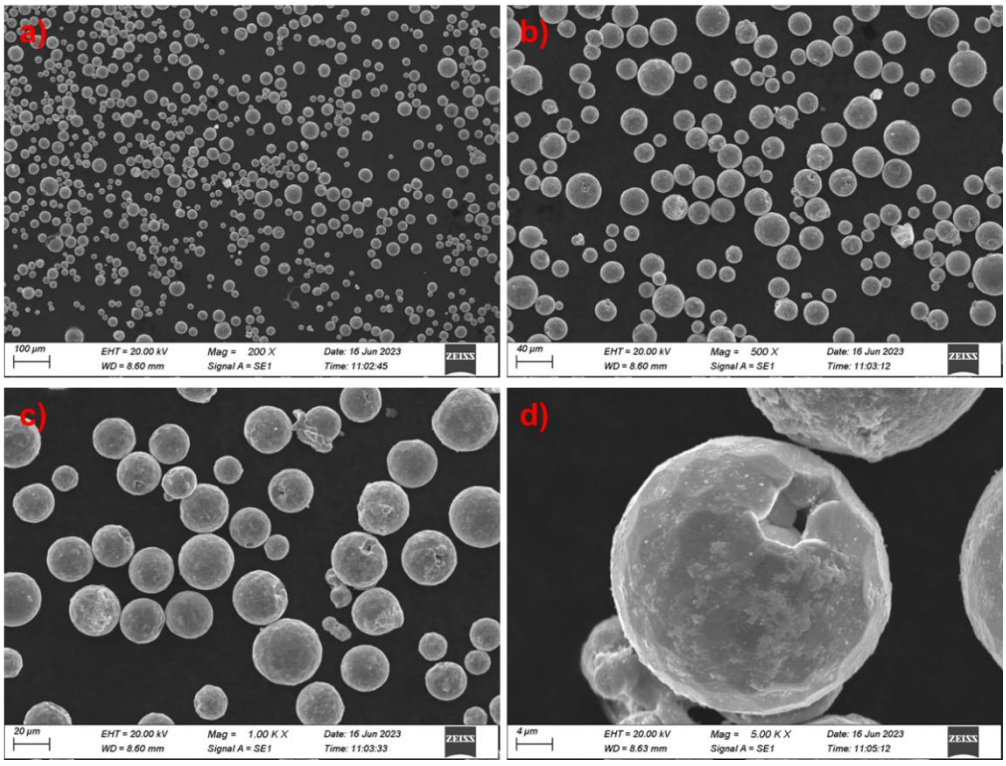

Figure 4.3.1 *SEM micrographs at different magnification of zinc powder used.*

Argon was used to decrease the oxygen level to 0.1% by filling the build chamber. Process parameters such as laser power, scanning rate and hatch were optimized to reduce the sample porosity.

The porosity values were calculated by using density, measured by a pycnometer, according to equation 4.3.1:

$$\%\, porosity = 100 - \frac{Density_{sample}}{Density_{powder}} . 100 \qquad (4.3.1)$$

In Figure 4.3.2 the porosity as a function of printing process parameters is represented.

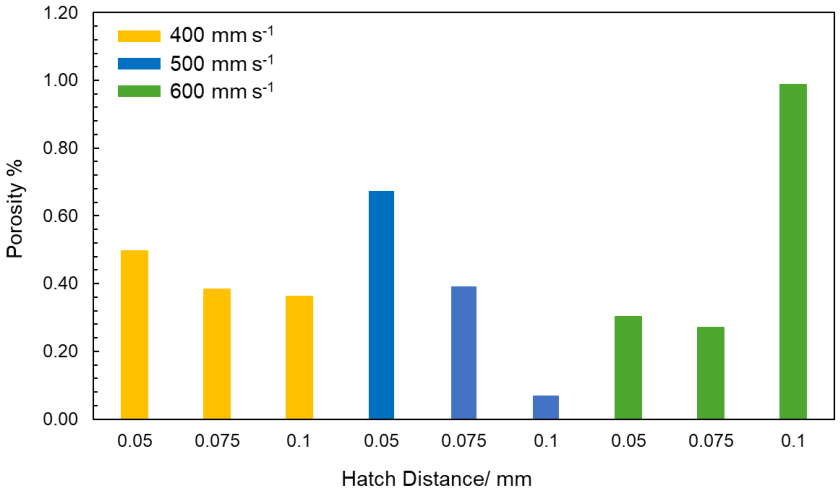

Figure 4.3.2 *Sample porosity for different printing process parameters.*

Considering the results, samples were printed using the best printing process parameters, in particular 50 W as laser power, 500 mm s^{-1} as scanning rate and 0.1 mm as hatch distance. Flat specimens with dimensions of 30 x 15 x 3 mm^3 were used for the experimental campaign.

Surface treatments were carried out in order to improve the corrosion resistance in simulated body environment. A chemical etching in 5% wt. nitric acid aqueous solution was used to remove the unfused powder from the surface. The etching process was carried out using an ultrasonic bath for 2 minutes at room temperature. In addition, chemical conversion processes were carried out to improve the corrosion resistance and reduce zinc ions release.

The $ZnSn(OH)_6$ coatings were grown by chemical conversion coating in a stannate-ion-containing aqueous medium at pH (~12.5), 80 °C for 60 min. The chemical composition of the bath is presented in Table 4.3.1:

Bath composition	**Concentration (g L^{-1})**
NaOH	10
$K_2SnO_3 \cdot 3H_2O$	50
$NaC_2H_3O_2 \cdot 3H_2O$	10
$Na_4P_2O_7$	50

Table 4.3.1 *Composition of the electrolyte bath for stannate conversion coating.*

The phosphate conversion coating was carried out in acidic aqueous solution containing calcium and phosphate ions. The process was conducted for 30 minutes at 50°C. The chemical composition of the bath is presented in Table 4.3.2:

Bath composition	Concentration (g L^{-1})
H_3PO_4	20
$NaNO_2$	10
$Ca(CH_3COO)_2$	10

Table 4.3.2 *Composition of the electrolyte bath for phosphate conversion coating.*

The bath mediums were not stirred and were exposed to air during the conversion process. The deposited samples were rinsed with DI water and dried under N_2 stream.

Figure 4.3.3 shows SEM micrograph of as printed sample (AP) at different magnifications.

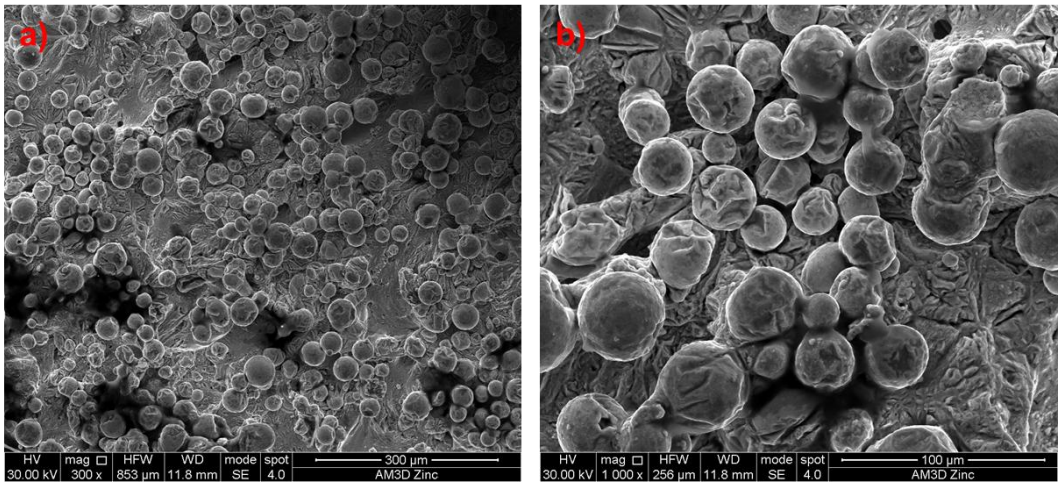

Figure 4.3.3 *SEM micrograph of as printed sample*

The as printed samples (AP) show unfused powder on the surface, that is typical of 3D samples printed by laser powder bed fusion (LPBF). The surface inhomogeneity can induce a not uniform wettability with consequent localized attack. In addition, these particles can be detached from the sample in physiological solution especially in the presence of flow.

Figure 4.3.4 shows SEM micrograph of a chemically etched sample (CE) at different magnifications.

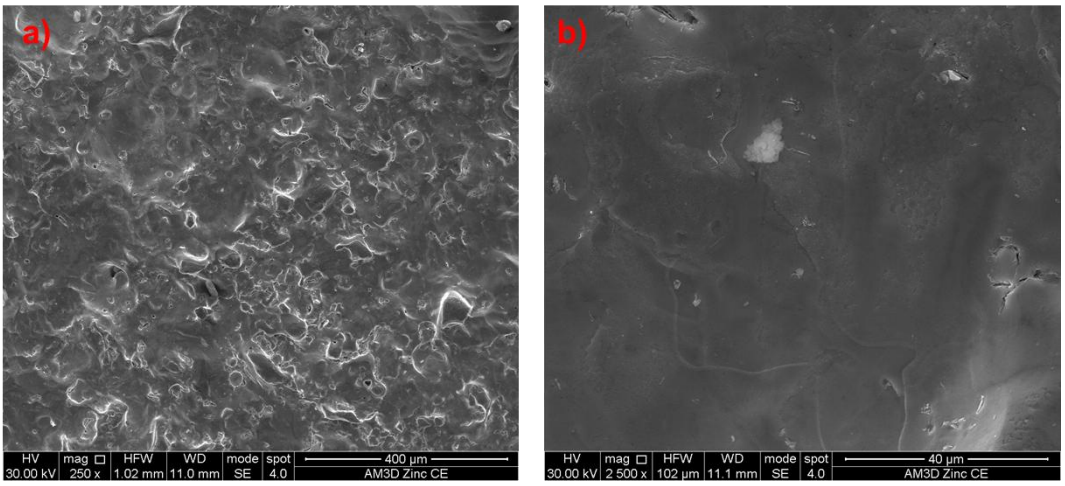

Figure 4.3.4 *SEM micrograph of as chemically etched sample*

The chemical etching allows the complete removal of the unfused powder with consequent improvement of the homogeneity of the sample surface as evident in the SEM micrograph.

As reported in before, Zinc implants can induce cytotoxic effects when implanted in the human body, so a surface treatment is necessary to improve corrosion resistance and thus reduce zinc ions release. Chemical conversion has advantages with respect to other surface modification techniques, such as low cost, rapid coating production, adaptability for uneven surfaces and for very complex shapes, and minimal impact on the mechanical properties of the metallic substrate.[180]

The stannate conversion consists of the deposition of a rough $ZnSn(OH)_6$ on the surface of zinc sample. The process started with the dissolution in a conversion bath at pH~12.5 where zinc substrate is not thermodynamically stable and, close to the electrode surface, dissolves as bizincate ions according to the following oxidation reaction:

$$Zn + 3OH^- \rightarrow HZnO^{2-} + H_2O + 2e^- \qquad (4.3.2)$$

The following cathodic processes can be coupled to zinc dissolution:

$$½\ O_2 + 2e^- + H_2O \rightarrow 2OH^- \qquad (4.3.3)$$

$$2H_2O + 2e^- \rightarrow H_2 + 2OH^- \qquad (4.3.4)$$

Due to the increased bizincate ions concentration and to the presence of SnO_3^{2-} (stannate) ions in the electrolyte, the corrosion process was followed by the $ZnSn(OH)^6$ precipitation, according to the reaction[163]:

$$HZnO_2^- + SnO_3^{2-} + 4H_2O \rightarrow ZnSn(OH)_6\downarrow + 3OH^- \qquad (4.3.5)$$

In the case of phosphate conversion process, the process started with the dissolution in a conversion bath at pH~2.5 where zinc substrate is not thermodynamically stable and, close to the electrode surface, dissolves as zinc ions according to the following oxidation reaction:

$$Zn \rightarrow Zn^{2+} + 2e^{-} \qquad (4.3.6)$$

The cathodic reactions are the same as in the stannate conversion process (see eq. 4.3.3 and 4.3.4) and induce local alkalization. The precipitation of phosphate conversion coating occurs according to the following reaction[180]:

$$3Zn^{2+} + 2H_2PO_4^{-} + 2H^{+} + 4H_2O + 6e^{-} \rightarrow Zn_3(PO_4)_2 \cdot 4H_2O_{(s)} \downarrow + 3H_2 \uparrow \qquad (4.3.7)$$

$$Ca^{2+} + 2Zn^{2+} + 2H_2PO_4^{-} + 2H_2O \rightarrow CaZn_2(PO_4)_2 \cdot 2H_2O_{(s)} + 4H^{+} \qquad (4.3.8)$$

In order to identify the composition of the coating, Raman spectra after the chemical conversion process were recorded. Figure 4.3.5 shows the Raman spectrum of SnCC sample.

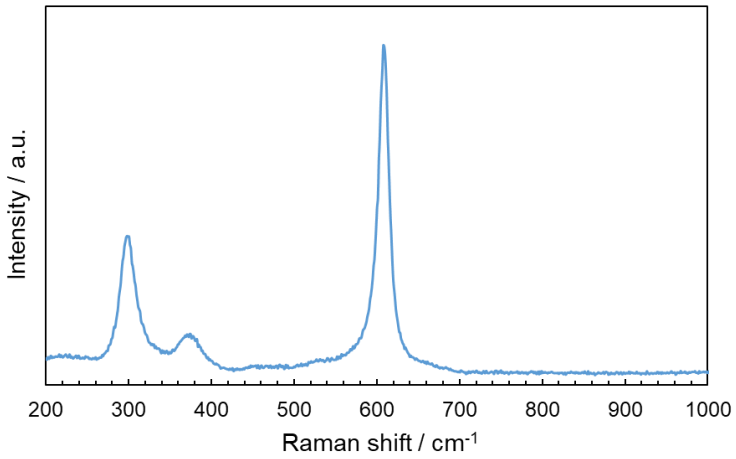

Figure 4.3.5 *Raman spectrum of zinc sample after stannate conversion process (SnCC)*

The Raman modes at 297, 374 and 608 cm^{-1} for $ZnSn(OH)_6$ arise from the breathing vibration of the M−OH bonds and M−OH−M (bridging OH group) bending modes, for the same material[163]. Figure 4.3.5 shows the Raman spectrum of PCC sample.

Figure 4.3.6 shows the Raman spectrum of PCC sample.

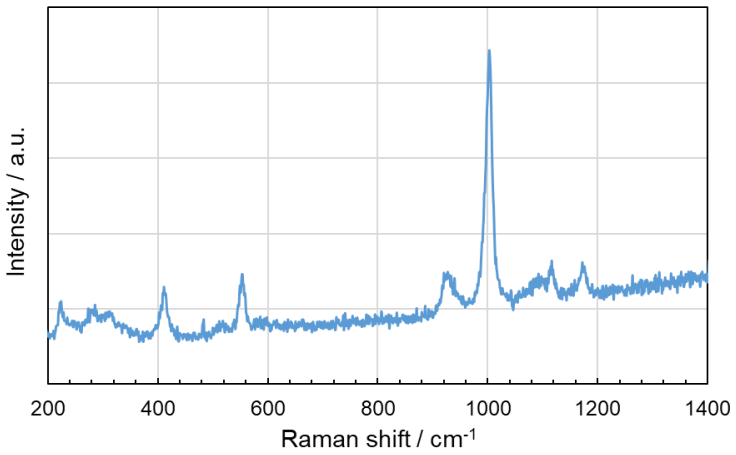

Figure 4.3.6 *Raman spectrum of zinc sample after phosphate conversion process (PCC)*

The Raman spectrum shows that the conversion process in calcium and phosphate bath induces the precipitation of scholzite ($CaZn_2(PO_4)_2$) coating on zinc samples. In particular, scholzite phase shows an intense band at 1000 cm^{-1} that is assigned to the v_3 antisymmetric stretching modes of the PO_4. A band is observed at 923 cm^{-1} with a second band at 935 cm^{-1}. These bands are assigned to the v_1 PO_4 symmetric stretching modes.[154–156]

Figure 4.3.7 and Figure 4.3.8 show SEM micrograph and relative EDX analysis related to SnCC and PCC samples respectively.

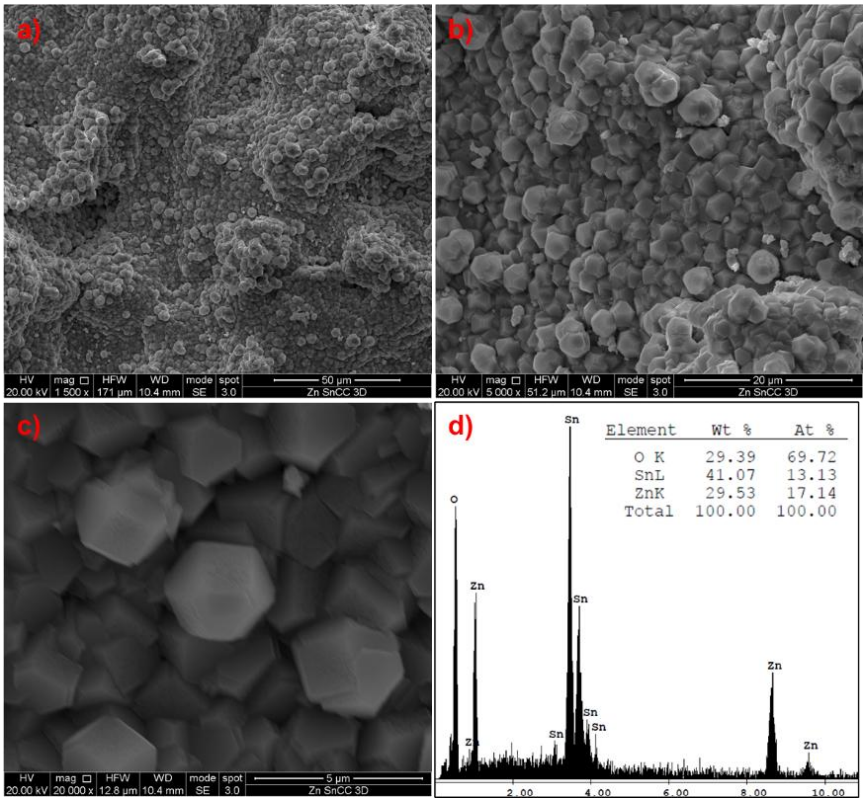

Figure 4.3.7 *SEM micrographs and relative EDX analysis of zinc sample after stannate conversion process (SnCC)*

SEM micrographs and relative EDX analysis in Figure 4.3.7 of zinc sample after the stannate conversion process show that the surface is totally covered by coating constituted by truncated octahedrons composed by both zinc and tin.

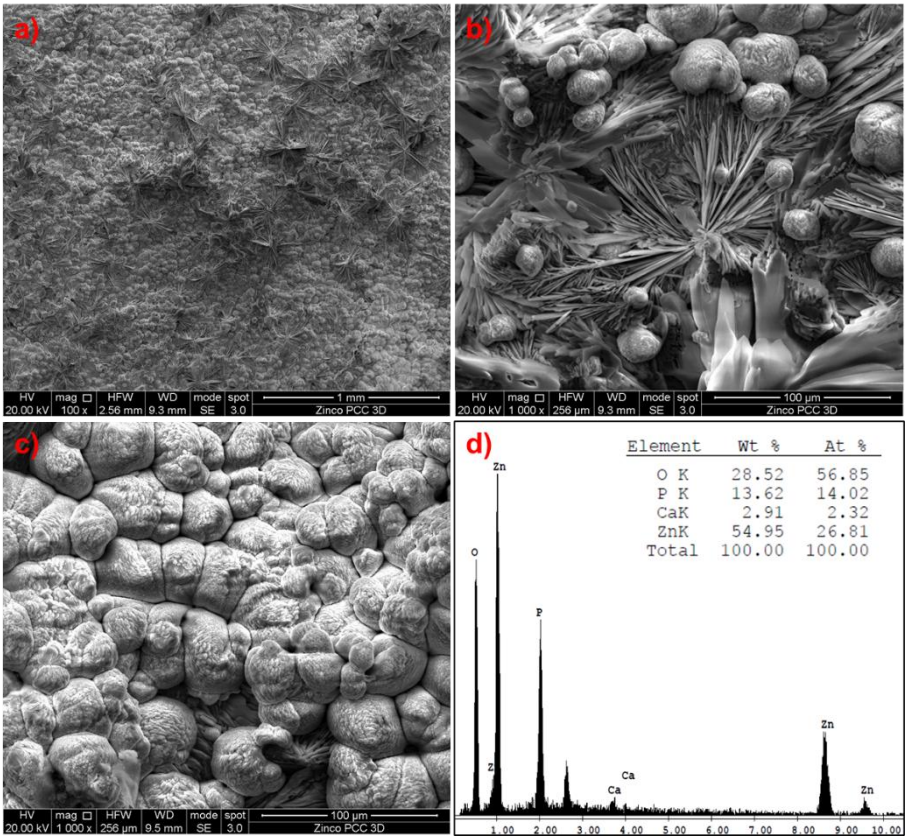

Figure 4.3.8 *SEM micrographs and relative EDX analysis of zinc sample after phosphate conversion coating (PCC)*

In the case of zinc sample after phosphate conversion process, SEM micrographs and relative EDX analysis in Figure 4.3.8 show that the surface is totally covered by irregular petal-like clusters formed by the accumulation of lamellar crystals composed by zinc, calcium and phosphorus. Besides, the lamellar crystals were closely packed, while the irregular petal-like clusters were distributed loosely on the substrate surface. As reported in the literature, the characteristic microstructure of scholzite coating promotes cell adhesion and osteogenesis[180].

To have information about the corrosion resistance in simulated body environments, electrochemical characterizations were carried out in Kokubo solution at 37°C. To compare the corrosion resistance of 3D printed samples with respect to cast materials, the same surface treatments were carried out for cast pure zinc. Figure 4.3.9 shows the EIS spectra recorded at corresponding open circuit potential for 3D printed samples in physiological environment.

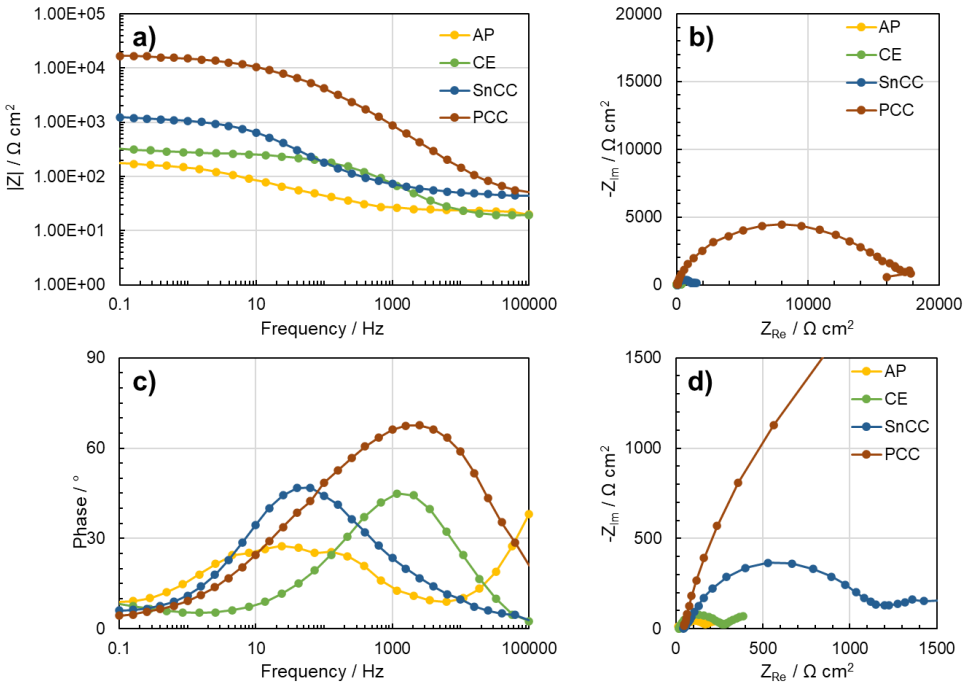

Figure 4.3.9 *EIS spectra recorded at corresponding open circuit potential in Kokubo solution at 37°C for 3D printed zinc sample after surface treatments.*

For comparison, in Figure 4.3.10 the same characterizations are presented for cast zinc samples.

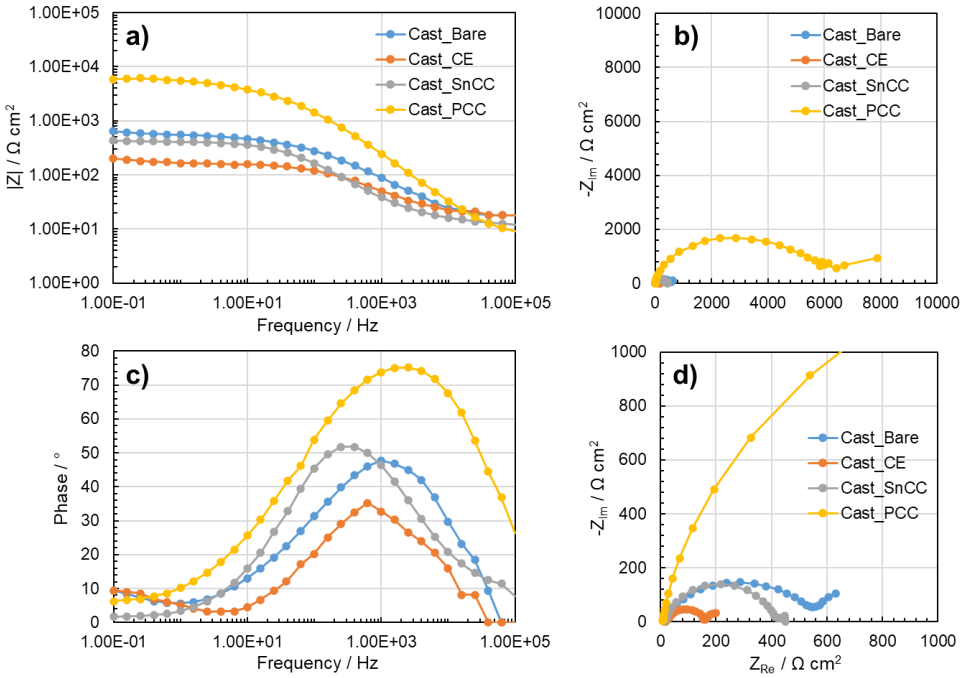

Figure 4.3.10 *EIS spectra recorded at corresponding open circuit potential in Kokubo solution at 37°C for cast zinc sample after surface treatments.*

The results show that the overall impedance for as printed sample is about 170 Ω cm^2 while for bare cast zinc is about 620 Ω cm^2 (see Figure 4.3.9 and Figure 4.3.10). The chemical etching process in 5% nitric acid aqueous solutions is necessary to remove unfused powder on the 3D printed sample to leave a smother surface (see Figure 4.3.4) and reduce any possible effect of printing process parameters. In addition, the surface treatment increases the overall impedance for 3D-printed zinc samples.

Chemical conversion processes were optimized to increase the corrosion resistance and thus reduce the zinc ions release, especially for the early stage of device implantation. The results related to 3D printed samples show that the overall impedances are 1200 Ω cm^2 in the case of SnCC and 17000 Ω cm^2 in the case of PCC, see Figure 4.3.9. In the case of cast samples, see Figure 4.3.10, the chemical conversion treatment allows a lower increase for the overall impedance measured.

In Figure 4.3.11 polarization curves related to 3D-printed samples in Kokubo solution are presented.

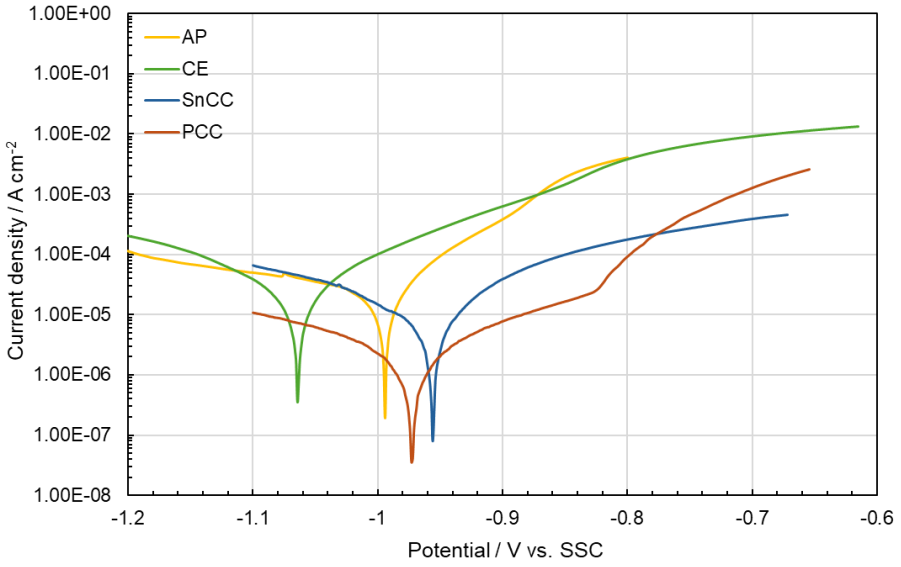

Figure 4.3.11 *Polarization curves recorded in Kokubo solution at 37°C for 3D printed zinc sample after surface treatments.*

The i-V curves show that the presence of the chemical conversion coatings reduces the current density in both anodic and cathodic brunches. Notably, there is also a substantial shift of the corrosion potential (E_{corr}) and of the pitting potential to more positive values in Kokubo solution. By using the Tafel method, it is possible to estimate the corrosion current density that is about 24 µA cm^{-2} for AP sample and 2.7 µA cm^{-2} for PCC sample.

To evaluate the corrosion protection of the optimized surface treatments, 3D zinc samples were immersed in Kokubo solution for 7 days. In Figure 4.3.12. SEM micrographs of AP, CE, SnCC and PCC samples are presented.

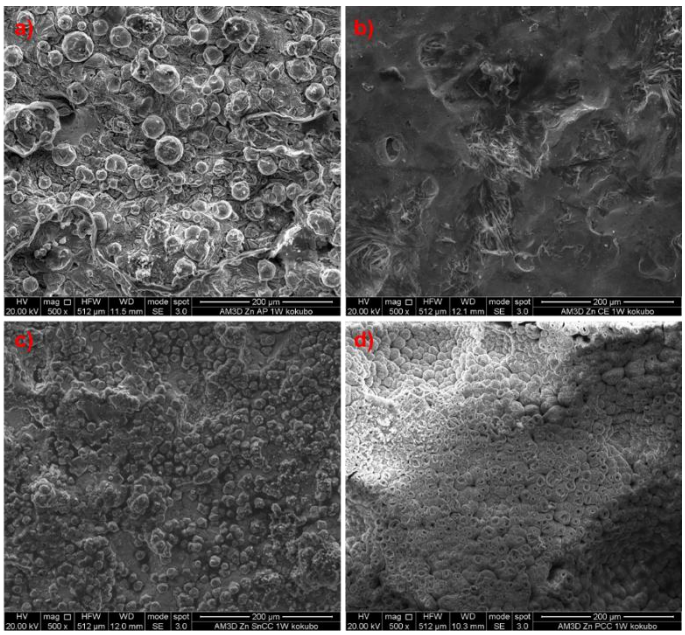

Figure 4.3.12 *SEM micrographs of a) AP, b) CE, c) SnCC and d) PCC samples after 7 days of immersion in Kokubo solution at 37°C.*

Figure 4.3.12a show that the as printed sample after 1 week of immersion in Kokubo solution is covered by corrosion products and a smaller number of unfused powders is still present on the surface if compared to Figure 4.3.3. After the chemical etching process, SEM micrograph shows that there is localized attack on the surface, see Figure 4.3.12b. The presence of the chemical conversion coatings reduces the corrosion attack, see Figure 4.3.12c-d.

To have information about the corrosion resistance of zinc samples after 7 days of immersion, electrochemical characterizations were carried out in Kokubo solution at 37°C. In Figure 4.3.13 electrochemical impedance spectra of AP, CE, SnCC and PCC recorded at corresponding open circuit potential are presented.

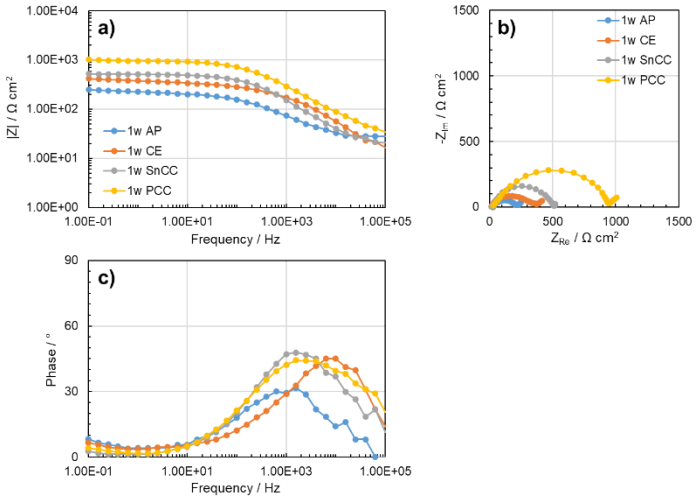

Figure 4.3.13 *EIS spectra recorded at corresponding open circuit potential after 1 week of immersion in Kokubo solution at 37°C for 3D printed zinc sample after surface treatments.*

The measured overall impedance is about 250 Ω cm^2 for AP sample, 420 Ω cm^2 for CE sample, 520 Ω cm^2 for SnCC sample and 1100 Ω cm^2 for PCC sample. These results show that the PCC coating is the best one in terms of corrosion protection.

In Figure 4.3.14 polarization curves of AP, CE, SnCC and PCC recorded in Kokubo solution are presented.

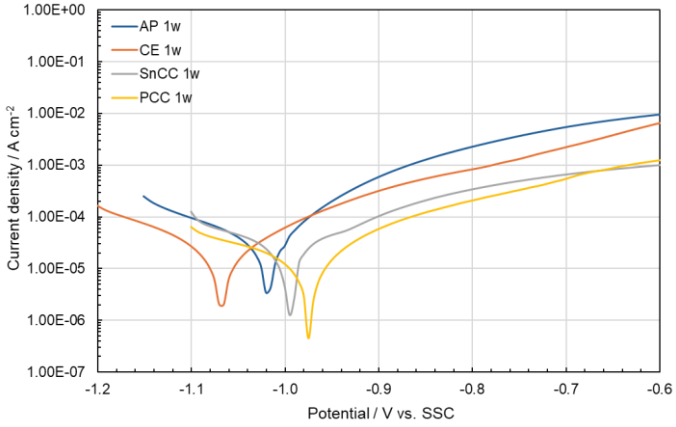

Figure 4.3.14 *Polarization curves recorded after 1 week of immersion in Kokubo solution at 37°C for 3D printed zinc sample after surface treatments.*

The i-V curves the lowest corrosion current density for the PCC sample with respect to the other samples. It is noteworthy to mention that for the PCC samples there is an increase of corrosion current density, starting from 2.7 µA cm^{-2} before the immersion to 11 µA cm^{-2} after 1 week of immersion in Kokubo solution. These results demonstrate that the phosphate conversion coating increases the corrosion resistance of 3D printed zinc prosthesis and reduces the cytotoxic effect at the early stage of implantation due to high zinc ion release but can be used for a biodegradable prosthesis because allows implant corrosion.

In summary, Zinc samples were fabricated by 3D printing using different process parameters in order to reduce sample porosity. Surface treatments such as chemical etching and chemical conversion were optimized to improve the corrosion resistance of 3D zinc samples in simulated body environment. The surface of the as-built samples shows the presence of unfused powder that can be successfully removed by chemical etching in acidic aqueous solution. In addition, chemical conversion processes increase the corrosion resistance and thus reduce the zinc ions release, especially for the early stage of device implantation. The conversion process in calcium and phosphate bath induces the precipitation of scholzite ($CaZn_2(PO_4)_2$) coating on zinc samples. The conversion process in the stannate bath induces the precipitation of a rough $ZnSn(OH)_6$ on the surface of zinc sample. Electrochemical measurements show that the PCC coating is the best one in terms of corrosion protection. These properties are confirmed also after 1 week of immersion in Kokubo solution at 37°C.

5 Conclusions

The research project aimed to optimize different surface treatments for both titanium alloys and zinc used for permanent and biodegradable biomedical applications respectively.

In the case of Ti6Al4V alloys used to realize permanent implants, several chemical and electrochemical surface treatments were carried out to improve osteointegration properties without affecting corrosion resistance. Porous layer was grown in calcium acetate and b-glycerol phosphate disodium pentahydrate aqueous solution up to formation voltages of 200 V. Photoelectrochemical measurements were carried out to study the electronic properties of porous TiO_2 layer grown by hard anodizing compared to barrier-type anodic layer. The results show that the hard anodizing process improves the reactivity of the alloy in biological environment without affecting the corrosion resistance (R_p is in the order of 10^5 Ω cm^2).

In addition, electrodeposition of silver and electrophoretic deposition of a mixture of alginate/hydroxyapatite were optimized to have a multi-functional coating. Characterization after 1 month of immersion in physiological media demonstrated good osteointegration by the precipitation of a thick hydroxyapatite layer with a typical "mud" structure. The coatings also demonstrated cytocompatibility, hemocompatibility, and antibacterial properties, distinguishing them from bare alloy and anodized samples.

Surface treatments were also optimized for Ti6Al4V plates, fabricated by 3D printing. In this case, chemical etching was proposed to leave a smoother surface without unfused powder. The anodizing process was found to reduce the formation of metastable pits and debris detachment on the surface, resulting in enhanced corrosion resistance under aggressive conditions like those typical of inflammatory situations. More specifically in the case of chemically etched samples R_p is in the order of 10^5 Ω cm^2 while for anodized samples is two orders of magnitudes higher.

In the case of zinc used to realize biodegradable implants, a preliminary characterization was carried out to have information about the corrosion mechanism as a function of the physiological solution used, namely HBSS, DMEM and DMEM + 10 % FBS as a function of immersion time. Samples immersed in HBSS show generalized corrosion with the formation of a corrosion product layer on the surface while those immersed in DMEM and DMEM + 10%FBS show corrosion without the formation of a corrosion product layer and consequently a higher zinc ion release. The corrosion rate in HBSS is ~ 0.7 mg cm^{-2} day^{-1} but decreases to $1.8 \cdot 10^{-2}$ mg cm^{-2} day^{-1} after 4 weeks of immersion. Conversely, the corrosion rate in DMEM w/o FBS is lower if compared to HBSS and decreases to $1.3 \cdot 10^{-2}$ mg cm^{-2} day^{-1} after 4 weeks of immersion. This does not mean that the corrosion process stops since the surface morphology of zinc changes according to the SEM micrographs. It is likely that the corrosion becomes more localized thus not

significantly contributing to total weight losses. The EIS spectra were rationalized in the frame of kinetic models for reaction involving the formation of an adsorbate intermediate and its successive oxidation. Electrochemical characterizations and hydrogen quantification test reveal that HER as cathodic process in Zn corrosion is negligible. In vitro tests confirm the cytotoxicity effect of zinc samples for osteoblast cells.

Surface treatments were optimized to enhance the corrosion resistance of zinc as a biodegradable material in physiological environment. In this case, a chemical conversion with zinc-hydroxystannate layer and UV grafting of hydrophobic PDMS were optimized to improve the corrosion resistance. The immersion for 7 days in physiological media demonstrated that the presence of PDMS reduces the corrosion attack and improves the osteointegration.

Zinc samples were fabricated by 3D printing and surface treatment, such as chemical etching and chemical conversion, were optimized to improve corrosion resistance in simulated body environment. The conversion process in calcium and phosphate bath induces the precipitation of scholzite ($CaZn_2(PO_4)_2$) coating instead the conversion process in stannate bath induces the precipitation a rough $ZnSn(OH)_6$. Results demonstrate that PCC coating is the best one in terms of corrosion protection also after 1 week of immersion in Kokubo solution. According to this, the overall impedance for PCC coated sample after 1 week of immersion in Kokubo is 1100 Ω cm^2 while for the as printed sample is 250 Ω cm^2 in the same conditions.

6 Scientific output

Publications in International Journals

- F. Di Franco, A. Zaffora, D. Pupillo, L. Iannucci, S. Grassini, M. Santamaria, The Effect of Electronic Properties of Anodized and Hard Anodized Ti and Ti6Al4V on Their Reactivity in Simulated Body Fluid, J Electrochem Soc 169 (2022) 071506. https://doi.org/10.1149/1945-7111/ac8316.

- D. Pupillo, A. Zaffora, F. Di Franco, P. Picone, D. Nuzzo, M. Santamaria, Enhancing Biocompatibility and Antibacterial Activity of Ti6Al4V by Entrapping Ag and Hydroxyapatite Inside Alginate Filled Pores of TiO_2 Layer Grown by Spark Anodizing, Adv Mater Interfaces 10 (2023). https://doi.org/10.1002/admi.202201725.

- D. Pupillo, F. Di Franco, D. Palmeri, G. Pollara, G. Buffa, L. Fratini, M. Santamaria, Surface treatments on 3D printed Ti6Al4V biomedical plates to enhance corrosion resistance in simulated physiological solutions and under inflammatory conditions, Corros Sci 240 (2024). https://doi.org/10.1016/j.corsci.2024.112451.

- D. Pupillo, M.P. Bruns, L.H. Prado, F. Di Franco, D. Böhringer, A. Mazare, W.H. Goldmann, S. Virtanen, M. Santamaria, A.B. Tesler, Corrosion Resistance of Biodegradable Zinc Surfaces Enhanced by UV-Grafted Polydimethylsiloxane Coating, ACS Biomater Sci Eng 10 (2024) 4891–4900. https://doi.org/10.1021/acsbiomaterials.4c00503.

Papers “Under review”

- D. Pupillo, F. Di Franco, L. Iannucci, S. Grassini, S. Virtanen, M. Santamaria, Following the biodegradation rate of zinc to assess the long-term immersion tests in different physiological solutions to assess the corrosion behaviour of zinc for biodegradable implants.

Conference Contributions

- *A. Rizzuti, A. Cusanno, D. Sorgente, A. De Bonis, A. Salvi, M. Santamaria, D. Pupillo, P. Mastrorilli, G. Palumbo,* Surface coating of magnesium alloy resorbable implants manufactured via superplastic forming, XXVIII Congresso Nazionale della Società Chimica Italiana, 26th august- 31st august 2024, Milano, Italy

- *M. Santamaria, D. Pupillo, V. Verro, G. Tranchida, A. B. Tesler, S. Virtanen, F. Di Franco,* Tuning the biodegradation rate of Mg alloys for bioresorbable implants, The 75th Annual Meeting of the International Society of Electrochemistry, 18th august- 23 august 2024, Montréal, Canada

- *F. Di Franco, D. Pupillo, L. Iannucci, S. Grassini, M. Santamaria,* The effect of different physiological solutions on corrosion behaviour of zinc for biodegradable implants, The 75th Annual Meeting of the International Society of Electrochemistry, 18th august- 23 august 2024, Montréal, Canada

- *D. Pupillo* ***(presenting author)****, L. Iannucci, F. Di Franco, S. Grassini, M. Santamaria,* Role of different physiological solutions on corrosion behaviour of zinc for biodegradable implants, Gordon research conference Aqueous corrosion, 7th July – 12th July 2024, New London, USA. (poster)

- *D. Pupillo* ***(presenting author),*** Workshop organized by University of Illinois Chicago Advancements in Biomaterials and Biomedical Engineering: Innovations and Applications in Dental and Medicine, 25th November 2023, Chicago, USA

- *F. Di Franco, A. Zaffora, D. Pupillo, L. Iannucci, S. Grassini, M. Santamaria,* The effect of electronic properties of anodized and hard anodized Ti and Ti6Al4V on their reactivity in Simulated Body Fluid, The 74th Annual Meeting of the International Society of Electrochemistry, 3rd September – 8th September 2023, Lyon, France.

- *D. Pupillo* ***(presenting author),*** *L. Iannucci, F. Di Franco, A. Zaffora, P. Picone, D. Nuzzo, S. Grassini M. Santamaria,* Improvement of bioactivity of Ti-6Al-4V by electrochemical processes, Eurocorr 2023, Brussels, Belgium, 27th august- 31st august 2023, Brussels, Belgium

- *D. Pupillo* ***(presenting author),*** *L. Iannucci, F. Di Franco, A. Zaffora, P. Picone, D. Nuzzo, S. Grassini M. Santamaria,* Miglioramento della bioattività di leghe Ti6Al4V mediante processi elettrochimici, XV edizione delle

Giornate Nazionali sulla Corrosione e Protezione, 5th July – 7th July 2023, Torino, Italy

- *F. Di Franco, D. Pupillo, A. Zaffora, P. Picone, D. Nuzzo, M. Santamaria,* Improvement of bioactivity of Ti-6Al-4V by anodizing and post-anodizing processes, Giornate dell'Elettrochimica Italiana (GEI), 11rd September – 15th September 2022, Orvieto, Italy

- *F. Di Franco, D. Pupillo, A. Zaffora, P. Picone, D. Nuzzo, M. Santamaria,* Improvement of bioactivity of Ti-6Al-4V by anodizing and post-anodizing processes, The 73rd Annual Meeting of the International Society of Electrochemistry, 11rd September – 16th September 2022 Online Meeting

7 References

[1] Q. Chen, G.A. Thouas, Metallic implant biomaterials, Materials Science and Engineering R: Reports 87 (2015) 1–57. https://doi.org/10.1016/j.mser.2014.10.001.

[2] D. Pupillo, A. Zaffora, F. Di Franco, P. Picone, D. Nuzzo, M. Santamaria, Enhancing Biocompatibility and Antibacterial Activity of Ti6Al4V by Entrapping Ag and Hydroxyapatite Inside Alginate Filled Pores of TiO2 Layer Grown by Spark Anodizing, Adv Mater Interfaces 10 (2023). https://doi.org/10.1002/admi.202201725.

[3] S. Virtanen, Corrosion in biomedical applications, in: Encyclopedia of Interfacial Chemistry: Surface Science and Electrochemistry, Elsevier, 2018: pp. 128–133. https://doi.org/10.1016/B978-0-12-409547-2.13432-8.

[4] B.L. Pereira, G. Beilner, C.M. Lepienski, E.S. Szameitat, B.S. Chee, N.K. Kuromoto, L.L. dos Santos, I. Mazzaro, A.P.R.A. Claro, M.J.D. Nugent, Oxide coating containing apatite formed on Ti-25Nb-25Ta alloy treated by Two-Step Plasma Electrolytic Oxidation, Surf Coat Technol 382 (2020). https://doi.org/10.1016/j.surfcoat.2019.125224.

[5] K. Yang, C. Zhou, H. Fan, Y. Fan, Q. Jiang, P. Song, H. Fan, Y. Chen, X. Zhang, Bio-functional design, application and trends in metallic biomaterials, Int J Mol Sci 19 (2018). https://doi.org/10.3390/ijms19010024.

[6] A. Zaffora, F. Di Franco, D. Virtù, F. Carfì Pavia, G. Ghersi, S. Virtanen, M. Santamaria, Tuning of the Mg Alloy AZ31 Anodizing Process for Biodegradable Implants, ACS Appl Mater Interfaces 13 (2021) 12866–12876. https://doi.org/10.1021/acsami.0c22933.

[7] H. Hermawan, D. Dubé, D. Mantovani, Developments in metallic biodegradable stents, Acta Biomater 6 (2010) 1693–1697. https://doi.org/10.1016/j.actbio.2009.10.006.

[8] A. Nouri, A. Rohani Shirvan, Y. Li, C. Wen, Biodegradable metallic suture anchors: A review, Smart Materials in Manufacturing 1 (2023) 100005. https://doi.org/10.1016/j.smmf.2022.100005.

[9] D. Pupillo, M.P. Bruns, L.H. Prado, F. Di Franco, D. Böhringer, A. Mazare, W.H. Goldmann, S. Virtanen, M. Santamaria, A.B. Tesler, Corrosion Resistance of Biodegradable Zinc Surfaces Enhanced by UV-Grafted Polydimethylsiloxane Coating, ACS Biomater Sci Eng 10 (2024) 4891–4900. https://doi.org/10.1021/acsbiomaterials.4c00503.

[10] N. Assefa, Y. Tsige, LECTURE NOTES Human Anatomy and Physiology, n.d.

[11] T. Kokubo, K. Hata, T. Nakamura, T. Yamamuro, Apatite Formation on Ceramics, Metals and Polymers Induced by a CaO SiO2 Based Glass in a Simulated Body Fluid, in: Bioceramics, Elsevier, 1991: pp. 113–120. https://doi.org/10.1016/b978-0-7506-0269-3.50020-7.

[12] M. Prestat, D. Thierry, Corrosion of titanium under simulated inflammation conditions: clinical context and in vitro investigations, Acta Biomater 136 (2021) 72–87. https://doi.org/10.1016/j.actbio.2021.10.002.

[13] A. Sotniczuk, W. Chromiński, B. Adamczyk-Cieślak, M. Pisarek, H. Garbacz, Corrosion behaviour of biomedical Ti under simulated inflammation: Exploring the relevance of grain refinement and crystallographic texture, Corros Sci 200 (2022). https://doi.org/10.1016/j.corsci.2022.110238.

[14] X. Liu, W. Yuan, D. Shen, Y. Cheng, D. Chen, Y. Zheng, Exploring the biodegradation of pure Zn under simulated inflammatory condition, Corros Sci 189 (2021). https://doi.org/10.1016/j.corsci.2021.109606.

[15] J. Toledano-Serrabona, B.M. Bosch, L. Díez-Tercero, F.J. Gil, O. Camps-Font, E. Valmaseda-Castellón, C. Gay-Escoda, M.Á. Sánchez-Garcés, Evaluation of the inflammatory and osteogenic response induced by titanium particles released during implantoplasty of dental implants, Sci Rep 12 (2022). https://doi.org/10.1038/s41598-022-20100-2.

[16] J. Walczak, F. Shahgaldi, F. Heatley, In vivo corrosion of 316L stainless-steel hip implants: morphology and elemental compositions of corrosion products, 1998.

[17] J. Wu, M. Li, Y. Zhou, K. Xu, X. Li, C. Lin, J. Zhang, K. Cai, Pitting behavior of 316L stainless steel in direct culture with mesenchymal stem cells, Corros Sci 204 (2022). https://doi.org/10.1016/j.corsci.2022.110380.

[18] W. Xu, F. Yu, L. Yang, B. Zhang, B. Hou, Y. Li, Accelerated corrosion of 316L stainless steel in simulated body fluids in the presence of H2O2 and albumin, Materials Science and Engineering C 92 (2018) 11–19. https://doi.org/10.1016/j.msec.2018.06.023.

[19] Z. Wang, F. Di-Franco, A. Seyeux, S. Zanna, V. Maurice, P. Marcus, Passivation-Induced Physicochemical Alterations of the Native Surface Oxide Film on 316L Austenitic Stainless Steel, J Electrochem Soc 166 (2019) C3376–C3388. https://doi.org/10.1149/2.0321911jes.

[20] M. Santamaria, F. Di Franco, F. Di Quarto, M. Pisarek, S. Zanna, P. Marcus, Photoelectrochemical and XPS characterisation of oxide layers on 316L stainless steel grown in high-temperature water, Journal of Solid State Electrochemistry 19 (2015) 3511–3519. https://doi.org/10.1007/s10008-015-2849-0.

[21] J.R.. Davis, Alloy digest sourcebook : stainless steels, ASM International, 2000.

[22] C. Lombard, P. Gillet, E. Germain, F. Boubaker, A. Blum, P.A. Gondim Teixeira, R. Gillet, Imaging in Hip Arthroplasty Management Part 2: Postoperative Diagnostic Imaging Strategy, J Clin Med 11 (2022). https://doi.org/10.3390/jcm11154416.

[23] M. Merola, S. Affatato, Materials for hip prostheses: A review of wear and loading considerations, Materials 12 (2019). https://doi.org/10.3390/ma12030495.

[24] S. Spriano, S. Yamaguchi, F. Baino, S. Ferraris, A critical review of multifunctional titanium surfaces: New frontiers for improving osseointegration and host response, avoiding bacteria contamination, Acta Biomater 79 (2018) 1–22. https://doi.org/10.1016/j.actbio.2018.08.013.

[25] L. Zhao, P.K. Chu, Y. Zhang, Z. Wu, Antibacterial coatings on titanium implants, J Biomed Mater Res B Appl Biomater 91 (2009) 470–480. https://doi.org/10.1002/jbm.b.31463.

[26] X. Han, J. Ma, A. Tian, Y. Wang, Y. Li, B. Dong, X. Tong, X. Ma, Surface modification techniques of titanium and titanium alloys for biomedical orthopaedics applications: A review, Colloids Surf B Biointerfaces 227 (2023). https://doi.org/10.1016/j.colsurfb.2023.113339.

[27] Y. Shi, Z. Xue, P. Li, S. Yang, D. Zhang, S. Zhou, Z. Guan, Y. Li, L.N. Wang, Surface modification on biodegradable zinc alloys, Journal of Materials Research and Technology 25 (2023) 3670–3687. https://doi.org/10.1016/j.jmrt.2023.06.149.

[28] S. V. Harb, N.J. Bassous, T.A.C. de Souza, A. Trentin, S.H. Pulcinelli, C. V. Santilli, T.J. Webster, A.O. Lobo, P. Hammer, Hydroxyapatite and β-TCP modified PMMA-TiO2 and PMMA-ZrO2 coatings for bioactive corrosion protection of Ti6Al4V implants, Materials Science and Engineering C 116 (2020) 111149. https://doi.org/10.1016/j.msec.2020.111149.

[29] B.L. Pereira, G. Beilner, C.M. Lepienski, E.S. Szameitat, B.S. Chee, N.K. Kuromoto, L.L. dos Santos, I. Mazzaro, A.P.R.A. Claro, M.J.D. Nugent, Oxide coating containing apatite formed on Ti-25Nb-25Ta alloy treated by Two-Step Plasma Electrolytic Oxidation, Surf Coat Technol 382 (2020). https://doi.org/10.1016/j.surfcoat.2019.125224.

[30] V. Müller, T. Pagnier, S. Tadier, L. Gremillard, M. Jobbagy, E. Djurado, Design of advanced one-step hydroxyapatite coatings for biomedical applications using the electrostatic spray deposition, Appl Surf Sci 541 (2021). https://doi.org/10.1016/j.apsusc.2020.148462.

[31] V.T. Nguyen, T.C. Cheng, T.H. Fang, M.H. Li, The fabrication and characteristics of hydroxyapatite film grown on titanium alloy Ti-6Al-4V by anodic treatment, Journal of Materials Research and Technology 9 (2020) 4817–4825. https://doi.org/10.1016/j.jmrt.2020.03.002.

[32] H. Ishizawa, M. Fujino, M. Ogino, Histomorphometric evaluation of the thin hydroxyapatite layer formed through anodization followed by hydrothermal treatment, J Biomed Mater Res 35 (1997) 199–206. https://doi.org/10.1002/(SICI)1097-4636(199705)35:2<199::AID-JBM8>3.0.CO;2-I.

[33] H. Ishizawa, M. Ogino, Formation and characterization of anodic titanium oxide films containing Ca and P, J Biomed Mater Res 29 (1995) 65–72. https://doi.org/10.1002/jbm.820290110.

[34] A.C. Alves, F. Wenger, P. Ponthiaux, J.P. Celis, A.M. Pinto, L.A. Rocha, J.C.S. Fernandes, Corrosion mechanisms in titanium oxide-based films produced by anodic treatment, Electrochim Acta 234 (2017) 16–27. https://doi.org/10.1016/j.electacta.2017.03.011.

[35] S. Yu, D. Guo, J. Han, L. Sun, H. Zhu, Z. Yu, M. Dargusch, G. Wang, Enhancing Antibacterial Performance and Biocompatibility of Pure Titanium by a Two-Step Electrochemical Surface Coating, ACS Appl Mater Interfaces 12 (2020) 44433–44446. https://doi.org/10.1021/acsami.0c10032.

[36] H. Dong, F. Lin, A.R. Boccaccini, S. Virtanen, Corrosion behavior of biodegradable metals in two different simulated physiological solutions: Comparison of Mg, Zn and Fe, Corros Sci 182 (2021). https://doi.org/10.1016/j.corsci.2021.109278.

[37] K. Sangeetha, A. V. Jisha Kumari, J. Venkatesan, A. Sukumaran, S. Aisverya, P.N. Sudha, Degradable metallic biomaterials for cardiovascular applications, in: Fundamental Biomaterials: Metals, Elsevier, 2018: pp. 285–298. https://doi.org/10.1016/B978-0-08-102205-4.00013-1.

[38] Y. Zheng, X. Liu, D. Shen, W. Li, Y. Cheng, M. Yang, Y. Kou, B. Jiang, Perceiving the connection between the bone healing process and biodegradation of biodegradable metal implants through precise bioadaptability principle, J Mater Sci Technol 147 (2023) 132–144. https://doi.org/10.1016/j.jmst.2022.12.004.

[39] C. Shuai, S. Li, S. Peng, P. Feng, Y. Lai, C. Gao, Biodegradable metallic bone implants, Mater Chem Front 3 (2019) 544–562. https://doi.org/10.1039/c8qm00507a.

[40] Y.F. Zheng, X.N. Gu, F. Witte, Biodegradable metals, Materials Science and Engineering R: Reports 77 (2014) 1–34. https://doi.org/10.1016/j.mser.2014.01.001.

[41] F. Witte, Biodegradable Metals, n.d.

[42] F. Witte, N. Hort, C. Vogt, S. Cohen, K.U. Kainer, R. Willumeit, F. Feyerabend, Degradable biomaterials based on magnesium corrosion, Curr Opin Solid State Mater Sci 12 (2008) 63–72. https://doi.org/10.1016/j.cossms.2009.04.001.

[43] F. Witte, The history of biodegradable magnesium implants: A review, Acta Biomater 6 (2010) 1680–1692. https://doi.org/10.1016/j.actbio.2010.02.028.

[44] A. Eliezer, F. Witte, Corrosion behavior of magnesium alloys in biomedical environments, in: Adv Mat Res, Trans Tech Publications Ltd, 2010: pp. 17–20. https://doi.org/10.4028/www.scientific.net/amr.95.17.

[45] Y. Wang, C.S. Lim, C.V. Lim, M.S. Yong, E.K. Teo, L.N. Moh, In vitro degradation behavior of M1A magnesium alloy in protein-containing simulated body fluid, Materials Science and Engineering C 31 (2011) 579–587. https://doi.org/10.1016/j.msec.2010.11.017.

[46] M. Liu, Q. Zhang, X. Tang, C. Liu, D. Mei, L. Wang, S. Zhu, M.L. Zheludkevich, S. Lamaka, S. Guan, Effect of medium renewal mode on the degradation behavior of Mg alloys for biomedical applications during the

long-term in vitro test, Corros Sci 229 (2024). https://doi.org/10.1016/j.corsci.2024.111851.

[47] S. Han, S. Loffredo, I. Jun, J. Edwards, Y.-C. Kim, H.-K. Seok, F. Witte, D. Mantovani, S. Glyn-Jones, Current status and outlook on the clinical translation of biodegradable metals, (2018). https://doi.org/10.1016/j.mattod.2018.05.018This.

[48] C. Rapetto, M. Leoncini, Magmaris: A new generation metallic sirolimus-eluting fully bioresorbable scaffold: Present status and future perspectives, J Thorac Dis 9 (2017) S903–S913. https://doi.org/10.21037/jtd.2017.06.34.

[49] L.M. de Andrade, C. Paternoster, P. Chevallier, S. Gambaro, P. Mengucci, D. Mantovani, Surface processing for iron-based degradable alloys: A preliminary study on the importance of acid pickling, Bioact Mater 11 (2022) 166–180. https://doi.org/10.1016/j.bioactmat.2021.09.026.

[50] M. Moravej, D. Mantovani, Biodegradable metals for cardiovascular stent application: Interests and new opportunities, Int J Mol Sci 12 (2011) 4250–4270. https://doi.org/10.3390/ijms12074250.

[51] D. Pupillo, M.P. Bruns, L.H. Prado, F. Di Franco, D. Böhringer, A. Mazare, W.H. Goldmann, S. Virtanen, M. Santamaria, A.B. Tesler, Corrosion Resistance of Biodegradable Zinc Surfaces Enhanced by UV-Grafted Polydimethylsiloxane Coating, ACS Biomater Sci Eng (2024). https://doi.org/10.1021/acsbiomaterials.4c00503.

[52] G.L. Wu, C.E. Yen, Y.S. Lin, M.L. Yeh, Evaluation of Biodegradability and Biocompatibility of Pure Zinc Coated with Zinc Phosphate for Cardiovascular Stent Applications, J Med Biol Eng 43 (2023) 732–740. https://doi.org/10.1007/s40846-023-00834-8.

[53] Z. Guan, C.S. Linsley, S. Pan, G. Yao, B.M. Wu, D.S. Levi, X. Li, Zn-Mg-WC Nanocomposites for Bioresorbable Cardiovascular Stents: Microstructure, Mechanical Properties, Fatigue, Shelf Life, and Corrosion, ACS Biomater Sci Eng 8 (2022) 328–339. https://doi.org/10.1021/acsbiomaterials.1c01358.

[54] J. Liu, C.S. Linsley, Y. Su, W. Abd-Elaziem, S. Pan, M. Sokoluk, A. Griebel, G. Chen, Y. Zeng, N. Murali, S. Bialo, A. Jiang, B.M. Wu, D. Zhu, X. Li, Nanoparticle-Enabled Zn-0.1Mg Alloy with Long-Term Stability, Refined Degradation, and Favorable Biocompatibility for Biodegradable Implant Devices, ACS Appl Mater Interfaces (2024). https://doi.org/10.1021/acsami.4c04714.

[55] J. Lin, Y. Chen, Y. Dai, X. Zhang, D. Zhang, Y. Li, C. Wen, Mechanical properties, degradation action, and biocompatibility of in situ nanoparticle-reinforced MgxZny/Zn composite prepared via roll bonding, Acta Biomater (2025). https://doi.org/10.1016/j.actbio.2025.01.048.

[56] X. Zhuo, Y. Wu, J. Ju, H. Liu, J. Jiang, Z. Hu, J. Bai, F. Xue, Recent progress of novel biodegradable zinc alloys: from the perspective of strengthening and toughening, Journal of Materials Research and Technology 17 (2022) 244–269. https://doi.org/10.1016/j.jmrt.2022.01.004.

[57] S. Ould Mohamed, S. Gambaro, A.L. Ramirez-Ledesma, C. Paternoster, D. Mantovani, Effects of Different CO2 Concentrations and Degradation Media on Static Corrosion of Commercially Pure Zinc, Crystals (Basel) 13 (2023). https://doi.org/10.3390/cryst13050753.

[58] X. Liu, H. Yang, Y. Liu, P. Xiong, H. Guo, H.H. Huang, Y. Zheng, Comparative Studies on Degradation Behavior of Pure Zinc in Various Simulated Body Fluids, JOM 71 (2019) 1414–1425. https://doi.org/10.1007/s11837-019-03357-3.

[59] C. Wang, X. Liu, D. Mei, M. Deng, Y. Zheng, M.L. Zheludkevich, S. V. Lamaka, Local pH and oxygen concentration at the interface of Zn alloys in Tris-HCl or HEPES buffered Hanks' balanced salt solution, Corros Sci 197 (2022). https://doi.org/10.1016/j.corsci.2021.110061.

[60] H. Dong, S. Virtanen, Influence of bovine serum albumin on biodegradation behavior of pure Zn, J Biomed Mater Res B Appl Biomater 110 (2022) 185–194. https://doi.org/10.1002/jbm.b.34901.

[61] V. Shkirskiy, P. Keil, H. Hintze-Bruening, F. Leroux, F. Brisset, K. Ogle, P. Volovitch, The effects of l-cysteine on the inhibition and accelerated dissolution processes of zinc metal, Corros Sci 100 (2015) 101–112. https://doi.org/10.1016/j.corsci.2015.07.010.

[62] H. Dong, J. Zhou, S. Virtanen, Fabrication of ZnO nanotube layer on Zn and evaluation of corrosion behavior and bioactivity in view of biodegradable applications, Appl Surf Sci 494 (2019) 259–265. https://doi.org/10.1016/j.apsusc.2019.07.165.

[63] G. Sun, J. Ma, S. Zhang, Electrophoretic deposition of zinc-substituted hydroxyapatite coatings, Materials Science and Engineering C 39 (2014) 67–72. https://doi.org/10.1016/j.msec.2014.02.023.

[64] Y. Shi, L. Yang, L. Wang, Q. Zhang, X. Zhu, W. Sun, J. Shen, T. Lu, Z. Song, H. Liu, Corrosion and Biocompatibility of Pure Zn with a Micro-Arc-Oxidized Layer Coated with Calcium Phosphate, Coatings 11 (2021). https://doi.org/10.3390/COATINGS11111425.

[65] S. Su, Q. Tang, D. Qu, In Vitro Study of Degradation and Cytocompatibility of Ceramics/PLA Composite Coating on Pure Zinc for Orthopedic Application, Front Bioeng Biotechnol 10 (2022). https://doi.org/10.3389/fbioe.2022.856986.

[66] Y. Su, K. Wang, J. Gao, Y. Yang, Y.X. Qin, Y. Zheng, D. Zhu, Enhanced cytocompatibility and antibacterial property of zinc phosphate coating on biodegradable zinc materials, Acta Biomater 98 (2019) 174–185. https://doi.org/10.1016/j.actbio.2019.03.055.

[67] F. La Mantia, H. Habazaki, M. Santamaria, F. Di Quarto, A critical assessment of the Mott-Schottky analysis for the characterisation of passive film-electrolyte junctions, Russian Journal of Electrochemistry 46 (2010) 1306–1322. https://doi.org/10.1134/S102319351011011X.

[68] T. Academy, R. Academy, S.S. Trakt, Handbook of Thin Film Materials, Appl. Phys. A 73 (n.d.) 1–21.

[69] P. Marcus, F. Mansfeld, Analytical Methods in Corrosion Science and Engineering, 2007.
[70] V. Maurice, P. Marcus, Modern Aspects of Electrochemistry, 2009.
[71] F. Di Quarto, C. Sunseri, S. Piazza, M.C. Romano, Semiempirical Correlation between Optical Band Gap Values of Oxides and the Difference of Electronegativity of the Elements. Its Importance for a Quantitative Use of Photocurrent Spectroscopy in Corrosion Studies, J Phys Chem B 101 (1997) 2519–2525. https://doi.org/10.1021/jp970046n.
[72] A. Chiba, I. Muto, Y. Sugawara, N. Hara, Pit Initiation Mechanism at MnS Inclusions in Stainless Steel: Synergistic Effect of Elemental Sulfür and Chloride Ions, J Electrochem Soc 160 (2013) C511–C520. https://doi.org/10.1149/2.081310jes.
[73] A.J. Bard, L.R. Faulkner, Fundamentals and Fundamentals and Applications, second, 2001. https://doi.org/10.1016/B978-0-08-098353-0.00003-8.
[74] M.E.O.& B. Tribollet, Electrochemical Impedance Spectroscopy, 2008.
[75] F. La Mantia, M. Fan, J. Stojadinović, M. Santamaria, S. Miraghaei, F. Di Quarto, Assessment on the use of the amorphous semiconductor theory for the analysis of oxide films, Electrochim Acta 179 (2015) 460–468. https://doi.org/10.1016/j.electacta.2015.03.179.
[76] F. Di Quarto, F. La Mantia, M. Santamaria, Physicochemical characterization of passive films on niobium by admittance and electrochemical impedance spectroscopy studies, Electrochim Acta 50 (2005) 5090–5102. https://doi.org/10.1016/j.electacta.2005.03.065.
[77] A. Alaoui Mouayd, M.E. Orazem, E.M.M. Sutter, B. Tribollet, A. Koltsov, Contribution of electrochemical dissolution during pickling of low carbon steel in acidic solutions, Corros Sci 82 (2014) 362–368. https://doi.org/10.1016/j.corsci.2014.01.036.
[78] M. Musiani, M.E. Orazem, N. Pébère, B. Tribollet, V. Vivier, Constant-phase-element behavior caused by coupled resistivity and permittivity distributions in films, J Electrochem Soc 158 (2011) 424–428. https://doi.org/10.1149/2.039112jes.
[79] M.E. Orazem, I. Frateur, B. Tribollet, V. Vivier, S. Marcelin, N. Pebere, A.L. Bunge, E.A. White, D.P. Riemer, M. Musiani, Dielectric properties of materials showing constant-phase-element (CPE) impedance response, J Electrochem Soc 160 (2013) 215–225. https://doi.org/10.1149/2.033306jes.
[80] B. Hirschorn, M.E. Orazem, B. Tribollet, V. Vivier, I. Frateur, M. Musiani, Constant-phase-element behavior caused by resistivity distributions in films: I. Theory, Journal of Electrochemical Society 157 (2010).
[81] S. Marcelin, B. Ter-Ovanessian, B. Normand, Electronic properties of passive films from the multi-frequency Mott-Schottky and power-law coupled approach, Electrochem Commun 66 (2016) 62–65. https://doi.org/10.1016/j.elecom.2016.03.003.
[82] A. Alaoui Mouayd, M.E. Orazem, E.M.M. Sutter, B. Tribollet, A. Koltsov, Contribution of electrochemical dissolution during pickling of low carbon

steel in acidic solutions, Corros Sci 82 (2014) 362–368. https://doi.org/10.1016/j.corsci.2014.01.036.
[83] P. Pedeferri, M. Ormellese, M. Pedeferri, CORROSIONE E PROTEZIONE DEI MATERIALI, 2005.
[84] R.G. Kelly, J.R. Scully, D. Shoesmith, R.G. Buchheit, Electrochemical Techniques in Corrosion Science and Engineering, CRC Press, 2002. https://doi.org/10.1201/9780203909133.
[85] F. Di Franco, A. Zaffora, D. Pupillo, L. Iannucci, S. Grassini, M. Santamaria, The Effect of Electronic Properties of Anodized and Hard Anodized Ti and Ti6Al4V on Their Reactivity in Simulated Body Fluid, J Electrochem Soc 169 (2022) 071506. https://doi.org/10.1149/1945-7111/ac8316.
[86] H. Habazaki, M. Uozumi, H. Konno, K. Shimizu, P. Skeldon, G.E. Thompson, Crystallization of anodic titania on titanium and its alloys, Corros Sci 45 (2003) 2063–2073.
[87] F. Di Quarto, F. Di Franco, C. Monarca, M. Santamaria, H. Habazaki, Photoelectrochemical characterization of amorphous anodic films on Ti–6at.%Si, Electrochim Acta 110 (2013) 517–525.
[88] A. Zaffora, M. Santamaria, F. Di Franco, H. Habazaki, F. Di Quarto, Photoelectrochemical evidence of inhomogeneous composition at nm length scale of anodic films on valve metals alloys, Electrochim Acta 201 (2016) 333–339.
[89] A. Zaffora, F. Di Franco, F. Di Quarto, R. Macaluso, M. Mosca, H. Habazaki, M. Santamaria, The Effect of Nb Incorporation on the Electronic Properties of Anodic HfO_2, ECS Journal of Solid State Science and Technology 6 (2017) N25–N31.
[90] N.F. Mott, E.A. Davis, Electronic Processes In Non-Crystalline Materials, 2nd ed., Clarendon Press, Oxford, U.K., 1979.
[91] F. Di Franco, A. Zaffora, M. Santamaria, Band gap narrowing and dielectric constant enhancement of $(Nb_xTa_{(1-x)})_2O_5$ by electrochemical nitrogen doping, Electrochim Acta 265 (2018) 326–335.
[92] M.M. Lohrengel, Thin anodic oxide layers on aluminium and other valve metals: high field regime, Materials Science and Engineering: R: Reports 11 (1993) 243–294.
[93] A. Zaffora, G. Tranchida, F. Di Franco, F. Di Quarto, M. Santamaria, Physico-Chemical Characterization of Anodic Oxides on Hf as a Function of the Anodizing Conditions, J Electrochem Soc 163 (2016) C563–C570.
[94] M.T. Tanvir, K. Fushimi, K. Shimizu, S. Nagata, P. Skeldon, G.E. Thompson, H. Habazaki, Influence of silicon on the growth of barrier-type anodic films on titanium, Electrochim Acta 52 (2007) 6834–6840.
[95] M. Pourbaix, Atlas of electrochemical equilibria in aqueous solutions, Pergamon Press, Oxford, UK, 1966.
[96] SURFACE SCIENCE AND ELECTROCHEMISTRY, n.d.
[97] F. Di Quarto, F. Di Franco, C. Monarca, M. Santamaria, H. Habazaki, Photoelectrochemical characterization of amorphous anodic films on Ti-

6at.%Si, Electrochim Acta 110 (2013) 517–525. https://doi.org/10.1016/j.electacta.2013.01.120.

[98] A. Zaffora, M. Santamaria, F. Di Franco, H. Habazaki, F. Di Quarto, Photoelectrochemical evidence of nitrogen incorporation during anodizing sputtering-deposited Al-Ta alloys, Physical Chemistry Chemical Physics 18 (2016) 351–360.

[99] A.L. Yerokhin, X. Nie, A. Leyland, A. Matthews, S.J. Dowey, Plasma electrolysis for surface engineering, Surf Coat Technol 122 (1999) 73–93. https://doi.org/10.1016/S0257-8972(99)00441-7.

[100] H. Ishizawa, M. Ogino, Formation and characterization of anodic titanium oxide films containing Ca and P, J Biomed Mater Res 29 (1995) 65–72. https://doi.org/10.1002/JBM.820290110.

[101] A.C. Alves, F. Wenger, P. Ponthiaux, J.P. Celis, A.M. Pinto, L.A. Rocha, J.C.S. Fernandes, Corrosion mechanisms in titanium oxide-based films produced by anodic treatment, Electrochim Acta 234 (2017) 16–27. https://doi.org/10.1016/J.ELECTACTA.2017.03.011.

[102] E. Matykina, M. Montuori, J. Gough, F. Monfort, A. Berkani, P. Skeldon, G.E. Thompson, H. Habazaki, Spark anodising of titanium for biomedical applications, Transactions of the Institute of Metal Finishing 84 (2006) 125–133. https://doi.org/10.1179/174591906X123967.

[103] M. Santamaria, G. Conigliaro, F. Di Franco, B. Megna, F. Di Quarto, Electronic properties of thermal oxides on ti and their influence on impedance and photoelectrochemical behavior of TiO2 nanotubes, J Electrochem Soc 164 (2017) C113–C120.

[104] N. Sato, Electrochemistry at Metal and Semiconductor Electrodes, Elsevier Science B.V., Amsterdam, 1998.

[105] M. Epifani, R. Díaz, C. Force, E. Comini, T. Andreu, R.R. Zamani, J. Arbiol, P. Siciliano, G. Faglia, J.R. Morante, Colloidal counterpart of the TiO2-supported V2O5 system: A case study of oxide-on-oxide deposition by wet chemical techniques. Synthesis, vanadium speciation, and gas-sensing enhancement, Journal of Physical Chemistry C 117 (2013) 20697–20705. https://doi.org/10.1021/jp406518w.

[106] M. Santamaria, F. Di Franco, F. Di Quarto, P. Skeldon, G.E. Thompson, Tailoring of the Solid State Properties of Al–Nb Mixed Oxides: A Photoelectrochemical Study, The Journal of Physical Chemistry C 117 (2013) 4201–4210.

[107] T. Moskalewicz, M. Warcaba, Ł. Cieniek, M. Sitarz, M. Gajewska, A.R. Boccaccini, Hydroxyapatite/sodium alginate coatings electrophoretically deposited on titanium substrates: microstructure and properties, Appl Surf Sci 540 (2021). https://doi.org/10.1016/j.apsusc.2020.148353.

[108] A. Zaffora, F. Di Franco, D. Virtù, F. Carfì Pavia, G. Ghersi, S. Virtanen, M. Santamaria, Tuning of the Mg Alloy AZ31 Anodizing Process for Biodegradable Implants, ACS Appl Mater Interfaces 13 (2021) 12866–12876. https://doi.org/10.1021/acsami.0c22933.

[109] E. Matykina, M. Montuori, J. Gough, F. Monfort, A. Berkani, P. Skeldon, G.E. Thompson, H. Habazaki, Spark anodising of titanium for biomedical applications, Transactions of the Institute of Metal Finishing 84 (2006) 125–133. https://doi.org/10.1179/174591906X123967.

[110] H.N. Pantaroto, J.M. Cordeiro, L.T. Pereira, A.B. de Almeida, F.H. Nociti Junior, E.C. Rangel, N.F. Azevedo Neto, J.H.D. da Silva, V.A.R. Barão, Sputtered crystalline TiO2 film drives improved surface properties of titanium-based biomedical implants, Materials Science and Engineering C 119 (2021). https://doi.org/10.1016/j.msec.2020.111638.

[111] D. Georgescu, L. Baia, O. Ersen, M. Baia, S. Simon, Experimental assessment of the phonon confinement in TiO2 anatase nanocrystallites by Raman spectroscopy, Journal of Raman Spectroscopy 43 (2012) 876–883. https://doi.org/10.1002/jrs.3103.

[112] H.N. Pantaroto, J.M. Cordeiro, L.T. Pereira, A.B. de Almeida, F.H. Nociti Junior, E.C. Rangel, N.F. Azevedo Neto, J.H.D. da Silva, V.A.R. Barão, Sputtered crystalline TiO2 film drives improved surface properties of titanium-based biomedical implants, Materials Science and Engineering C 119 (2021). https://doi.org/10.1016/j.msec.2020.111638.

[113] D.A. Crespo-Yapur, A.S. Elizondo, D. Herrera, M. Videa, Galvanostatic electrodeposition of silver nanoparticles: Nucleation and growth studies, Mater Today Proc 48 (2022) 1–4. https://doi.org/10.1016/j.matpr.2020.04.760.

[114] Y.S. Hedberg, F. Gamna, G. Padoan, S. Ferraris, M. Cazzola, G. Herting, M. Atapour, S. Spriano, I. Odnevall Wallinder, Surface modified Ti6Al4V for enhanced bone bonding ability – Effects of silver and corrosivity at simulated physiological conditions from a corrosion and metal release perspective, Corros Sci 168 (2020) 108566. https://doi.org/10.1016/j.corsci.2020.108566.

[115] H. Singh, J. Du, P. Singh, T.H. Yi, Ecofriendly synthesis of silver and gold nanoparticles by Euphrasia officinalis leaf extract and its biomedical applications, Artif Cells Nanomed Biotechnol 46 (2018) 1163–1170. https://doi.org/10.1080/21691401.2017.1362417.

[116] B.K. Mehta, M. Chhajlani, B.D. Shrivastava, Green synthesis of silver nanoparticles and their characterization by XRD, J Phys Conf Ser 836 (2017). https://doi.org/10.1088/1742-6596/836/1/012050.

[117] T. Akiyama, H. Miyamoto, Y. Yonekura, M. Tsukamoto, Y. Ando, I. Noda, M. Sonohata, M. Mawatari, Silver oxide-containing hydroxyapatite coating has in vivo antibacterial activity in the rat tibia, Journal of Orthopaedic Research 31 (2013) 1195–1200. https://doi.org/10.1002/jor.22357.

[118] D. Zhitomirsky, J.A. Roether, A.R. Boccaccini, I. Zhitomirsky, Electrophoretic deposition of bioactive glass/polymer composite coatings with and without HA nanoparticle inclusions for biomedical applications, J Mater Process Technol 209 (2009) 1853–1860. https://doi.org/10.1016/j.jmatprotec.2008.04.034.

[119] J.A. Stammeier, B. Purgstaller, D. Hippler, V. Mavromatis, M. Dietzel, In-situ Raman spectroscopy of amorphous calcium phosphate to crystalline hydroxyapatite transformation, MethodsX 5 (2018) 1241–1250. https://doi.org/10.1016/j.mex.2018.09.015.
[120] V. V. Nosenko, A.M. Yaremko, V.M. Dzhagan, I.P. Vorona, Y.A. Romanyuk, I. V. Zatovsky, Nature of some features in Raman spectra of hydroxyapatite-containing materials, Journal of Raman Spectroscopy 47 (2016) 726–730. https://doi.org/10.1002/jrs.4883.
[121] C. Zhu, Y. Lv, C. Qian, Z. Ding, T. Jiao, X. Gu, E. Lu, L. Wang, F. Zhang, Microstructures, mechanical, and biological properties of a novel Ti-6V-4V/zinc surface nanocomposite prepared by friction stir processing, Int J Nanomedicine 13 (2018) 1881–1898. https://doi.org/10.2147/IJN.S154260.
[122] L. Hong, L. Yuan, X. Xu, Y. Ma, L. Meng, J. Wang, N. Zhao, X. Wang, J. Ma, Biocompatible Nanotube-Strontium/polydopamine-arginine–glycine–aspartic acid coating on Ti6Al4V enhances osteogenic properties for biomedical applications, Microsc Res Tech 85 (2022) 1518–1526. https://doi.org/10.1002/JEMT.24014.
[123] M.I. Neves, L. Moroni, C.C. Barrias, Modulating Alginate Hydrogels for Improved Biological Performance as Cellular 3D Microenvironments, Front Bioeng Biotechnol 8 (2020). https://doi.org/10.3389/fbioe.2020.00665.
[124] F. Di Franco, A. Zaffora, P. Vassallo, M. Santamaria, Double Step Electrochemical Process for the Deposition of Superhydrophobic Coatings for Enhanced Corrosion Resistance, J Electrochem Soc 168 (2021) 101502. https://doi.org/10.1149/1945-7111/ac29df.
[125] F. Di Franco, A. Zaffora, D. Pupillo, L. Iannucci, S. Grassini, M. Santamaria, The Effect of Electronic Properties of Anodized and Hard Anodized Ti and Ti6Al4V on Their Reactivity in Simulated Body Fluid, J Electrochem Soc 169 (2022) 071506. https://doi.org/10.1149/1945-7111/AC8316.
[126] X. He, K. Tang, X. Li, F. Wang, J. Liu, F. Zou, M. Yang, M. Li, A porous collagen-carboxymethyl cellulose/hydroxyapatite composite for bone tissue engineering by bi-molecular template method, Int J Biol Macromol 137 (2019) 45–53. https://doi.org/10.1016/j.ijbiomac.2019.06.098.
[127] V. Babuska, J. Dobra, V. Kulda, M. Kripnerova, A. Moztarzadeh, L. Bolek, J. Lahoda, D. Hrusak, Comparison of fibroblast and osteoblast response to cultivation on titanium implants with different grain sizes, J Nanomater 2015 (2015). https://doi.org/10.1155/2015/920893.
[128] A. Bruinink, R. Luginbuehl, Evaluation of biocompatibility using in vitro methods: interpretation and limitations., Adv Biochem Eng Biotechnol 126 (2012) 117–152. https://doi.org/10.1007/10_2011_111.
[129] ISO 10993-5 Biological Evaluation of Medical Devices. Part 5: Tests for in Vitro Cytotoxicity, (2009).
[130] A. Bruinink, R. Luginbuehl, Evaluation of biocompatibility using in vitro methods: interpretation and limitations., Adv Biochem Eng Biotechnol 126 (2012) 117–152. https://doi.org/10.1007/10_2011_111.

[131] ISO 10993-5 Biological Evaluation of Medical Devices. Part 5: Tests for in Vitro Cytotoxicity, (2009).
[132] F. Rupp, L. Liang, J. Geis-Gerstorfer, L. Scheideler, F. Hüttig, Surface characteristics of dental implants: A review, Dental Materials 34 (2018) 40–57. https://doi.org/10.1016/j.dental.2017.09.007.
[133] ISO 10993-4 Biological evaluation of medical devices — Part 4: Selection of tests for interactions with blooditle, (2002).
[134] T.F. Moriarty, S.A.J. Zaat, H.J. Busscher, Biomaterials associated infection: Immunological aspects and antimicrobial strategies, 2013. https://doi.org/10.1007/978-1-4614-1031-7.
[135] J.D. Caplin, A.J. García, Implantable antimicrobial biomaterials for local drug delivery in bone infection models, Acta Biomater 93 (2019) 2–11. https://doi.org/10.1016/j.actbio.2019.01.015.
[136] M. Contardi, D. Kossyvaki, P. Picone, M. Summa, X. Guo, J.A. Heredia-Guerrero, D. Giacomazza, R. Carzino, L. Goldoni, G. Scoponi, F. Rancan, R. Bertorelli, M. Di Carlo, A. Athanassiou, I.S. Bayer, Electrospun polyvinylpyrrolidone (PVP) hydrogels containing hydroxycinnamic acid derivatives as potential wound dressings, Chemical Engineering Journal 409 (2021). https://doi.org/10.1016/j.cej.2020.128144.
[137] M.L.W. Knetsch, L.H. Koole, New strategies in the development of antimicrobial coatings: The example of increasing usage of silver and silver nanoparticles, Polymers (Basel) 3 (2011) 340–366. https://doi.org/10.3390/polym3010340.
[138] L. Rojo, J.M. Barcenilla, B. Vázquez, R. González, J. San Román, Intrinsically antibacterial materials based on polymeric derivatives of eugenol for biomedical applications, Biomacromolecules 9 (2008) 2530–2535. https://doi.org/10.1021/bm800570u.
[139] J.Y. Cho, W. Xu, M. Brandt, M. Qian, Selective laser melting-fabricated Ti-6Al-4V alloy: Microstructural inhomogeneity, consequent variations in elastic modulus and implications, Opt Laser Technol 111 (2019) 664–670. https://doi.org/10.1016/j.optlastec.2018.08.052.
[140] G. Buffa, D. Palmeri, G. Pollara, F. Di Franco, M. Santamaria, L. Fratini, Process parameters and surface treatment effects on the mechanical and corrosion resistance properties of Ti6Al4V components produced by laser powder bed fusion, Progress in Additive Manufacturing 9 (2024) 151–167. https://doi.org/10.1007/s40964-023-00440-9.
[141] H. Ishizawa, M. Ogino, J. Wiley, Formation and characterization of anodic titanium oxide films containing Ca and P, n.d.
[142] H. Ishizawa, M. Fujino, M. Ogino, Mechanical and histological investigation of hvdrothermallv treated and untreated anodic titanium okde films cohtaining Ca and P, n.d.
[143] H. Ishizawa, M. Ogino, Characterization of thin hydroxyapatite layers formed on anodic titanium oxide films containing Ca and P by hydrothermal treatment, n.d.

[144] B. Hirschorn, M.E. Orazem, B. Tribollet, V. Vivier, I. Frateur, M. Musiani, Determination of effective capacitance and film thickness from constant-phase-element parameters, Electrochim Acta 55 (2010) 6218–6227. https://doi.org/10.1016/j.electacta.2009.10.065.
[145] N. Sato, Electrochemistry at Metal and Semiconductor Electrodes, 1998.
[146] F. Di Franco, A. Zaffora, D. Pupillo, L. Iannucci, S. Grassini, M. Santamaria, The Effect of Electronic Properties of Anodized and Hard Anodized Ti and Ti6Al4V on Their Reactivity in Simulated Body Fluid, J Electrochem Soc 169 (2022) 071506. https://doi.org/10.1149/1945-7111/ac8316.
[147] B. Zheng, V. Trofimov, Y. Yang, C. Han, Z. Zheng, S.F. Abbas, S. Li, L. Lei, J. Sang, J. Zhang, D. Wang, Enhancing the dimensional accuracy and manufacturing limits of laser powder bed fusion through dual-laser hybrid additive-subtractive manufacturing, Opt Laser Technol 188 (2025). https://doi.org/10.1016/j.optlastec.2025.112947.
[148] M.A. Kurtz, A.C. Wessinger, L.M. Taylor, J.L. Gilbert, Electrode potential, inflammatory solution chemistry and temperature alter Ti-6Al-4V oxide film properties, Electrochim Acta 462 (2023). https://doi.org/10.1016/j.electacta.2023.142770.
[149] C. Fonseca, M.A. Barbosa, Corrosion behaviour of titanium in bio¯uids containing H 2 O 2 studied by electrochemical impedance spectroscopy, n.d. www.elsevier.com/locate/corsciCorrosionScience43.
[150] M.B. Leban, T. Kosec, M. Finšgar, Corrosion characterization and ion release in SLM-manufactured and wrought Ti6Al4V alloy in an oral environment, Corros Sci 209 (2022). https://doi.org/10.1016/j.corsci.2022.110716.
[151] A. Sotniczuk, J.L. Gilbert, Y. Liu, M. Matczuk, W. Chromiński, D. Kalita, M. Pisarek, H. Garbacz, Corrosion resistance of β-phase titanium alloys under simulated inflammatory conditions: Exploring the relevance of biocompatible alloying elements, Corros Sci 220 (2023). https://doi.org/10.1016/j.corsci.2023.111271.
[152] F. Yu, O. Addison, A.J. Davenport, A synergistic effect of albumin and H2O2 accelerates corrosion of Ti6Al4V, Acta Biomater 26 (2015) 355–365. https://doi.org/10.1016/j.actbio.2015.07.046.
[153] D. Pupillo, F. Di Franco, D. Palmeri, G. Pollara, G. Buffa, L. Fratini, M. Santamaria, Surface treatments on 3D printed Ti6Al4V biomedical plates to enhance corrosion resistance in simulated physiological solutions and under inflammatory conditions, Corros Sci 240 (2024). https://doi.org/10.1016/j.corsci.2024.112451.
[154] R.L. Frost, An infrared and Raman spectroscopic study of natural zinc phosphates, Spectrochim Acta A Mol Biomol Spectrosc 60 (2004) 1439–1445. https://doi.org/10.1016/j.saa.2003.08.009.
[155] H. Zhang, Z. Chen, Q. Huang, Study of the toxicity of ZnO nanoparticles toChlorella sorokinianaunder the influence of phosphate: spectroscopic quantification, photosynthetic efficiency and gene expression analysis, Environ Sci Nano 7 (2020) 1431–1443. https://doi.org/10.1039/c9en01464k.

[156] A. Chennah, Y. Naciri, A. Taoufyq, B. Bakiz, L. Bazzi, F. Guinneton, S. Villain, J.R. Gavarri, A. Benlhachemi, Electrodeposited zinc phosphate hydrate electrodes for electrocatalytic applications, J Appl Electrochem 49 (2019) 163–177. https://doi.org/10.1007/s10800-018-1261-8.
[157] L. Liu, Y. Meng, A.A. Volinsky, H.J. Zhang, L.N. Wang, Influences of albumin on in vitro corrosion of pure Zn in artificial plasma, Corros Sci 153 (2019) 341–356. https://doi.org/10.1016/j.corsci.2019.04.003.
[158] H. Fang, X. Qi, S. Zhou, S. Yang, C. Hang, Y. Tian, C. Wang, High-Efficient Vacuum Ultraviolet-Ozone Assist-Deposited Polydopamine for Poly(lactic-co-glycolic acid)-Coated Pure Zn toward Biodegradable Cardiovascular Stent Applications, ACS Appl Mater Interfaces 14 (2022) 3536–3550. https://doi.org/10.1021/acsami.1c21567.
[159] C. Cachet, F. Ganne, G. Maurin, J. Petitjean, V. Vivier, R. Wiart, EIS investigation of zinc dissolution in aerated sulfate medium. Part I: bulk zinc, 2001. www.elsevier.com/locate/electacta.
[160] M.E. Orazem, B. Tribollet, ELECTROCHEMICAL IMPEDANCE SPECTROSCOPY, 2008. https://doi.org/10.1002/9780470381588.
[161] Dieter. Landolt, Corrosion and surface chemistry of metals, EPFL Press, 2007.
[162] Biological evaluation of medical devices-16:45:28 MDT No reproduction or networking permitted without license from IHS COPYRIGHT PROTECTED DOCUMENT 16:45:28 MDT No reproduction or networking permitted without license from IHS, 2009.
[163] F. Di Franco, A. Zaffora, B. Megna, M. Santamaria, Heterogeneous crystallization of zinc hydroxystannate on galvanized steel for enhancing the bond strength at the rebar/concrete interface, Chemical Engineering Journal 405 (2021). https://doi.org/10.1016/j.cej.2020.126943.
[164] D.B. Louria, M.M. Joselow, A.A. Browder, The Human Toxicity of Certain Trace Elements, n.d. http://annals.org/.
[165] M. Rausch, D. Böhringer, M. Steinmann, D.W. Schubert, S. Schrüfer, C. Mark, B. Fabry, Measurement of Skeletal Muscle Fiber Contractility with High-Speed Traction Microscopy, Biophys J 118 (2020) 657–666. https://doi.org/10.1016/j.bpj.2019.12.014.
[166] J.A. Myers, B.S. Curtis, W.R. Curtis, Improving accuracy of cell and chromophore concentration measurements using optical density, BMC Biophys 6 (2013). https://doi.org/10.1186/2046-1682-6-4.
[167] J. Liu, Y. Sun, X. Zhou, X. Li, M. Kappl, W. Steffen, H.J. Butt, One-Step Synthesis of a Durable and Liquid-Repellent Poly(dimethylsiloxane) Coating, Advanced Materials 33 (2021). https://doi.org/10.1002/adma.202100237.
[168] A.B. Tesler, S. Kolle, L.H. Prado, I. Thievessen, D. Böhringer, M. Backholm, B. Karunakaran, H.A. Nurmi, M. Latikka, L. Fischer, S. Stafslien, Z.M. Cenev, J.V.I. Timonen, M. Bruns, A. Mazare, U. Lohbauer, S. Virtanen, B. Fabry, P. Schmuki, R.H.A. Ras, J. Aizenberg, W.H. Goldmann, Long-term stability of aerophilic metallic surfaces underwater,

Nat Mater 22 (2023) 1548–1555. https://doi.org/10.1038/s41563-023-01670-6.

[169] A.B. Tesler, L.H. Prado, I. Thievessen, A. Mazare, P. Schmuki, S. Virtanen, W.H. Goldmann, Nontoxic Liquid-Infused Slippery Coating Prepared on Steel Substrates Inhibits Corrosion and Biofouling Adhesion, ACS Appl Mater Interfaces 14 (2022) 29386–29397. https://doi.org/10.1021/acsami.2c04960.

[170] L.H. Prado, D. Böhringer, A. Mazare, L. Sotelo, G. Sarau, S. Christiansen, B. Fabry, P. Schmuki, S. Virtanen, W.H. Goldmann, A.B. Tesler, Silicone-Based Lubricant-Infused Slippery Coating Covalently Bound to Aluminum Substrates for Underwater Applications, ACS Appl Mater Interfaces 15 (2023) 31776–31786. https://doi.org/10.1021/acsami.3c04508.

[171] S. Nikpour, J.D. Henderson, S. Matin, H.Y. Nie, J. Hedberg, V. Dehnavi, Y.K. Hosein, D.W. Holdsworth, M. Biesinger, Y.S. Hedberg, Effect of passivation and surface treatment of a laser powder bed fusion biomedical titanium alloy on corrosion resistance and protein adsorption, Electrochim Acta 475 (2024). https://doi.org/10.1016/j.electacta.2023.143650.

[172] M. Curioni, L. Salamone, F. Scenini, M. Santamaria, M. Di Natale, A mathematical description accounting for the superfluous hydrogen evolution and the inductive behaviour observed during electrochemical measurements on magnesium, Electrochim Acta 274 (2018) 343–352. https://doi.org/10.1016/j.electacta.2018.04.116.

[173] ELECTROCHEMICAL IMPEDANCE SPECTROSCOPY, n.d. http://w.electrochem.org.

[174] M. Strebl, M. Bruns, S. Virtanen, Editors' Choice—Respirometric in Situ Methods for Real-Time Monitoring of Corrosion Rates: Part I. Atmospheric Corrosion, J Electrochem Soc 167 (2020) 021510. https://doi.org/10.1149/1945-7111/ab6c61.

[175] B.S. Kim, S.S. Yang, J.H. Yoon, J. Lee, Enhanced bone regeneration by silicon-substituted hydroxyapatite derived from cuttlefish bone, Clin Oral Implants Res 28 (2017) 49–56. https://doi.org/10.1111/clr.12613.

[176] L. Liu, L. Lu, H.J. Zhang, L.N. Wang, Influence of bovine serum albumin on corrosion behaviour of pure Zn in phosphate buffered saline, J Mater Sci Mater Med 32 (2021). https://doi.org/10.1007/s10856-021-06567-x.

[177] B.D. Corbin, E.H. Seeley, A. Raab, J. Feldmann, M.R. Miller, V.J. Torres, K.L. Anderson, B.M. Dattilo, P.M. Dunman, R. Gerads, R.M. Caprioli, W. Nacken, W.J. Chazin, E.P. Skaar, Metal chelation and inhibition of bacterial growth in tissue abscesses, Science (1979) 319 (2008) 962–965. https://doi.org/10.1126/science.1152449.

[178] A.B. Tesler, L.H. Prado, M.M. Khusniyarov, I. Thievessen, A. Mazare, L. Fischer, S. Virtanen, W.H. Goldmann, P. Schmuki, A One-Pot Universal Approach to Fabricate Lubricant-Infused Slippery Surfaces on Solid Substrates, Adv Funct Mater 31 (2021). https://doi.org/10.1002/adfm.202101090.

[179] A. Abbas, G.G. Wells, G. McHale, K. Sefiane, D. Orejon, Silicone Oil-Grafted Low-Hysteresis Water-Repellent Surfaces, ACS Appl Mater Interfaces 15 (2023) 11281–11295. https://doi.org/10.1021/acsami.2c20718.
[180] D.W. Zhao, C.M. Du, K.Q. Zuo, Y.X. Zhao, X.Q. Xu, Y.B. Li, S. Tian, H.R. Yang, Y.P. Lu, L. Cheng, G.Y. Xiao, Calcium–Zinc Phosphate Chemical Conversion Coating Facilitates the Osteointegration of Biodegradable Zinc Alloy Implants by Orchestrating Macrophage Phenotype, Adv Healthc Mater 12 (2023). https://doi.org/10.1002/adhm.202202537.